Development of Direct Numerical Simulations for Multiphase Fluid Flow Benchmarking

David Andrew Rupp

UNIVERSITY OF LEEDS

School of Chemical and Process Engineering

June 2021

Declaration

The candidate confirms that the work submitted is his own, except where work which has formed part of jointly authored publications has been included. The contribution of the candidate and the other authors to this work has been explicitly indicated below. The candidate confirms that appropriate credit has been given within the thesis where reference has been made to the work of others.

Conference proceedings - PARTICLES 2017 - The impact of coupling and particle volume fraction on fluid-particle interactions in a turbulent channel flow - D. A. Rupp, D. O. Njobuenwu and M. Fairweather: Results Chapters 1 and 2.

Conference proceedings - ETMM12 - Particle volume fraction effects in simulations of turbulent channel flows - D.A. Rupp, D.O. Njobuenwu and M. Fairweather: Results Chapters 1 and 2.

In the case of jointly authored publications, the other authors contributed to biweekly supervisory meetings, as well as offering their advice and sharing ideas for progression. They also proofread the papers prior to publication. All work on simulation, data-handling, analysis, and the writing of the paper itself is attributed to myself.

Acknowledgments

I would here like to offer my gratitude to the many people who gave me their support on the arduous journey to this PhD's completion.

Firstly, let it be known that Professor Mike Fairweather is a supervisor of the highest calibre. But for his constant support and vast well of experience, guiding me along the way, I doubt I would have been able to see the project through to the end. I applaud his patience! Also, Dr Derrick Njobuenwu played a vital role in my in-office support during the first few years of the PhD. Dr Lee Mortimer too must be applauded for his patience and support, and I greatly appreciate his guidance throughout the whole process, even as he worked on his own PhD.

This is to say nothing of my other colleagues in room 2.22, all of whom were always there whenever I required help, or simply somebody to talk to. Be it on topic advice or off topic trivia, it was a rare moment where I found myself with nobody to reach out to. The regular attendees of the nuclear research group meetings also proved to be a very helpful community, and I feel that missing out on the company of all these people proved for me to be one of the greater tragedies of the pandemic.

I lost two grandparents, John and Joyce, over the course of my PhD, and am grateful to the motivation they gave me to work hard, as well as the engineering legacy left to me by my grandfather.

My mother and father were incredible throughout my work on my PhD, supporting me, visiting me in Leeds, and regularly inviting me home to Wigston. I also wish to offer thanks to the old guard of Callum, Jack, and Arran, friends who I could always rely on for practically anything whenever I was in town. Special thanks to Helen, my younger sister, a presence in my life so constant that even in moving to Leeds I could not shake her off. Without her I may not have retained what little sanity I have.

Abstract

This study investigates the dynamics of multiphase turbulent flows and various coupling methods between the solid particles and the liquid at different particle concentrations and Stokes numbers. Simulations are performed altering the treatment of the particle phase to assess how the coupling method used affects model predictions. Direct numerical simulation (DNS) of a single-phase turbulent channel flow at a shear Reynolds number of 300 is performed and coupled to a Lagrangian particle tracker (LPT) to simulate the particle phase. These techniques are first validated against previous DNS-based results with good agreement obtained. A series of deterministic simulations using one-, two- and four-way coupling between the fluid and the particles is then performed at two particle concentrations and two Stokes numbers. Differences in the velocity, turbulence and drag forces on both the fluid and the particles, caused by changes in the latter variables, are assessed and differences explained in terms of the effects of forces acting on the particles, particle collisions and turbophoresis. To reduce model run times, a stochastic collision metric is added to the LPT and tested for its effectiveness. Both fictional particle and direct simulation Monte Carlo techniques are investigated, with the latter producing superior results after some modification, and in all but one case is found to reduce model run times, albeit with some loss in accuracy. Finally, the agglomeration of particles is considered using both deterministic and stochastic approaches. The stochastic technique requires further development where agglomeration is implemented, and although successful the rate of particle collision remains high, with agglomerates being formed faster than turbophoretic effects can disperse them. Overall, the study improves our understanding of particle-laden flows, provides benchmark solutions against which more pragmatic predictive approaches can be assessed, and represents a significant step in the development of more computationally efficient stochastic techniques.

Table of Contents

List of Tables

List of Figures

xiv

Chapter 1 Introduction

1.1 Background

Accurately simulating particle-laden flows is of fundamental importance to any area of industry that will at some point be required to transport a multiphase component of its process or waste to a new location. Multiphase flow simulations are frequently performed in industries which refine and transport chemicals, such as agriculture (Lee et al., 2013), pharmaceuticals (Chakravarty et al., 2019), and mineral processing (Guha et al., 2007). The core electrical energy generation methods, coal, oil and gas (Raynal et al., 2016), are also obvious examples that handle multiphase flows. Due to the presence of high flow rates these are also likely to be subject to turbulent effects. The nuclear industry poses a particular challenge, with methods needing to be developed for modulating the flow of nuclear reactor coolant, as well as particulate sludge containing heavy metal salts, left over fissile materials, and other dangerous waste products (Efremenkov, 1989).
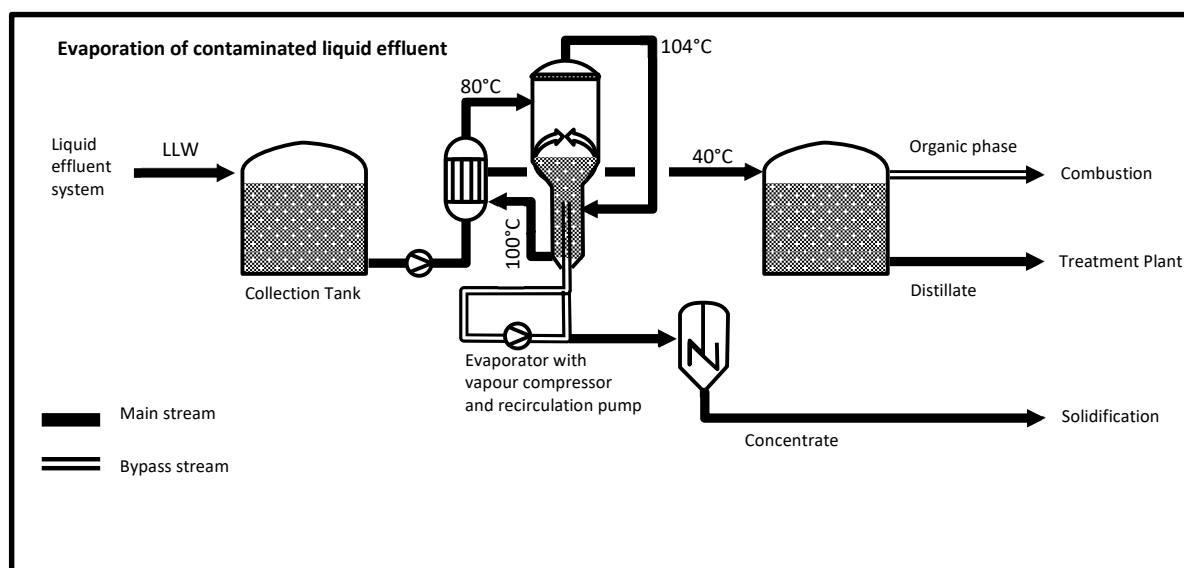
Figure 1: An example of a typical process involved in the treatment of nuclear waste (as Efremenkov, 1989). This features many instances of multiphase fluid transport.

Multiphase flows such as those required by systems as in Figure 1, have complex properties, and if left unchecked are liable to cause issues such as erosion, deposition and agglomeration leading to clogging or reduced flow rates, which could lead to problematic pressure gradients or even catastrophic failures later down the line. Those flows found in the nuclear industry are often too dangerous to examine in situ (Höhne et al., 2010). Extreme temperature, radioactive or high-pressure flows are all difficult to probe and understand without the aid of computational fluid dynamics (CFD).

Without proper optimization, industrial processes can be inefficient, unsafe and costly, due to the amount of maintenance required, or the process of part replacement, which can often be hazardous in the case of exposure to radioactive or otherwise dangerous materials. In the nuclear industry particularly, it is often difficult to clean out and dispose of structures that are

out of commission. If a system is not effectively designed around the high concentrations of particles that occur in certain wall-bounded flows the behaviour of these particles, and their resultant impact on the flow itself, can have unpredictable, even dangerous effects. In other words, without a thorough understanding of the fluid flows used in industry, many of these issues (up to and including the early decommissioning of the system), can occur. This project explores the methods used to get the most accurate simulations of industrial fluid flows and examines new ways to make these computations more efficient and achieve greater understanding of the underlying properties that drive an industrial multiphase flow.

1.2 Nuclear Industry

Within the nuclear industry, CFD is used to simulate both single phase and multiphase fluids such as titrated nuclear coolant and molten salts, which are naturally important for maintaining the health of a nuclear facility. Further to this, also considered is the removal, transport and relocation of waste nuclear materials after the fission cycle completes. Of particular interest is the 50 years' worth of legacy nuclear waste currently stored by Sellafield Ltd. The waste in question was initially spent nuclear fuel from the original Magnox reactors (NDA, 2017), and from the UK's nuclear weapons programme. These were deposited in the first-generation Magnox storage pond (FGMSP), and the pile fuel storage pond (PFSP) respectively, such as shown in Figure 2.
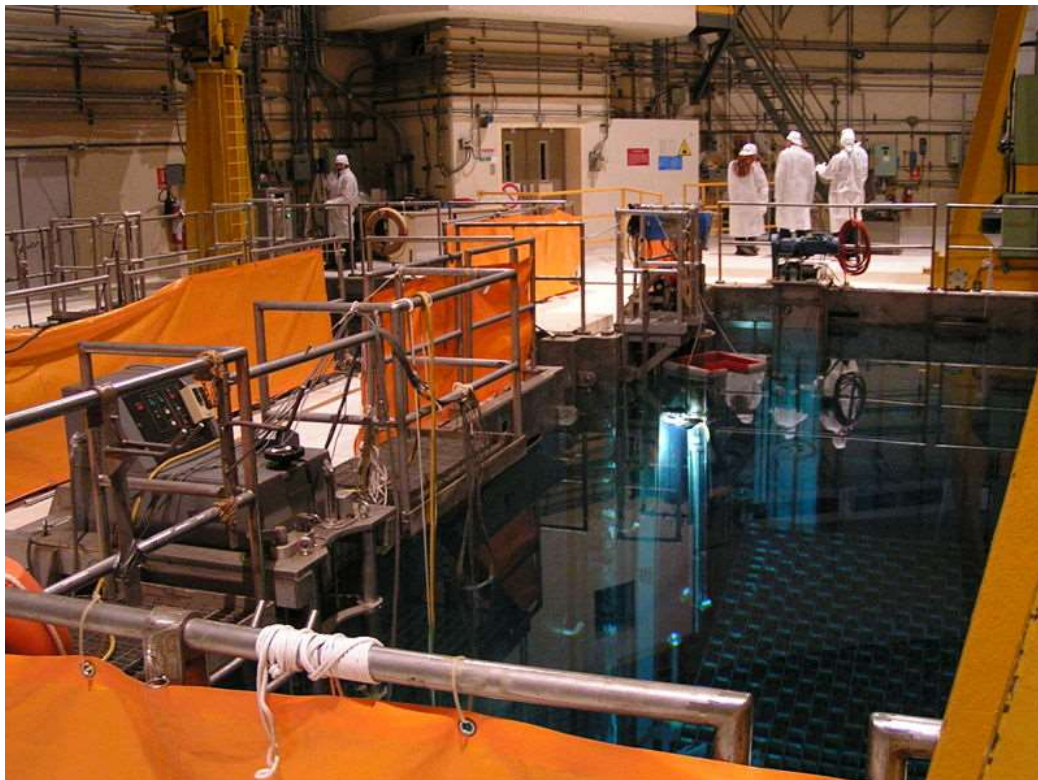
Figure 2: A typical spent fuel pool in a nuclear facility. The fluid stored here must be transported to new locations for processing.

This method of disposal was designed only as a short-term solution and to facilitate the cooling of the fuel, while a more permanent method of disposal was devised. However, the submerged fuel containers as well as the fuel have since undergone a high level of corrosion over the long timeframe since original storage. This has resulted in the production of large quantities of highly radioactive sludge. In the ponds at the first generation Sellafield Magnox Storage and Decanning Facility, for instance, this was estimated to be at least 1,200 cubic metres of sludge mixed in with proportional amounts of solid scrap metal and spent fuel which was still in a state of decay (WMSYM, 2007). The sludge consists of mainly dissolved metal salts along with a suspension of corroded material from the fuel cladding, long since irradiated, as well as miscellaneous waste and algae.

The Nuclear Decommissioning Authority (NDA), which is the government agency in charge of processing this waste, intends "to deliver a world class programme of safe, cost-effective, accelerated and environmentally responsible decommissioning of the UK's civil nuclear legacy in an open and transparent manner and with due regard to the socio-economic impacts on our communities" (NDA 2006). An estimate for the total clean-up cost of Sellafield's legacy waste was established in 2015 to be around £53 billion (NAO, 2015), over three quarters of the UK's total nuclear clean-up cost, although this figure has in recent times increased dramatically (at 75.6% of a total clean-up cost of £124 billion according to (NDA, 2019)). For the NDA to achieve success with this goal, all of this legacy waste must be mobilised and processed. So far there has been some degree of success. Approximately 10% of the waste stored in the FGMSP has been cleaned out, with completion anticipated in 2033. The waste in the PFSP has begun to be processed in a nearby treatment plant.

Processing nuclear sludge involves several stages of pumping and channelling to facilitate the removal of supernatant liquid, then the liquid sequestered in the porous salt cake, the dissolved salt cake itself and finally the remaining slurries of sludge, salt, and water. The water is retained throughout this process for its radiation absorbing properties. Wall-bounded multiphase systems such as this can have complex properties dependent on the temperature, pressure, rate of flow, shape of particles, and particle concentration and density (WMSYM, 2016). The specific chemical properties such as alkalinity make understanding the optimisation of sludge handling techniques a major technical challenge, as the NDA states in its "Needs, Risks, and Opportunities" paper (NDA, 2006).

Beyond waste management considerations, flows with multiple phases can be generated undesirably as part of the natural running and degrading of a system, such as the coolant circuits in nuclear reactors. CRUD (corrosion related unidentified deposits), is material ejected within these systems due to erosive effects, and has been known to aggregate and subsequently deposit on the fuel rods, which will naturally cause issues not limited to the further production of CRUD in regions where heat transfer is uncontrolled (Short et al., 2013), as well as neutron activation in the aggregate leading to increased radioactivity, and CRUD-induced power shifts because of boron neutron absorption (Secker et al., 2004).

This process demands a thorough understanding of the flow conditions in order to maximise efficiency. Likewise, the pipelines carrying hazardous waste may be subject to blockages and corrosion caused by an underpredicted solid to fluid ratio or too low rate of flow leading to the unwanted settling of solid particles, forming beds. The agglomeration of particulates could lead to a change in the flow regime, making the properties of the flow unpredictable. The surface of the pipe, duct, or channel carrying the material might itself react with the material passing through it causing a change in the flow dynamics. These and many other issues are dependent on both the bulk and micro-scale properties of the particle-laden wall bounded flows in question.

1.3 Computational Modelling

The dynamic properties and complex mechanisms of turbulent wall-bounded flows demand high levels of mathematical accuracy for the purpose of making predictions of chaotic behaviour. A minute change in initial conditions will inextricably lead to differing results. In the case of experimental studies, this sensitivity to initial conditions can lead to unreliable reproducibility, for said conditions are tremendously difficult to isolate, more so as the Reynolds number increases. The solution to this is to measure the time and space averages of the relevant statistics. In the case of nuclear waste, however, such studies are particularly difficult to perform and even dangerous in situ. Work with ultrasonic probes by those such as Denslow et al. (2012) goes some way towards alleviating this and provides good data to validate computational models against.

When the flows are modelled using CFD, this problem disappears. Initial conditions in a fluid model can be saved and repeated. Minute changes in properties can be checked and rechecked against experimental results and those in similar models. The advancement in modern computers has enabled the simulation of higher Reynolds numbers, more complex fluid domains, and higher concentrations of particles. CFD has quickly become a popular choice for industrial and academic usage. The non-linear nature of turbulence, however, means that a practically infinite set of equations is required to calculate an exact solution to the Navier-Stokes equations. This issue is often termed the closure problem. In the majority of cases, assumptions are made which approximate the solution in no more than four equations.

The typical method of fluid flow modelling used by industry is the Reynolds-averaged Navier-Stokes technique, or RANS. These resolve solely the mean qualities of the flow using, most commonly, the k-ω or k-ε turbulence models which close the mean flow equations using a further two particular differential equations, although higher moment closures are available. Smaller scale turbulence effects that cause the fluctuation of the properties of the flow are disregarded. As such, information surrounding fluid flow behaviours smaller than the turbulence length scale employed is relatively imprecise. It compensates for this through its relative simplicity, making it a somewhat effective and fast tool for uncomplicated systems, due to requiring less computing power than alternative approaches. This in turn makes it fairly

adaptable across domains, if only because the basic demand is low enough that customizations to the code do not substantially increase its computational requirements.

For a more accurate representation of the flow, methods such as large eddy simulation (LES) and direct numerical simulation (DNS) are preferred. Both of these methods involve constructing a mesh for resolving small scale effects with high accuracy, and then solving the Navier-Stokes equations at all the relevant scales. LES approximates the smallest turbulent effects on the sub-grid scale through a turbulence model, only fully resolving some of the fluid's turbulent behaviour, and in particular the large scale energy-containing motions. This therefore produces information more precise than one would receive from RANS, whilst still maintaining a relatively low computational cost, albeit significantly greater than for RANS. LES can be considered the middle ground between RANS and DNS in terms of computational speed and precision.

DNS is the most first principles-based method of performing fluid flow simulations, intended to resolve every turbulence structure exhibited in a flow over the smallest time and length scales necessary. The mesh constructed for a DNS has an element spacing on the order of η, the Kolmogorov length scale, at which kinetic energy from the eddies is dissipated into internal energy (Kolmogorov, 1941). This also means that it uses an extremely high number of fluid elements or computational nodes compared to LES. The computational power required to perform a DNS is right on the edge of current technology. The number of floating-point operations required to accurately model a flow with a Reynolds number Re is proportional to Re^3 (Re being the ratio between inertial and viscous forces acting on a system, a measure of turbulence).

The highest Reynolds number of a flow that can be simulated by using DNS is contingent entirely on the upper limits of current computers. This makes it impractical for use in industry, or for highly turbulent flows. Though its solutions are of the highest precision, this is achieved by sacrificing resource efficiency and a great deal of time. However, DNS is the best method for examining the physical properties of a flow in and of itself. Many of the models used in LES and RANS are generated on the basis of DNS, and by resolving the Kolmogorov scale, DNS produces very dense information about flow dynamics that cannot be achieved through the faster simulations provided by RANS and LES methods.

1.4 Particle Simulation Methods

Key to this project is the modelling of multiphase flows. As the particle concentration increases, or rather the comparative densities of particulate to fluid matter increases, the chance of a blockage within a wall bounded flow increases. This is due to an increasing rate of collision between particles, hence particle agglomeration, as well as deposition. Whilst modifying the pH of the fluid in accordance with the isoelectric points of the particles can help to prevent this (Berg et al. 2009), precise knowledge of the way high particle concentrations interact with the flow, and themselves, is vital for optimizing the movement of complex,

potentially dangerous payloads such as nuclear sludge. Since it is non-trivial to predict the exact particle volume fractions of waste materials in systems like that shown in Figure 2, multiple particle concentrations will be tested in order to account for the properties of flows where inter-particle collisions both are and are not a significant factor.

DNS, or direct numerical simulation, is designed to simulate the behaviour of a fluid down to the smallest relevant turbulence scale, the Kolmogorov length scale. Naturally this also means that a simulation of particles would be able to model accurately the interactions of particles with the fluid and each other at these small scales and all others. Traditionally the Lagrangian method has been used to simulate the movement of particles and the collisions thereof. This method, whilst undeniably accurate, suffers from similar computational problems to DNS. As the concentration of particles increases, the code will compare more particle positions with each other. The number of checks that need to be made is proportional to the square of the number of particle points in the same area, which sacrifices a lot of time in the long runs necessary for simulating high concentrations.

One alternative to the Lagrangian method of colliding particles is the stochastic method, which models the collisions continuously, calculating the likelihood of a particular particle colliding, and then resolving the correct number of collisions for the flow, based on those probabilities and the averaged statistics of the particles in the same region.

1.5 Specific Aims and Goals

The National Nuclear Laboratory (NNL), amongst others in the supply chain, currently uses standard RANS fluid flow predictive methods which give only approximate solutions and need to be validated in order to assess the accuracy of the solutions. The data used for testing may have deficiencies in it (from either experimental or analytical sources). DNS is a technology that yields exact solutions to the equations governing fluid flow, provided sufficiently accurate numerical solution methods are employed. Its use had been limited in the past due to the huge computing resource required to achieve the required level of grid refinement needed in obtaining sufficiently resolved (spatially and temporally) solutions. Given the availability of modern high-performance computers, however, this situation has changed in recent years, and it is now possible to obtain DNS solutions to practically relevant problems in reasonable computational run times.

In this project, methodologies will be developed using DNS such that fluid flow benchmark problems can be subsequently studied to give much needed data to compare existing, more pragmatic predictive methods against. Applications where there is a particular sparsity of data include multiphase flows (i.e. flows containing fluids and solids), such as found in nuclear waste management and decommissioning. A channel flow is the most basic representation of a wall-bounded flow system, and as such is representative, at a simplistic level, of the wall-bounded flows encountered in waste management and processing systems. The analysis of results obtained for flows in such a geometry is, however, useful for assessing more

practically-relevant flow geometries such as ducts, pipes free-surface flows and even more complex geometries.

The project will therefore focus on such flows, obtaining high accuracy solutions to a range of generic flows of value to the validation of various particle-fluid models used in industry. Given the fundamental nature of such simulations, the information derived from them will also be analysed to provide improved understanding of a range of practically relevant flows. Where computational expense can be spared by the implementation of novel techniques such as cell-based particle collisions and the stochastic method of interparticle collision, results will be compared with more rigorous methods.

The specific goals of this study are as follows:

1.) Utilise the CFD code, Nek5000, to produce a statistically settled single-phase flow at shear Reynolds number Re_τ = 300. This will then be validated against DNS findings previously performed at the same Reynolds number. It will also be affirmed that the grid-scale used for this particular study is within the bounds of the Kolmogorov scale.

2.) Employ a one-way coupled Lagrangian particle tracker (LPT) which synchronises with the Nek5000 fluid code in order to create correct advective forces on the particles by applying the instantaneous flow field to them. This will ensure that all the relevant fluid-particle forces within the time and length scales used are implemented. The DNS used for validation of the single phase simulation shall likewise be used to validate this multiphase model.

3.) Use the LPT to model different multiphase flows for the purposes of validation, as well as to conduct a detailed analysis on the effects that different particle sizes and volume fractions have on the flow properties when one-way coupled.

4.) Use an extended version of the LPT to employ two-way coupling and four-way coupling between the fluid flow and the particles. The same varied particle distributions will be simulated in order to determine the most efficient, accurate, and above all practical method of discerning the turbulent effects of any multiphase flow. The collision detection used by the LPT will be optimised to avoid long run times.

5.) Perform a study of stochastic particle-particle collision methods such that the four-way coupled simulation may be further optimised for time. Proven methods of stochastic simulation will be tested for effectiveness in a channel flow situation. (why channel)

6.) Develop a contemporary stochastic model that works well with the channel flow domain, as well as any wall-bounded geometry, based on the results gleaned from testing the other models.

7.) Validate the results for the stochastic model against the deterministic particle collision model over the same varied particle domains.

8.) Modify the LPT to implement a deterministic particle-particle agglomeration model. Particles will aggregate based on energy-balance conditions. Modify the stochastic version of the LPT to agglomerate particles using the same considerations.

9.) Simulate multiphase channel flows using the deterministic and stochastic agglomeration codes across all tested particle sizes and volume fractions. Test aggregation rates to see if the deterministic and stochastic results are comparable. Determine to what extent the agglomeration of particles affects the fluid flow field.

10.) Compare the run times of the stochastic collision techniques with the deterministic ones. Perform an analysis on whether the predicted loss in accuracy is a fair trade in the interests of keeping an otherwise slow DNS quick at simulating high densities of particles.

1.6 Thesis Structure

Chapter 2 is a literature review where previous materials on the modelling techniques used to analyse turbulent single phase and multiple phase flows are compared across their history for the purpose of isolating areas of study with room for growth.

Chapter 3 provides the equations which govern the behaviour of the fluid flow and particles being modelled in this study, as well as the modelling methods and channel flow geometry used herein.

Chapter 4 validates the DNS method used to simulate the fluid-particle systems used in this thesis against previous successful models of channel flow. With that done, simulations are performed assessing the effect of changing the level of coupling on the accuracy of the results.

Chapter 5 develops and implements a stochastic method of interparticle collisions, and compares its accuracy and speed to the four-way coupled results from chapter 4.

Chapter 6 considers the effects of agglomeration on the fluid-particle statistics. The stochastic method of interparticle collision is modified to account for this and implemented to see if the method will remain effective under these conditions.

Chapter 7 finally describes the overall conclusions from the work performed, and suggests areas for future work.

Chapter 2 Literature Review

2.1 Introduction

This literature review shall detail the experimental and numerical findings upon which this thesis shall be built. The experimental results and the predictions of single phase and multiphase channel flows, through various literature shall be examined in a chronological order, starting with the simpler single phase then focusing on the multiphase channel flows.

With an understanding of how the level of particle-fluid coupling affects the interaction between the fluid and particle phases, the contrasting deterministic and stochastic methods of predicting the behaviour of the particle phases in turbulent channel flows can be reviewed in terms of both mathematical theory and the comparative accuracy and computational cost of such techniques in various conditions, which will lead onto their use within this thesis.

2.2 Single-phase Turbulent Fluid Flows

The study of single-phase flow, or fluid flow in and of itself, is the most basic part of fluid dynamics, and as a result the most fundamental when considering a method of simulation. Discussed here will be how the process of simulating single-phase flow has changed over time, as well as how thorough the analysis of the fluid flow has been under different circumstances.

2.2.1 The Reynolds Number

The first studies of turbulence, performed by the likes of Leonardo da Vinci, examined the streamlines of velocity in various fluid systems. By injecting coloured dye into the flow, it is possible to view these velocity streamlines directly. By changing the parameters of the flow being studied, these velocity streamlines would go from a stable, laminar arrangement, to an unpredictable and turbulent flow. The point at which the various instabilities in a laminar flow form eddies and vortices is known as the 'onset of turbulence' and defines a category of flow between laminar and turbulent, a transitional phase. Later researchers such as Reynolds (1895) and Stokes (1851) worked to quantify these three categories, and the flow properties that defined them. The result of this was the concept which would eventually become known as the Reynolds number. This is defined as the ratio between the inertial forces, and the viscous (friction) forces. Given any fluid system with a general velocity scale U, a length scale L, and a fluid kinematic viscosity ν_F, the Reynolds number can be calculated to be:

$$Re = \frac{UL}{\nu_F} \tag{1}$$

2.2.2 Reynolds Decomposition and Turbulence Kinetic Energy

Reynolds decomposition refers to the process where the velocity of a turbulent flow field, $\boldsymbol{u}_F(\boldsymbol{x}, t)$, is split into into its mean and time dependent components:

$$\boldsymbol{u}_F(\boldsymbol{x}, t) = \overline{\boldsymbol{u}_F}(\boldsymbol{x}) + \boldsymbol{u'}_F(\boldsymbol{x}, t) \tag{2}$$

Here, $\boldsymbol{u}_F(\boldsymbol{x}, t)$ represents the local instantaneous fluid velocity at any Cartesian point $\boldsymbol{x}$ or time t, and $\overline{\boldsymbol{u}_F}(\boldsymbol{x})$ is the mean fluid velocity, time averaged over a sample time which greatly exceeds that associated with turbulent effects. What remains when the mean fluid velocity is subtracted from the instantaneous fluid velocity is $\boldsymbol{u'}_F(\boldsymbol{x}, t)$, the instantaneous velocity fluctuation due to turbulence, a useful measure of turbulence which can be further transformed to:

$$\boldsymbol{u'}_{rms}(\boldsymbol{x}) = \sqrt{\overline{\boldsymbol{u'}_F(\boldsymbol{x}, t)^2}} \tag{3}$$

This is the root mean square fluid velocity fluctuation, or, when non-dimensionalised against the fluid bulk velocity, the intensity of the turbulence. In any literature measuring the turbulence in different flow regions, this term is calculated across multiple dimensions and is ubiquitous. Such terms are also referred to as the Reynolds normal stresses. Furthermore, the turbulence kinetic energy, k, can be derived from the measures of fluctuation, as follows:

$$k = \frac{1}{2}\langle \boldsymbol{u'}_F \cdot \boldsymbol{u'}_F \rangle = \frac{1}{2}\left(\overline{u'^2_F} + \overline{v'^2_F} + \overline{w'^2_F}\right) \tag{4}$$

2.2.3 The Kolmogorov Scale and the Theory of Energy Cascade

Work on quantifying the eddies and vortices within a turbulent flow eventually led to Kolmogorov's theory of energy cascade, an important development in the study of turbulence. It was initially observed that the behaviour of small eddies was governed by larger eddies (Richardson, 1922). Kolmogorov's theory describes how energy transfer takes place between turbulent structures at various length scales (Pope, 2001). Kolmogorov studied how the energy of turbulence would dissipate, with larger eddies breaking down into smaller eddies due to their inherent instability. Eventually the Reynolds number associated with the motion of a particular eddy becomes small enough that the energy can be dissipated by viscous forces into local heat. The rate of dissipation for this energy is given as ϵ, which is expressed as

$$\epsilon = \frac{1}{2}\nu \cdot \sum_{i,j}\left(\frac{\partial u'_i}{\partial x_j} + \frac{\partial u'_j}{\partial x_i}\right), u'_i = u_i - u_j \tag{5}$$

According to Kolmogorov (1941), at the smallest scales, turbulence becomes isotropic such that $\overline{u'^2_F} = \overline{v'^2_F} = \overline{w'^2_F}$. This Kolmogorov length scale, η, and the time scale τ_η, are defined to be:

$$\eta = \left(\frac{v_F^3}{\epsilon}\right)^{\frac{1}{4}} \tag{6}$$

$$\tau_\eta = \left(\frac{v_F}{\epsilon}\right)^{\frac{1}{2}} \tag{7}$$

The typical relationships apply, with a Reynolds number at the Kolmogorov scale Re_η, relating to the Kolmogorov velocity scale, which is $u_\eta = (\epsilon v_F)^{1/4}$, such that $Re_\eta = \eta u_\eta / v_F = 1$.

2.2.4 The Taylor Microscale

A scale slightly larger than the Kolmogorov scale, but still small enough that the majority of the energy is contained within the eddies at higher length scales, is known as the Taylor microscale, λ. In isotropic turbulence it is defined as:

$$\left(\frac{\partial u'}{\partial x}\right)^2 = \left(\frac{u'^2}{\lambda^2}\right) \tag{8}$$

with an equivalent Taylor microscale Reynolds number being:

$$Re_\lambda = \frac{u'_{rms}\lambda}{v_F} \tag{9}$$

2.2.5 Energy Spectra

The distribution of energy between the different length scales of turbulent eddy is known as an energy spectrum. This provides an association between any particular eddy wavenumber κ, and the typical energy for the size of that structure, given as $E(\kappa)$. κ is a translation from the eddy length scale l as $\kappa = 2\pi/l$. The works of Pao (1965), Lin (1972), and Hill (1978) demonstrate a strong agreement throughout different regions of the energy spectrum. Using these as a basis, Driscoll et al. (1983) developed a simple empirical model which can produce the spectral distribution for the isotropic turbulent kinetic energy spectrum $E(\kappa)$, at all wavenumbers, as a function of the Taylor microscale Reynolds number, Re_λ.

2.2.6 Experimental Studies

Experiments involving turbulent single-phase flow are performed over a wide range of geometries, with the most common being setups involving pipes and ducts. For the purpose of analysing near-wall effects, the channel flow represents an ideal theoretical notion with the span and length of the geometry being infinite. Obviously, this is somewhat difficult to arrange in an experimental setting. Some of the earliest studies of duct flows, as performed by Nikuradse (1926) and later Prandtl (1927), examine the turbulent structures and flow statistics of such. It transpires that, though duct flow is quite a close analogue to channel flow, it is not a perfect match, since the lines of velocity are drawn towards the corners of the ducts. Prandtl notes that this is due to secondary turbulent effects, caused by the changed

properties of fluid flow in the corners of the ducts. Such secondary effects were not found to be present in pipe flows, but the author concludes that the geometrical symmetry of a pipe still allows for useful analysis of turbulent effects, not to mention their prevalence in industry.

Laufer (1954) used hot-wire anemometry (HWA) to gather data on the mean and statistical quantities of a fully developed turbulent pipe flow. At the time, HWA was a popular flow measurement technique. One of the first such techniques developed, it involves passing a current between a pair of probes, through a thin tungsten, platinum, or platinum iridium wire. This now hot wire, once immersed in a flow field, will transfer its heat to the flow at a rate proportional to the local fluid velocity, allowing the velocity to be determined. What Laufer (1954) found was that the rates of turbulent-energy dissipation, production and diffusion were highest in the viscous sublayer.

A deeper investigation into the turbulent effects in ducts was later performed by Hoagland (1962). Through an analysis of three different duct geometries, with aspect ratios 1:1, 1:2 and 1:3, the author observed the consistently large effect the secondary turbulent motions were having on the primary flow, as well as consistency between the various aspect ratio ducts, in terms of the behaviour and magnitude of the secondary flows. The technique used to measure these secondary flows was HWA. But, as shown in later studies, HWA has a tendency to accumulate inaccuracies as turbulence increases. The author also neglected to measure the Reynolds stresses of the flow.

This was improved upon in a study by Brundrett and Baines (1964), whose HWA probes were positioned across multiple axes in all three dimensions. This enabled them to obtain values for the Reynolds stresses and other statistics in all directions, as well as to calculate the Reynolds stress tensor from these values. They were also able to determine an important relationship between the vorticity of the flow field and the distance from the wall. The secondary turbulent effects were found to remain comparatively unchanged with increasing Reynolds number, but the associated currents were drawn closer to the wall boundary. Gessner and Jones (1965) used the same experimental setup and investigated the secondary flow velocities at different Reynolds numbers. By non-dimensionalizing their results against the bulk velocity of the flow, they found that increasing the Reynolds numbers corresponded to a decrease in the secondary flow velocities.

Authors such as Clark (1968) used HWA to great effect, analysing the viscous sublayer, a region of low turbulence near to the wall, and gaining new insights about its structure. Clark (1968) was able to obtain a frequency spectral analysis of the fluctuating velocity components in the inner section of a fully developed turbulent boundary layer, as well as a sufficiently accurate velocity distribution of the sublayer that allowed a prediction of skin friction to be made. Eckelmann (1974) also used a variant of HWA, hot-film anemometry. This study was performed in oil at a low Reynolds number, which produced a thick viscous sublayer permitting detailed analyses of areas very close to the wall. Ueda and Hinze (1975) also used hot wire anemometry to measure the fine structure of the turbulence near the wall region of

a turbulent flow. They were able to clearly demonstrate the change in the mechanism for turbulence as it changed with the distance from the wall.

A later experimental study performed by Kreplin and Eckelmann (1979) measured the three fluctuating velocity components, as well as the fluctuating wall shear stress, of a fully developed turbulent channel flow at a bulk Reynolds number of 7700. This was performed using hot-film probes, and some useful discoveries were made surrounding turbulent structures, and the way they align themselves with the streamwise direction while remaining free to rotate. At this point it was becoming apparent that HWA methods were poorer at analysing the turbulent structures in a high Reynolds number flow, because the method could not resolve the turbulence microstructures in the viscous sublayer to an acceptably high resolution. Fortunately, at this point a new measurement technique was growing in popularity.

The emerging technique of laser Doppler anemometry, or laser Doppler velocimetry, developed by Yeh and Cummins (1964), and improved upon by the likes of Durst et al. (1976), used the principle of Doppler shifting to determine the speed of neutrally buoyant particles dispersed in a fluid flow. By gathering the light reflected from these particles in a photomultiplier tube, an electric current is produced based on the frequency of the scattered photons. This information, in conjunction with the incident light frequency and the orientation of the detector, can be used to measure the velocity of the tracer particles, and thus the fluid flow. Lacking the invasive properties of techniques that probed the flow directly with hot wires, LDA proved useful for gathering accurate secondary velocity information as well as data on Reynolds stresses and mean velocity (Melling and Whitelaw, 1976). LDA became quite popular in this period of time, used by those such as Po (1975), Lund (1977), and Gessner et al. (1979), to great effect.

These LDA experiments were compared and summarized by Demuren and Rodi (1984), who determined that the agreement between them was good. The review discusses adaptations to a mathematical stress model produced by Launder and Ying (1972), which was determined to diverge from the experimental data at points. Other experiments discussed by this review were the works of Gessner and Jones (1965), Tracy (1965) and Aly et al. (1978). These authors all diverged from the standard square duct geometry by using non-trivial cross-sectional geometries such as rectangles and triangles.

Cenedese et al. (1991, 1992) also performed several experiments using LDA. In these, turbulent boundary layers were explored. In their 1991 paper, LDA was used for comparing the spatial and temporal correlations so that the validity of Taylor's frozen turbulence hypothesis could be tested over different limits. The 1992 paper showed how LDA could be used to analyse the qualities of the flow near to the wall. The advanced method used was highly efficient at gathering data, using two independent systems to measure three velocity components at once. This led to calculations of correlation and spectral density functions.

In 1997, a new technique known as holographic particle image velocimetry or HPIV was used for the first time by Zhang et al. (1997). This method takes two-dimensional images of tracer particles within the fluid flow, but uses a more complex setup than its direct precursor, PIV (Grant, 1997), projecting the particle images onto holographic plates and allowing near enough instantaneous three-dimensional data on the fluid flow to be obtained, with no more intrusiveness than LDA. Hinsch (2002) summarises the technique. Zhang et al's results matched extremely well with those produced by both previous models and experimentation. An attempt was made to compare sub-grid scale models with this data with the intent of improving LES models, but not until the work of Tao et al. (1999) using HPIV to measure flows at 120,000 bulk Reynolds number was there sufficient data on high Reynolds number flows. With this new data, however, the quality of eddy viscosity models could be assessed in detail and their positives and negatives summarized.

A technique developed even more recently was used by Große and Schröder (2008) and involves the use of micro-pillar wall-shear stress sensors. These are extended to the inner wall boundaries, where the deflection of the tip allows a value for the shear stress to be calculated. These measurements proved to match up well with pre-existing literature on both experimental techniques and DNS. This technique was examined in more detail by Gnanamanickam et al. (2013), who discussed the dimensions required for such a sensor not to impact the flow. A manufacturing technique is described for the production of sensors 100μm in length. Many results were obtained for the wall shear stress values in both water and air, which were compared to hot-wire experiments and which show "promise".

A more recent study by Owolabi et al. (2016) investigated the turbulent flow through a square duct at particularly small turbulent Reynolds numbers of 81 and 161. The LDV method used produced results which were comparable to those from DNS. This is a case where experiments were performed to validate results from a simulation. The authors show that the Coriolis effect has a significant impact on the onset of turbulence. Their investigations into transitional Reynolds numbers confirm that a marginally turbulent flow, with its larger integral timescale, has more correlation than a fully turbulent one.

2.2.7 Numerical studies

It was not until the 1960s that computational performance increased to the point where it became feasible to run simulations of fluid flow, as opposed to RANS-based predictions. Before this time, the runtimes would simply have been too long. Deardorff (1970) carried out an LES assuming an infinitely large Reynolds number. This was performed using a 6720 grid-point model of a three-dimensional channel. The Reynolds stresses at the sub-grid scale were simulated using eddy coefficients as used by Smagorinsky et al. (1965) in their LES model of the circulating atmosphere. Deardorff (1970) discusses the statistical similarity between his results and those of Laufer (1950) but notes that the level of agreement between the two studies ranges from good to marginal. It is further stated that the primary contributors to these errors are the form of the SGS Reynolds stresses chosen, and also the boundary

condition assumptions inherent in LES, a factor that could be improved upon by means of an increase in computing power.

Three classes of numerical technique exist for the solution to the incompressible Navier-Stokes equations: the finite difference method, the finite element method, and the spectral element method. The finite element procedure is a weighted-residual technique applied to a series of expansions over small regions of space, or elements, with an implicit satisfaction of boundary conditions where this technique is given by a variational principle. The main attraction of it is its generality. The spectral methods expand the solution to a differential equation in a high order orthogonal expansion with coefficients that are determined by a weighted-residual projection technique. The spectral methods have potentially infinite order accuracy, which is their main attraction. Patera (1984) noted an intrinsic connection between those two methods and developed the spectral element technique, which combines generality with high accuracy, and is therefore an efficient and stable technique for solving the Navier-Stokes equations.

A later LES performed by Moin and Kim (1985), investigated the "hairpin vortices" which occur in the boundary region of a turbulent flow. They describe these vortical structures as "An agglomeration of vortex lines in a compact region (with higher vorticity than the neighbouring points) that has a hairpin or horseshoe shape", and produce evidence for these structures, which were observed to emerge at an angle of around 45° to the channel wall. The lines of vorticity were also found to form horseshoe shapes. Further investigation into turbulence producing effects such as these led to the development of the concept of the sweep (inverted horseshoe) and ejection (upright horseshoe) forms of vortical motion. Since these structures are all produced as a consequence of vortex stretching, it was concluded that these would be present in all conceivable turbulent shear flows, regardless of the wall state, and even at extended distance from the wall boundary.

In 1987, Kim et al. (1987) performed a simulation which solved the unsteady Navier-Stokes equations at a bulk Reynolds number of 3300. This must have been one of, if not the first, direct numerical simulations ever documented. It was certainly the first which produced results which were highly complementary to existing experimental data. A spectral element method numerical scheme was employed to expand the solutions to the Navier-Stokes and continuity equations, allowing all of the essential turbulence scales within the computational grid to be resolved, utilizing 4 million grid points without using a sub-grid model. The statistics calculated are compared with comparable experimental data, and though discrepancies were found in the near-wall region, these were assumed to be because the aspect ratios of the experimental set-ups were not sufficiently similar to a fully two-dimensional system.

Later that year Moser and Moin (1987) extended this DNS to a curved model at low Reynolds number, intended to determine the effects a concave or convex boundary condition had on the mean quantities measured in the flow. This was determined to be of interest from the authors of experimental works on these geometries, such as Wilcken (1967) and Wattendorf

(1935). The differences in flow statistics due to centrifugal forces were studied in detail, and the authors determine the magnitude of this effect.

Madabhushi and Vanka (1991) performed an LES which used a mixed spectral-finite difference method, with an additional Smagorinsky eddy-velocity model used for the sub-grid scales. The shear Reynolds number used was 360 (or 5810 in terms of bulk properties), and under these conditions secondary flows were produced which matched the authors' expectations. Further work by Kajishima and Miyake (1992) examined bulk Reynolds numbers of 6200 and 67,400, focusing on explaining the mechanisms of the secondary flows. These papers both proved the accuracy of the LES technique at increasing Reynolds numbers, for the simulated results were in good quantitative agreement with the experimental results.

Rai and Moin (1991) produced a paper making a comprehensive comparison between finite-difference and spectral methods of simulating fluid flow, using a wide range of different techniques and comparing the results. These methods included a central difference scheme which conserved kinetic energy and an upwind difference scheme which was high order accurate, and which proved to be effective at simulating complex geometries, though it can be said that the methods overall compared well to experiments.

DNS began to be used for more complex geometries. Gavrilakis (1992) used it to simulate a turbulent duct flow and produced turbulence data for the near-wall regions which agreed well with comparable planar flows, further gathering strong statistics regarding the concept of secondary flow. A similar LES performed by Su and Friedrich (1994) produced results in good agreement, determining the high resolution required to properly observe the secondary flows. By plotting the streaklines of the fluid particles they were able to see these flows clearly and effectively describe the turbulent structures present in the duct.

Eggels et al. (1993) developed a DNS code for a cylindrical geometry based on the finite volume method. The statistical results of the simulation were compared with experimental data from PIV and LDA techniques and showed good agreement. They suggested that it was the implementation of the finite volume technique that gave them improved results over those from Kim et al. (1987). Their following paper, Eggels et al. (1994), compared their DNS results for a cylindrical geometry with the same study and a study of a planar channel flow. By using the same Reynolds number for the pipe flow as for the planar setup, they were able to get a clear picture of the changes in the velocity distributions due to the geometry. The pipe velocity profile noticeably did not conform to the accepted law of the wall (a function that derives the turbulence conditions at a boundary from the conditions at that boundary alone) as a channel flow would, a trend confirmed by previous experimental literature. The fluctuating velocity components, however, showed comparatively little change between the two geometries. Ascertaining the dynamical differences between geometries demonstrates their importance when simulating systems with a high accuracy requirement.

In 1999, Moser et al. (1999) continued their work on straight, wall bounded flows, performing DNS at a variety of different turbulent Reynolds numbers, in this case 180, which correlates with the 3300 bulk Reynolds number they used in their 1987 study, along with the higher Reynolds numbers, 395 and 590. This was to measure the effects of a more turbulent flow. They determined that the higher Reynolds number simulations exhibited fewer low Reynolds number effects, as one might expect. This study outputted a very comprehensive set of statistics for posterity. The later date of this study is presumably due to the fact that computers powerful enough to run simulations at these higher Reynolds numbers would not have been computationally economical in 1987.

A report by Schmidt et al. (2001) compares the results of DNS with LES, using the spectral element method. The statistics produced from both Cartesian and cylindrical geometries were in excellent agreement with previous experimental and numerical studies, and in some cases the predictions of LES were able to match up well to DNS in terms of accuracy, especially for calculating mean flow rates.

Morinishi and Tamano (2005), performed an investigation into the differences between the turbulence statistics of compressible and incompressible turbulent channel flows at a few small Reynolds numbers. This study revealed that the reduction of the pressure-strain term was correlated directly to reductions in the velocity fluctuations. The absolute correlations between pressure and velocity-derivative fluctuations were discussed and found to be responsible for this effect. Of use to this study was the fact that the highest shear Reynolds number the authors studied was 300.

Zhu (2009) shows the results of a direct numerical simulation in a straight square duct, at a shear Reynolds number of 600, based on the duct width and mean wall shear velocity. The turbulence statistics along the wall bisector were examined. It was found that the duct flow solutions produced at a spatial resolution of 12×10^6 grid points are sufficiently comparable to existing results. The author also indicates that at this resolution and Reynolds number, the sub-grid scale can be neglected.

Boersma (2011) presents the results of several DNS studies for turbulent pipe flows, following the work of Eggels et al. (1993). The numerical model used Fourier expansions of the velocity field both axially and circumferentially, and 6th-order staggered compact finite difference techniques were used for the wall normal direction. These simulations were performed at bulk Reynolds numbers of 5300, 24,500, and 61,000.

A later paper by El Khoury et al. (2013) utilises the spectral element based code developed by Fischer et al. (2008), Nek5000. Direct numerical simulations were performed at a variety of shear Reynolds numbers, 180, 360, 550 and 1000. The results were then compared with data from previous runs. The pressure was shown to be the statistic which differed the most depending on the geometries of said flows. The turbulence kinetic energy profiles in the wall

region were entirely uniform between the simulations. Reynolds number dependencies were isolated and recorded.

Vreman et al. (2014) compared different DNS databases. Two different codes were comprehensively studied and found to produce mean flow velocities, root-mean-square (rms) velocity fluctuations and turbulent dissipation values with deviations of approximately 1%. In order to ascertain a clear difference between the simulations, fine grids, a long averaging time, and enhanced resolution are necessary. The conclusions made in this paper reflect directly on different physical properties of turbulent flows. Particularly, the repeatability and similarity between the results in the different simulations supports the hypothesis that the statistically stationary state of an incompressible turbulent channel flow is unique, but also the consistency of the differences between the two methods of simulation allow greater understanding of the structures responsible, potentially improving simulation accuracy.

The increased accessibility of simulations of turbulent flow, even DNS, can be seen in recent papers such as Graham et al (2016) which describes the development of an accessible online spatio-temporal database. The database was then used to test a new integral wall model, comparing it with the integral wall model to achieve good agreement and an understanding of the model's strengths. Prat et al (2020) later used this database while developing an LES model which employed an artificial neural network, a relatively new tool in the arsenal of simulation techniques. This proved to be remarkably effective at simulating the sub-grid scales, with high coefficients of correlation across the board.

2.3 Multiphase Flows

Moving on from single phase flows, the next step in the simulation of the systems presently of interest is to consider flows with multiple phases. This might include bubbles or particulate phases within a fluid or gas phase. Methods to describe these are detailed and reviewed in this section.

2.3.1 Particle-laden Flow Regimes and Their Parameters

In multiphase flow theory, a particle-laden flow can be categorised into one of a number of different expected flow regimes based on the physical properties of the solid phase: density, particle size, and volume fraction ϕ_P, which is defined as

$$\phi_P = N_P V_P / V_F \qquad (10)$$

Here N_P and V_P are the total number and volume, respectively, of the particles within the flow geometry, thus multiplied together to give a total volume for the particle phase, then compared with the total volume of the flow geometry, V_F.

Another property given to particles is the Stokes number, which is the ratio between the characteristic timescales of the fluid phase and of the particles within it.

$$St_B = \frac{\tau_P}{\tau_{F,B}} \tag{11}$$

$$St^+ = \frac{\tau_P}{\tau_{F,\nu}} \tag{12}$$

St_B and St^+ are the bulk Stokes number and viscous Stokes number given by the ratios between the characteristic bulk and viscous timescales of the fluid; $\tau_{F,B}$ and $\tau_{F,\nu}$ and the particle relaxation time; τ_P which are given as:

$$\tau_{F,B} = \frac{\delta}{U_B} \tag{13}$$

$$\tau_{F,\nu} = \frac{\nu_F}{U_B} \tag{14}$$

$$\tau_P = \frac{\rho_P d_p^2}{18\mu f_D} \tag{15}$$

The term f_D is the Stokes drag function and will be described in more detail in Chapter 3's section on the drag force.

The works of Elghobashi (1991, 1994, 2007) define these regimes based on both the volume fraction and the particle Stokes number calculated using the Kolmogorov time scale, St_K, which relates to the bulk Stokes timescale like so:

$$St_K = \frac{\tau_P}{\tau_\eta} \tag{16}$$
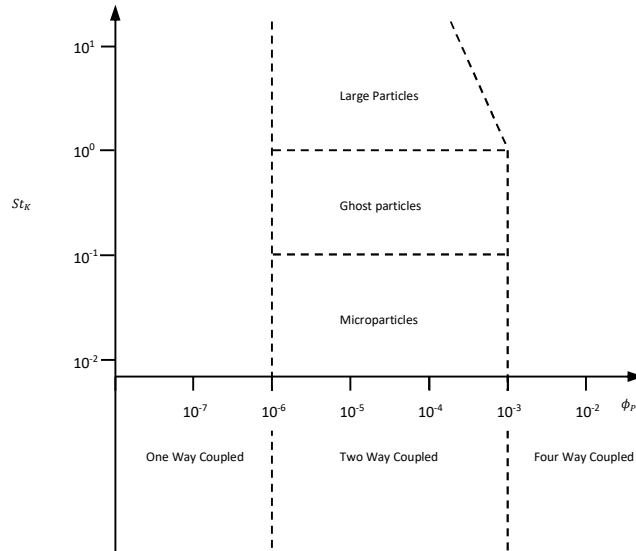
Figure 3: Particle-fluid interaction regimes in turbulence.

With reference to Figure 3, at values of ϕ_P smaller than 10^{-6} the flow can be considered one-way coupled, whereby the effects of the particles on the fluid phase as well as on each other are negligible enough to be disregarded, and only the effects of the fluid on the particle phase need be considered.

Where ϕ_P falls between 10^{-6} and 10^{-3} the particle phase has a sufficiently large effect upon the fluid phase that they must be considered two-way coupled and the transfer of momentum between the phases becomes significant. In this regime the size and density of the particles, or specifically St_K, defines the nature of the interaction between the two phases. The largest particles, with $St_K > 10$, cause vortex shedding to occur which increases the production of kinetic energy in the flow, while the smallest particles, in the region of $St_K < 0.1$, are referred to as microparticles. These particles primarily function as tracers, but at a sufficiently high volume fraction they will cause an increase in the energy dissipation rate, and a decrease in the decay rate of turbulence kinetic energy.

Other flow regimes produce different particle-fluid responses depending on their size in relation to these extreme cases. In the regime where $1 \leq St_K < 10$, the particles are large enough that the particle response time far exceeds the Kolmogorov time scale. These particles will cross fluid streamlines and escape from vortices, which overall causes a reduction in the energy dissipation rate of the turbulence field.

In the $0.1 \leq St_K < 1$ region, the reduction in turbulence kinetic energy from the large particles and the increase from small ones cancels out, leaving the turbulence field relatively

unaffected. As such these are known as ghost particles. At $St_K \approx 1$ the particles display a high rate of cohesion compared with other particle sizes, and are thus known as critical particles.

Finally, in the region where $10^{-3} \leq \phi_P < 10^{-1}$, particle-particle collisions are frequent enough that they have an effect on the interactions between the fluid and particle phases. The phases are here described as four-way coupled. The effects of this coupling grow in magnitude faster when the Stokes number is higher.

2.3.2 Turbophoresis and Preferential Concentration

Preferential concentration is a key effect in particle-laden flows, caused by high momenta particles decoupling from the flow's vortex motion and accumulating in specific regions of the geometry, as described by Fessler et al (1994). For a wall bounded geometry, this effect is driven by the process of turbophoresis, where particles, over time, naturally migrate to the walls of the geometry. This process was found by Crowe et al. (1985) to be correlated with the ratio between the particle relaxation time and the fluid viscosity time scale, or the viscous Stokes number St^+.

Particles with an $St^+ \ll 1$, tending towards zero, trace the fluid streamlines directly, producing a mostly homogeneous concentration profile, and particle motion statistics which match those of the fluid motion. Where St^+ is very large, the particle response time is much greater than the viscous time scale and the particles undergo strong turbophoretic effects which drag them to a near-wall region. Particles here behave differently to those within the bulk flow. Studies performed by Li et al. (2001), Rouson and Eaton (2001), and Zhao et al. (2015) predict that in a channel flow the streamwise turbulence intensity of particles in a near-wall region will be enhanced.

Further predictions by the likes of Marchioli and Soldati (2002), Picciotto et al. (2005), Dritselis and Vlachos (2008), and Lee and Lee (2015), show middle of the range Stokes number particles accumulating in low speed streaks, and Soldati and Marchioli (2009) also show that within the buffer layer and the viscous sublayer, particles travel according to the localised topology of the flow where the Stokes number is low. Two more papers by Sardinia et al. (2012, 2014) study both the turbophoretic effect and small scale clustering, and draw a connection between the two mechanisms in wall bounded flows, showing that they are both representative of the same process, which causes a high intensity of clustering in the wall region dependent on the particle inertia.

2.3.3 Experimental Studies

Experimental studies of multiphase flow are comparatively difficult to perform compared to numerical studies. Techniques such as PIV and HPIV which rely on tracer particles to analyse the statistics of the fluid phase cannot easily distinguish these from the particle phase being studied. One of the earliest examples of turbulent multiphase flow experimental modelling is the work of Friedlander and Johnstone (1957), who studied the deposition of particles within

brass and glass tubes. Though they were limited by the measuring equipment of the time, they successfully demonstrated key features of a particle laden flow. They demonstrated a relationship between the rate of deposition and the particle-wall transfer and re-entrainment rates, found a positive correlation between the rate of resuspension and particle size, and discussed the deviation between the particle and fluid phases closer to the walls, describing the way fluid eddies influence the transport of particles in those regions.

An interesting technique was employed by Snyder and Lumley (1971), who used hollow glass beads which were light enough to approximate points in the fluid phase and compared the particle velocity autocorrelations of these with those produced by heavier particles. The particle velocity correlations were found to be consistent with the Eulerian spatial correlation and the hollow beads could also be used to develop an estimate of the Lagrangian properties of the fluid.

Liu and Agarwal (1974) measured the deposition rate of aerosol particles in turbulent flow through vertical pipes, at bulk Reynolds numbers of 10,000 and 50,000, finding a relationship between the deposition velocity and the particle relaxation time St^+, over a range of St^+ from 0.21 to 774. The dependency of deposition velocity on particle size and St^+ was shown to vary with St^+, with the dependence dropping noticeably at St^+ greater than 30. This and similar experiments were collated by McCoy and Hanratty (1977) who produced a comprehensive analysis of the predictive capabilities of experimentally based correlations with regards to two-phase annular flows at that time. Among those compared were the work of Farmer (1969), Forney and Spielman (1974), Ilori (1971) and Sehmel (1980). Only the particles studied by Farmer (1969) were deemed large enough to be of relevance to the two-phase pipe flows being studied. In the Farmer (1969) paper a relationship between particle diameter and deposition rate was observed, albeit with a suggestion for further studies in order to improve the understanding of this phenomena.

Lee and Durst (1982) used laser Doppler velocimetry to assess the dispersion and deposition processes of glass particles in air within a vertical duct. Surprisingly, the particles here displayed velocity profiles more reminiscent of laminar shear flow than turbulent flow. This behaviour was analysed in detail and a cut off frequency was theorized beyond which the turbulent fluctuations would no longer affect the particles. At the same time, Tsuji and Morikawa (1982) were also using LDV to analyse two-phase flow. They successfully isolated the plastic particle phase from the ammonium chloride particles tracing the fluid phase by setting threshold values against the components of the photomultiplier signal. Using this technique they analysed a turbulent pipe flow with an inner diameter of 30mm, both horizontally, and in a later paper Tsuji et al. (1984), vertically. By increasing the mass-loading and decreasing the flow rate they created the conditions for a more asymmetric mean fluid velocity profile. The size of the particles here directly affected the fluid turbulence, with larger particles generally enhancing the turbulence, while smaller particles caused attenuation. Of

note is that medium sized particles produced both attenuation and enhancement effects depending on their location within the flow field.

Kulick et al. (1994) used LDA to measure various glass and copper particles in air. The particles were smaller than the Kolmogorov length-scale of the flow and were therefore responsive to most of the measured turbulent motion. In the streamwise direction it was noted that particles had a greater velocity fluctuation than the fluid but this effect was reversed in the transverse direction. Turbulence was also found to be more attenuated in the streamwise direction. Work by Fessler et al. (1994) at this time used photographic images of illuminated channel flows (glass and copper beads inserted into a flow with half-height 20mm) to assess the effect the reaction time of the particles had on clustering and the magnitude of the random deviation present in the statistics of these particles. In particular, the effects of having reaction times with order matching the Kolmogorov scale were analysed, although the authors also noted that large dense particles had an attenuation effect on localised turbulent fluctuations.

Longmire et al. (2001) used a PIV technique which let them determine simultaneously the velocity fields of both the fluid and particle phases of turbulent gas flows at a bulk Reynolds number of 9000, containing a dilute loading of particles. This was done with the intent of creating statistics for use in validations of future works. In addition, they experimented using a piezoelectric actuator to control the fluid flow more finely and alter particle distribution near to the channel walls.

Kussin and Sommerfeld (2002) measured a developed particle-laden flow using phase-Doppler anemometry (PDA) to determine the behaviour of the air and the particles, which were glass beads. Using this method they were able to simultaneously measure the velocity of both the gas and particle phases. This experiment stood out because the setup enabled the wall roughness to be varied by exchanging the wall plates. It was found that increased wall roughness diminished the particle mean velocity but increased the particle velocity fluctuations. An increase in turbulence dissipation due to two-way coupling was also correlated with the roughness of the walls.

Other studies were also able to use PDA effectively. In the Caraman et al. (2003) paper, the authors studied particle-particle collisions in a horizontal pipe. Interparticle collisions turned out not to greatly affect the longitudinal velocity fluctuations of the particles, but their radial velocity fluctuations were significantly enhanced through the transfer of the streamwise velocity variance to the radial velocity variance. Inertial particles near the wall were proposed to have a strong influence on the overall kinetic-energy balance, particularly in a circular geometry, due to colliding particles transferring the lower streamwise velocities near the wall region into the bulk flow. Later, Caraman and Borée (2005) assessed a bidispersed two-phase pipe flow at various mass loadings so that they could analyse the role of interclass particle collisions. As became apparent, even at the highest mass loading, the mean collision timescale was of a higher order than the aerodynamic time constant of the particles, which meant that

collisions had a minimal effect on the mean free path of the particle fluctuating motion, and that particle transport terms based on the particle's fluctuating kinetic stresses continued to dominate.

Certain authors have extended the study of multiphase flows to include non-spherical particles. For instance, Parsheh et al. (2005) used high-speed imaging and laser-Doppler velocimetry (LDV) techniques to investigate the turbulent characteristics of a suspension of stiff fibres, particularly the orientation of said fibres. It emerged that Fokker-Planck type equations are accurate predictors of particle orientation, but that the influence of flow Reynolds number on this is negligible. Further work on this by Paschkewitz et al. (2005) involved the use of a rod-like polymer to investigate the effects such a fibre would have on the drag in a turbulent boundary layer. A direct numerical simulation was performed simultaneously with results that compared favourably with the spatial development observed in the experiment.

In more recent times, Li et al. (2012) used the simultaneous two-phase PIV measurement technique to investigate the way turbulence is modified in the lower boundary layer of a horizontal channel. Like their forebears they tested differing mass-loading ratios, with these all being low values between 10^{-4} and 10^{-3}, facilitated by 60 μm polythene beads. Adding the particles noticeably modified the mean velocities and turbulence of the fluid phase, in particular narrowing the viscous sub-layer region and enhancing the streamwise velocity gradient, and thus the streamwise fluctuation velocity, u'_{rms}. As well as reducing the viscous sublayer, the physical scale of the coherent structures near to the wall was also decreased with the addition of the particles. The authors also observed particle deposition, which, as noted earlier in this review, had an incremental effect on the non-streamwise velocity fluctuations.

More experimental investigations into the effects of deposition were made by Li et al. (2013). This study was performed on an interesting geometry, the inner wall of a 180° bend. LDV was used here to measure the deposition patterns resulting from different inlet velocities, ratios of curvature and materials used for the bend, and particle concentrations. The deposition pattern turned out to be remarkably consistent regardless of the parameters studied, but particle concentration greatly affected the deposition time, while increased inlet velocity and particle size both reduced the mass of particles that could be deposited over time. Note that this particular study was not limited to experiments. The authors also simulated this geometry using a Reynolds stress-based RANS model, which puts it among studies that use experiments to validate simulated results and vice versa. The history and effectiveness of simulating multiphase flows will be discussed in the following section.

2.3.4 Numerical Studies

Predicting the behaviour of particles in a multiphase flow can be traced back as far as Einsteins's (1911) consideration of the effects of spherical particles on the flow field of a fluid.

Jeffery's (1922) treatment of this, where the author considered ellipsoidal particles immersed in a creeping viscous fluid flow, allowed an extension of to these concepts to the realm of non-spherical particles. In this paper the torque components acting on the principal axis of given ellipsoidal particles were analytically derived. These considerations of particle shape and behaviour were taken even further by Brenner (1963, 1964a, 1964b, 1964c). This author undertook further analysis on a variety of different geometrical shapes, developing various tensors, culminating in a general phenomenological scheme for calculating the quasistatic Stokes force and torque on particles in an arbitrary Stokes flow at infinity.

Thus, by the 70s, when DNS and LES methods were beginning to become successful in a variety of different geometries, there was already a reasonable amount of work performed with regards to how to mathematically treat particles of various shapes and sizes. The simulation work at the time then naturally progressed to investigating particle-laden flows, starting with those of industrial relevance, such as those containing micron scale particles.

An early review of the difficulties associated with modelling a particle phase within a fluid was produced by Elghobashi (1994). For instance, the properties of particles with smaller diameters than the smallest length scale of a flow resist simulation, for no information can be gleaned about the specific regional forces acting upon them. The review describes in detail the methods one might use to describe any of the many regimes particle-fluid interactions may take. One method is to model both phases as though they were fluid phases with additional coupling terms applied. However, on balance this method requires a large amount of computational power unless being simulated using a fast or averaged method such as by using the Reynolds-averaged Navier-Stokes equations.

The Lagrangian particle tracking method (LPT) treats every particle as an independent solid computational point-sphere, with respective equations of motion being calculated and integrated at every time-step. These particles can only be accurately treated as points where the particle diameter is less than the Kolmogorov length scale of the surrounding fluid. LPT uses either the Maxey-Riley equation developed by Maxey and Riley (1983), or a variation upon it, alongside the fluid phase solver. This equation calculates force terms for drag, lift, specific gravity, virtual mass, and pressure gradient, all of which are described in more detail in the methodology section. The Basset history force can also be calculated as part of this equation (Fairweather and Hurn, 2008), but is more normally neglected due to high computational cost and minimal effect on the particles under most practical conditions.

LPT methods are subdivided based on the level of coupling that is being simulated between the fluid and particle phases. Where the volume fraction of the particles is low enough, as shown in Figure 3, only the effect of the fluid on the particles is considered, i.e. one-way coupling. Larger volume fractions of particles push back on the fluid phase in two-way coupling, and eventually, in four-way coupling, the particle-particle interactions become noticeable enough that they too must be considered in the simulation. A more detailed treatment of particle behaviour can be created by using particle resolved methods, which

model the interaction between the fluid and the particle boundary. To perform this level of simulation requires a grid spacing denser than required simply to resolve the Kolmogorov scale, with a comparably increased computational requirement.

The level of computation required to simulate a multiphase flow informs the type of LPT method used as much as the precision. For instance, four-way coupled flows, by necessity, contain enough particles that the number of collisions is both large and relevant. The transition from one-way coupling to two-way to four-way coupling therefore consumes resources that are already stretched by the simulation of the fluid phase. The solution presented to this by many authors is not to model the particle collisions directly at all, but to develop functions that describe the likelihood of collision accurately and use these to simulate the collisions stochastically. The following chapters describe the use of all these numerical methods in the literature.

2.3.4.1 One-way Coupling

An early example of an LPT in turbulent flow was performed by Riley and Patterson Jr (1974), who injected particles into a pre-existing isotropic box. Considering only the drag force, they calculated trajectories with the intent of determining the level of autocorrelation between the particle and fluid velocities. This was determined to be linked with the particle Stokes number, with an increase in Stokes number increasing the level of velocity correlation. The authors note that the results could be made more accurate if the number of particles and the density of the grid points were to be increased. This would have entailed increasing the number of grid points from 32^3 to 64^3, which, given the computational technology at the time, would be unreasonable. The problem that simply doubling accuracy requires an increase in data memory or computational power of almost an order of magnitude remains a feature of the landscape of CFD to this day.

A decade and a half later Yeung and Pope (1989) performed a study of isotropic turbulence in isotropic boxes with 64^3 and 128^3 grids, which parallels the growth in computer technology. These authors came to the conclusion that the improvements to the nodal density of the fluid phase solving grid directly improved the accuracy of the simulation. When comparing interpolation techniques the authors did find that third order interpolation is a reasonable minimum requirement for accuracy. Balachandar and Maxey (1989) considered four different interpolation techniques at around the same time, although the node densities they used were smaller.

Numerical simulations which extended these techniques to a turbulent channel flow were performed, the same year, by McLaughlin (1989), who calculated the trajectories of particles in a vertical channel at $Re_B = 2000$, using a pseudospectral method. The author analysed the migration of particles within the channel, finding a tendency for them to accumulate in the viscous sublayer, whilst also finding that deposition of particles on the wall would take place typically with particles that retained the velocity imparted to them by the bulk flow. The

effects of the lift force were noted to be minimal in all regions of the flow except the viscous sublayer, where it was significant in the processes of accumulation and inertial deposition of particles.

A paper by Li and Ahmadi (1992) investigated how particles are dispersed and deposited within a turbulent channel flow. This entailed simulating turbulent velocity fluctuations using a continuous Gaussian random field. Various sizes of aerosol particles were given generated trajectories before being statistically analysed. The effects of Brownian diffusion on the dispersion effect were also specifically studied, in addition. Lift and drag were accounted for within this simulation but virtual mass and pressure gradient forces were deemed as too small relative to the Stokes drag force and were thus neglected. Their later paper, Li et al. (1994), used a similar turbulent flow to investigate the transport and deposition of particles around an obstruction in a duct geometry. They used both rectangular and trapezoidal blocks for this and found that a more streamlined obstruction would greatly decrease the rate of deposition.

Wang and Squires performed LES of a turbulent channel flow in their two studies (Wang and Squires, 1996a, 1996b), with their first paper considering vertical channel flows at Re_B = 11,160 and 79,400. As with previous studies they found an accumulation of particles in the near-wall region, finding their measurements comparable to those from the DNS performed by McLaughlin (1989), with the greatest discrepancy between DNS and LES shown where particles had small relaxation times. The second study involved channel flows with Re_τ of 180 and 644. The properties of the lower Reynolds number flow were in good agreement with DNS results. While the higher Reynolds number flow did not have a DNS to compare to, it showed reasonable agreement with experimental results. The effect of vortex production from fluid gradients and fluid-particle correlations were analysed by means of the particle fluctuations and were shown to be highly relevant. The particle number density across the channel also showed a distribution that was comparable to DNS.

Uijttewaal and Oliemans (1996) progressed LPT to the domain of pipe-like geometries. They injected particles with dimensionless reaction times ranging from 5 to 10^4 into three different single phase turbulent pipe flows. Two higher Reynolds number flows were simulated by LES, and a third flow had a low enough Reynolds number to permit a DNS. They showed that for small particles, deposition is determined by the low turbulence in the near-wall layer. Large particles are inertial and their potential collision and deposition is governed by the turbulent dispersion of the flow. Those particles demonstrated a range of motion which scaled with the Lagrangian integral timescale of the turbulence. The authors also noted a gradual segregation effect as particles moved towards the wall.

Zhang et al. (2001) investigated the transport and deposition of ellipsoidal particles using a DNS with a pseudospectral method. Euler's quaternions were used here for describing the orientation of the particles over time in order to avoid issues with integration. The ellipsoidal particles were compared to spherical equivalents and the differences assessed. The coherent vortical structure close to the wall was found to have a strong influence on the transport of

these particles, as seen in previous studies, and the deposition velocity was found to increase sharply when the aspect ratio of the particles was increased. These results were compared to experimental data and a good agreement was achieved.

Marchioli and Soldati (2002) performed a DNS at a shear Reynolds number of 150 with the intent of isolating the effects which draw particles towards the wall within a channel flow. It was confirmed that the sweeps and ejections covered in previous studies of the phenomenon were the most prolific means by which particles were moved between regions of the channel, but this study also was able to quantify those effects and determine a characteristic pattern as can be seen in previous papers on the subject. In a later study, Marchioli et al. (2003) investigated deposition and resuspension in a turbulent pipe flow. This DNS was performed at a shear Reynolds number of 337, and considered drag, lift, and gravitational forces. The results demonstrated the expected segregation of particles in the near-wall region, and recognised the importance of instantaneous Reynolds stresses regarding particle flow to and from the wall, as well as the free-flight and diffusion mechanisms of particle deposition.

Another investigation performed using LES was by Winkler et al. (2004) who used it to investigate a particle-laden vertical duct flow at a shear Reynolds number of 360. A finite volume scheme was used to simulate the fluid flow, and the forces on the particles (drag, lift and gravity) were integrated using the fourth order Runge-Kutta method. They investigated four representative cross-sections of the duct with six different settings for the particle response time, which let them study in detail the effects of location and particle inertia on preferential concentration. They found that the relationship between vorticity and preferential concentration was imprecise, deriving a "swirling strength" measurement that proved more accurate in regions of high shear. A progression of the work in 2006 (Winkler et al., 2006) focused more on wall deposition in the same downwards facing flow, testing two different values of the particle-fluid volume fraction and five of diameter. Comparing their results to those of a circular pipe flow, they found a greater rate of deposition in a duct, particularly at low Stokes numbers. Higher Stokes numbers also correlated to an increase in the average streamwise and wall-normal deposition velocities.

Sharma and Phares (2006) carried out the first DNS of a particle-laden square duct flow. This was done at a shear Reynolds number of 300, and only the drag force was considered for the simulation of the particles. The authors compared the behaviours of tracer particles and more inertial particles, with the intention of investigating the way secondary flows interact with these in a duct. The duct geometry has an implicit lateral advective transport effect that is not found in channel or pipe flows. This effect produced a high rate of mixing in the lateral direction for tracer particles and those with low inertia. Heavier particles were relatively unaffected by this, instead accumulating near to the wall and mixing more efficiently in the streamwise direction. The authors provided images of instantaneous particle positions to emphasise their results.

Marchioli and Soldati (2007) tested the clustering of heavy particles in low-vorticity regions by using DNS with a grid resolution of up to 256^3 with shear Reynolds numbers 150 and 300. The intent was to discover how the tendency of particles to occupy certain areas changes with the Reynolds number. The results were consistent with the Kolmogorov scaling argument which predicts saturation at even higher Reynolds numbers. It is this paper against which the results of this study are validated, since few studies have been performed at 300 shear Reynolds number.

Mortensen et al. (2008) considered the dynamics of prolate ellipsoids within a turbulent flow, a situation known to occur within various natural and industrial settings, performing a DNS, simulating the fluid in an Eulerian fashion, and treating the particles using a Lagrangian framework. The paper demonstrates that inertia can be neglected in favour of higher magnitude viscous effects. Increasing the Reynolds number causes the particles in a flow to display a more homogenous orientation. It also shows how the Euler parameters can be used to calculate the direction cosines and thus calculate the rotational motion of ellipsoids.

A comprehensive review of Lagrangian particle tracking was performed collaboratively by Marchioli et al. (2008). This compared a great variety of codes that simulated particle dispersion by means of Lagrangian particle tracking. Most of the codes were direct numerical simulations. Drag force was deemed to be the dominant force, with the other forces considered to be negligible in these cases, which had density ratios significantly greater than unity. Most of the codes they tested were DNS based, and the authors found a good agreement between all of these, generating an inclusive database detailing the turbulent flow statistics generated by the different methods they used. The effects of Stokes number were given particular consideration, and it was observed that an increase in Stokes number caused a dampening of the particle turbulent fluctuations in the wall-normal and spanwise directions.

In a spectral solution, the flow variables are approximated as expansions of functions involving complex solutions of a Sturm-Liouville problem, solved using boundary conditions. Spectral methods are unable to consider non-simple flow geometries, model discontinuities accurately, or enforce in/outflow boundary conditions. Finite difference solutions are simple to implement, suitable for parallelization, and can potentially carry a high order of accuracy. They therefore gained popularity at the time of Coleman's (2010) primer on DNS use. There are many options in using finite difference methods. Low order approaches allow for complex geometries and irregular grids, like finite-volume methods, but their efficiency is often unacceptable. Though extremely complex geometries can only be run via low-order finite difference approximations, the low resolution for each grid point in the geometry will limit the parameter space for important quantities like Reynolds number and domain size. High-order finite difference approximations have more involved coding but can be an excellent compromise between accuracy and flexibility. They usually use Runge-Kutta methods as their solution basis.

The finite element solution is a hybrid of the spectral and finite difference solutions, noted for its combination of precision and generality, as an optimal solution it shall be employed to model the flows in this study. Compilations of CFD methods have been produced by Loth (2000), and later by Coleman (2010). Further information on experimental and computational procedures as well as general information with regards to multiphase flows may be found in the textbooks Crowe et al. (1998) and Crowe (2005).

Fairweather and Yao (2009) investigated the dispersion in a turbulent duct flow at a very high bulk Reynolds number of 250,000, considering a range of particle sizes from 5μm to 1mm. The continuous phase was modelled using LES, with the particle phase modelled using an LPT that considered the Stokes drag force as well as gravity and buoyancy. The force of gravity proved to be an important part of the dispersive forces on the particles, in addition to the secondary flows. Particles with high inertia were most affected by gravity, with the secondary flows dispersing smaller particles more strongly. As noted in previous literature, particles tended to migrate to regions of low streamwise velocity. But the corners of the ducts seemed to be an exception to this rule, with an increased occurrence of deposition in these regions., however an increased amount of deposition was also observed in the corner regions of the duct.

The same authors, Yao and Fairweather (2010), later performed another simulation under the same one-way coupled conditions, but this time the lift force on the particles was taken into consideration and the range of particle categories was reduced (5μm to 500μm). They studied the effects that lead to the resuspension of particles, and the drag force produced by secondary flows was found to be a major contributor for the resuspension of small and large particles, while the lift force also proved to be a factor for large particles. The effects of the orientation of these forces were described in detail.

Marchioli et al. (2010) investigated the behaviour of fibres in a turbulent flow in detail, covering a wide range of different prolate particles and analysing orientation, preferential distribution and accumulation near to the wall. The aspect ratios were shown to have little effect on the grouping behaviours of the particles, but did increase the drift velocity near to the wall.

Puragliesi et al. (2011) initiated an investigation into buoyancy driven flow of a differentially heated cavity. They used Lagrangian particle tracking to describe the deposition that takes place in the dispersed phase. A thorough analysis of lift forces and thermophoretic forces on the particles was performed though drag, gravity and buoyancy were also taken into account. They found a high rate of deposition on the bottom wall, mostly driven by gravity, and a strong contribution of lift to the deposition of particles on the cooler vertical surface. High order data was gathered on the turbulence kinetic energy and temperature variance in the system.

Zhao and van Wachem (2013) considered the three main frameworks for describing the orientation and rotation of non-spherical particles. These are Euler angles, rotation matrices

and unit quaternions. Noting that quaternions were particularly well suited to modelling the behaviour of non-spherical particles, they went about solving the various problems which came about from using the method. A framework for transforming vectors and tensors was developed, and the need for explicit rotation matrices was eliminated. Also, a novel corrector-predictor method for integrating unit quaternions so that the length is conserved was developed. This was then tested against various other methods, showing a significant improvement over other algorithms that existed at the time.

A recent study by Njobuenwu and Fairweather (2015a) used LPT to analyse three different shapes of particles: discs, spheres, and needles. Individual examples of each of these particles were injected into three different regions of a turbulent channel flow with a shear Reynolds number of 300. As in previous works, Euler quaternions were used to simulate the behaviour of these particles, and the torque function was divided into three components: torque incident on the particle, resistive torque caused by a difference in angular momentum between the fluid and the particle, and a cross-term torque derived from fluid rotation around the perpendicular axes. Each class of particle displayed idiosyncratic behaviour regardless of its location in the channel. The authors defined a variety of different rotational states for the particles based on the local turbulence.

2.3.4.2 Two-way Coupling

Above a certain volume fraction, the effects of the particles on the fluid become non-negligible, and further terms in the Navier-Stokes equations need to be implemented to accurately simulate the feedback of momentum from the particles back into the flow.

The force-balance terms which usually drive the particles are dependent on being able to calculate the fluid velocity at the centre-point of each particle. Though this is simple enough for resolving a one-way coupled flow, for a two-way coupled flow the velocity at the centre-point of a particle is being constantly changed by definition. Fortunately, Boivin et al. (2000) argues that where the particle diameter is smaller than the grid spacing, as it is for point particle based DNS techniques which require that the particle scale be smaller than both the Kolmogorov and grid spacing scales, the differences between disturbed and undisturbed velocities can be assumed to be negligible.

To model the forces exerted by the particle phase onto the fluid phase, a Dirac delta function is often used, with the effect of each particle being considered in a localised fashion. These forces are summed up in the cells for the Eulerian phase and applied to the momentum feedback term when the velocity of the fluid in the cell is being recalculated. This method is known as the particle-source-in-cell (PSIC) method.

An example of a simulation which uses two-way coupling is the work of Pan and Banerjee (1996), who applied two-way coupling to a particle-laden turbulent channel flow where $\phi_P \approx 4 \times 10^{-4}$. Coupling was established through the feedback of calculated velocity disturbance, assuming a Stokesian flow, for each timestep. As observed in previous studies, heavier-than-

fluid particles tended to accumulate in low-speed streaks. Smaller particles typically suppress turbulence and large particles typically enhance it, which was again demonstrated in this study.

Zhao et al. (2010) studied the impact of the particle phase on the turbulent fluid phase in a two-way coupled channel flow at Re_τ = 180. Adding particles to the channel was found to increase the bulk flow rate and enhance the coherent turbulent structures in the wall region. The authors reconfirmed the attenuation of the spanwise and wall-normal stresses, while the streamwise turbulence was proportionally enhanced.

Adams (2011) performed a comprehensive study focused mainly on the deposition, dispersion and resuspension of particles. The author used RANS in conjunction with LPT in circular pipes with flat beds. RANS was found to be accurate in describing key features in the flows through ducts. It was inaccurate when describing secondary velocities in square ducts or pipes with beds. RANS combined with a Reynolds stress turbulence model and a two-way coupled LPT can be useful in modelling particle flows through ducts and pipes. But for more detailed studies, LES and DNS should be used. This corroborates previous remarks.

The authors of experimental works, Kiger and Pan (2002) presented ways in which inertial particles are bound to modify the turbulence within a fluid flow by measurably affecting the vortical structures. Zamansky et al. (2011) performed two-way coupled DNS and LES in order to analyse these effects at high Stokes and Reynolds numbers. The authors observed the anticipated effects of particle segregation and clustering. In addition, the extended LES they used which considered the acceleration contribution at the sub-grid scale displayed results more accurate than the standard LES, at least when compared to DNS.

Lee and Lee (2015) also undertook an investigation into the effects of Stokes number. Again using a $Re_\tau = 180$ turbulent channel flow with two way coupling, they kept the mass fraction constant whilst changing the Stokes number. By analysing the way that heavy and light particles transfer kinetic energy to and from the high-speed flow regions and low-speed streaks, as well as the changes produced in near-wall turbulence, they were able to explain why lower Stokes numbers led to enhanced rms stresses, while higher Stokes numbers reduced these same stresses.

2.3.4.3 Four-way Coupling

Where the particle volume fraction is in excess of $\phi_P > 10^{-3}$ collisions between particles are frequent enough that the particle dynamics, and by extension the fluid dynamics, are noticeably affected. These additional effects may be simulated deterministically, where the vast majority of particle-particle collisions are accounted for, or stochastically, where collisions are assumed based on calculating the probabilities of collisions in order to produce an approximation of fully determined collisions. Note that with the way deterministic collisions normally work, collisions between particles across cell boundaries are generally not considered. This can lead to artefacts which have a small effect on the collision rate.

Determining the resultant velocity of two particles after colliding relies on making assumptions about the properties of said particles. When colliding particles deterministically or stochastically one can either use a hard-sphere or soft-sphere model. The hard-sphere model uses conservation of momentum and energy laws to adjust the position and velocity of particles when a collision occurs, since particles are not permitted to overlap in this model. The soft-sphere model allows the particles to compress and expand off of one another, based on the mechanical properties of the particle material and the amount of overlap detected.

Four-way coupled simulations require a lot more computing power than either two-way or one-way coupled simulations, so only more recent studies should be expected to investigate this level of coupling, according to the growth of computing power through time. One such study by Li et al. (2001) considered a highly particle-laden gas flow down a vertical channel with a bulk Reynolds number of 7000. Both elastic and inelastic collisions were considered. The addition of particles generally caused an increase in the bulk gas flow rate. The length scales associated with the streamwise velocity fluctuations were also increased, leading to a reduction in energy transfer between those velocity components and the wall-normal/spanwise components. With regards to interparticle collision, it was found that considering this leads to a significant reduction in near-wall accumulation, for all the mass loadings considered, and even regardless of the collision method used.

Vreman et al. (2009) increased the volume fraction somewhat for their similar study, to the order of $\phi_P \approx 10^{-2}$, making the effects of two-way and-four way coupling unambiguous. Similarly to Li et al. (2001), a vertical channel with a gas-particle flow was considered. The mean velocity profile of the simulation was much flatter by the presence of the particles, and the boundary layer was made much thinner. In line with previous studies the turbulence modulation caused by the particles made the streamwise turbulence stronger, while the turbulence components perpendicular to this were weakened. The authors showed that for multiphase flows with a volume fraction in the region of 1%, particle-particle interactions must be modelled to ensure accuracy.

For their four-way coupled LES of a turbulent channel flow at a bulk Reynolds of 11,900, Breuer et al. (2012) developed a search algorithm which increased the efficiency of the deterministic collision model substantially, by using virtual cells to limit the particles considered for collision to those in a small region around the particle concerned. This reduced the computational cost by orders of magnitude in high density flows, in the region of $O(N_P^2)$ to $O(N_P)$. Though stochastic methods are capable of greater efficiency, this methodology sacrifices less accuracy, and when applied to various test cases in this study, the computational results were very comparable to experimental data.

Van Wachem (2015) described a novel framework for predicting the behaviour of non-spherical particles with large Stokes numbers in turbulent flow. This can be taken as a direct continuation of the work of Zhao and van Wachem (2013), with the quaternions used to simulate particle behaviour. DNS-LES was used to simulate a sphere, a disk, a fibre and two

different ellipsoids. The study showed that non-spherical particles will tend to maximize drag by aligning their longest axis perpendicular to the flow. The study showed various properties of non-spherical particles such as disks having a steadier trajectory than comparable particles, and wall roughness having a greater effect on non-spherical particles.

The work by Zhao et al. (2015) considered more carefully the way particle fluid coupling was affected by the Stokes number and shape of particles. At the turbulent Reynolds number of 150 being studied, the non-spherical particles were found to cause attenuation of turbulence in the wall region. Particles in that region would align their longest axis perpendicularly to the flow in the wall regions, but in the bulk flow this effect would not take place. Kuerten and Vreman (2015) also investigated a flow at the same Reynolds number at the same time. They investigated the collisions between droplets and showed that these affect the droplet concentration substantially, with the maximum local concentrations near to the walls dropping by close to an order of magnitude. Heat transfer at the wall region was surprisingly affected much less.

In another study by Vreman (2015) the wall roughness in a vertical channel at $Re_\tau = 642$ was investigated. As the walls were made rougher the attenuation of turbulence was shown to increase. A "feedback force" exerted by the solid particles on the gas phase was described, and the uniformity of this force was directly correlated with both the wall roughness and with the turbulence attenuation, with a more non-uniform feedback force being instigated by greater wall roughness, and contributing greatly to turbulence attenuation.

2.3.4.4 The Stochastic Method

Since deterministic Lagrangian particle trackers tend to require large amounts of computing power as the concentration increases, stochastic methods are certainly worthy of consideration where accuracy is a given and the main concern is simulation runtime. Specifically, the deterministic method of colliding particles, i.e. checking the location of all nearby particles to determine whether a collision has taken place, has a computer clock time that scales with the square of the particle number. Numerous studies have been performed on the calculable collision rates of particles within a turbulent fluid flow, and the resulting theories have been applied to particle trackers that handle the collisions stochastically.

With the intention of creating a model which would describe the behaviour of the particulate phase of cloud vapour, Saffman and Turner (1956) proposed an advective theory of collision for small particles in a turbulent fluid. Using an assumption of droplets that were smaller than the turbulent eddies, but similar in size to each other, an equation was derived for calculating the probability of a collision between two particles that only needs to consider the kinematic viscosity and the rate of energy dissipation. The equation was successfully applied to its original purpose, but notably remains useful for predicting the behaviour of low Stokes number particles to this day, remaining relatively unchanged from its original formulation.

The direct simulation Monte Carlo (DSMC) method was proposed by Bird in (1976). This method detects particle-particle collisions stochastically, as opposed to the more traditional deterministic particle method. DSMC proved to be very popular in conditions with large numbers of particles, for it not only accounts for a reduction in computational time from the deterministic model, but it also applies very well to simulations where a small number of tracked particles are used to represent the collisions between parcels of particles. Thus, the computational costs can be reduced by orders of magnitude this way.

In one of the first stochastic particle-particle collision models that retain a Lagrangian framework for particle tracking, O'Rourke (1981) traced the movement of droplets through the flow field, implementing random processes to resolve collisions and accumulations between either chosen pairs of particles, or particle "packages" representing groups or clusters of particles. The author compared the results from this method to other numerical and experimental implementations of the same system, discussing the dilemma of which particular numerical solution is the best choice to resolve the unsteady two-dimensional equations of motion.

The 1983 paper produced by Williams and Crane (1983) analysed the relationship between the velocities of particles contained within the same fluid eddy and produced an expression for the rate of collision of particles in turbulent flows. By considering medium sized particles, which are neither fully correlated to the fluid nor fully independent of it, a universal kinetic theory was described for calculating the probability of collision depending on the mean relative velocity between particles.

In the 90s, Tanaka and Tsuji (1991) produced data from a coarse particle-fluid system that is considered in this study. Though the study did not use stochastic methods, the interesting result of increased isotropy in fluctuations of particle velocity with increased particle mass loading/collision frequency is of interest, and the paper is frequently referenced in the implementation of stochastic collision systems. Indeed, shortly after this paper was published, Sommerfeld and Zivkovic (1992), and Oesterle and Petitjean (1993), independently developed stochastic interparticle collision models which calculated the probability of collision based on the kinetic theory of gases. Where a collision was detected, it would be resolved through the generation of a fictitious particle with properties determined by the local probability density functions of particle diameter and velocity.

Kruis and Kusters (1997) later undertook a review of derivations for particle collision rates in turbulent fluid flow, showing that the previous equations were only applicable to a limited number of cases. They performed a general derivation and produced a universal solution for the comparative velocities of particles accelerated by a fluid within the same region of space. This derivation loses efficiency above the Kolmogorov scale, where accelerative and inertial effects begin to dominate.

Tsuji et al. (1998) then undertook their own work into stochastic techniques. They described a discrete particle model or DPM (any model which calculates the motion of particles individually) which they then enhanced using a trajectory method DSMC to nullify some of the computer limits, such that "the trajectory approach can be used for any number of real particles". Using this method, they simulated a circulating fluidised bed at a few different fluid velocities and duct sizes. They compared the results from their DSMC to a two-fluid method from Tsuo and Gidaspow (1990). Though the effects of fluid velocity, and particle loading and size were consistent between the two methods, although cluster population was not consistent between the models, and the authors deemed the results for fluid and particle velocity distribution, and particle concentration, unsatisfactory.

Sommerfeld (1999, 2001) would go on to further validate the stochastic inter-particle collision model in isotropic turbulence. In the earlier paper the author described a correlation effect between the velocities of colliding particles. This effect is accounted for in the 2001 paper. LES models of isotropic boxes containing monodisperse particles, as well as granular binary mixtures of particles with and without the consideration of a turbulence flow effect, were considered. By drawing size classes from the local area and sampling Gaussian velocity distributions, the model was able to effectively simulate the collisions between particles on different scales. The results produced by LES were found to agree well with those of the stochastic model.

At around the same time, Wang et al. (2000) undertook an investigation into the way the turbulent transport effect and the accumulation effect change the nature and frequency of inter-particle collisions. Using a DNS to assess these two contributions, they were able to relate the magnitude of each effect to how close the particle inertial response time is to either the fluid Kolmogorov timescale (for a dominant accumulation effect) or the flow integral scale (for a dominant turbulent transport effect). From this information they were able to generate an improved statistical description of the collision kernel, leading to the derivation of an integrated model for calculating collision probabilities for flows with arbitrary Reynolds numbers and particle properties.

Further work into the probabilities of interparticle collisions was performed by Wilkinson et al. (2006), who investigated the collision rate of droplets in turbulent air. Showing that the turbulence intensity has a drastic effect on the collision rate, the author derived a Stokes number dependency which was then applied to the derived probability equation. The new equation considered factors from the kinetic and advective models of collision probability, and was used to predict a turbulence threshold above which the onset of rain occurs.

Pawar et al. (2014) demonstrated a version of the DSMC model where the region of selection for particle collision is a spherical searching scope with a radius centred on the particle under consideration. This was intended to limit the lattice artefacts produced by more uniform selection regions. The authors performed many modifications to the method, in the process making useful determinations of the number of random particles required in a selection

region so as not to cause detrimental effects on the averaging needed to estimate the collision frequency.

2.3.4.5 Further Techniques

Beyond basic four-way coupling, other inter-particle mechanisms such as agglomeration can be implemented to more accurately model certain types of particle-fluid system. The DLVO-theory (Derjaguin and Landau, 1941; Verwey and Overbeek, 1955) encompasses the van der Waals attraction and the electric double-layer Coulombic repulsion inter-particle forces. An improvement to this theory was proposed by Schenkel and Kitchener (1960), who considered in addition the Casimir-Polder retardation effect, which allows for a minimum distance of inter-particle interaction to be presumed in the case of similar spheres.

An LES performed under the same conditions as Breuer et al. (2012) by Breuer and Almohammed (2015) also considered particle agglomeration. This agglomeration was simulated using a model of the van der Waals forces, approximating the resulting agglomerates as larger spheres. The performance of this agglomeration model was exhaustively tested, with sub-grid scale, wall roughness, particle mass loading and even the two-way coupling effect being modulated. The results of the study showed that this particular agglomeration model matched experimental data well, although the authors noted plans for comparing their closely-packed sphere model with momentum-based and energy-based agglomeration models.

The approach of Njobuenwu and Fairweather (2015b) to agglomeration used an energy momentum balance, coefficient of restitution, and van der Waals' interactions to treat deterministically collided particles. The authors' results demonstrate that low particle and fluid inertia is conducive to the agglomeration of particles, as well as being highly dependent on the particle normal coefficient of restitution.

The highest order of accuracy can be achieved by tracking the particle-fluid interface directly, without making the usual particles-as-points assumptions that are common in LPT. Modelling the particle as its own mesh within the fluid mesh, with the calculations of particle trajectory being performed for each face of particle every timestep, is extremely computationally expensive. Nevertheless, studies have been performed using the technique to simulate small numbers of particles in simple fluid geometries.

Bagchi and Balachandar (2003) for instance, performed a DNS of a single spherical particle with an immersed boundary condition, and found that while the traditionally calculated drag and lift correlations are not inaccurate by comparison, this accuracy is reduced as the particle size increases, and not even the addition of added mass and history forces would counteract this accuracy loss. Vreman (2016) used a similar method to study the behaviour of 64 fixed spherical particles with diameters twice the Kolmogorov scale in an isotropic box at $Re_\lambda = 32$. Comparing the results from this to point-particle simulations, the author spoke in favour of the latter's accuracy for the situations considered. The immersed boundary particles

showed unusually high turbulent dissipation around the particles, and did not display the expected amount of turbulence attenuation.

As part of a larger study, Mortimer et al. (2018) implemented an immersed boundary method which was able to simulate binary particle collisions between fully resolved particle meshes. The inter-surface forces of van der Waals attraction and electric double-layer repulsion were implemented so that particle-particle interactions, including agglomeration, could be studied exhaustively at the particle scale. Similar to previous studies of agglomeration, low turbulence regions were found to be most conducive to aggregation. By varying the chemical and mechanical properties the author found that changing the coefficient of restitution was particularly impactful on the dynamics.

2.4 Conclusions

Methodologies for the study of single-phase and multiphase flows in a variety of geometries have been assessed and compiled. As computer technology improves, more highly coupled simulations are becoming popular, even including such expensive methodologies as interface tracking. Higher resolutions of turbulence are also of interest, not least because high order accuracy results are necessary to validate faster, less complex simulations. See Tables 1 and 2 for a summary of single-phase and particle-laden turbulent flow experimental and numerical simulation studies over time.

In two phase CFD, the bulk of the problem concerns defining which equation should be solved rather than deriving a method with which to solve them. DNS differs from conventional CFD in that the turbulence is explicitly resolved. It differs from large-eddy simulation because it covers the dynamics at all scales. DNS therefore provides specific information at all times without approximation, but does so at the great expense of computing power and therefore the inability to be used at any particularly high Reynolds number. Computing power required can be calculated as proportionate to Re_τ, though depending on the operations required, say per direction per grid point, would result in an elevenfold increase in computer requirement for only a doubling of Reynolds number. This means that at the current rate of computer advancement, enough extra power to double the Reynolds number is only provided every 5 years or so. DNS codes are efficient and specialized. DNS is dominated by spectral and finite difference solution methods.

There is a noticeable absence of DNS work for multiphase flows at reasonably high Reynolds numbers, of the order of a shear Reynolds number of 300, in the literature, and the work presented in this thesis will attempt to resolve that with a variety of DNS runs performed at this Reynolds number. What shall also be performed is a detailed analysis of the differences between simulations with one-way, two-way and four-way coupling. Particular interest shall be given to particle concentration and behaviour, as well as its effect on the fluid. Agglomeration modelling at low Stokes numbers is also relatively sparse, so this shall also be considered for its effect on the system.

In addition to this the results of an implemented stochastic collision metric shall be compared to the purely Lagrangian form. Even with the advancement of computer technology, simulating many particles taxes resources, and simulations of more granular flows have an unfortunate tendency to spend an inordinate amount of resources and time on inter-particle collisions, a problem that can be resolved with the implementation of a stochastic method. Determining how these different techniques affect the runtime of simulations will be a key factor in this research. Also, finding new ways to use stochastic methods to model particle behaviours like agglomeration are open for consideration and will be attempted.

Table 1: Summarisation of key features within the collated experimental studies of turbulence.

Study	Key Focus	Reynolds Number(s)	Particles	Techniques Employed
Laufer (1954)	Pipe flow	$Re_B = 50,000, 500,000$	N/A	Hot wire anemometry
Friedlander and Johnstone (1957)	Particle deposition rate in pipes	$Re_B = 20,000$	0.8—2.63 µm, brass/iron	N/A
Hoagland (1962)	Duct flow	$Re_B = 10,000 - 100,000$	N/A	HWA
Brundrett and Baines (1964)	Duct flow	$Re_B = 20,000 - 83,000$	N/A	HWA (in 3 dimensions)
Gessner and Jones (1965)	Duct flow	$Re_B = 50,000 - 300,000$	N/A	HWA (in 3 dimensions)
Clark (1968)	Channel flow	$Re_B = 15,000 - 45,600$	N/A	HWA
Tracy (1965)	Channel flow	$Re_B = 50,000$	N/A	HWA
Ilori (1971)	Particle deposition rate in pipes	$Re_B = 5000, 50,000$	6,9 µm aerosol	N/A
Snyder and Lumley (1971)	Particle velocity autocorrelation	$Re_B = 10,000$	46.5,87 µm glass, etc.	N/A
Eckelmann (1974)	Channel flow	$Re_B = 5600, 8200$	N/A	Hot film anemometry
Forney and Spielman (1974)	Particle deposition rate in pipes	$Re_B = 4,000 - 60,000$	19.5—48.5 µm pollen, etc.	N/A
Liu and Agarwal (1974)	Pipe flow	$Re_B = 10,000, 50,000$	$St^+ = 0.21 - 774$	N/A
Melling and Whitelaw, (1976)	Duct flow	$Re_B = 42,000$	N/A	Laser Doppler anemometry
Aly et al. (1978)	Duct flow	$Re_B = 53,000 - 107,000$	N/A	HWA
Gessner et al. (1979)	Duct flow	$Re_B = 250,000$	N/A	LDA
Kreplin and Eckelmann (1979)	Channel flow	$Re_B = 7700$	N/A	HFA
Lee and Durst (1982)	Pipe flow	N/A	100—800 µm glass	Laser Doppler velocimetry
Tsuji and Morikawa (1982)	Pipe flow	$Re_+ = 470$	200, 3400 µm plastic	LDV
Tsuji et al. (1984)	Pipe flow	$Re_B = 16,000 - 32,000$	200, 3400 µm plastic	LDV
Cenedese et al. (1991)	Duct flow	$Re_B = 3500$	N/A	LDA
Cenedese et al. (1992)	Duct flow	$Re_B = 4800$	N/A	LDA

Fessler et al. (1994)	Channel flow	$Re_B = 138,000$	$St^+ = 1.7 - 130$	Photographic image analysis
Kulick et al. (1994)	Channel flow	$Re_B = 138,000$	50—90 μm glass, copper	LDA
Zhang et al. (1997).	Duct flow	$Re_B = 123,000$	3—15 μm tracers	Holographic particle image velocimetry
Tao et al. (1999)	Duct flow	$Re_B = 120,000$	20 μm tracers	HPIV
Kussin and Sommerfeld (2002)	Channel flow	$Re_B = 38,805 - 57,284$	$St^+ = 5.01 - 386$	Phase-Doppler anemometry
Caraman et al. (2003)	Pipe flow	$Re_B = 5300$	30—100 μm glass	PDA
Caraman and Borée (2005)	Pipe flow	$Re_B = 5300$	60—90 μm glass	PDA
Parsheh et al. (2005)	Planar contraction of fibres	$Re_B = 85,000 - 170,000$	3.2mm × 5.7μm fibres	LDV
Große and Schröder (2008)	Pipe flow	$Re_B = 10,000 - 20,000$	N/A	Micro-pillar wall-shear stress sensors
Li et al. (2012)	Channel flow	$Re_B = 6385$	60 μm polythene	PIV
Gnanamanickam et al. (2013)	Duct flow	$Re_B = 15,000$	N/A	MPS3
Owolabi et al. (2016)	Duct flow	$Re_B = 1205, 2205$	N/A	LDV

Table 2: Summarisation of key features within the collated numerical studies of turbulence.

Study	Key Focus	Reynolds Number(s)	Particles	Techniques Employed
Deardorff (1970)	Channel flow	N/A	N/A	Large eddy simulation
Moin and Kim (1985)	Channel flow	$Re_B = 13,800$	N/A	LES
Kim et al. (1987)	Channel flow	$Re_B = 3300$	N/A	Direct numerical simulation
Moser and Moin (1987)	Channel flow	$Re_B = 2990$	N/A	DNS
McLaughlin (1989)	Channel flow	$Re_B = 2000$	1-way coupled	DNS
Yeung and Pope (1989)	Isotropic turbulence field	$Re_\lambda = 38 - 93$	1W	DNS
Madabhushi and Vanka (1991)	Duct flow	$Re_B = 5810$	N/A	LES
Gavrilakis (1992)	Duct flow	$Re_B = 4410$	N/A	DNS
Li and Ahmadi (1992)	Channel flow	$Re_B = 6657$	1W	Gaussian field model
Eggels et al. (1993)	Pipe flow	$Re_B = 7000$	N/A	DNS
Li et al. (1994)	Duct flow	$Re_B = 6657$	1W	Gaussian field model
Su and Friedrich (1994)	Duct flow	$Re_B = 49,000$	N/A	LES
Pan and Banerjee (1996)	Channel flow	$Re_B = 2592 - 5156$	2-way coupled	DNS
Uijttewaal and Oliemans (1996)	Pipe flow	$Re_B = 5300 - 42,000$	1W	LES/DNS
Wang and Squires (1996a)	Channel flow	$Re_B = 11,160, 79,400$	1W	LES
Wang and Squires (1996b)	Channel flow	$Re_\tau = 180, 644$	1W	LES
Moser et al. (1999)	Channel flow	$Re_\tau = 180, 395, 590$	N/A	DNS
Li et al. (2001)	Channel flow	$Re_B = 7000$	4-way coupled	DNS
Zhang et al. (2001)	Channel flow	$Re_B = 8000$	1W ellipsoidal	DNS
Marchioli and Soldati (2002)	Channel flow	$Re_\tau = 150$	1W	DNS
Marchioli et al. (2003)	Pipe flow	$Re_\tau = 337$	1W	DNS
Winkler et al. (2004)	Duct flow	$Re_\tau = 360$	1W	LES

Morinishi and Tamano (2005)	Channel flow	$Re_\tau = 100 - 300$	N/A	DNS
Sharma and Phares (2006)	Duct flow	$Re_\tau = 300$	1W drag only	DNS
Marchioli and Soldati (2007)	Channel flow	$Re_\tau = 150, 300$	1W	DNS
Mortensen et al. (2008)	Channel flow	$Re_\tau = 360$	1W ellipsoidal	DNS
Fairweather and Yao (2009)	Duct flow	$Re_B = 250,000$	1W, 5-1000 µm	LES
Vreman et al. (2009)	Channel flow	N/A	4W, high ϕ_P	LES
Zhu (2009)	Duct flow	$Re_\tau = 600$	N/A	DNS
Marchioli et al. (2010)	Channel flow	$Re_\tau = 150$	1W fibres	DNS
Yao and Fairweather (2010)	Duct flow	$Re_B = 250,000$	1W, 5-500 µm	LES
Zhao et al. (2010)	Channel flow	$Re_\tau = 180$	2W	DNS
Adams (2011)	Pipe flow	$Re_B = 10,000$	2W	Reynolds averaged Navier-Stokes equations
Boersma (2011)	Pipe flow	$Re_B = 5300 - 61,000$	N/A	DNS
Zamansky et al. (2011)	Channel flow	$Re_B = 125,000$	2W	DNS/LES
Breuer et al. (2012)	Channel flow	$Re_B = 11,900$	4W	LES
El Khoury et al. (2013)	Pipe flow	$Re_\tau = 180 - 1000$	N/A	DNS
Breuer and Almohammed (2015)	Channel flow	$Re_B = 11,900$	4W with agglomeration	LES
Kuerten and Vreman (2015)	Channel flow	$Re_\tau = 150$	4W	DNS
Lee and Lee (2015)	Channel flow	$Re_\tau = 180$	2W	DNS
Njobuenwu and Fairweather (2015a)	Channel flow	$Re_\tau = 300$	1W non-sphericals	DNS
Van Wachem (2015)	Channel flow	$Re_B = 42,585$	4W non-sphericals	DNS/LES
Vreman (2015)	Channel flow with rough walls	$Re_\tau = 642$	4W	DNS
Zhao et al. (2015)	Channel flow	$Re_\tau = 150$	4W	DNS
Prat et al (2020)	Channel flow	$Re_\tau = 160 - 610$	N/A	LES (with neural network)

Chapter 3 Methodology

3.1 Introduction

This chapter shall explain the numerical methods, computations and scientific theory employed in this project. First the DNS code, Nek5000, used to model the fluid flow will be introduced. Then the LPT in its most basic form, along with the modifications made to facilitate a stochastic approach capable of predicting agglomerating particles.

3.2 Modelling the Fluid Phase

3.2.1 Non-dimensionalising the Navier-Stokes Equations

The model of the fluid phase flow over time is developed through repeatedly solving the mass, momentum, and energy conservation equations over small three-dimensional elements. Given a fluid that is both Newtonian and incompressible the incompressible Navier-Stokes (17) and continuity (18) equations are used, as shown below, where $\boldsymbol{v}$ is the fluid velocity vector and p is the fluid pressure. ρ_F and ν_F are respectively the density and viscosity of the continuous phase.

$$\frac{d\boldsymbol{v}}{dt} = -\frac{1}{\rho_F}\nabla p + \nu_F \nabla^2 \boldsymbol{v} \tag{17}$$

$$\nabla.\boldsymbol{v} = 0 \tag{18}$$

For the purpose of this study, these equations are non-dimensionalised, and transformed into the incompressible non-dimensional Navier-Stokes and continuity equations:

$$\frac{d\boldsymbol{u}^*}{dt^*} + (\boldsymbol{u}^* \cdot \nabla)\boldsymbol{u}^* = -\nabla p^* + \frac{1}{Re_B}\nabla \cdot \tau^* + f_i \tag{19}$$

$$\nabla.\boldsymbol{u}^* = 0 \tag{20}$$

Here, $\boldsymbol{u}^*$ is the fluid velocity vector, which has been non-dimensionalised in terms of the bulk velocity U_B, and t^* is an expression of non-dimensionalised time $\frac{tU_B}{\delta}$, where δ is half the height of the channel. p^* is a non-dimensionalised pressure term equal to $\frac{p}{\rho U_B{}^2}$, where ρ is the density of the continuous phase. Re_B is the bulk Reynolds number given by $\frac{\delta U_B}{\nu}$, and τ^* is the non-dimensionalised deviatoric stress tensor, which is given by:

$$\tau^* = (\nabla \boldsymbol{u}^* + \nabla \boldsymbol{u}^{*T}) \qquad\qquad (21)$$

In equation (19), f_i is an additional forcing term implemented based on the desired properties of the flow. In this case it consists of a pressure gradient term, a forcing function that is applied in order to facilitate a constant flow through the channel, and the cell dependent term, which is applied to flows with multiple phases, and accounts for the coupling of momenta between particles within a specific cell and the fluid therein. The equations used to calculate this value will be examined in more detail in section 3.3. The formulae hitherto shown form the basis of simulating fluid dynamics, and define the problems and solutions for the vast majority of single-phase fluid cases.

3.2.2 Direct Numerical Simulation

Given that the intention of this work is to create a precise benchmark for simulations of channel flow, it is imperative that the fluid dynamics as well as any particle-fluid or particle-particle interactions are resolved at all of the relevant scales. As such, direct numerical simulation (DNS) is the method used. DNS models resolve turbulent effects on the Kolmogorov length scale η, up to the integral length scale L. The time-steps utilised by the simulation are also scaled down in accordance with the smallest turbulent events in the fluid.

3.2.3 The Nek5000 Fluid Simulation Code

In order to simulate the fluid flow, a spectral element method (SEM) is used to determine the action of the fluid. The SEM is a hybrid of the finite element method and the spectral method. Combining the accuracy of the spectral method with the generality of the finite element method leads to a much more flexible technique for solving the incompressible Navier-Stokes equations. The code Nek5000 (Fischer et al., 2008) has been extensively tested and validated, and contains efficient parallelisation capabilities as well as the flexibility to include an effective particle phase model.

The SEM is implemented by dividing the fluid domain into smaller elements, the number and shape of which are determined by the geometry of the domain and by the intended resolution of the program, with enough flexibility to accommodate common and indeed uncommon fluid domains. This project is using DNS, so the elements used have an upper bound for size, which, as shown by Moser and Moin (1984), is ideally no greater than 15 times the Kolmogorov length scale.

The incompressible Navier-Stokes equation, with the continuity equation, is expanded as N^{th} order polynomials within each of these separate elements. For the purpose of this study N=7, so each of the elements used contain 8^3 grid points. This process is easily parallelised, which is highly useful for a program which potentially requires a great deal of computational power. In this specific case the equations below are indeed solved in parallel by the program. The Galerkin approximation is used to produce a discrete form of the equations in space. N^{th}-order

Lagrangian polynomial interpolants on Gauss-Lobatto-Legendre (GLL) points are used as a basis for the velocity space. The pressure space uses Lagrangian interpolants with an order of N-2 on Gauss-Legendre quadrature points. This is the structure of the $P_N - P_{N-2}$ spectral element method produced by Maday and Patera (1989).

Nek5000 uses semi-implicit time-steps where the viscous terms of the Navier-Stokes equations are treated by third-order backward differentiation and the non-linear terms are treated by a third-order extrapolation scheme. This results in a formulation which solves the basis coefficient vectors at each time-step:

$$\underline{H}\underline{\boldsymbol{u}}_{n+1} = \underline{D}^t_{n+1}\underline{\boldsymbol{u}}_{n+1}$$
$$+ \underline{B}\underline{f}_{n+1}$$
(22)

$$\underline{D}_{n+1}\underline{\boldsymbol{u}}_{n+1} = 0$$
(23)

Here, $\underline{D}$ is the discrete divergence operator. $\underline{H} = Re_B^{-1}A + \beta_0/\Delta t\ \underline{B}$ is the discrete equivalent of the Helmholtz operator, $\underline{H} = Re_B^{-1}\nabla^2 + \beta_0/\Delta t$ with the discrete Laplacian A and the mass matrix B being associated with the velocity mesh. $\beta_0 = 11/3$, a coefficient of third order backward differentiation. $\underline{f}_{n+1}$ accounts for the remaining differentiation terms, as well as the nonlinear terms and the body force, which is determined implicitly to satisfy a fixed rate of flow. Underlined terms represent basis coefficients.
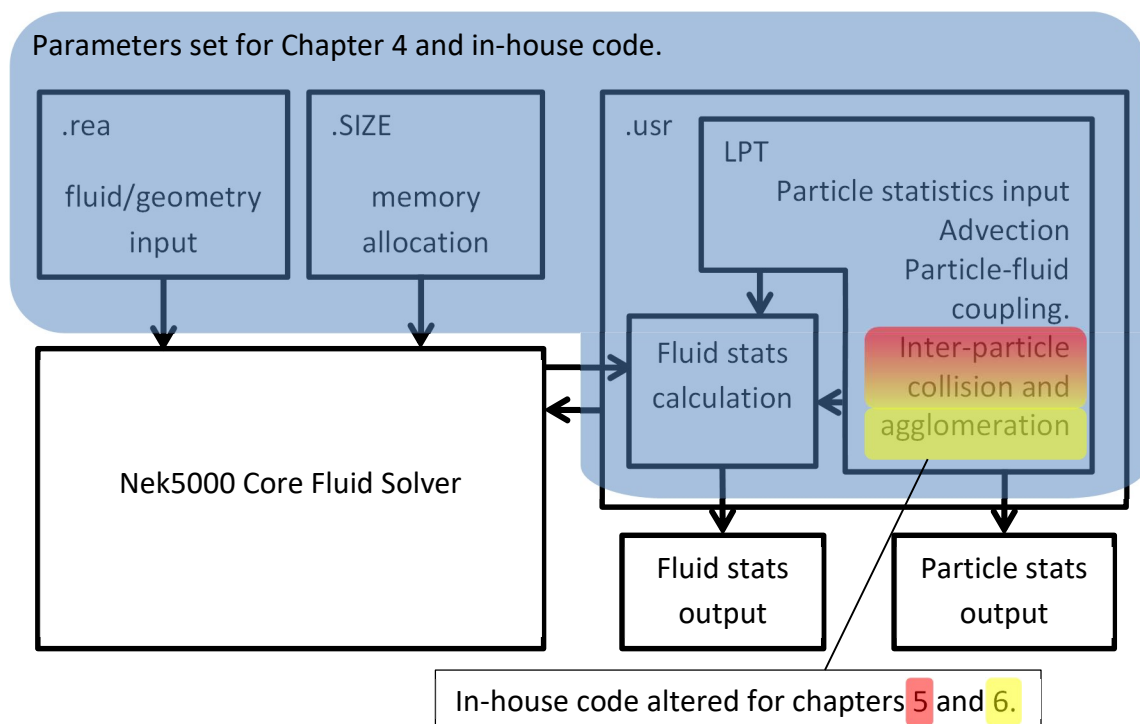
Figure 4: Representation of the code structure used by Nek5000, detailing the parameters modified for this study.

In Figure 4 the basic structure of the Nek5000 fluid simulation code is described, highlighting the parts of the input and simulation code that are relevant within the various parts of this study. The core fluid solver of Nek5000 receives input from files which define computer resources as well as fluid properties and simulation geometry. These have all been tested as part of the in-house code by multiple researchers, and with the majority of the .usr file that contains the fluid forcing function, statistics calculations, and the entirety of the particle handling algorithms, these are fully decided for Chapter 4 and onwards. Chapters 5 and 6 involve the modification of a single part of the LPT code which handles inter-particle collision effects.

3.2.4 Geometry of the Fluid Domain

For the purposes of this study, Nek5000 solves equations (19) and (20) for a turbulent fluid flow in a channel with dimensions $12\delta \times 2\delta \times 6\delta$, where δ is the half-height of the channel. The longest dimensions of the channel; the streamwise direction: x^* at 12δ, and the spanwise direction: z^* at 6δ have boundaries which are continuous and periodic, while the height of the channel, or the wall normal direction; y^* is bounded by walls that have a non-slip condition (see Figure 5). The mesh used to simulate the channel consists of $32 \times 32 \times 32$ elements, which, with spectral order N=7, each have $8 \times 8 \times 8$ nodes, for a total number of equivalent nodes in the order of 10^7. Figures 6 and 7 show the mesh that is implemented, where element sizes are uniform in the x^* and z^* directions and scaled in the wall normal (y^*) direction. As the wall is approached, the turbulent effects reach smaller, more complex scales, and the near-wall region and the buffer layer require a finer mesh so that their turbulence might be fully resolved.

Figure 5: Representation of the channel geometry, with continuous boundaries shaded and solid surfaces as the upper and lower planes.
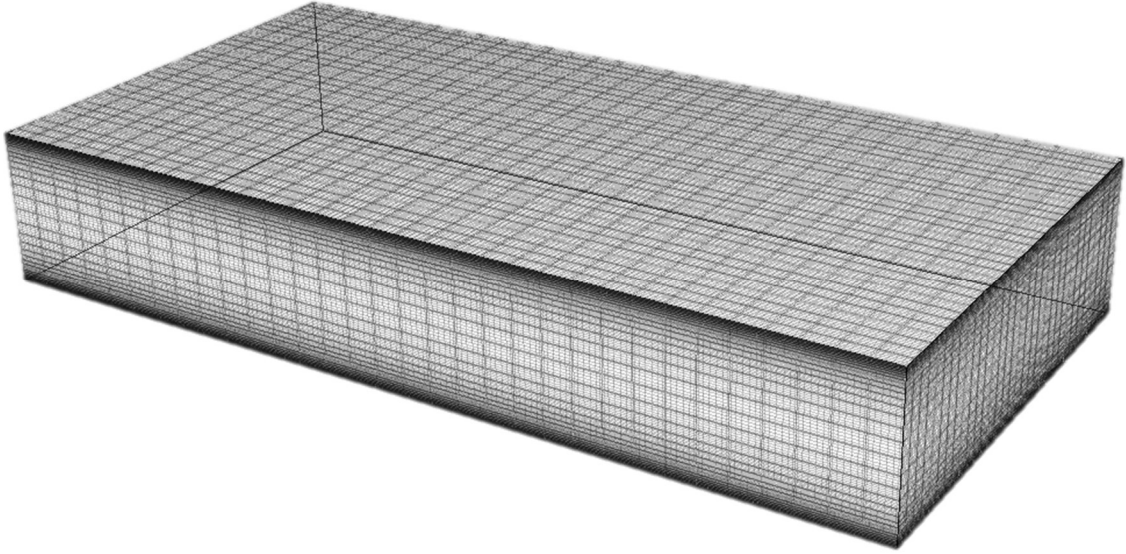
Figure 6: Visualisation of the computational mesh for the channel geometry (solid surfaces are the upper and lower planes),
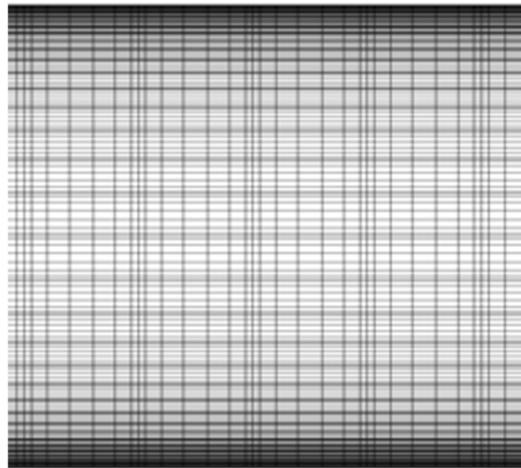
Figure 7: Visualisation of the computational mesh across the channel in the wall-normal direction (solid surfaces at top and bottom).

3.2.5 The Forcing Function

The channel flow is driven using a constant pressure gradient in the streamwise (x^*) direction. The magnitude of this is given, using non-dimensional parameters, by:

$$\frac{\delta p^*}{\delta x^*} = \left(\frac{Re_\tau}{Re_B}\right)^2 \qquad (24)$$

Here, $Re_\tau = u_\tau \delta / v_F$ is the shear Reynolds number given by the shear velocity, which is $u_\tau = \sqrt{\tau_W/\rho_F}$, where τ_W is the mean wall shear stress. In this work, the channel flows are

performed at a shear Reynolds number of 300, which translates to a bulk Reynolds number of 4900.

3.3 Lagrangian Particle Tracking

In order to model the dispersed particle phase of a multiphase flow, a Lagrangian particle tracker (LPT) is employed which was developed in conjunction with the Nek5000 code used in this study. The Lagrangian particle tracking routine tracks individual particles synchronously with the Eulerian fluid flow model, operating over the same timesteps and realistically representing the fluid-particle interactions by solving the non-dimensional equations of motion described below.

The fourth order Runge-Kutta scheme, described later in this chapter, is employed for the solution of the differential equations that are necessary for calculating the position and the velocity of the simulated particles. The equations for particle motion, resolved by the LPT used in this study, consider the effects of drag, lift, virtual mass, and pressure gradient forces. Gravity is neglected for the purpose of this study, in order to ultimately focus on particle collisions and agglomeration, without the added complication of particle deposition. The Basset history force is also not used, since its high computational cost outweighs its negligible impact on accuracy demonstrated in studies such as Fairweather and Hurn (2008).

3.3.1 Non-dimensional Parameters

In this study the LPT calculates particle motion from non-dimensionalised parameters, much the same as those used by the fluid flow DNS. Given below are the relationships giving the position (x), velocity (u), density (ρ) and time (t) parameters in their non-dimensional forms:

$$x^* = \frac{x}{\delta} \tag{25}$$

$$u^* = \frac{u}{U_B} \tag{26}$$

$$\rho^* = \frac{\rho}{\rho_F} \tag{27}$$

$$t^* = \frac{tU_B}{\delta} \tag{28}$$

Here, δ is the channel half height, U_B is the fluid bulk velocity, and ρ_F is the density of the fluid phase

3.3.2 Particle Equations of Motion

The below equations for force are combined together to get the full non-dimensional equations of motion for a typical spherical particle as calculated in the code:

$$\frac{\partial \boldsymbol{x}_P^*}{\partial t^*} = \boldsymbol{u}_P^* \tag{29}$$

$$\frac{\partial \boldsymbol{u}_P^*}{\partial t^*} = \frac{1}{M_{VM}} \left[\underbrace{\frac{3C_D |\boldsymbol{u}_s^*|}{4d_p^* \rho_P^*} \boldsymbol{u}_s^*}_{Drag} + \underbrace{\frac{3}{4} \frac{C_L}{\rho_P^*} (\boldsymbol{u}_s^* \times \boldsymbol{\omega}_F^*)}_{Lift} + \underbrace{\frac{1}{2\rho_P^*} \frac{D\boldsymbol{u}_F^*}{Dt^*}}_{Virtual\ Mass} \right. \tag{30}$$

$$\left. + \underbrace{\frac{1}{\rho_P^*} \frac{D\boldsymbol{u}_F^*}{Dt^*}}_{Pressure\ Gradient} \right]$$

The fourth order Runge-Kutta method, also known as RK4, is used to solve these equations for every particle within every time-step in the Lagrangian particle tracker. The RK4 method is fully described by Süli and Mayers (2003).

Given a time dependent function, y, such that:

$$\dot{y} = f(t, y) \tag{31}$$

$$y(t_0) = y_0,$$

the time-step length h is used to define the change over time for the particles subject to the equation as the fourth order approximation:

$$y_{n+1} = y_n + \frac{h}{6}(\boldsymbol{k}_1 + 2\boldsymbol{k}_2 + 2\boldsymbol{k}_3 + \boldsymbol{k}_4) \tag{32}$$

$$t_{n+1} = t_n + h \tag{33}$$

for n = 0, 1, 2…

where k_1 through k_4 are a series of incremental approximations based upon the gradient of the function:

$$\boldsymbol{k}_1 = f(t_n, y_n) \tag{34}$$

$$\boldsymbol{k}_2 = f\left(t_n + \frac{h}{2}, y_n + \frac{h}{2}\boldsymbol{k}_1\right) \tag{35}$$

$$\boldsymbol{k}_3 = f\left(t_n + \frac{h}{2}, y_n + \frac{h}{2}\boldsymbol{k}_2\right) \tag{36}$$

$$\boldsymbol{k}_4 = f(t_{n+h}, y_n + h\boldsymbol{k}_3) \tag{37}$$

k_1 is an increment which is based on the slope at the start of the function, k_2 and k_3 are defined by the slope at the midpoint of the function and the previous k_n function, and k_4 uses the slope at the end by reference to k_3.

Aside from the constant effect of the forces described below, the particles are also subject to the same boundary conditions that the fluid is. If the trajectory of a particle places it on the side of the boundary not contained by the computational domain, it is repositioned to the other side of the flow in the case of a periodic boundary, or rebounded and given a reversed wall-normal velocity in the case of a channel wall.

3.3.3 Non-dimensional Drag Force

Frictional drag is generally the dominant force on the particle phase of multiphase systems. For a spherical particle this is given by:

$$\boldsymbol{F}_D = \frac{3}{4}\frac{m_p}{\rho_P d_P} C_D (\boldsymbol{u}_F - \boldsymbol{u}_P)|\boldsymbol{u}_F - \boldsymbol{u}_P| \tag{38}$$

Here, ρ_P is the particle phase density, m_p is the particle mass and d_p is the diameter. C_D is the drag coefficient, whilst $\boldsymbol{u}_F$ and $\boldsymbol{u}_P$ are, respectively, the instantaneous velocities of the fluid, and the particle. The particle Reynolds number, Re_p is used to define C_D and is given by:

$$Re_p = \frac{\rho_F d_P|\boldsymbol{u}_F - \boldsymbol{u}_P|}{\mu_F} \tag{39}$$

where μ_F is the kinematic viscosity of the fluid phase in this equation. By applying the non-dimensional parameters to this equation and substituting in the slip velocity, defined as:

$$\boldsymbol{u}_s = \boldsymbol{u}_F - \boldsymbol{u}_P \tag{40}$$

the particle Reynolds number can now be written in terms of the bulk Reynolds number $Re_B = U_B\delta/v$, as:

$$Re_p = Re_B d_P^*|\boldsymbol{u}_s^*| \tag{41}$$

This allows us to get a value for f_D, which is the Stokes drag function defined by Schiller (1933) and Clift et al. (2005) as:

$$f_D = \begin{cases} 1 & 0 < Re_P \leq 0.5 \\ 1 + 0.15 Re_P^{0.687} & 0.5 < Re_P \leq 1000 \\ \dfrac{0.44}{24} Re_P & 1000 < Re_P \leq 250,000 \end{cases}$$

This allows for the calculation of the drag coefficient, C_D:

$$C_D = \frac{24}{Re_p} f_D \tag{42}$$

It also allows the non-dimensional particle Stokes number to be calculated as:

$$St_B = \frac{\tau_P}{\tau_F} = \tau_P^* = \frac{d_P^{2*} \rho_P^* Re_B}{18 f_D} \tag{43}$$

Altogether this allows the non-dimensional drag force equation to be calculated:

$$\boldsymbol{F}_D = m_P \frac{\partial \boldsymbol{u}_P}{\partial t} = \frac{3}{4} \frac{\rho_F}{\rho_P} \frac{m_p}{d_p} C_D \boldsymbol{u}_s |\boldsymbol{u}_s| \tag{44}$$

$$m_P \frac{\partial \boldsymbol{u}_P^*}{\partial t^*} \left(\frac{U_B^2}{\delta} \right) = \frac{3}{4} \frac{m_p}{d_p^* \rho_P^*} C_D \boldsymbol{u}_s^* |\boldsymbol{u}_s^*| \left(\frac{U_B^2}{\delta} \right) \tag{45}$$

giving
$$\frac{\partial \boldsymbol{u}_P^*}{\partial t^*} = \frac{3 C_D |\boldsymbol{u}_s^*|}{4 d_p^* \rho_P^*} \boldsymbol{u}_s^* \tag{46}$$

3.3.4 Lift Force

Lift is a force which acts as a result of velocity gradients over the particle. Saffman (1965, 1968) studied the effects and direction of this lift force at a low Reynolds number, finding that this lifting force influences the particles in a transverse direction compared to the local fluid streamlines. Later, Mei (1992) and Dandy and Dwyer (1990), extended the expression for lift force for particles at a high Reynolds number, giving the expression for this force as:

$$\boldsymbol{F}_L = \frac{\rho_F}{2} \frac{\pi}{4} d_p^2 C_L d_p (\boldsymbol{u}_s \times \boldsymbol{\omega}_F) \tag{47}$$

$$C_L = \frac{4.1126}{Re_S^{0.5}} f(Re_P, Re_S) = \frac{4.1126}{Re_S^{0.5}} f_L \tag{48}$$

$$\boldsymbol{\omega}_F = \nabla \times \boldsymbol{u}_F \qquad (49)$$

Re_S is the Reynolds number of the shear flow around the particle, where:

$$Re_S = \frac{\rho_F d_P^2 |\omega_F|}{\mu_F} \qquad (50)$$

Nondimensionalised, this is:

$$Re_S = d_P^{*2} Re_B |\boldsymbol{\omega}_F^*| \qquad (51)$$

where f_L represents a Reynolds scaling factor for the lift force:

$$f_L = \begin{cases} \left(1 - 0.3314\beta^{\frac{1}{2}}\right) exp\left(-\dfrac{Re_P}{10}\right) + 0.3314\beta^{\frac{1}{2}} & if \ 0 < Re_P \leq 40 \\[2mm] 0.0524(Re_P)^{\frac{1}{2}} & if \ Re_P \geq 40 \end{cases} \qquad (52)$$

$$\beta = 0.5\frac{Re_S}{Re_P} \qquad (53)$$

This gives a non-dimensionalised equation for the particle's motion based on the force of lift according to:

$$\frac{\partial \boldsymbol{u}_P^*}{\partial t^*} = \frac{3}{4}\frac{C_L}{\rho_P^*}(\boldsymbol{u}_S^* \times \boldsymbol{\omega}_F^*) \qquad (54)$$

3.3.5 Virtual Mass Force

Virtual mass force terms appear when considerations are made regarding the acceleration or deceleration effect of the fluid field surrounding the particle. Friedrich Bessel first observed the unsteady forces applied to the particle by these effects, which were eventually quantified by Stokes (1851), and written as:

$$\boldsymbol{F}_V = \frac{1}{2}\rho_F V_P\left(\frac{D\boldsymbol{u}_F}{Dt} - \frac{\partial \boldsymbol{u}_P}{\partial t}\right) \qquad (55)$$

Moving the velocity term to the left hand side of the equation gives an additional mass term, which can be further non-dimensionalised into:

$$\frac{\partial \boldsymbol{u}_P^*}{\partial t^*} = \frac{1}{2\rho_P^*} \frac{D\boldsymbol{u}_F^*}{Dt^*} \qquad (56)$$

Through substitution the virtual mass term is obtained, by which the momentum equation is divided:

$$M_{VM} = (1 + \frac{1}{2\rho_P^*}) \qquad (57)$$

In general this term is only useful in particle-fluid systems with low density ratios like the one used in this study. At higher density ratios, i.e. where $\rho_P^* \gg 1$, it tends towards unity.

3.3.6 Pressure gradient force

The force produced by the differences in pressure from one part of the flow to another is given by:

$$F_P = \rho_F V_P \frac{D\boldsymbol{u}_F^*}{Dt} \qquad (58)$$

This is non-dimensionalised to:

$$\frac{\partial \boldsymbol{u}_P^*}{\partial t^*} = \frac{1}{\rho_P^*} \frac{D\boldsymbol{u}_F^*}{Dt^*} \qquad (59)$$

3.3.7 Other Body Forces

Under some circumstances it is acceptable to neglect the forces of gravity and buoyancy as in the case of this study's simulations, however, they are calculated in the code as follows:

$$\boldsymbol{F}_G = \boldsymbol{g}(1 - \rho^*)m_p \qquad (60)$$

This is the force of gravity/buoyancy on a spherical particle m_p, which can then be non-dimensionalised to:

$$\boldsymbol{F}_G = \frac{\widehat{\boldsymbol{g}}}{Fr}(1 - \rho_P^*) \qquad (61)$$

where $\widehat{\boldsymbol{g}}$ is the vector in the direction of gravitational attraction, and Fr is the Froude number, $U_B^2/(|\boldsymbol{g}|\delta)$.

Brownian motion is a random motion which is a consequence of the atomic scale of matter in which particles are present. Therefore it has to be calculated in the tracker according to:

$$n_i(t) = G_i \sqrt{\frac{\pi S_0}{\Delta t}} \qquad (62)$$

G_i is a zero mean, unit variance independent Gaussian random number. S_0 is a parameter given as:

$$S_0 = \frac{216 \nu kT}{\pi^2 \rho d_p^5 S^2 C_0} \qquad (63)$$

This force is miniscule at the micron scale and can be neglected. Therefore in the code this particular equation shall not be initiated in order to save computational resources.

3.3.8 Two-way Coupling

In the case of two-way coupling, the effect of the particles on the fluid is considered as well as the effects of the fluid on the particles. This is achieved by adding an additional source term to the Navier-Stokes equations, which considers the effect of the particles' inertia on the fluid:

$$\boldsymbol{f}_{2W}^{*i} = \frac{1}{V_i^*} \sum_j \frac{\partial \boldsymbol{u}_{P\,j}^*}{\partial t^*} \qquad (64)$$

where V_i^* is the volume of a computational cell, and j is a function applied to each particle in that cell. This force tends only to have a meaningful impact at higher volume fractions.

3.3.9 Four-way Coupling and Boundary Interactions

The LPT code is also capable of performing four-way coupling, which considers collisions between particles as well as particle fluid dynamics. This is important for the accurate simulation of systems with particle volume fractions $\phi_P \geq 10^{-3}$. The particles are treated as having hard sphere collisions, with collision times smaller than the LPT timestep, and additional interparticle forces are either ignored as negligible, or implemented in the agglomeration section where necessary.

In order to determine whether a collision has taken place, the position and velocity of each particle is checked against the position and velocity of all the others, to see if a collision will happen within the time-step. To reduce computational demand, the domain is reduced into smaller cells, with only particles in the same cell considered as potential collision partners, as illustrated in Figure 8. The cells here were chosen to be consistent with the work of Mortimer et al. (2016), and had a side length of $\frac{\delta}{16}$.
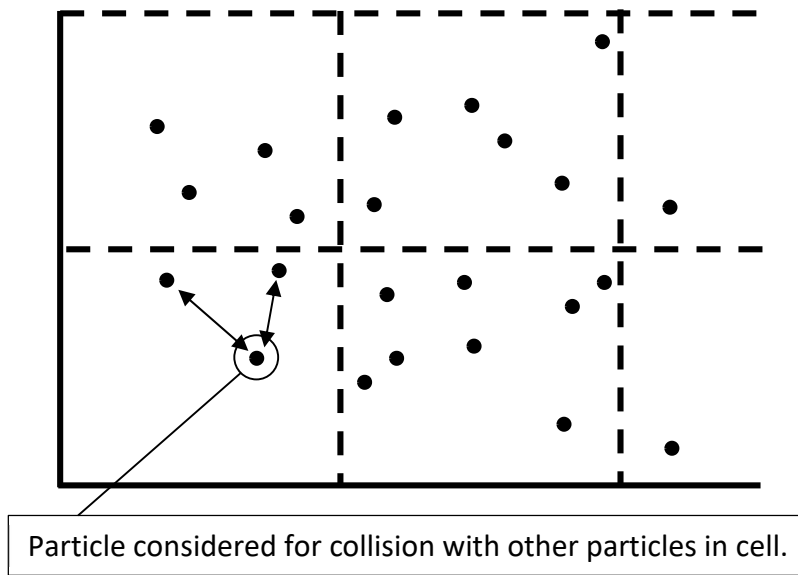
Figure 8: Visualisation of typical particle searching grid.

The collisions are calculated using the typical kinetic energy and momentum equations. In addition, overlap between particles is considered by applying an expected deflection distance which is based on calculating the precise time of collision occurrence through comparing the amount of overlap between the particles with their velocities. The collisions are treated as fully elastic, and the same process is used to calculate any collisions between the particles and the channel walls.

Interactions between particles and the periodic or wall boundaries of the channel are calculated at the end of the particle timestep, to allow for particles that might be deflected into the boundaries by other particles. Collisions with the *y* axis wall boundaries invert the

respective component of velocity, while particles that collide with the periodic boundaries are relocated to the opposite boundaries, retaining their velocities, as illustrated in Figure 9.
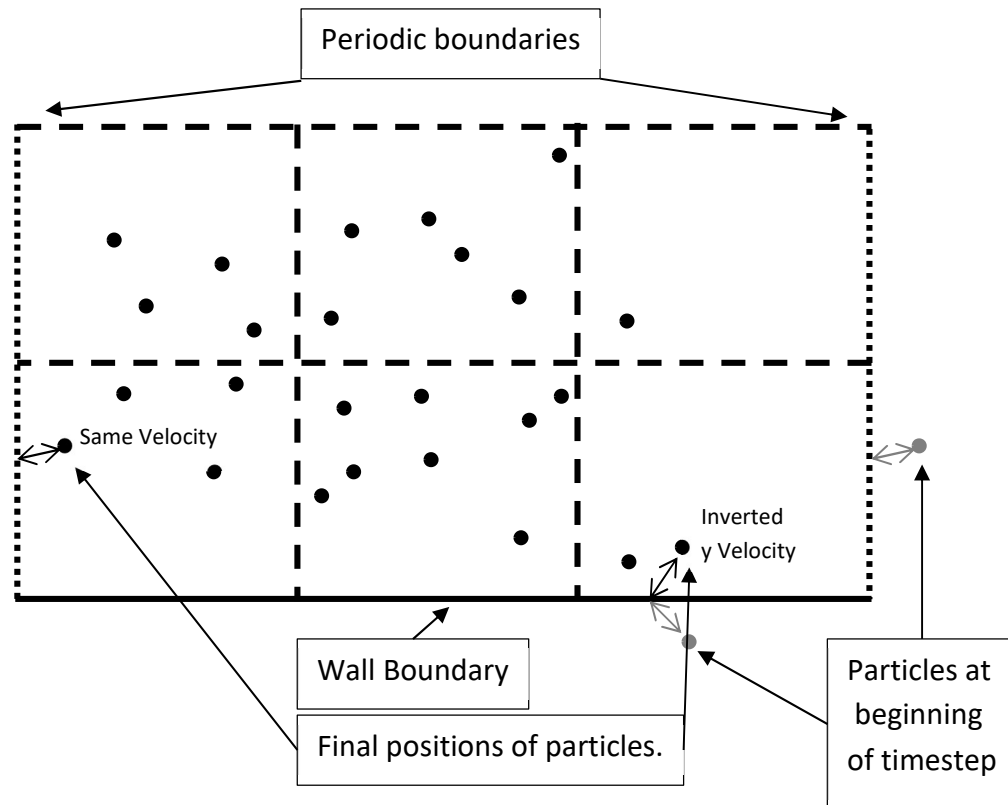
Figure 9: Visualisation of calculations at boundaries.

3.3.10 Particle Phase Parameters

The statistics of the particles used in this work differ between the validations of the model against the results of Marchioli and Soldati (2007) and other numerical simulations covered by this study.

Marcholi and Soldati's simulation (2007) was of fly ash in air, the particles having a density of 1500 kg m^{-3}, in air of density 1.3 kgm^{-3}. The first set of simulations was a validation of the results from three different particle classes, as shown in Table 1, as well as a run with no particles.

Table 2: Statistics of the particles used for validation purposes.

Stokes number	Particle diameter
1	10.2μm
5	22.8μm
25	51.0μm

The next series of runs performed were simulating glass beads, with density 2500 kg m^{-3} in water of density 1000 kg m^{-3}. The validation runs were only run with one-way coupling as in Marchioli and Soldati (2007), however the independent runs implement variously one-way, two-way, and four-way coupling with the intent of comparing these results. Table 2 covers the runs interactions accommodated within the.

Table 3: Explanation of different coupling principles.

Level of Coupling	Fluid-Particle Interaction	Particle-Fluid Interaction	Particle-Particle Interaction
One-way	Yes	No	No
Two-way	Yes	Yes	No
Four-way	Yes	Yes	Yes

For all runs following the validation, results are presented from four different scenarios with differing volume fractions and particle sizes, as shown in Table 3 below.

Table 4: Statistics of the particles used independently.

Case	Diameter	Number of Particles	Stokes Number	Volume Fraction
1	100μm	300000	0.3125	0.00013
2		2201834		0.0010
3	200μm	300000	1.25	0.0010
4		2201834		0.0080

3.4 The Stochastic Method of Particle Collision

3.4.1 Introduction

A potential method of reducing the computational demand in simulations of high concentrations of particles is to model the collisions between particles stochastically, rather than deterministically, as shown by Sommerfeld (2001). The stochastic family of particle simulations is based on making assumptions about the properties of the particles and fluid flow in a particular region, then calculating the expected rate of collision in said region. This gives the probability of a collision per particle per unit time.

3.4.2 Calculating the Probability of Collision

Simulating a particle-particle collision stochastically means obtaining an expression for the probability of any one particle colliding in a particular region of the channel at a particular time. There are two limiting cases for predicting a rate of interparticle collision per unit volume and time.

The first limiting case is for particles which completely follow the turbulence, having a Stokes number which tends towards zero. The expression for the rate of collision for such particles

was derived by Saffman and Turner (1956), and relies on the turbulence energy dissipation rate ε, as well as the kinematic viscosity ν_F and the overall volume fraction of the particles. In other words, the rate of collision is weighted heavily on fluid properties. It is given as:

$$N_{ij} = \left(\frac{8\pi}{15}\right)^{1/2} n_{p,i} n_{p,j} (R_{p,i} + R_{p,j})^3 \left(\frac{\varepsilon}{\nu_F}\right)^{1/2} \tag{65}$$

n_p and R_p refer, respectively, to the number concentrations of particles present of classes i and j. For the purposes of this study, the equation may be simplified somewhat, since only considered are uniformly sized particles colliding with a member of their own class, so:

$$N_{ij} = \left(\frac{8\pi}{15}\right)^{1/2} n_p (d_p)^3 \left(\frac{\varepsilon}{\nu}\right)^{1/2} \tag{66}$$

with two identical radii R conveniently summing to a diameter d_p, becoming a somewhat tidier equation for this use case. Note that with the consideration of agglomeration, a new term is added, but this is described further in its own section. From this it is trivial to multiply by the particle timestep, Δt, and transform from a collision rate to a collision probability:

$$P_{coll} = \left(\frac{8\pi}{15}\right)^{1/2} n_p D_p \left(\frac{\varepsilon}{\nu}\right)^{1/2} \Delta t \tag{67}$$

This set of equations and the theory surrounding it will be referred to as the advective theory of particle collision, in contrast to the kinetic theory of particle collision, which describes the other limiting case, where the Stokes number approaches infinity. Abrahamson (1975) examined this case, wherein the external forces of the fluid do not impact the particles, and there is no mean drift present, and determined that it would correctly apply to particles. The collision rate here derives from the mean fluctuating velocity of the heavy particles σ, and the size of their cross sections as they travel, hence the relationship with $R_p{}^2$, rather than $R_p{}^3$, as shown:

$$N_{ij} = 2^{3/2} \pi^{1/2} n_{p,i} n_{p,j} (R_{p,i} + R_{p,j})^2 \sqrt{\sigma_{p,i}^2 + \sigma_{p,j}^2} \tag{68}$$

Sommerfeld (2001) calculates a collision frequency for a single particle using the kinetic theory of gases, and from it, derives a probability for the collision between a given pair of particles:

$$P_{coll} = \frac{\pi}{4} (D_{p,i} + D_{p,j})^2 |\boldsymbol{u}_{p,i} - \boldsymbol{u}_{p,j}| \Delta t \tag{69}$$

Here, $|\boldsymbol{u}_{p,i} - \boldsymbol{u}_{p,j}|$ is the instantaneous relative velocity between the two particles. This is another equation which can be simplified for uniform particles, to:

$$P_{coll} = \pi D_p^2 |\boldsymbol{u}_{p,i} - \boldsymbol{u}_{p,j}| \Delta t \qquad (70)$$

Note that when these formulas are implemented in the Nek5000 particle tracker their quantities are non-dimensionalised.

3.4.3 The Fictional Particle Collision

When using a stochastic collision metric it is automatically assumed that particles which are close enough to undergo collision will have similar velocities. The fictional particle method generates a collision partner for each particle based on the statistics of those surrounding it. As in the deterministic method the domain is split into smaller cells. Fictional particles are then generated with a velocity given by the equation:

$$\boldsymbol{u}'_{fict,i} = R(St)\boldsymbol{u}'_{real,i} + \sigma_{p,i}\sqrt{1 - R(St)^2}\xi \qquad (71)$$

Here, $\boldsymbol{u}'_{fict,i}$ and $\boldsymbol{u}'_{real,i}$ are, respectively, the particle velocity component i for the fictional and real particles, with the right hand side expressing the relationship between the real particle and said fictional particle. $\sigma_{p,i}$ is the root mean squared value for the local particle velocity component, averaged over all the particles in that cell. ξ is a zero mean Gaussian random number with a standard deviation of one. Random numbers are generated using the base FORTRAN code, and Gaussian random numbers can be calculated using two such numbers.

The sampled velocity components therefore consist of a function correlated with the particle's velocity and one correlated with the Gaussian random number. With increasing Stokes number, the correlated component decreases while the random component increases. This is expected to account for the fact that real particles do not completely ignore turbulence. A Stokes correlation function, $R(St)$, (Sommerfeld, 2001) quantifies the amount of variance expected in the velocity of a fictional particle. It is stated to be dependent on the particle Stokes number St as:

$$R(St) = exp\left(-0.55 \times St^{0.4}\right) \qquad (72)$$

In order to determine if the real particle has undergone a collision with the fictional particle, a random number from a uniform distribution in the interval [0,1] is generated. If the number generated is smaller than the probability of a collision, then a collision is stated to have occurred. This fictional particle method was intended for use alongside the kinetic theory probability equation, but it is possible to adapt it to the advective model.

Although every particle is assumed to undergo the same number of collisions with fictitious counterparts, determining the relative position of an imaginary particle and therefore the point of contact between the fictitious particle and the real one is more problematic. The position of contact could lie at any point on the particle's surface with varying probability based on the relative motion of the particles.

Transferring the colliders into a coordinate system where the fictitious particle is stationary vastly simplifies the calculations. It means that the point of contact is then limited to the hemisphere on the real particle which is facing towards the fictitious particle. A collision cylinder is constructed where the centre of the fictitious particle is bound to be located with a uniform probability.

The location of the collision on the particle's surface is not however determined by a uniform probability. Instead, two random numbers in the range [0,1] are generated to determine the lateral displacement L, normalized by the summed radii of the colliding particles. An angle, φ, can then be calculated from this value as shown in Figure 10. Particle 2 is the stationary fictitious particle and particle 1 is the real moving particle. A second angle, Ψ, is randomly sampled from the interval $[0, 2\pi]$. This accounts for the orientation of the collision within the cylinder's cross section, and is shown in Figure 10. The collision can then be treated according to the same conservation of momentum laws that were used for the deterministic collision.
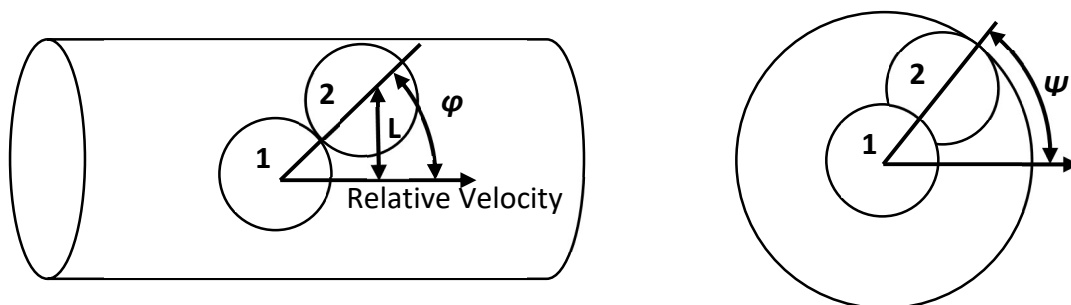
Figure 10: Collision angles calculated for fictional particles.

3.4.4 The Direct Simulation Monte Carlo Method

An alternative to the fictional particle creation method of stochastically simulating particle collision is the Direct Simulation Monte Carlo method or DSMC, as used by O'Rourke (1981) and Pawar et al. (2014). This method takes a slightly more deterministic approach, wherein a given particle is allocated a collision partner chosen from amongst its neighbours producing a distribution and rate of collision that matches up with the deterministic approach.

The region or searching scope surrounding a given particle, from which the collision partner will be selected, is crucial to this approach because there needs to be enough particles present in that region such that an unbiased statistical average can be achieved. Pawar et al. (2014) found empirically that 8 was the absolute minimum number of particles necessary to achieve this, so even though the methods used in this thesis are based on hexahedral cells and

reminiscent of O'Rourke (1981), that number can still be used advantageously when determining the boundaries of said cells, as covered in detail later in the thesis.

Since the particles have real velocities and positions it is not necessary to generate a collision angle as with the fictional particle method. The conservation of momentum equations may be solved as if the two particles had collided rigidly before being returned to their original positions.

3.5 The Particle-particle Agglomeration Model

3.5.1 Standard Calculations of Agglomeration

Incorporated into the collision code of the LPT is an agglomeration code. This can be activated to allow aggregation between two particles following a collision. Using DLVO (Derjaguin and Landau, 1941; Verwey and Overbeek, 1955) theory a lower limit of particle kinetic energy can be derived which would be required to prevent agglomeration during a collision. The agglomeration model is based on the work of Njobuenwu and Fairweather (2015b), and calculates the limit as:

$$
\boldsymbol{u}_{P,rel}^{*2} - \frac{(1 - e_n^{*2})(\boldsymbol{u}_{P,rel}^* \cdot \widehat{\boldsymbol{n}})^2}{|(\boldsymbol{u}_{P,rel}^* \cdot \widehat{\boldsymbol{n}})|}
$$
$$
\leq \frac{H^*}{6\delta_0^{*2}} \left[\frac{6(1 - e_n^{*2})}{\pi^2 \rho_P^* \sigma^*} \left(\frac{d_{P,i}^{*3} + d_{P,j}^{*3}}{d_{P,i}^{*2} d_{P,j}^{*2} (d_{P,i}^* + d_{P,j}^*)} \right) \right]^{\frac{1}{2}}
\tag{73}
$$

Here, H^* is the non-dimensional Hamaker constant, given by $H^* = H/\rho_F U_B^2 \delta^3$, $\delta_0^* = \delta_0/\delta$ and is the minimum contact distance, also non-dimensionalised, and e_n^{*2} is the coefficient of restitution. $\widehat{\boldsymbol{n}}$ is the unit vector and $\boldsymbol{u}_{P,rel}^{*2}$ is the relative velocity between the colliding particles. Where the conditions in equation (73) are met, the two particles combine into one agglomerate, having the combined spherical volume of its constituents. In the code this is non-dimensionalised, and an agglomeration number represents the volume of any particular agglomerate in terms of the original smallest particle.

New agglomerates are given a non-dimensionalised diameter; d_{agg}^* velocity; u_{agg}^* and position; x_{agg}^* from standard conservation of momentum arguments, such that:

$$
\boldsymbol{u}_{agg}^* = \left(d_{P,i}^{*3} \boldsymbol{u}_i^* + d_{P,j}^{*3} \boldsymbol{u}_j^* \right) / d_{agg}^{*3}
\tag{74}
$$

$$
x_{agg}^* = \left(x_i^* + x_j^* \right)/2 + t_{col} \boldsymbol{u}_{agg}^*
\tag{75}
$$

$$d_{agg}^* = \sqrt[3]{d_{P,i}^{*3} + d_{P,j}^{*3}} \tag{76}$$

where x represents the positions of, variously, particles i and j, d_{agg} is the final diameter of the agglomerate, and t_{col} is the collision overlap time.

3.5.2 Extensions Required for the Stochastic Model

Chapter 6 describes an implementation of the stochastic method of particle collision to systems with agglomeration. In order to accommodate this a modification to the stochastic method had to be made in order to account for the reduction in collision rate caused by the implementation of agglomeration, since the collision rate is tied directly to the turbulence of the flow and does not account for small scale inter-particle effects such as the accumulation effect. The magnitude of these effects is calculated in Wang et al (2000) to be:

$$\frac{\Gamma}{\Gamma_0} = 4.85 \frac{\eta}{r} g(r) \frac{\langle |w_r| \rangle}{u_\eta} \tag{77}$$

where η and v_k represent, respectively, the Kolmogorov length and velocity scales and are given by the equations:

$$\eta = \left(\frac{v^3}{\varepsilon} \right)^{\frac{1}{4}} \tag{78}$$

$$\tau_\eta = \left(\frac{v}{\varepsilon} \right)^{\frac{1}{2}} \tag{79}$$

$$u_\eta = \frac{\eta}{\tau_\eta} \tag{80}$$

which use the kinematic viscosity, v, and the average rate of dissipation of turbulence kinetic energy per unit mass, ε, with τ_η being the Kolmogorov timescale. r is the radius, and $g(r)$ is a statistical function of the radius known as the radial distribution at contact which directly measures the accumulation effect and through analysis is calculated to follow the relationship:

$$\frac{g(r) - 1}{Re_\lambda} = f(\varphi) \tag{81}$$

$f(\varphi)$ is a composite function of $\varphi \equiv \tau_P/\tau_\eta$ where τ_P is the inertial particle response time. The function is derived from an analytical form such that:

$$\begin{cases} y_1(\varphi) = 0.36\varphi^{2.5}\exp(-\varphi^{2.5}) & \text{for } 0.5 < \varphi < 1.25 \\ y_2(\varphi) = 0.24\exp(-0.5\varphi) & \text{for } 1.25 < \varphi < 5 \\ y_3(\varphi) = 0.013\exp(-0.07\varphi) & \text{for } \varphi > 10 \end{cases} \tag{82}$$

and assembled such that:

$$f(\varphi) = \frac{y_0(\varphi)[1 - z_0^2(\varphi)]}{R_\lambda} \tag{83}$$
$$+ z_0^2(\varphi)\{y_1(\varphi)[1 - z_1(\varphi)] + y_2(\varphi)z_1(\varphi) + y_3(\varphi)z_2(\varphi)\}$$

$$y_0(\varphi) = 18\varphi^2$$
$$z_0(\varphi) = \frac{1}{2}\left[1 + \tanh\frac{\varphi - 0.5}{0.25}\right]$$

$$z_1(\varphi) = \frac{1}{2}\left[1 + \tanh\frac{\varphi - 1.25}{0.1}\right]$$
$$z_2(\varphi) = \frac{1}{2}\left[1 + \tanh\frac{\varphi - 6.5}{2.5}\right]$$

Here, $\langle|w_r|\rangle$ represents the Lagrangian pair relative velocity statistics of particles and is a measurement of the turbulent transport effect, calculated from components derived from the shear and acceleration mechanisms, where:

$$\langle|w_r|\rangle = \left[\frac{2}{\pi}\left(\langle w_{r,accel}^2\rangle + \langle w_{r,accel}^2\rangle\right)\right]^{\frac{1}{2}} \tag{84}$$

$$\frac{\langle w_{r,accel}^2\rangle}{u'^2} = C_w\frac{2\gamma\theta}{\gamma - 1}\left[1 - \frac{(1 + 2\theta)^{\frac{1}{2}}}{1 - \theta}\right] \times \left[\frac{1}{(1 + \theta)^2} - \frac{1}{(1 + \gamma\theta)^2}\right]$$

$$\frac{\langle w_{r,shear}^2\rangle}{u_\eta} = \frac{1}{15}\left(\frac{r}{\eta}\right)^2$$

Here, $\gamma = 1.83u'^2/u_\eta^2$, $\theta = 2.5\tau_p/T_e$ where T_e is the flow integral timescale, and C_w is a curve fitting term calculated to be 1.68.

Chapter 4 Validation and Particle-Fluid Coupling Effects

4.1 Introduction

In this chapter, validation of the methodology used to simulate the particle-fluid systems is performed. The results from the DNS and accompanying LPT described in the methodology section are compared with those produced in studies by previous authors simulating the same systems. The LPT code in particular was created and developed during the course of this study and simultaneously by Mortimer et al. (2019), therefore its suitability under various conditions requires assessment. In the aforementioned concurrent study, multiphase flows were simulated in a channel flow at a shear Reynolds number of 180, which are ubiquitous in the literature. This study by comparison investigates a less common system, at a shear Reynolds number of 300, which equates to a bulk Reynolds number of 4900, approaching the critical Reynolds number for a turbulent flow in this geometry, where the fluid stops behaving laminarly and becomes turbulent.

The work of Marchioli and Soldati (2007) considered a channel geometry very similar to the one used in this work, and simulated multiphase channel flows using similar techniques at shear Reynolds numbers of 150 and 300. The latter of these therefore will be used for validation. Simulations are performed for the three particle sizes shown in Table 1 of Chapter 3 Methodology. These ensure that both the DNS and LPT generate results which fit the standards set by the existing literature.

Further to this a comprehensive analysis is undertaken into how the level of particle-fluid coupling directly affects both the accuracy of the produced results, and the rate at which they are computed, at differing Stokes numbers and volume fractions (see Table 3 of Chapter 3 Methodology). From this a benchmark standard shall be produced appropriate for the typical methods of simulation used in industry, which can be used as a guidepost when determining the level of coupling best suited for efficiently modelling a particular physical system. In later chapters this benchmark will be compared to novel techniques intended to reduce computational load whilst maintaining accuracy.

4.2 Assessment of the Single-phase Flow

4.2.1 Properties of the Flow and Geometry

In the concurrent study (Mortimer et al., 2019) the number of fluid elements was chosen to match a gridpoint density similar to that of Kim et al. (1987), whose results set a standard for comparison between experimental and simulated results. The number of fluid elements for this study was chosen to match that used by Marchioli and Soldati (2007) since the Reynolds number is higher than that used by Mortimer et al. (2019), and so a greater mesh density is required for the domain in order to reflect this, with a $32 \times 32 \times 32$ element 7th order mesh being used. Also of note is that at a shear Reynolds number of 300, fewer previous examples exist for the fluid phase results to be compared with.

Using the computational domain as described in Chapter 3, the fluid phase is initialised using a flow field condition from a base channel flow case in Nek5000 (Fischer et al. 2008) where:

$$u_x^* = \frac{5}{4}(1 - y^{*4}) + 0.3\cos(12z^*)\, e^{0.5 - 32.4(1 - |y^*|)^2}(1 - |y^*|) \tag{85}$$

$$u_y^* = 0 \tag{86}$$

$$u_z^* = 21.6\sin(12x^*)\, e^{0 - 32.4(1 - |y^*|)^2}(1 - |y^*|) \tag{87}$$

This initial condition approximates the mean flow profile, but also adds noise so that the flow more rapidly becomes turbulent. Under these conditions, with a spectral element method timestep of $\delta t^* = 0.02$, the continuous phase is simulated up to a timeframe in excess of $t^* = 1000$. The mean and fluctuating fluid velocity profiles were observed throughout this process in order to ensure that the continuous phase had reached a steady state.

The resulting settled flow was then analysed using visualisation software, as shown in the following figures. Instantaneous values were taken across the entire domain for such properties as the streamwise fluid velocity, as shown in Figure 11 in a pseudocolour plot.
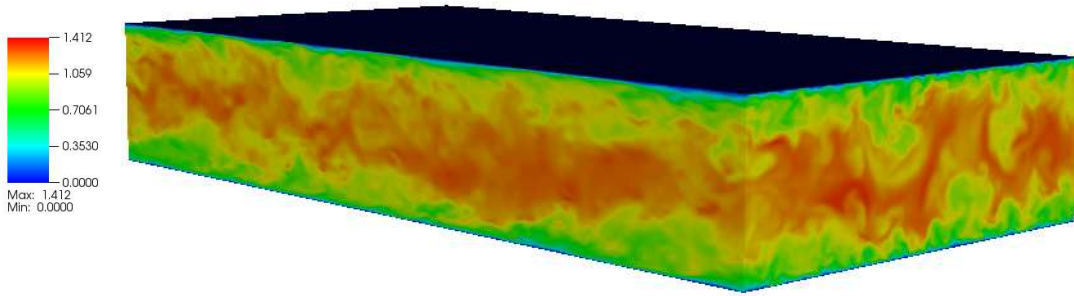
Figure 11: Three-dimensional plot of the instantaneous streamwise fluid velocity normalised by the bulk velocity in pseudocolour for a turbulent channel flow with $\boldsymbol{Re_\tau = 300}$.

As can be seen in Figure 11, the flow demonstrates the presence of turbulence. The interaction between the low speed regions at the walls of the channel, in green, and the high speed region in the bulk of the flow appears to be chaotic, as expected. Comparisons can be drawn between this visualisation and similar ones found in Mortimer et al. (2019) of a channel flow where $Re_\tau = 180$. For the $Re_\tau = 300$ channel, the boundary between the low speed and high speed regions has much less definition. In addition, the maximum velocity, compared to the mean velocity, is increased by a factor of about 15%.

Factors which more strongly indicate turbulence are those based on identifying velocity gradients in the flow, which are inherent to vortical structures. The velocity gradient tensor, D_{ij}, is given by:

$$D_{ij} = \frac{\delta u_i}{\delta x_j} \tag{88}$$

The Q-criterion is a concept which directly illustrates vorticity assuming that a vortex is: "a connected fluid region with a positive second invariant of Δu_F^*" (Holmén, 2012). Specifically the "Q" value of any particular region of a flow must be greater than zero in order to be considered vortex-like. This Q value is calculated as follows:

$$Q = \frac{1}{2}|tr(\overline{D})^2 - tr(\overline{D}^2)| = \frac{1}{2}\left(||\overline{\Omega}||^2 - ||\overline{S}||^2\right) \tag{89}$$

where

$$\Omega_{ij} = \frac{1}{2}\left(\frac{\delta u_i}{\delta x_j} - \frac{\delta u_j}{\delta x_i}\right) \tag{90}$$

and

$$S_{ij} = \frac{1}{2}\left(\frac{\delta u_i}{\delta x_j} + \frac{\delta u_j}{\delta x_i}\right). \tag{91}$$

Here, Ω_{ij} and S_{ij} are the symmetric and skew symmetric components of the velocity gradient tensor, representing the vorticity magnitude and shear strain rate of a particular region of the flow. According to these equations, this magnitude of vorticity has to be greater than the shear strain rate for that particular fluid structure to be considered a vortex.

Figures 12 and 13 illustrate examples of these vortex structures appearing in the fluid domain used for this study at $Re_\tau = 300$. Among other things, the so called "hairpin" or "horseshoe" vortices can be observed. These structures are somewhat more visible at smaller scales.
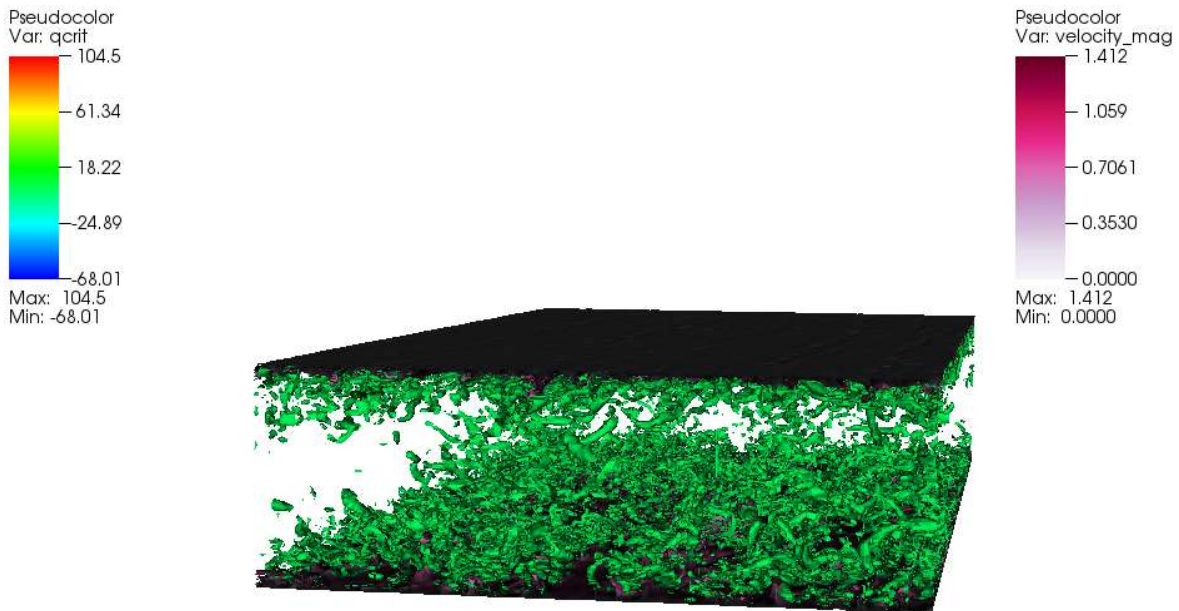
Figure 12: Three-dimensional isosurface plot of the Q-criterion across the entire turbulent channel flow at $\boldsymbol{Re_\tau = 300}$. The wall boundary is demarcated by an isosurface plot representing the low fluid velocities that occur in that region.
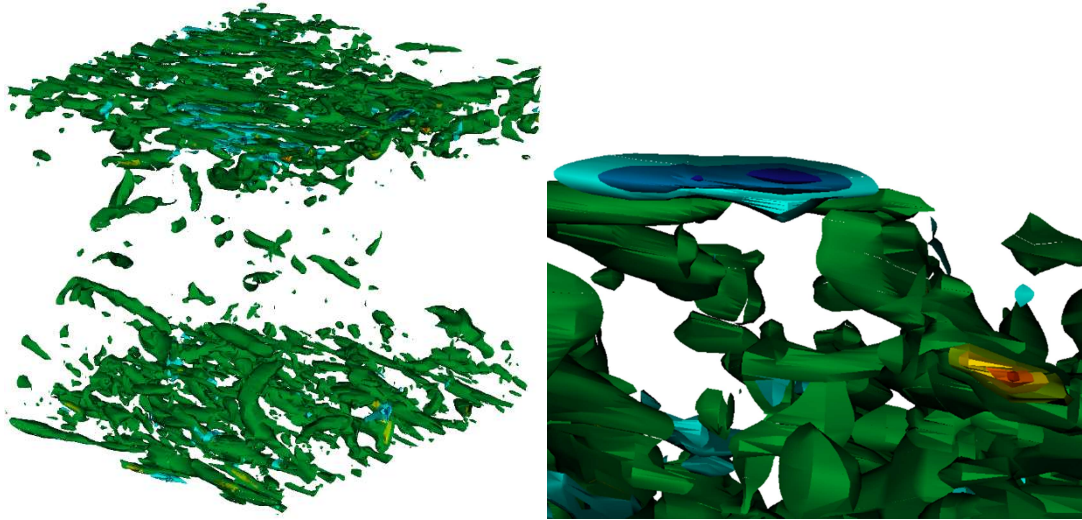
Figure 13: Cross-sections of the Q-criterion isosurface plot shown in Figure 12 showing (left) a $2\delta \times 2\delta \times 2\delta$ segment of the plot and (right) sufficient magnification to show the cross-sections of two "hairpin vortices" displaying both positive and negative vorticity at high magnitudes.

4.2.2 Kolmogorov Resolution

Equation (78) defines η, which is the Kolmogorov length scale. This is the smallest scale of turbulence possible, where the energy associated with the dynamics of turbulence structures dissipate into heat. The prediction of fluid effects at this scale is a defining quality of DNS. Figure 14 shows the magnitude of this length scale across the width of the channel, compared to some of the particle sizes used in this study.
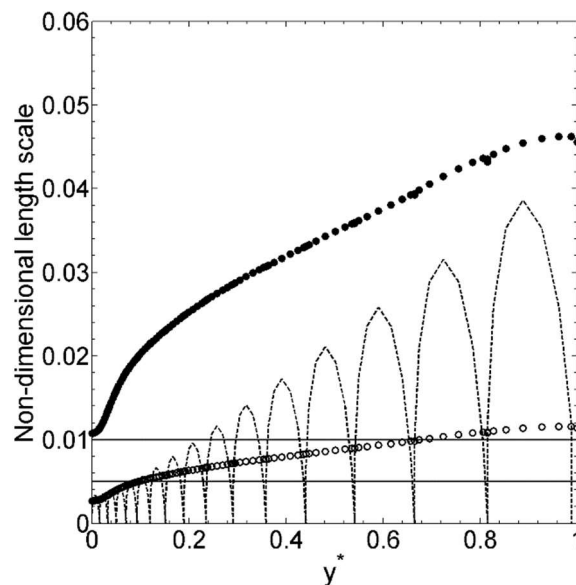
Figure 14: Important scales for the fluid model. ○ Kolmogorov length scale for fluid at 300 shear Reynolds number, ● 4 × Kolmogorov length scale. - - Element height in wall normal direction, — non-dimensional particle diameters used.

The width of the computational elements across the channel are at most three times the Kolmogorov length scale, and far less than the 15η which Moser and Moin (1984) showed to be an acceptable lower limit in terms of accuracy when modelling and interacting with the smallest scales of turbulence. The incrementing sizes of the computational elements is representative of a mesh architecture designed to concentrate data points close to the channel wall. The fact that the Kolmogorov length scale itself shows a general reduction with proximity to the wall, and in fact matches the size of the elements almost point for point at around 0.1δ, is good evidence that the elements were implemented at the correct scale, though fewer larger elements could theoretically be used in this scenario, although the extra precision is still valuable in these studies. It can also be observed that the particle sizes line up well with the Kolmogorov length scale over the width of the channel.

4.2.3 Single-Phase Validation

Given that the mesh used in this study is deemed appropriate to model both the fluid and particle phases, based on the Kolmogorov scale, the first task is to validate the simulation of the fluid phase against pre-existing results. To that end the data from Marcholi and Soldati (2007) and Morinishi and Tamano (2005), both of whom performed simulations at $Re_\tau = 300$, is acquired. In the case of Marchioli and Soldati (2007) these results were obtained through a DNS which had a fluid mesh comparable to the one used in this study, with 256^3 grid points, making it an ideal choice for comparison.

A planar average (across the nodes on the y* axis) of the mean streamwise velocity of the fully developed turbulent channel flow was taken over 1000 ≤ t* ≤ 2000 and thus averaged across that timescale. As well as the mean streamwise velocity, an important comparison can be made with the root mean squared velocity fluctuations, defined using:

$$u'^* = u^* - \bar{u}^* \qquad (92)$$

This result was averaged in much the same way, except for being squared before the planar and temporal averages were taken, and finally being square rooted, giving a final value for u'^*_{RMS}.
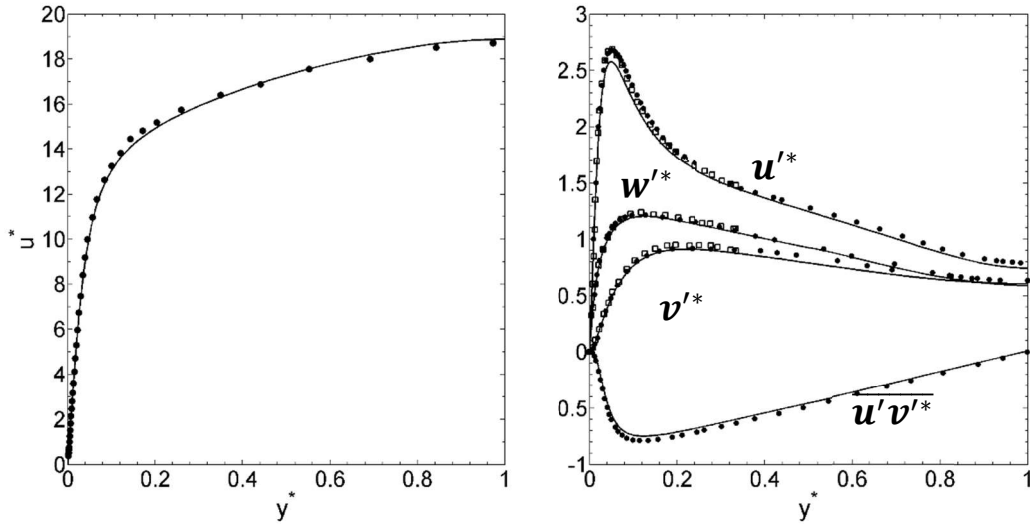
Figure 15: Validation of the mean streamwise fluid velocity; u^*, the fluid normal stresses; u'^*, v'^*, w'^*, and the shear stress; $\overline{u'v'}^*$. □ Morinishi and Tamano (2005), ● Marchioli and Soldati (2007), —— Current research.

Figure 15 shows the results of the single-phase validation simulations. There is comparatively little information available for fluids at a shear Reynolds of 300 and the Morinishi and Tamano (2005) paper in particular only produced statistics for the near wall region, at $y^* < 0.33$. Overall, there is good agreement between the present predictions and the results available in the literature. There is a slight discrepancy between the height of the peaks of the streamwise fluid normal stress, but this is at an acceptable level, and is likely related to small differences in the codes used for the simulations. The solution order may have changed between the codes, for instance, and the geometry's streamwise length has been rounded down in the present work from 2π to 6.

4.2.4 Multiphase Validation

Next, the LPT used to simulate the particles was validated using the study performed by Marchioli and Soldati (2007). The investigation considered drag force alone in its calculation of the particle trajectories, with particles possessing shear Stokes numbers of $St^+ = 1, 5, 25$, having the same densities but differing radii. Three separate cases were simulated whereby 300,000 particles with these properties were injected into a previously settled flow at $Re_\tau = 300$.

The results of these simulations are plotted in Figure 16. Besides the largest particle class, $St^+ = 25$, the particles showed uniform mean streamwise velocity values which were in near perfect accordance with the validation results. Towards the wall region, the present simulation begins to diverge slightly in the case with larger particles. For the rms velocity profiles, the agreement is excellent for all cases, besides, again, for the largest particle class, this time towards the centre of the flow. It is possible that in this case, an extended runtime would eventually force the particles results into agreement, since higher Stokes numbers

70

reflect a reduced impact on the particle velocity by the fluid phase. Also, there is some discrepancy in the streamwise peaks, towards the wall. This again is likely due to the small differences in the solution order and channel geometry. Marchioli et al (2008) note that such differences are endemic to the DNS methodology, and, regardless of these differences, DNS results still make for accurate benchmarks with which simpler models may be compared.
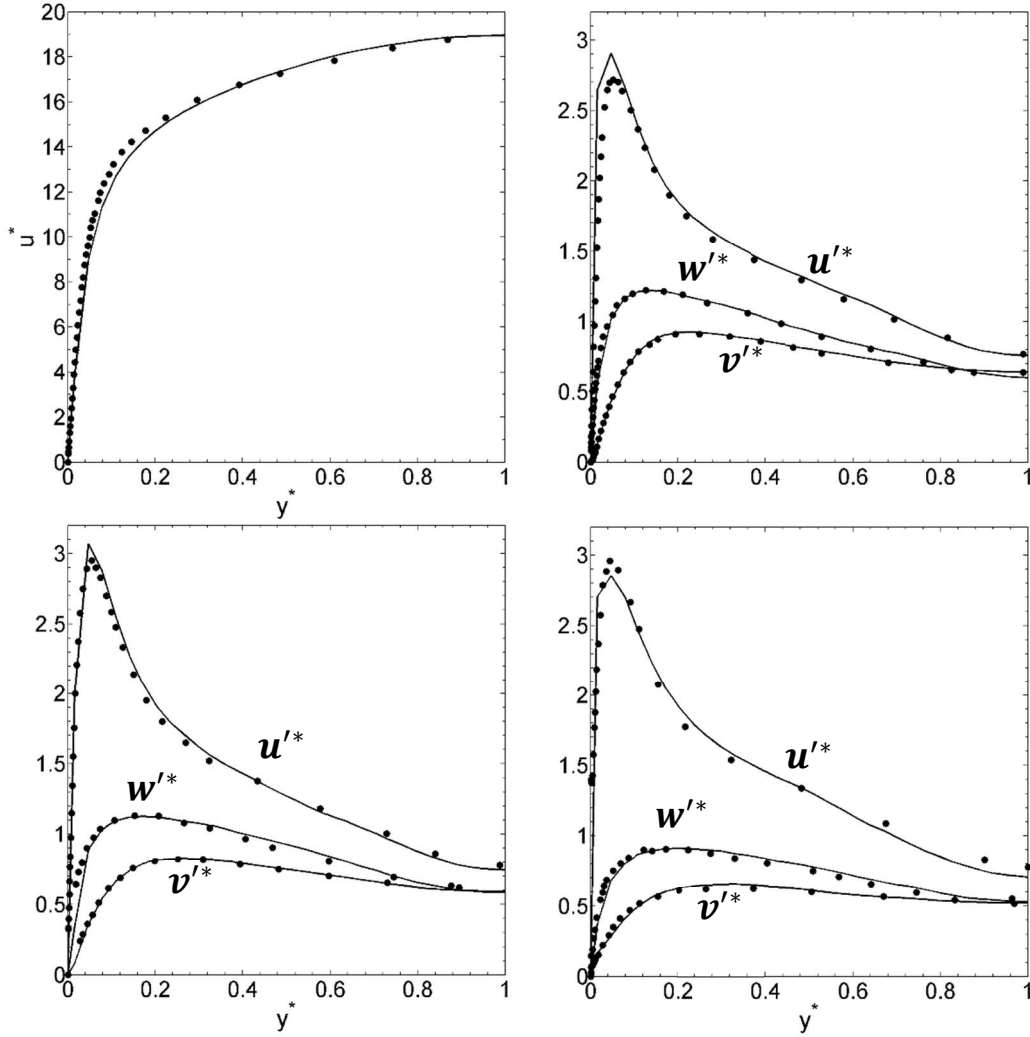
Figure 16: Validation of the mean streamwise particle velocity u^*, for a particle with $St^+ = 25$ (top left), and the normal stresses; u'^*, v'^*, w'^* for particles with $St^+ = 1$ (top right), $St^+ = 5$ (bottom left), and $St^+ = 25$ (bottom right). —— Fluid, ● Particles

4.3 Effect of Coupling Level on the Particle and Turbulence Statistics

The validation performed above was limited to a single level of coupling (one-way) between the fluid and the particles, and the solver only considered the drag term in the force balance equation. With the implementation of particle-fluid and additional interparticle forces, it can be expected that the accuracy of the simulation when compared to real-world systems will be greatly enhanced. In this section the effects of these levels of coupling will be compared for four test cases. The first of these cases was set up to match the one simulated by Mortimer

71

et al (2019), with particle and fluid statistics that correspond to 100μm glass particles in water at low volume fraction. The second and third test cases were performed with the volume fraction an order of magnitude higher, by doubling the radius to 200μm in the second case, and increasing the number of particles in the third. The final test was a more extreme case, where the number and size of particles were both increased. The specifics of the parameters used can be found in Table 3 of Chapter 3 Methodology.

The forces of drag, lift, virtual mass, and pressure gradient are considered in the one-way coupled simulations of these cases, and applied with the addition of particle-fluid forces for the two-way simulations, and interparticle forces for the four-way simulations. Snapshots of the particle phase early in the simulation for case 1 (100 μm particles at 0.00013 volume fraction in Table 3 of Chapter 3 Methodology) are shown in Figures 17 and 18. In these images it can be observed that the particles are relatively dispersed, and motion towards the wall has not yet occurred. Figure 19 shows a smaller sample of only 60,000 particles, but with colours visualised to elucidate the particle velocities.

Statistics for the particle phase were taken by dividing the channel domain into 128 wall-normal slices, which, similarly to the distribution of fluid nodes, were made smaller towards the wall to better account for resolving the small-scale motions in these regions. The length of a given slice i is given by the relationship $s_f^i = -\cos(\pi i/128)$. This method was used to produce all the mean quantities presented for particles in the following three chapters. Note that the results for the validation runs were multiplied so that they used the same terms as the Morinishi and Tamano (2005) paper, which is in terms of the shear Reynolds number. Further runs use the bulk quantities as generated directly by Nek5000.
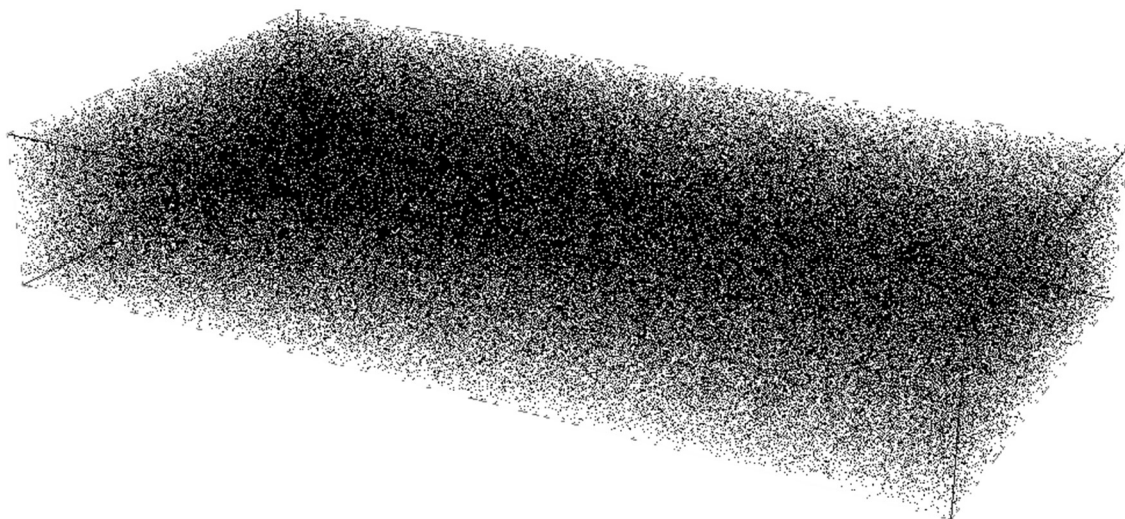
Figure 17: Three-dimensional representation of the particles for a four-way coupled multiphase flow with 300,000 particles with non-dimensional diameter, $d_P^* = 0.005$.
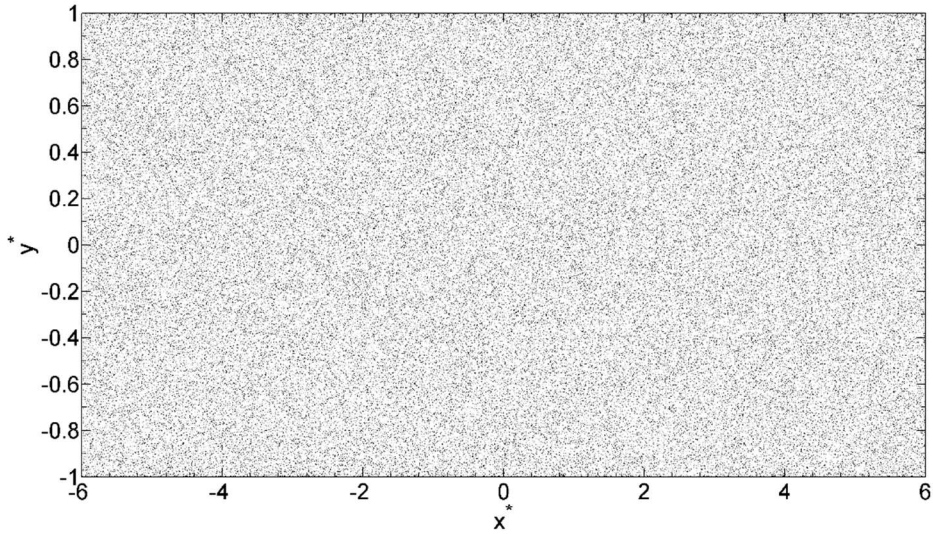
Figure 18: Two-dimensional scatter plot of the instantaneous particle positions for a four-way coupled multiphase flow with 300,000 particles with non-dimensional diameter, $d_P^* = 0.005$.
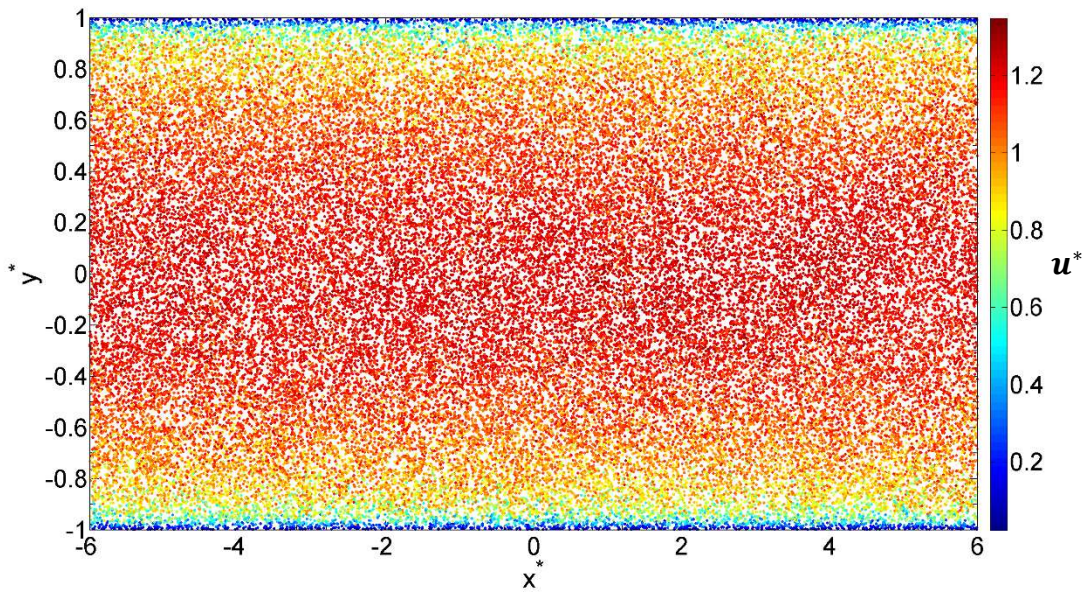
Figure 19: Two-dimensional scatter plot of the instantaneous particle positions for a four-way coupled multiphase flow with 60,000 sampled particles with non-dimensional diameter, $d_P^* = 0.005$, colour coded by streamwise velocity u^*.

4.3.1 300k, 100μm Particles (Case 1)

Figures 20 through 23 show the mean streamwise velocities and the normal and shear stresses for the fluid and particles in the first case (see Tables 2 and 3 of Chapter 3 Methodology). Both linear and logarithmic scales are presented for the first and second-order statistics so that any near wall effects become more discernible. Results for two-way

coupling and four-way coupling have been chosen to alternate so that the trends are clearer. At first glance, the difference in the fluid velocities between the different modes of coupling appears negligible, at least where the normal stresses peak near to the wall. This is to be expected since the volume fraction, $\phi_P \approx 10^{-4}$, and viscous Stokes number, $St^+ = 0.3125$, are both smallest in this case.
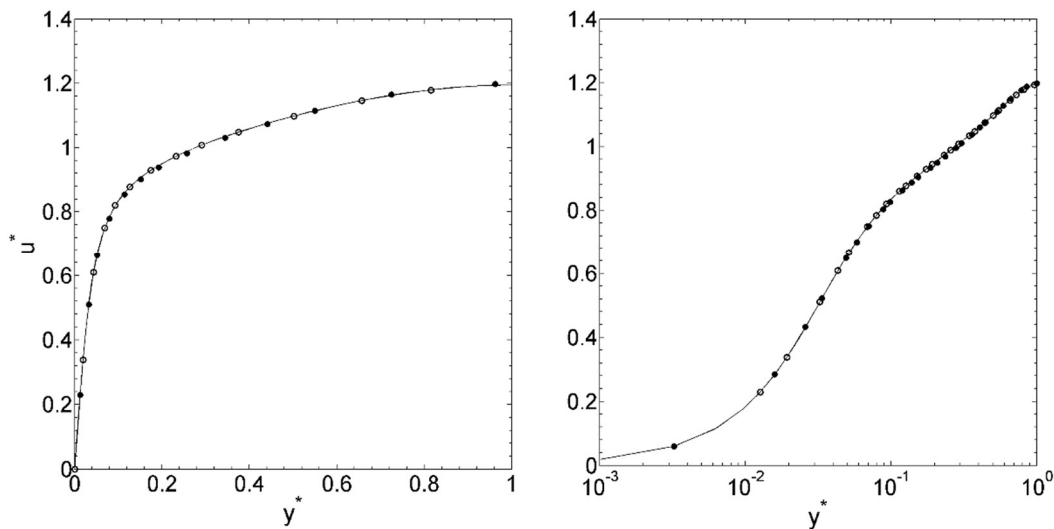
Figure 20: The mean streamwise fluid velocity $\boldsymbol{u}^*$ for a flow with 300k 100μm particles. —— One-way coupled, ○ two-way, ● four-way.
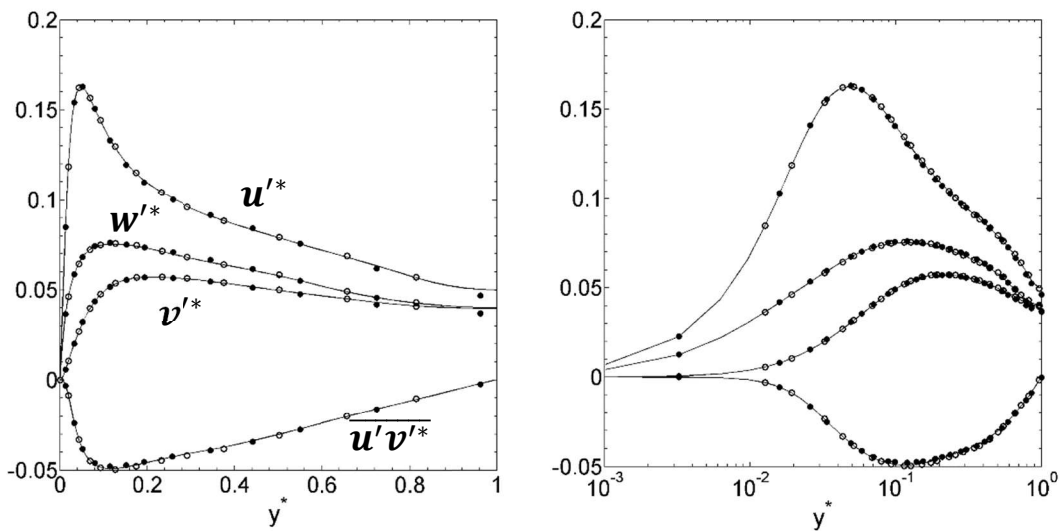
Figure 21: The fluid normal stresses $\boldsymbol{u'}^*, \boldsymbol{v'}^*, \boldsymbol{w'}^*$, and fluid shear stress, $\overline{\boldsymbol{u'v'}}^*$ for a flow with 300k 100μm particles. —— One-way coupled, ○ two-way, ● four-way.
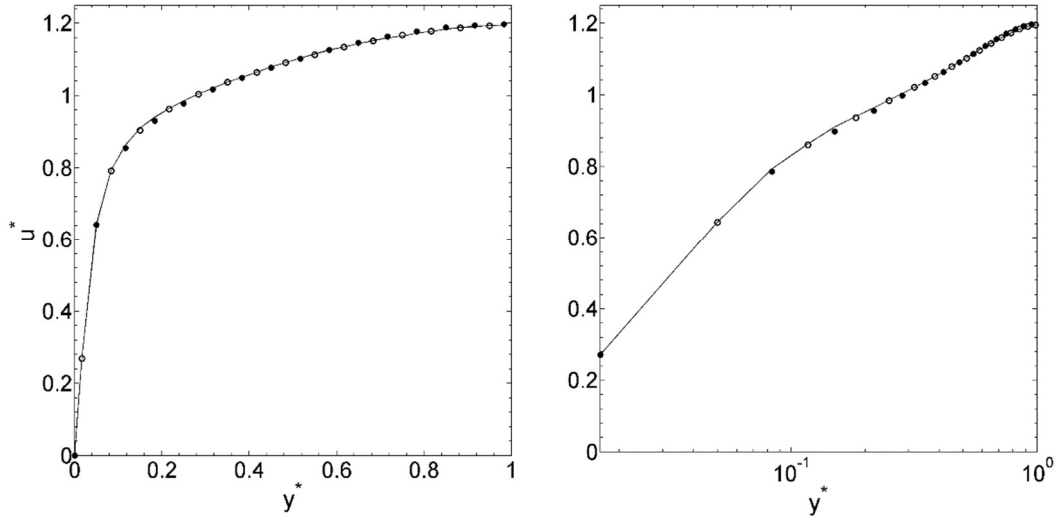
Figure 22: The mean stream-wise particle velocity u^* for a flow with 300k 100μm particles.
⎯⎯ One-way coupled, ○ two-way, ● four-way.
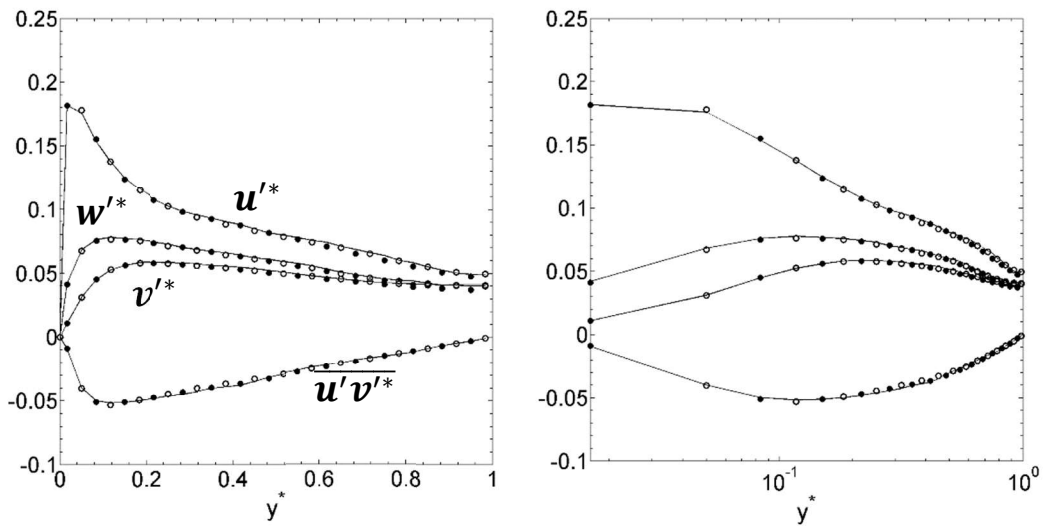
Figure 23: The particle normal stresses u'^*, v'^*, w'^*, and particle shear stress, $\overline{u'v'^*}$ for a flow with 300k 100μm particles. ⎯⎯ One-way coupled, ○ two-way, ● four-way.
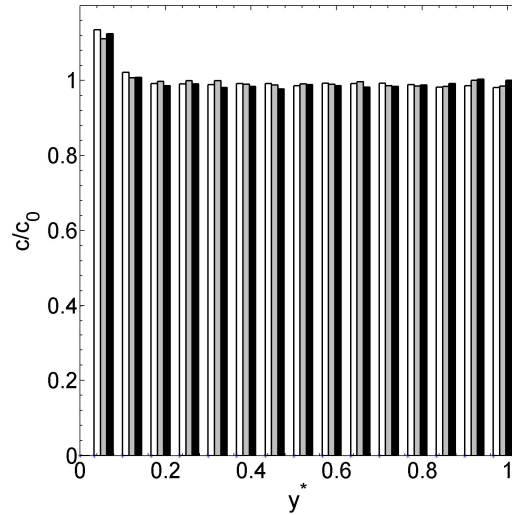
Figure 24: 300k 100μm particle concentration (c/c₀) across the channel for: □ one-way; ▨ two-way; ◼ four-way coupled flows.

Turbophoresis, a behaviour likely to be affected by the change in coupling is similarly small, so the attenuation of this behaviour, predicted to occur in the case of two-way coupling by the likes of Kuerten and Vreman (2005), and Gigoriadis and Guerts (2011), has only a minimal effect. The particle concentration c/c_0, where the number of particles c in each slice is normalised by c_0, the expected number per slice for a uniform distribution, is shown in Figure 24, displayed across half the channel, with the distribution appearing uniform aside from a small increase close to the wall. The few differences that can be observed are small enough that they might be attributable to statistical fluctuations in the predictions, although build-up near the wall is due to the effects of turbophoresis.

4.3.2 2.2M 100μm Particles (Case 2)

The effect of the 100μm particles on the resulting turbulence field becomes more apparent as the concentration increases. For the second case, with a low Stokes number but a higher volume fraction, the mean fluid velocity (Figure 25) and the mean particle velocity (Figure 27) are consistent and seemingly unchanged by the level of coupling. For the normal and shear stresses, however, both the fluid (Figure 26) and particles (Figure 28) show evidence of an interaction which is somewhat dependent on the coupling, in that the peaks for u'^* near the wall for the one-way coupled system are visibly higher than for the two-way and four-way systems. This occurs between the wall where $y^* = 0$, and approximately $y^* = 0.3$. Notably the change in magnitude for the velocity fluctuations in the streamwise direction is similar to that in the spanwise and wall-normal directions, where the relationship is reversed, with the results from one-way coupling underestimating the magnitude of the normal and shear stresses in those directions.
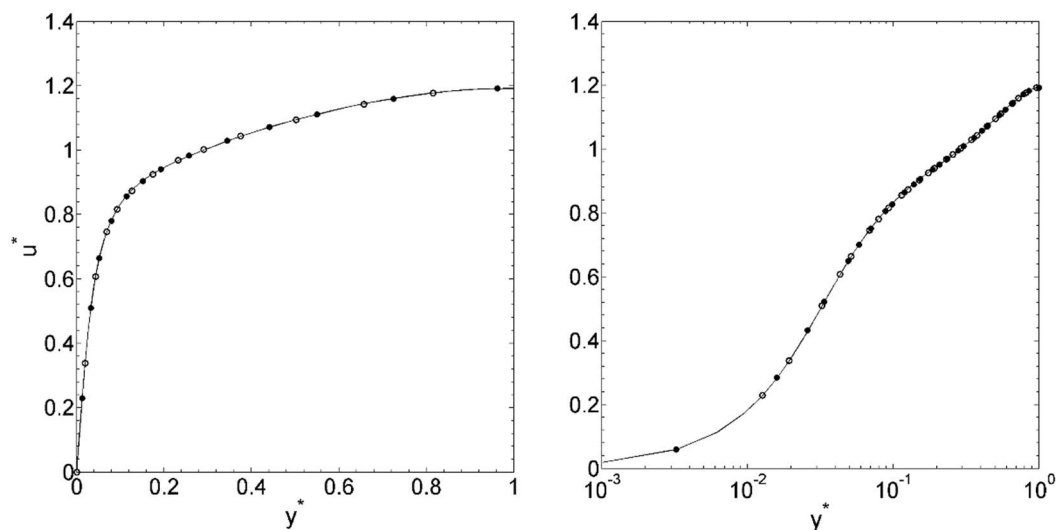
Figure 25: The mean streamwise fluid velocity $\boldsymbol{u}^*$ for a flow with 2.2M 100μm particles. ——
One-way coupled, ○ two-way, ● four-way.
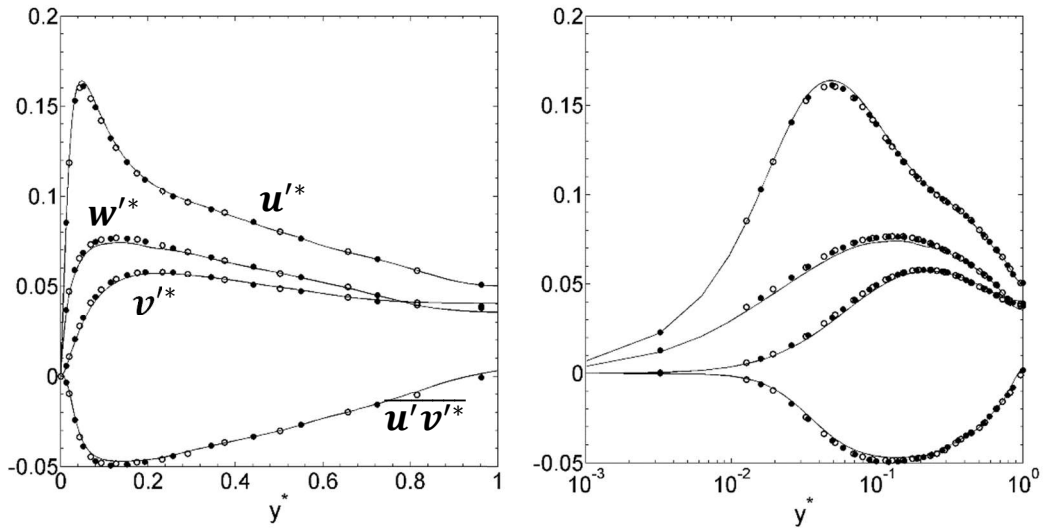
Figure 26: The fluid normal stresses u'^*, v'^*, w'^*, and fluid shear stress, $\overline{u'v'^*}$ for a flow with 2.2M 100µm particles. —— One-way coupled, ○ two-way, ● four-way.
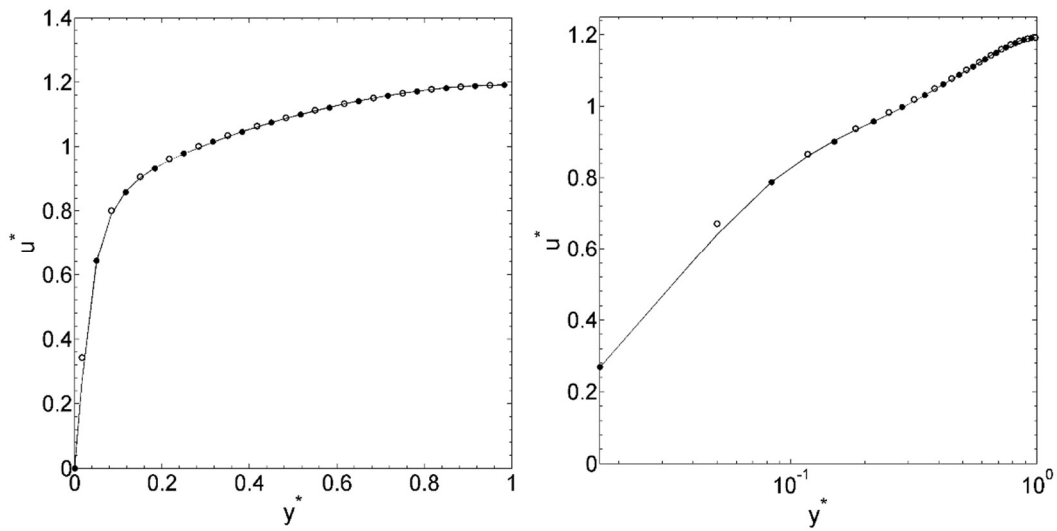
Figure 27: The mean streamwise particle velocity u^* for a flow with 2.2M 100µm particles. —— One-way coupled, ○ two-way, ● four-way.
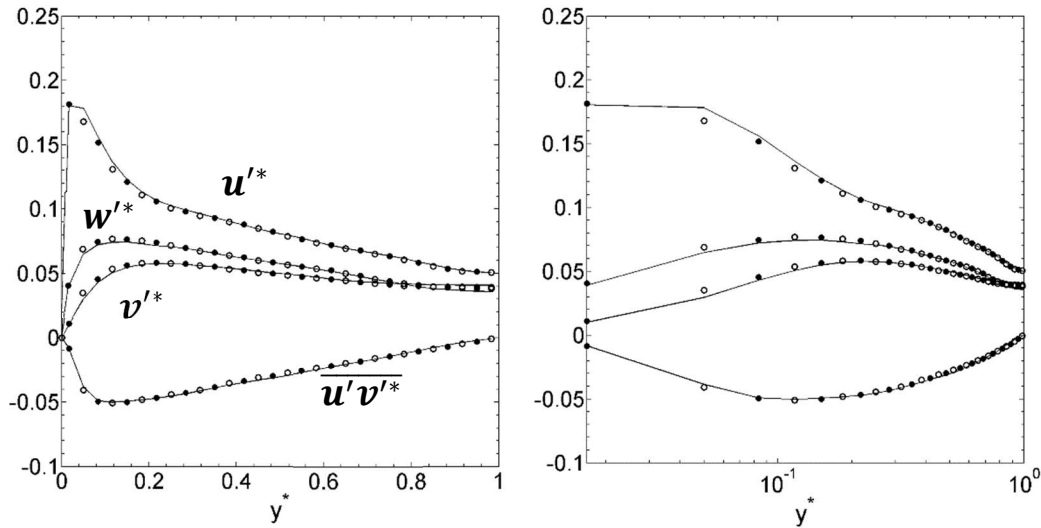
Figure 28: The particle normal stresses u'^*, v'^*, w'^*, and particle shear stress, $\overline{u'v'^*}$, for a flow with 2.2M 100μm particles. ⎯ One-way coupled, ○ two-way, ● four-way.
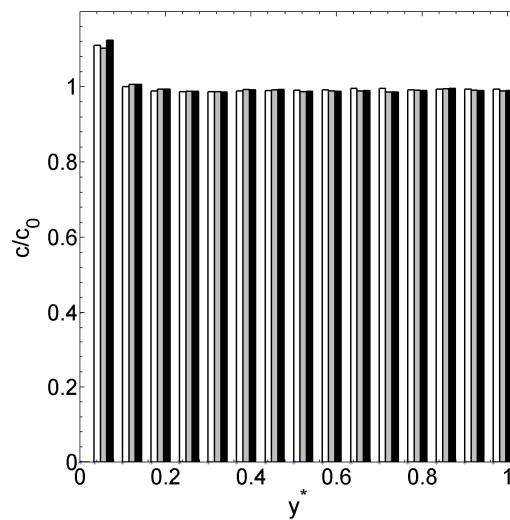
Figure 29: 2.2M 100μm particles concentration (c/c_0) across the channel for: □ one-way; ▣ two-way; ■ four-way coupled flows.

Increasing the number of particles has a side effect of reducing the amount of statistical deviation for the particle concentration (beyond the wall region) being gathered from the simulation, as shown in Figures 29 and 39. This makes the plot of particle concentration, as well to a lesser extent, the mean and stress plots, appear smoother. The similarity between these statistics and those from the first case, as well as the lack of deviation between different levels of coupling on both, suggests that coupling has a relatively small effect on systems where the Stokes number is this small, regardless of volume fraction.

4.3.3 300k 200μm Particles (Case 3)

The final two cases performed used a particle with a diameter of 200μm, hence increasing the likelihood of collisions in the four-way coupled case and the magnitude of the two-way coupling effect on the fluid's behaviour. The volume fraction is consistent between the second and third cases (see Table 3 in Chapter 3 Methodology), though the Stokes number differs.
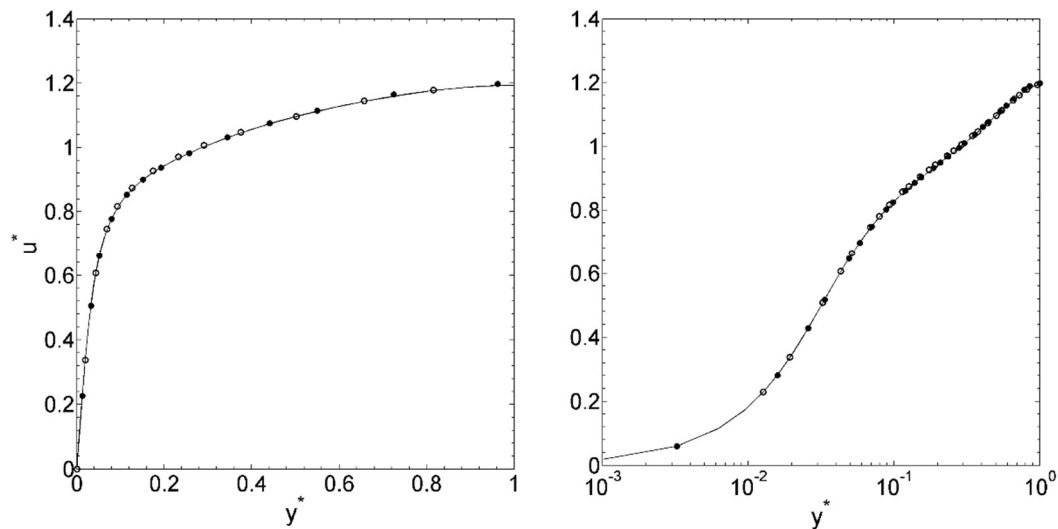
Figure 30: The mean stream-wise fluid velocity u^* for a flow with 300k 200μm particles. —— One-way coupled, ○ two-way, ● four-way.
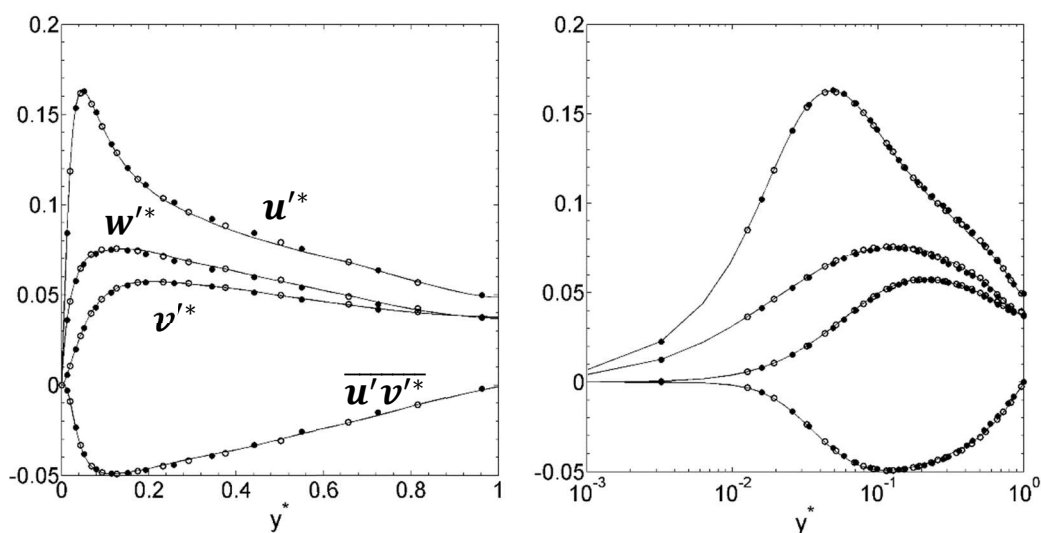
Figure 31: The fluid normal stresses u'^*, v'^*, w'^*, and fluid shear stress, $\overline{u'v'^*}$ for a flow with 300k 200μm particles. —— One-way coupled, ○ two-way, ● four-way.
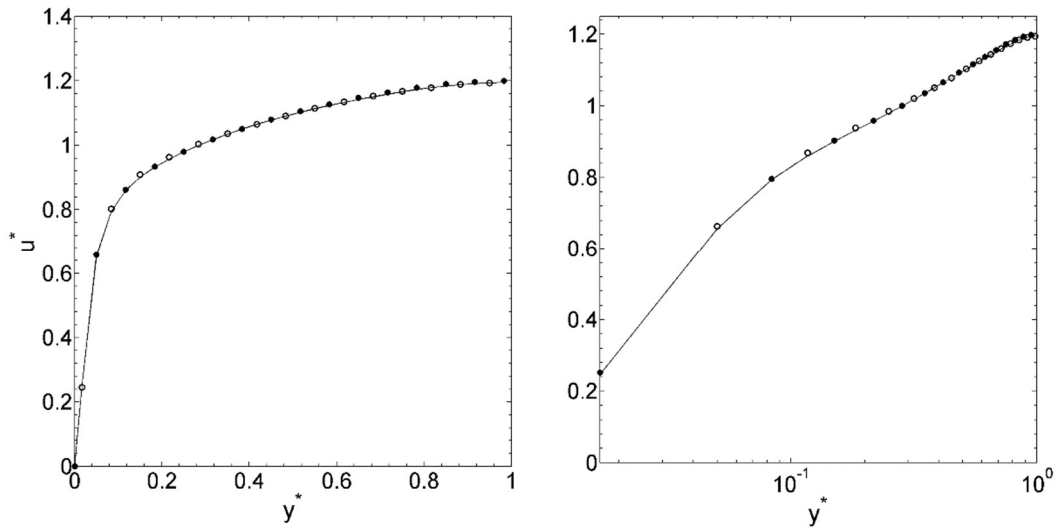
Figure 32: The mean streamwise particle velocity u^* for a flow with 300k 200μm particles. —— One-way coupled, ○ two-way, ● four-way.
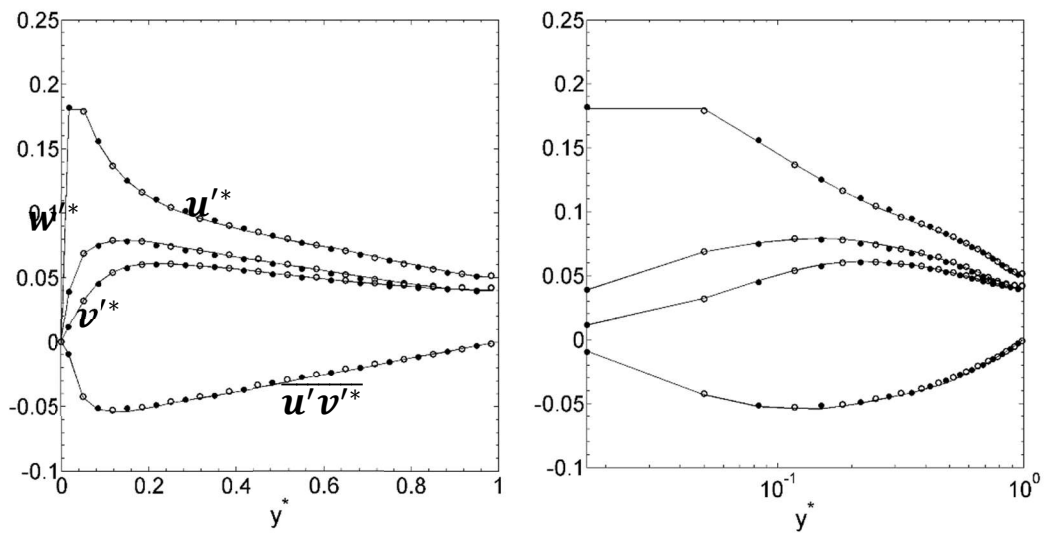
Figure 33: The particle normal stresses u'^*, v'^*, w'^*, and particle shear stress, $\overline{u'v'^*}$, for a flow with 300k 200μm particles. —— One-way coupled, ○ two-way, ● four-way.
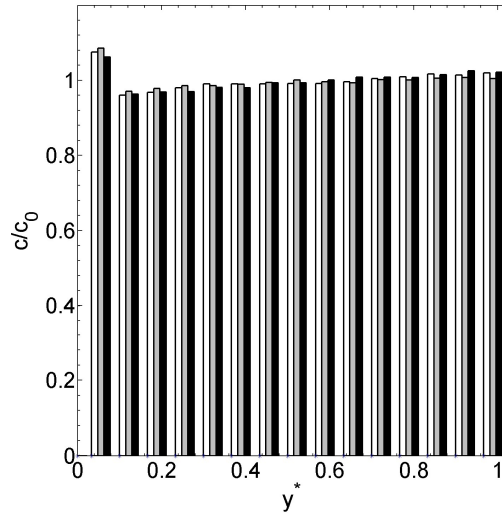
Figure 34: 300k 200µm particles concentration (c/c₀) across the channel for: □ one-way; ▨ two-way; ▪ four-way coupled flows.

Unlike with the 100µm particles, the discrepancy between the levels of coupling is very marginal but visible. Figures 30 and 32 show the first evidence of an influence from the level of coupling on the magnitude of the mean streamwise fluid and particle velocities. The one-way coupled and, more so the two-way coupled statistics, both show a reduction in the mean streamwise velocity towards the centre of the channel by a small margin, compared to the four-way coupled results. The velocity fluctuations shown in Figures 31 and 33, however, seem relatively consistent.

Considering the concentration of particles across the channel (Figure 34) and comparing to Figure 29, there is a clear difference between the behaviour of the 100µm and 200µm particles. Both have the same signature peak in particle concentration at the wall, due to turbophoresis, but in the case of the larger particles, the concentration also grows towards the centre of the channel. Interestingly, this growth is hampered somewhat for the particles which are only two-way coupled. Li et al (2001) show that particle concentration profiles become substantially more homogeneous as the volume fraction increases, with an increased collision rate in the wall region tending to mix particles back into the bulk of the flow, reducing the effects of turbophoresis (Kuerten 2016). In the present case with a volume fraction of $\phi_P \approx 10^{-3}$, and viscous Stokes number, $St^+ = 1.25$, the forces from collisions which are pushing the particles back to the centre of the flow counteract those of turbophoresis, making the four-way coupled simulation have a peak in concentration at the wall that is more similar to the simulation with one-way coupling than with two-way coupling.

4.3.4 2.2M 200µm Particles (Case 4)

Case four subverts expectations somewhat. Having the largest volume fraction of the four cases, and using the larger 200µm particle size, it might be expected that for different levels of coupling the trend would continue and there would be more variance than in the previous

cases. Instead, Figures 35 through 38 show results that are almost uniform. Figure 39 shows that some of the same behaviour from the third case is still present, with particle concentration rising towards the centre of the channel and a comparatively small peak at the wall compared to the cases with the smaller $St^+ = 0.3125$ particle. The two-way coupled simulation shows this peak at the wall being made higher by a very small margin because of turbophoresis.
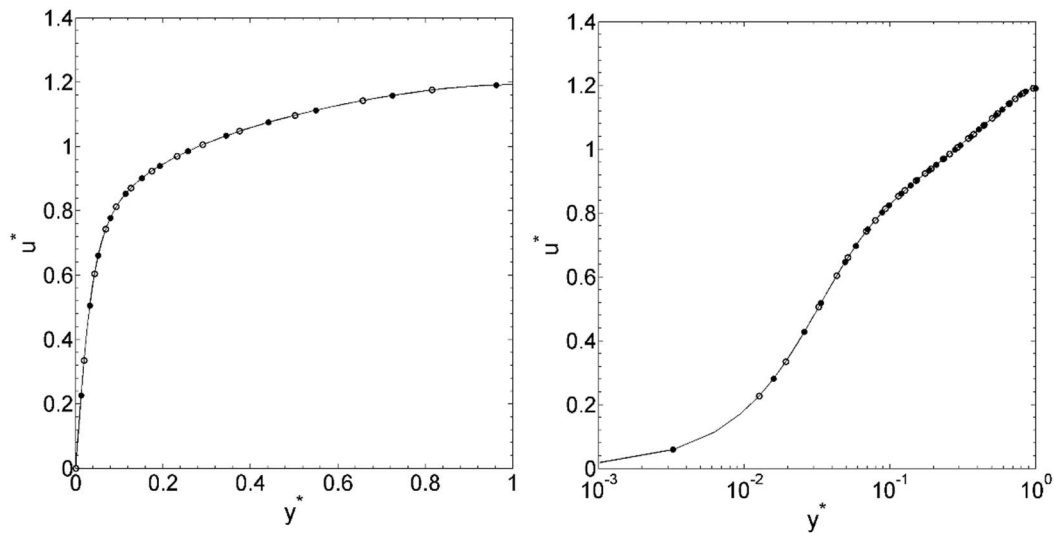
Figure 35: The mean stream-wise fluid velocity $\boldsymbol{u}^*$ for a flow with 2.2M 200 μm particles. — One-way coupled, ○ two-way, ● four-way.
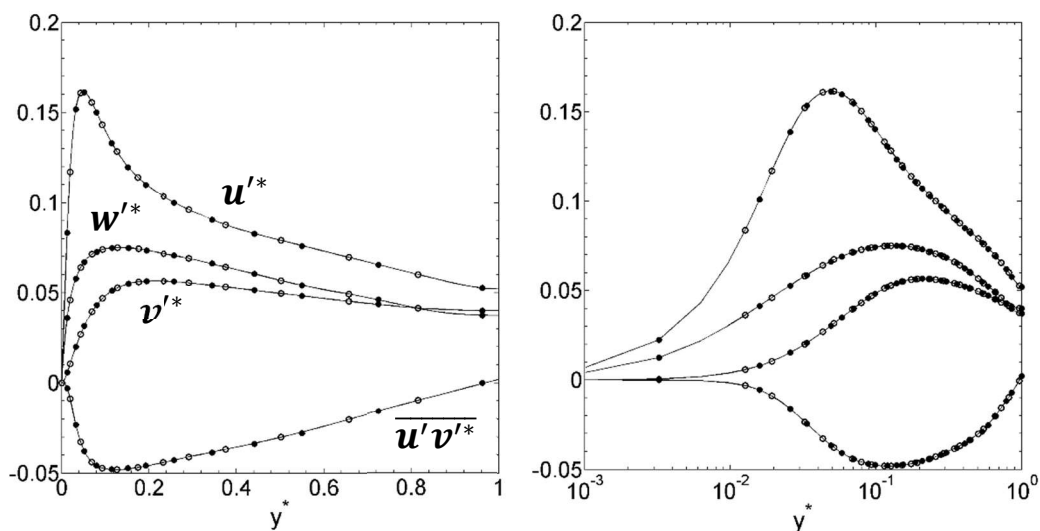
Figure 36: The fluid normal stresses $\boldsymbol{u'}^*, \boldsymbol{v'}^*, \boldsymbol{w'}^*$, and fluid shear stress, $\overline{\boldsymbol{u'v'}^*}$ for a flow with 2.2M 200 μm particles. — One-way coupled, ○ two-way, ● four-way.
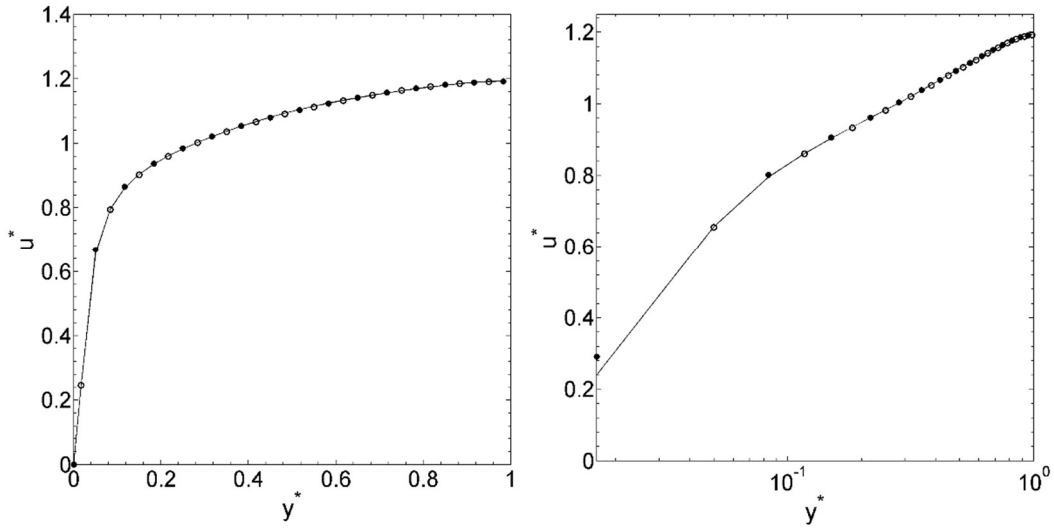
Figure 37: The mean streamwise particle velocity u^* for a flow with 2.2M 200 µm particles. —— One-way coupled, ○ two-way, ● four-way.
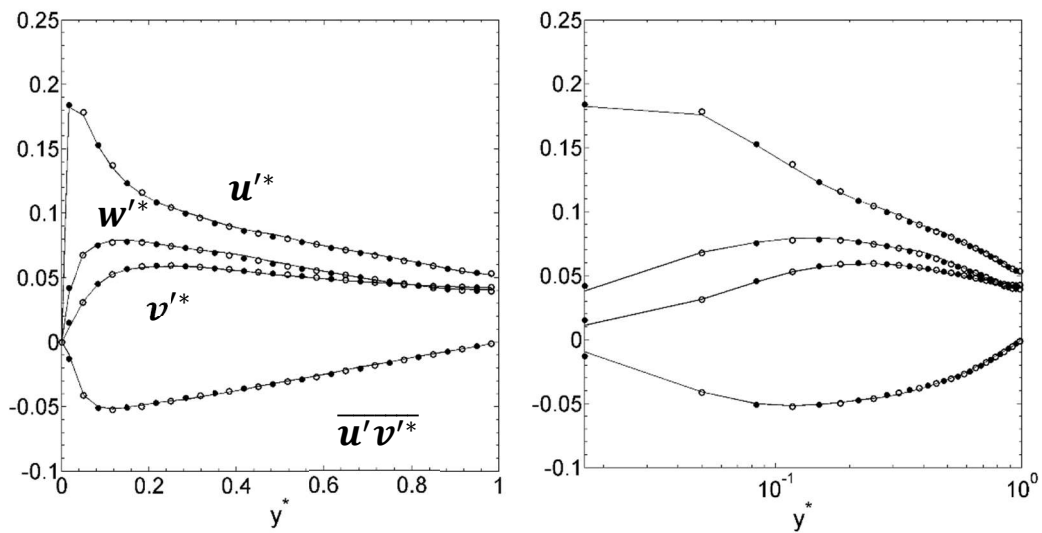
Figure 38: The particle normal stresses u'^*, v'^*, w'^*, and particle shear stress, $\overline{u'v'^*}$, for a flow with 2.2M 200µm particles. —— One-way coupled, ○ two-way, ● four-way.
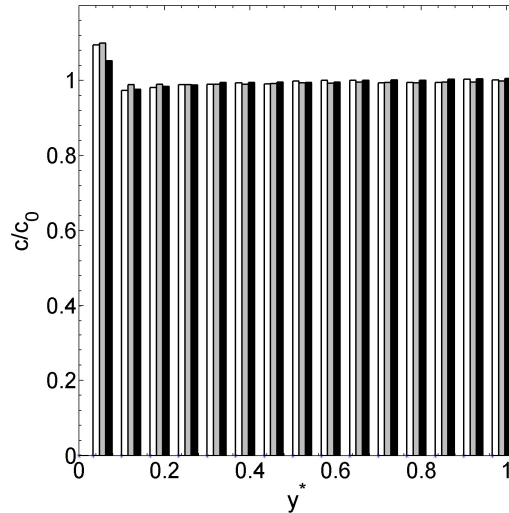
Figure 39: 2.2M 200μm particles concentration (c/c$_0$) across the channel for: □ one-way; ▣ two-way; ◼ four-way coupled flows.

One source of this uniformity might be that the volume fraction of particles is so large that it simply takes longer for energy to transfer between the fluid and particle phases. In addition, with a larger number of particles, there is less room for statistical variance in the data. In a system such as this with many interparticle collisions happening every timestep, and an abundance of particle surfaces on which drag can act, the overall rate of change for the system is made lower. As seen here, the concentration profile of the four-way coupled simulation has quite a small peak at the wall compared with the other cases. This is in accordance with the homogeneity caused by collisions which was observed to a lesser extent in Figure 34.

4.3.5 Effects on the Magnitude of Forces

To help explain the observations of the previous subsection, a more direct analysis is performed considering the forces acting between the fluid and the particles, and the ways in which they are modified between the four test cases, and with differing levels of particle-fluid coupling.

85
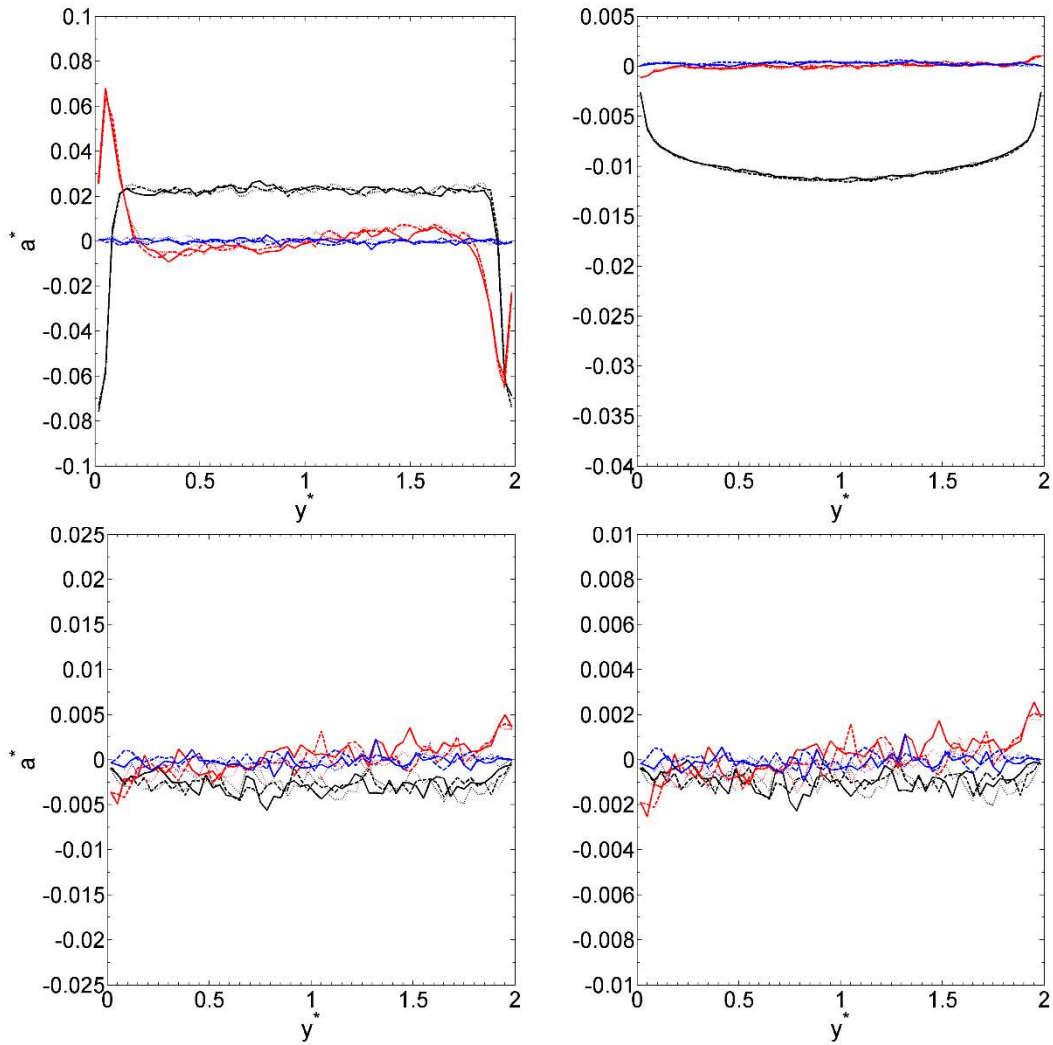
Figure 40: The non-dimensional acceleration produced by the drag (upper left), lift (upper right), virtual mass (lower left), and pressure gradient (lower right) forces in the streamwise (black), spanwise (blue) and wall normal (red) directions applied to 300k particles with a radius of 100μm at different levels of coupling: · · · one-way; - - - two-way; —— four-way.
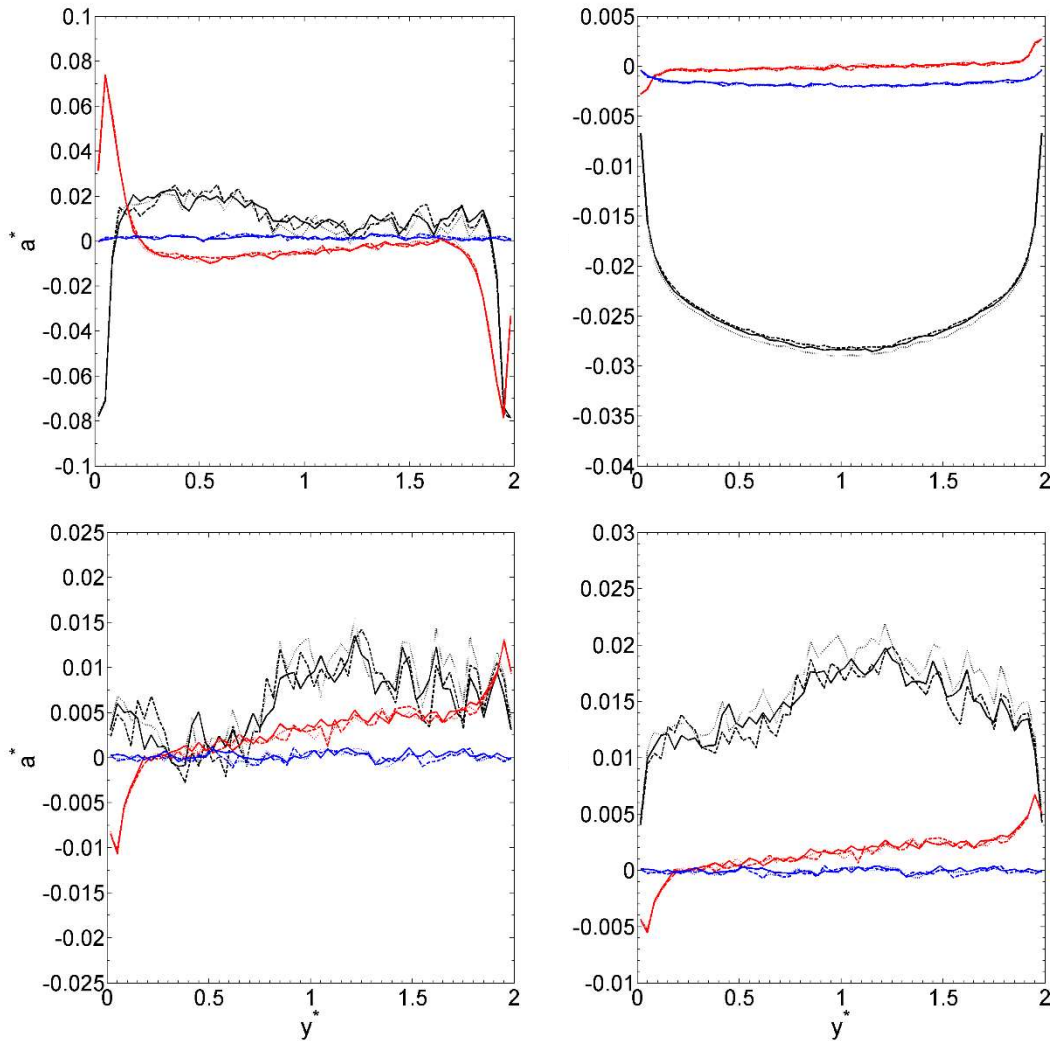
Figure 41: The non-dimensional acceleration produced by the drag (upper left), lift (upper right), virtual mass (lower left), and pressure gradient (lower right) forces in the streamwise (black), spanwise (blue) and wall normal (red) directions applied to 2.2M particles with a radius of 100μm at different levels of coupling: · · · one-way; - - - two-way; —— four-way.

The force statistics of the first two cases given in Figures 40 and 41 show a trend of the higher concentration case resulting in an increased magnitude for the forces outputted by the simulation, in all cases. With the exception of streamwise drag force, which is somewhat reduced compared to the lower concentration case, all of the forces in the streamwise and wall normal directions have been affected by the increase in the volume fraction. The forces in the wall-normal direction are approximately doubled with the increase in volume fraction, while the streamwise forces are affected more drastically by the presence of the particles, with the force being asymmetrically reduced for drag and doubled for lift. The streamwise pressure gradient and virtual mass forces also go from small forces averaging around zero to significant positive values as the volume fraction increases.

The spanwise forces average at nearly zero for the virtual mass and pressure gradient forces, and have been slightly flattened due to the statistical averaging being carried out over a larger

number of particles in the high concentration case. For the spanwise drag and lift forces a small increase towards the centre of the channel can be observed, reflecting those locations where the particles have transferred energy from the streamwise and wall normal directions to the spanwise direction.

The level of coupling does not greatly affect the change due to increasing concentration, indeed, in most cases the forces are consistent regardless of the level of coupling, with the pressure gradient force being a notable exception where for the one-way coupled simulation the force in the streamwise direction is higher. This can be explained by the small scale effects that two-way coupling has on local eddies. One-way coupled particles do not affect the fluid that they are travelling through, so increases to the pressure gradient force imply that the particles have a consistent property of either moving against or creating pressure gradients within the flow, heightened by the increased number of particles.
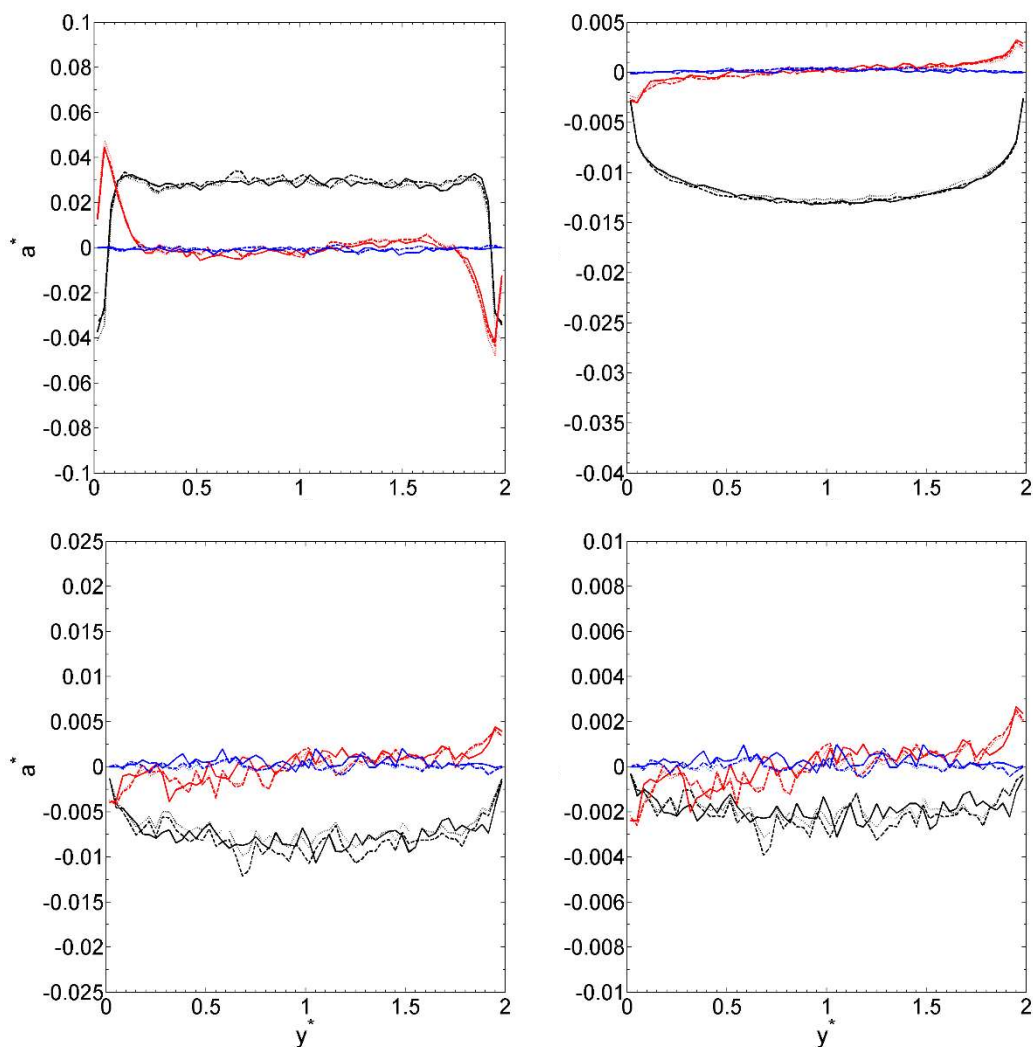
Figure 42: The non-dimensional acceleration produced by the drag (upper left), lift (upper right), virtual mass (lower left), and pressure gradient (lower right) forces in the streamwise

88

(black), spanwise (blue) and wall normal (red) directions applied to 300k particles with a radius of 200μm at different levels of coupling: · · · one-way; - - - two-way; —— four-way.
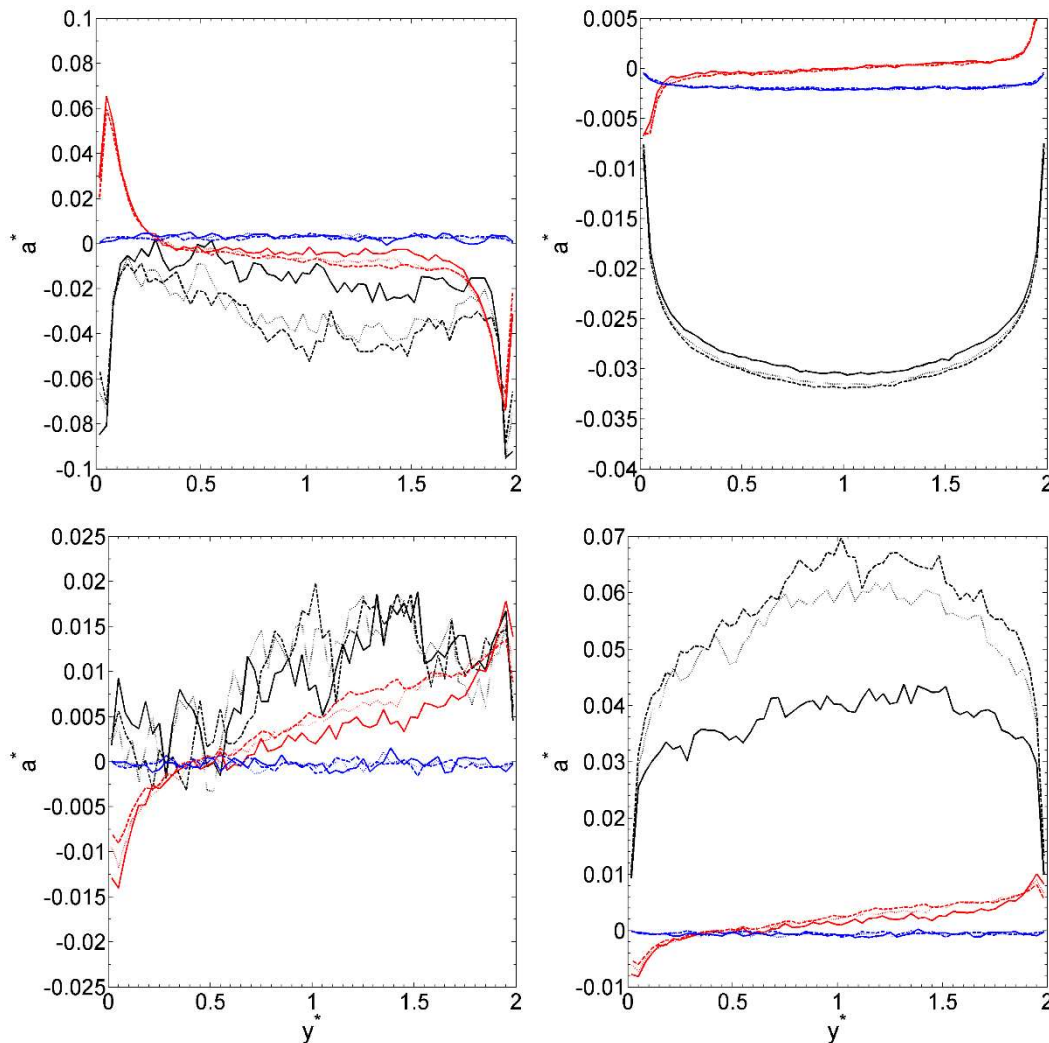
Figure 43: The non-dimensional acceleration produced by the drag (upper left), lift (upper right), virtual mass (lower left), and pressure gradient (lower right) forces in the streamwise (black), spanwise (blue) and wall normal (red) directions applied to 2.2M particles with a radius of 200μm at different levels of coupling: · · · one-way; - - - two-way; —— four-way.

For the higher Stokes number particles, the effect of the level of coupling is again small, at least in Figure 42, the case where the concentration is lower. Figure 43 shows that at a higher concentration, for the case with the largest volume fraction, some highly significant effects are taking place. For both of the higher concentration simulations, the streamwise drag force is impaired substantially and asymmetrically, seemingly in accordance with the wall normal forces, which suggests a great deal of energy transfer happening between the particles and the fluid. Additionally, the drag, virtual mass and pressure gradient forces in the wall-normal and spanwise directions show themselves to be dependent on the level of coupling, significantly so for the streamwise direction in all four cases. The inclusion of collisions has a particularly noticeable effect on the pressure gradient force for case 4.
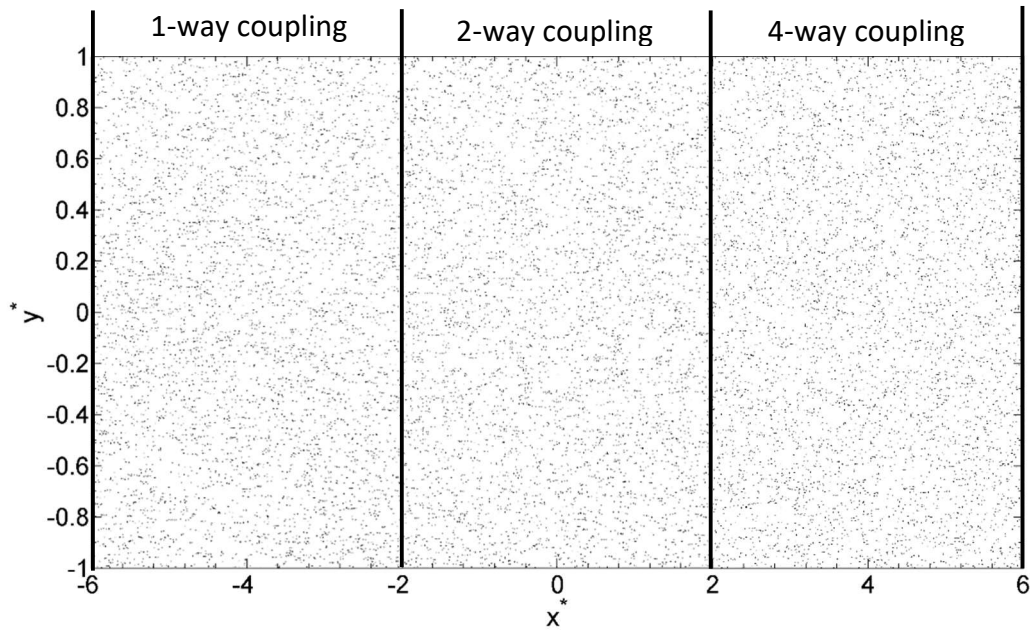
Figure 44: Visualisation of the trajectories of sampled particles for case 4 at different levels of coupling. Particles shown are a selection taken from the central -0.5<z*<0.5 axis of the channel.

Figure 44 shows that even for the highest volume fraction and particle Stokes number, the behaviour of particles is relatively uniform between the different levels of coupling, with particles mostly seen following the fluid streamlines. The main change shown in Figure 43 was a diminishment of the pressure gradient force when particle collisions were introduced. For this and the general increase in pressure gradient force shown in both of the higher concentration cases, the implication is that a larger number of particles allows for a larger number of "rogue" particles with enough energy to pass through pressure gradients, thus swaying the measured averages of the force towards higher values. These same particles can also be seen to have an effect on the drag force. In Figures 41 and 43, the drag force is diminished even as the pressure gradient force increases, with the two forces having a direct inverse relationship, to the point where even small fluctuations on the drag force graph are mirrored on the pressure gradient graph. The drag force on the particles is in essence, responsible for the pressure gradient force on the same.

The effect that causes the drop in pressure gradient for the four-way coupled particles in case 4 is that of energy redistribution between colliding particles. A high particle travelling against the fluid flow is likely to lose some of that energy during a collision, which in turn will make it more likely to go with the flow, which reduces the pressure gradient force on it.
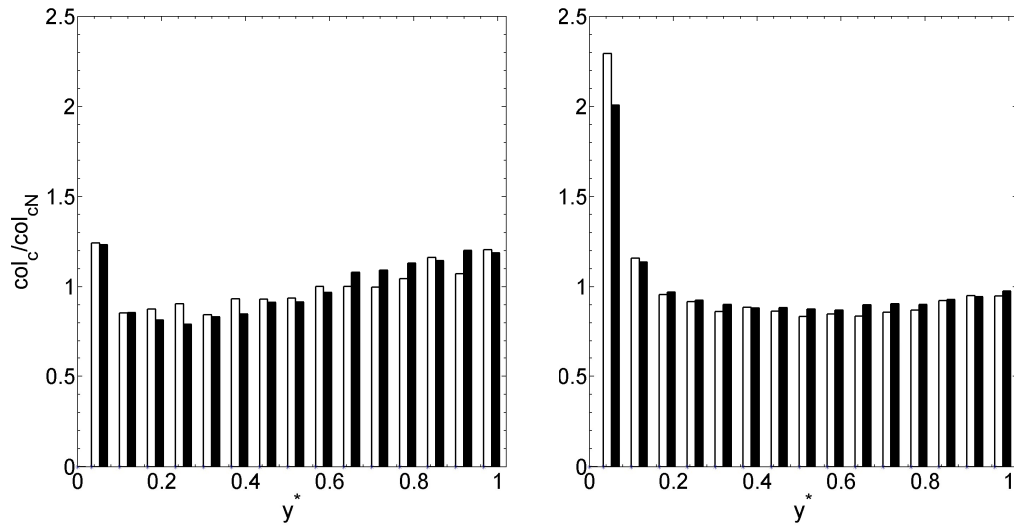
Figure 45: Distribution of collisions col_c/col_{cN} across the channel for 100μm (left) and 200μm particles (right), at different concentrations. □ 300k, ■ 2.2M.
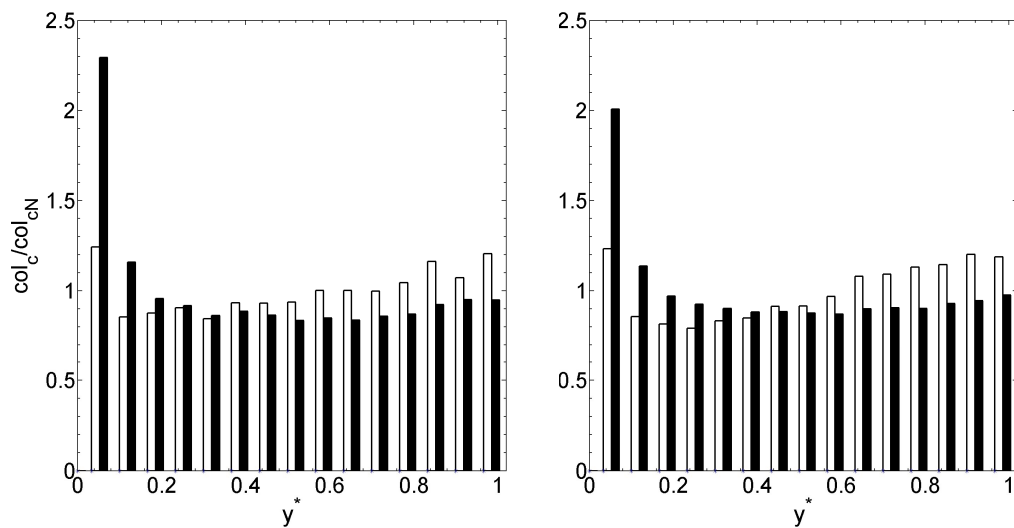
Figure 46: Distribution of collisions col_c/col_{cN} across the channel for 300k (left) and 2.2M particles (right), for different particle sizes. □ 100μm, ■ 200μm.
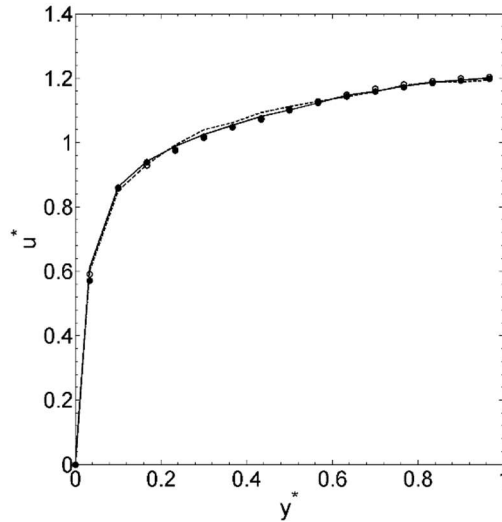
Figure 47: Mean streamwise particle velocity u^* profile for colliding: —— 300k 100μm particles; --- 2.2M 100μm particles; ○ 300k 200μm particles; ● 2.2M 200μm particles.

In order to understand the impact that collisions have on the flow more directly, the collision rate across the channel itself can be measured. Here, the collision rate in each section of the channel is normalised by the total number of collisions, and like cases are compared. Figure 45 shows that cases with the same particle size but different volume fractions have largely similar distributions across the channel, with the changes between volume fractions mostly accounted for by having a larger number of particles over which to average the statistics in the higher concentration case.

When comparing the two different particle sizes in Figure 46, the difference in the collision distribution demonstrates a reasonably uniform distribution across the channel, for the cases with 100μm particles, with a rise in collision rate in the bulk flow region, while the collision rate for the 200μm particles has a distinctive peak in the wall region. This high collision rate near the wall is responsible for mixing between the wall and bulk regions of the flow (Caraman et al., 2003), and reducing the effect of turbophoresis, which is unhindered where only two-way coupling is modelled.

The relationship between the particle sizes remains consistent even when the number of particles changes, showing that the Stokes number is a much better indicator of particle behaviour at this Reynolds number than the volume fraction. Investigations into the velocities of colliding particles (Johnson, 2020) show that a colliding particle pair will be more likely to have similar velocities, the lower the Stokes number. As a rule this applies to any high velocity particles in a given region, such as those from the bulk flow region which have migrated to the wall region. A larger Stokes number indicates a particle taking a longer time to match its speed to that of the local fluid, which in turn gives it a higher likelihood of interacting with another particle in the same region. This accounts for the increased collision rate at the wall.

Figure 47 shows the mean streamwise velocity of particles at the point of collision. Though this corresponds mostly with the particle velocities shown in earlier figures, the two lower concentration cases display a small increase in expected velocity compared with the higher concentration cases. Particles which travel towards the wall from the bulk will at lower concentrations be less likely to encounter another particle along the way and have its speed reduced by the collision (Mortimer et al, 2019). This aspect is further investigated in chapter 5.

4.4 Computational Timescale Considerations

Analysing the different cases shows the result that for the particular cases considered, the level of coupling has little effect on the overall statistics for mean velocities, and normal and shear stresses, for the range of Stokes numbers employed, although the forces on the particles are seen to differ more when there is an increased volume fraction/collision rate.

Based on the observations earlier in the chapter, and in line with the findings of other researchers, one-way coupled simulations appear to be sufficient to model multiphase systems where the Stokes number is sufficiently low. As the volume fraction and Stokes number increase, however, the effects of both turbophoresis and interparticle collision start to become too large to disregard. For such situations it is much more difficult to produce accurate results on particle behaviour and force statistics with one-way coupling alone. As a system grows larger or more complex, the computational resources needed to simulate it likewise increase, until the trade-off between accuracy and computational time becomes critical. In this chapter it has been demonstrated that four-way coupling captures important behaviours of the fluid flow and particles, as well as dampening mechanics like turbophoresis that become exaggerated where solely two-way coupling is used.

Table 5: Effects of the level of coupling on computational time.

	Test Case			
	1	**2**	**3**	**4**
Level of Coupling	**300k, 100µm particles**	**2.2M, 100µm particles**	**300k, 200µm particles**	**2.2M, 200µm particles**
One-way	1.00	8.09	0.99	7.69
Two-way	2.23	17.32	2.42	19.81
Four-way	2.26	19.36	2.27	18.61

In Table 5, the time taken for the code to simulate the particle-laden flow was, for each case, normalised by the time taken for the one-way coupled simulation with 300k, 100µm particles.

This base case run time was on average 14.38 seconds per step, running on 32 standard cores in the Leeds University ARC3 system (https://arcdocs.leeds.ac.uk/systems/arc3.html). The single-phase equivalent of the base case completed timesteps at a similar rate, and was run for around 20 days of full simulation time to ensure the fluid had fully settled, or around 100000 timesteps. The result was used as the initial conditions for the multi-phase cases which followed.

All of the other cases were performed on the same system, with particles being injected into the previously settled fluid flow. These cases were performed for approximately 10 days each. At this point the number of simulation timesteps per wall-clock time was variable, so care was taken to ensure that the two-way and four-way coupling systems. As the particle number increases, the amount of extra computational time required to simulate the flow increases, with the largest increase taking place with the implementation of two-way coupling. As observed earlier in the chapter, four-way coupling reduces the effect of turbophoresis, but this has an interesting effect on the computational operations taking place in the simulation. The motion of particles between different fluid cells triggers the two-way coupling step to recheck which cell a particle is located in. This happens sufficiently often for the two higher Stokes number cases that the dampening of this motion by the implementation of four-way coupling actually reduces the computational time, although both steps are clearly highly dependent on the particle concentration.

4.5 Conclusions

In this chapter, Lagrangian particle tracking coupled with direct numerical simulation was validated before being used to compare four different cases across a range of volume fractions and Stokes numbers. Studying a shear Reynolds number, $Re_\tau = 300$, which is firmly on the turbulent end of transitional flow in a channel, and which is relatively unexplored, allows for the generation of new understanding for this kind of fluid system, while the initial particle size used was chosen in-line with the work of Mortimer et al. (2019). Testing volume fractions at three different orders of magnitude allows a comprehensive view of the way in which a turbulent flow might be affected by a large number of particles through various coupling mechanisms.

The validation of the DNS against the results of both Morinishi and Tamano (2005) and Marcholi and Soldati (2007), who in particular used a mesh with the same number of grid points as this study, showed that the code used would produce results excellently aligned with previous work at this particular level of turbulence, and the results from the LPT of the same three particle classes which were simulated in the same Marchioli and Soldati (2007) paper were also in good agreement.

The level of coupling was changed in order to test the effect this would have on the predictions of the streamwise fluid and particle velocities and the normal and shear fluid and particle stresses. This effect was in fact quite small in general but was observed to increase in

size as the volume fraction increased. This is a consequence of the turbulent Stokes numbers being used for the particles in this study, with the 100µm particles being just massive enough not to be considered tracer particles, while the 200µm particles have a Stokes number larger than but still close to unity, and so will deviate from the fluid streamlines infrequently. The most drastic changes caused were to the forces on the particles, and of course, to the computational time required to run the simulation, by a substantial margin.

The effects from changing the Stokes number were much more apparent, with the 200µm particles having a higher concentration in the centre of the flow than the 100µm particles, showing a surprising resistance to turbophoretic effects. A higher rate of collision towards the channel walls was also observed for these particles, which might be expected to cause more particles to travel towards the bulk region, an effect that was more visible on the plots of particle concentration. Changing the volume fraction by adjusting the number of particles produced a much smaller effect, showing that the flow properties are dependent more on the Stokes number, with the largest change produced from increasing the particle number being to the streamwise drag force on the particles. The observations from Zhao et al (2015) show the particle and fluid velocity fluctuations rise with Stokes number, but these effects were small in this study, which used comparatively small Stokes numbers in a liquid-solid setting, where it is less likely for the particles to have any drastic effects on the fluid phase. The computational time was affected drastically by the change in particle number, however, regardless of Stokes number. This is due to the increased number of operations performed to determine whether any of the particles are overlapping, as well as the general increase in the number of operations in the steps governing particle advection.

Across all four cases, particles were observed to gather in the wall region of the channel, but two-way coupling enhanced this effect for the cases with the higher Stokes number. The four-way coupled simulations typically showed a stronger agreement with the one-way coupled simulations than the two-way coupled simulations. It has been noted that increasing the collision rate creates a more homogeneous concentration of particles across the channel, and it can be equally argued that the effects of two-way fluid-particle coupling without collisions dampening them creates an asymmetry over time, as particles are drawn inexorably towards the wall. This highlights the importance of collisions in these kinds of geometries. Ironically, the importance of modelling particle-particle collisions increases as the cost of modelling them does.

Chapter 5 Development of Stochastic Techniques

5.1 Introduction

In the previous chapter, direct numerical simulations were performed for the baseline case of a multiphase channel flow at a shear Reynolds number, $Re_\tau = 300$. Multiple cases were tested having different volume fractions and particle radii with the intent of making a comparison between simulations employing three different levels of coupling, one-way, two-way, and four-way. Though it was ascertained that four-way coupling allows for a greater level of precision, as far as demonstrating the effects of increasing volume fraction on particle concentration and associated properties of the continuum flow, this nevertheless came at the expense of computing time, with the incorporation of higher levels of coupling causing the simulation to take at least twice as long in all cases, which for the higher concentration cases resulted in a sixteenfold computational load compared to the base one-way coupled low concentration case.

By implementing a stochastic method, four-way coupling can be achieved through means of a probabilistic interparticle collision calculation as a less computationally expensive alternative to a Lagrangian one. The investigations performed in this chapter will pertain to the same four cases as described in Chapter 4. The use of a stochastic methodology as opposed to Lagrangian methodology by definition entails a reduction in the level of accuracy with regards to the interactions between particles. Where a Lagrangian based technique will consider directly the position and velocity of a particle as well as the forces acting on it when it collides with another particle, a stochastic technique describes a treatment where the expected value of such impulse forces are applied on all of the particles in the system, with the overall effect of statistically probable collisions intended to match those determined through Lagrangian means.

The work in this chapter is focused towards the understanding of different stochastic techniques and the determination of those most effective for simulating the four-way coupled cases with both speed and accuracy. The progress made towards reconciling the results of the stochastically simulated cases with the results of the deterministic cases using Lagrangian four-way coupling which are being emulated, shall be detailed throughout the chapter. Over the course of the chapter the stochastic techniques shall be assessed, specifically in the case of any discrepancies between Lagrangian and stochastic cases. The causes of such discrepancies shall be investigated, and the stochastic techniques used shall be modified and discarded where necessary to achieve the best agreement with the Lagrangian cases. Novel extensions to the techniques initially considered in this chapter are expected to be required, especially where higher particle concentrations are concerned.

5.2 Comparing the results of the stochastic methods

The initial iterations of the stochastic particle collider implemented a fictional particle generator, whereby each particle would have generated a fictional potential collision partner

with properties dependent on the properties of local particles. The probability of collision would then be based on the relationship between the velocities of the two particles, with the Stokes number playing a significant role. This is the same methodology that Sommerfeld (1999, 2001) employed.

This technique produced promising initial results, discussed further in this section. It was, however, determined that the kinetic theory equation for determining the probability of collision might not be the most suitable for the particles in the cases studied. As the Stokes number approaches zero the advective model of particle collision becomes more appropriate, and so this was used to determine the likelihood of collision for the second stochastic technique investigated, which was a direct simulation Monte Carlo (DSMC) technique utilised by O'Rourke (1981) and Pawar et al. (2014). The current test case, a channel flow, bears some similarity to the dynamic systems of impinging jets and sprays through nozzles which these authors investigated, potentially more so than the isotropic boxes used for demonstrations of the fictional particle technique. This made it a good candidate for a second round of testing using the advective model. A version of this technique using kinetic theory was trialled previously in Rupp et al. (2018), finding good agreement with the deterministic results, but with a slight decrease in accuracy in the lower Stokes number case.

Both of these techniques were performed for all four simulated cases in order to determine if either was a good match for the deterministic collision model. Also being assessed were the computation times of the stochastic codes, which would ideally be shorter than the deterministic equivalents in all cases. In addition, the rates of collision across the channel were investigated. This investigation was in aid of identifying behaviours that were being incorrectly or predicted with insufficient accuracy by the stochastic codes, which would go on to explain any deviations in the results and highlight any areas where the techniques required alteration.

5.2.1 300k, 100μm Particles (Case 1)

Figures 48 and 49 show the mean streamwise velocities and the normal and shear stresses for the simplest test case, case 1. In this case, the particle phase possesses the lowest volume fraction, with the particles having a low Stokes number and therefore an inclination to follow the flow without drastically altering it, as has already been determined in the previous chapter. Any deviations from the deterministic model shown here are only marginal, although the fictional particle model has deviated by slightly more than the DSMC model. Of note is a small region, approximately $0.2 < y^* < 0.3$, where the fluid and particle streamwise Reynolds stresses have been enhanced compared to the results from the deterministic case.
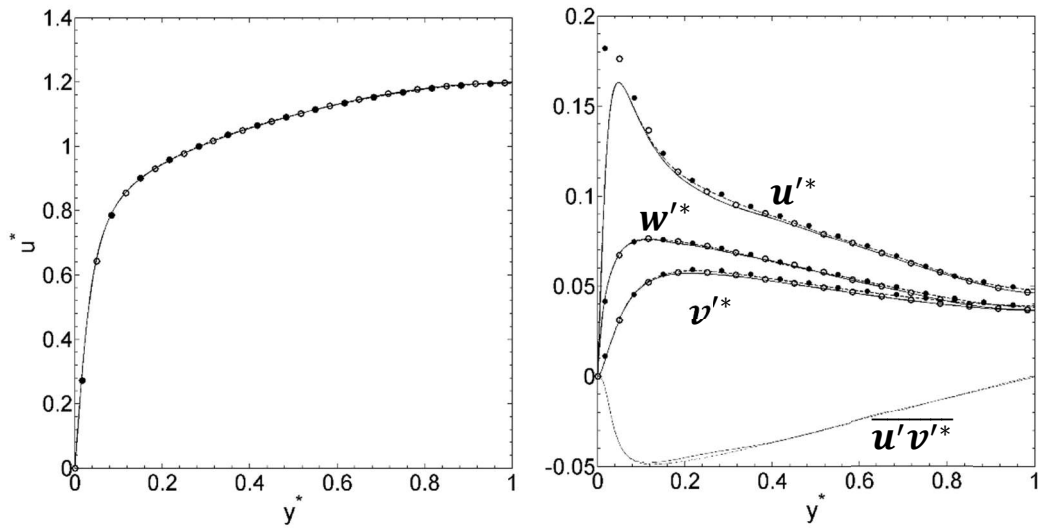
Figure 48: Compared mean streamwise velocities $\boldsymbol{u}^*$, and normal and shear stresses $\boldsymbol{u'^*}, \boldsymbol{v'^*}, \boldsymbol{w'^*}, \overline{\boldsymbol{u'v'^*}}$ for four-way coupled flows with particles collided deterministically and stochastically with fictional particle collisions. With 300k, 100μm particles. —— Deterministic and - - - stochastic fluid, and ○ deterministic and ● stochastic particles.
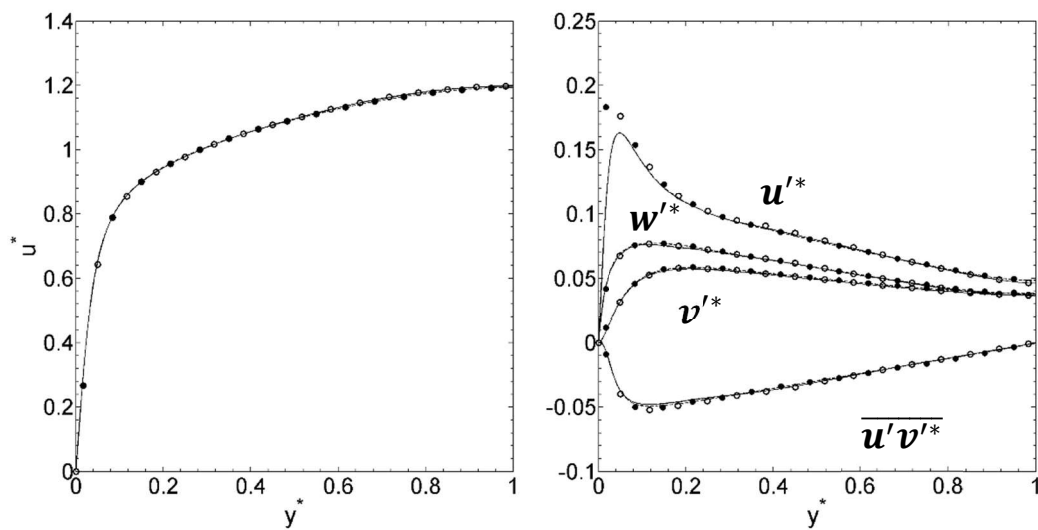
Figure 49: Compared mean streamwise velocities u^*, and normal and shear stresses $\boldsymbol{u'^*}, \boldsymbol{v'^*}, \boldsymbol{w'^*}, \overline{\boldsymbol{u'v'^*}}$ for four-way coupled flows with particles collided deterministically and
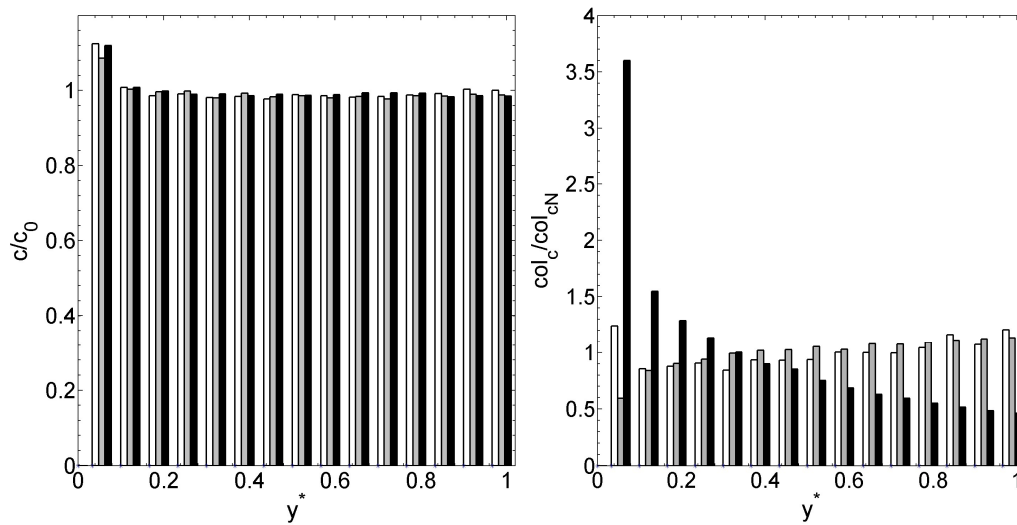
Figure 50: Particle (300k, 100µm) concentration (c/c_0, left) and collision distributions (col_c/col_{cN}, right) across the channel for four-way coupled flows. □ deterministic collisions, ▣ stochastic collisions using fictional particle collisions, and ▪ stochastic collisions using DSMC.

The distribution of the particles across the channel half-height, and associated collisions, shown in Figure 50 are considered in the following section.

5.2.2 2.2M, 100µm particles (Case 2)

The deviations for case 2, with a larger concentration of low Stokes number particles, were similarly low as can be seen in Figures 50 and 51, with the most notable changes common to both 100µm cases being within the $0.2 < y^* < 0.3$ region where the streamwise velocity fluctuations were slightly overestimated for the fictionally generated particles. Since this is a region where fast particles from the bulk travelling towards the walls through turbophoresis would encounter slower moving particles, it is possible that more energetic particles were generated as collision partners near to this region. Alternatively this could simply be a region that is easily affected by an altered collision rate. In later sub-sections enhanced versions of this effect are observed that extend all the way to the bulk region.
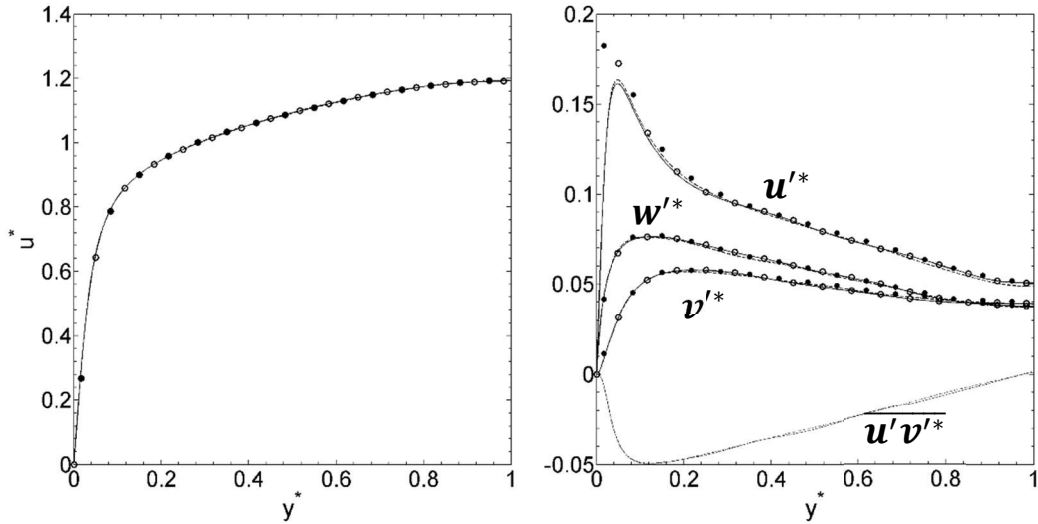
Figure 51: Compared mean streamwise velocities u^*, and normal and shear stresses $u'^*, v'^*, w'^*, \overline{u'v'^*}$ for four-way coupled flows with particles collided deterministically, and stochastically with fictional particle collision. With 2.2M, 100μm particles. —— Deterministic and - - - stochastic fluid, and ○ deterministic and ● stochastic particles.
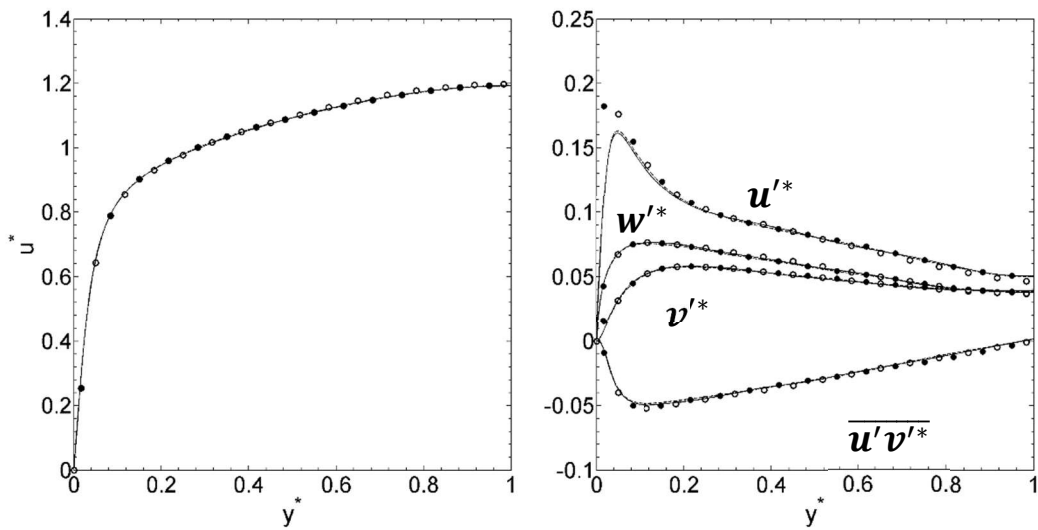
Figure 52: Compared mean streamwise velocities u'^*, and normal and shear stresses $u'^*, v'^*, w'^*, \overline{u'v'^*}$ for four-way coupled flows with particles collided deterministically, and stochastically with DSMC. With 2.2M, 100μm particles. —— Deterministic and - - - stochastic fluid, and ○ deterministic and ● stochastic particles.
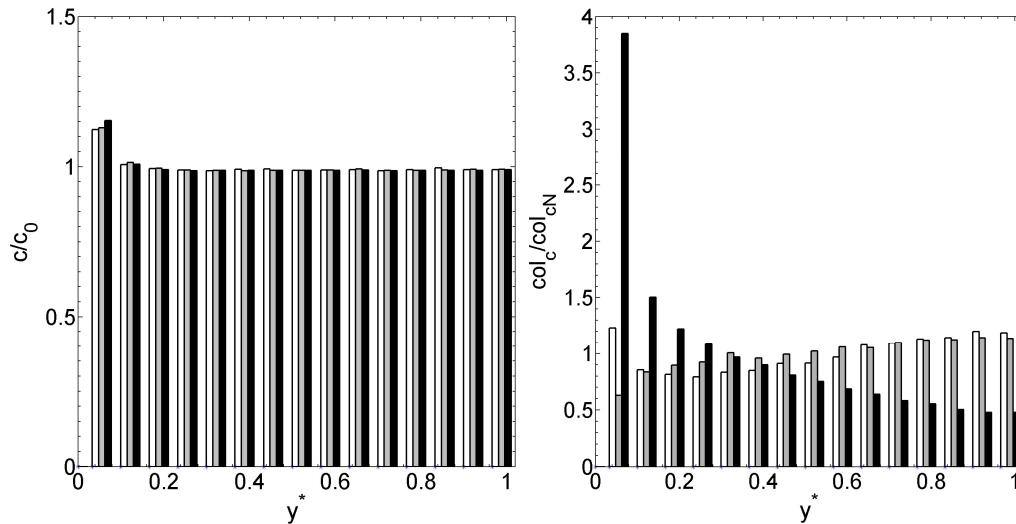
Figure 53: Particles (2.2M, 100μm) concentration (c/c_0, left) and collision distributions (col_c/col_{cN}, right) across the channel for four-way coupled flows. □ deterministic collisions, ▣ :stochastic using fictional particle collisions, and ■ stochastic collisions using DSMC.

Further, the distributions of the particles were considered across the channel half-height in Figures 50 and 53, along with the distribution (normalised assuming an even distribution) of particle-particle collision events. While the particle concentrations remained relatively unchanged where a stochastic method was employed, the distribution of collisions was markedly different for both the fictional particle and DSMC methods. It can be observed that the rate of collisions produced deterministically has a sharp peak within the wall region, which then decreases and grows gradually towards the centre of the bulk region. This growth towards the centre is correctly replicated by the technique using the fictional particles, but the behaviour near to the wall is not. Conversely, the DSMC technique shows the near-wall peak, albeit overpredicted, but diminishes towards the centre of the channel instead of increasing. The streamwise particle velocity fluctuations in Figure 52 show a slight reduction towards the bulk region, compared to the fluid, potentially due to the relatively low collision rate there creating an overall less energetic region.

5.2.3 300k, 200μm particles (Case 3)

The particles in cases 3 and 4 are larger, possessing a greater Stokes number, but also an accordingly higher collision rate because of their size. In Chapter 4 this was observed to manifest as increased homogeneity in the particle concentration. Here, other issues are encountered, at least with the fictional particle technique, with the stresses acting on the particles being exaggerated. In the next section the velocities of the generated fictional particles will be directly considered, but what is being observed here is due to the relative influence of the increased collision rate. For the low Stokes number particles, a deviation in the amount of energy in the collisions will not have a large effect, since overactive particles tend to be quickly decelerated by the fluid phase. In conditions with high Stokes numbers and large collision rates, however, each collision has the potential to affect the particle and fluid

phase over time. Here, collisions are being predicted with overly energetic fictional particles, and energy is being injected into the particle phase. Given time the fluid phase will also likely be affected, and even in the lower concentration case shown on Figure 54.
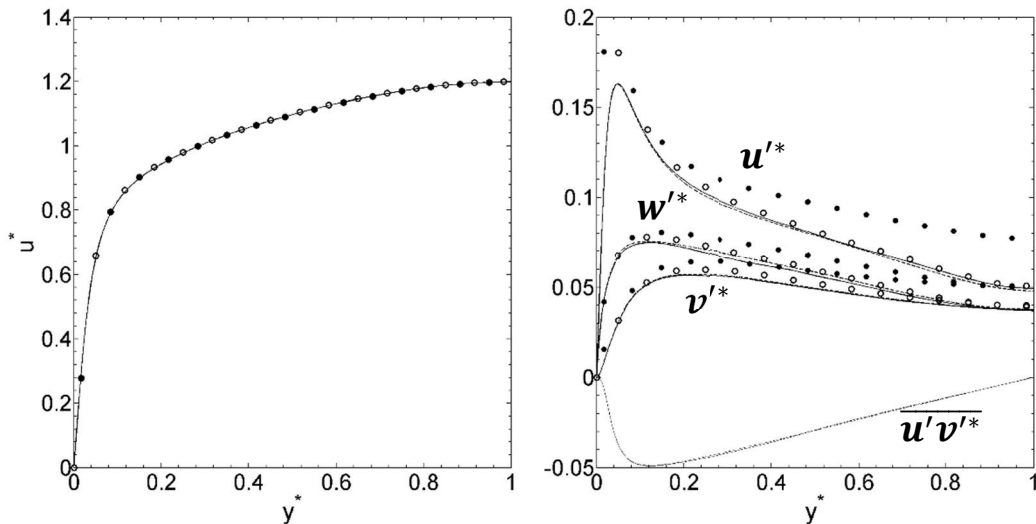
Figure 54: Compared mean streamwise velocities u^*, and normal and shear stresses $u'^*, v'^*, w'^*, \overline{u'v'^*}$ for four-way coupled flows with particles collided deterministically and stochastically with fictional particle collision. With 300k, 200μm particles. —— Deterministic and - - - stochastic fluid, and ○ deterministic and ● stochastic particles.
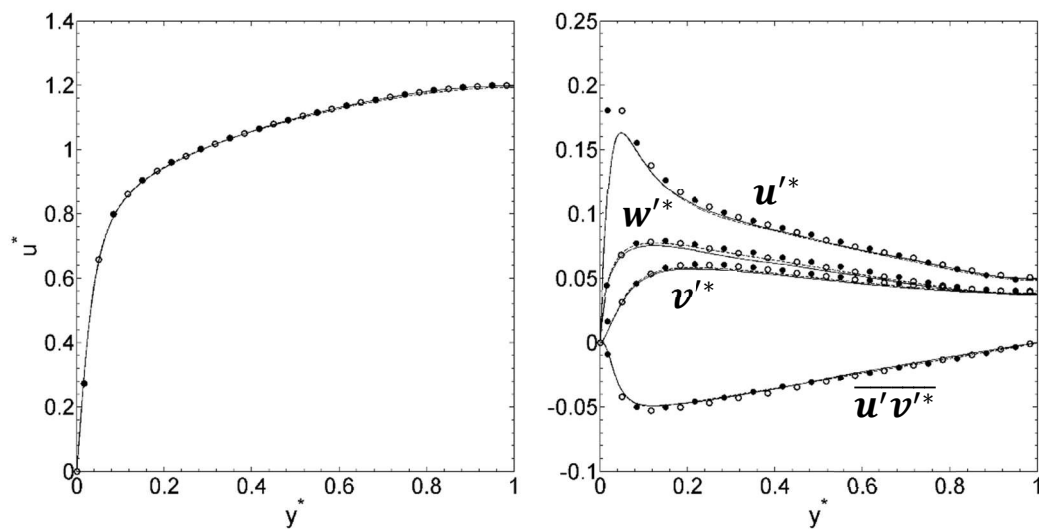
Figure 55: Compared mean streamwise velocities u^*, and normal and shear stresses $u'^*, v'^*, w'^*, \overline{u'v'^*}$ for four-way coupled flows with particles collided deterministically, and stochastically with DSMC. With 300k, 200μm particles. —— Deterministic and - - - stochastic fluid, and ○ deterministic and ● stochastic particles.
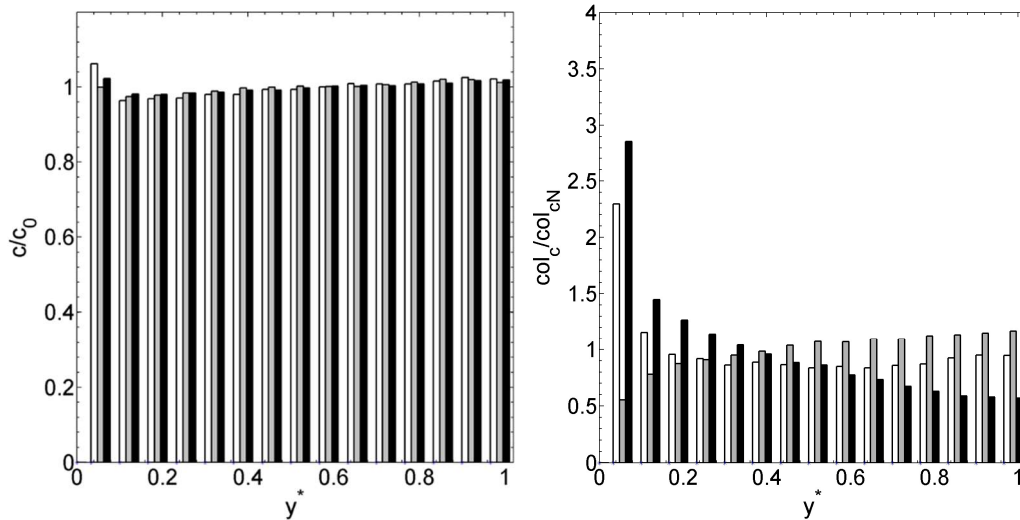
Figure 56: Particles (300k, 200μm) concentration (c/c$_0$, left) and collision distributions (col$_c$/col$_{cN}$, right) across the channel for four-way coupled flows. □ deterministic collisions, ▣ stochastic using fictional particle collisions, and ▪ stochastic using DSMC.

Where the DSMC technique is used, Figure 55, while the agreement is not perfect, the results do not suffer from this same over-energisation of the system, since any high velocity particles selected for collision must already have been present in the flow, and both collision partners remain in the channel after the collision has taken place, which is not the case for the fictional particles. This means that even a selection of overly energetic collisions will not just add energy to the system. The deviations that do occur are a small enhancement of fluid and particle stresses at $0.1 < y^* < 0.6$. This reflects a region of the channel between the bulk and wall regions, and is likely due to a transfer of energy between the two regions.

The distribution of the particles across the channel half-height, and associated collisions, shown in Figure 56 are considered in the following section.

5.2.4 2.2M, 200μm particles (Case 4)

For the highest volume fraction case with the largest particles, the overly energetic fictional particles also begin to affect the mean streamwise particle velocity and the stresses acting on the fluid. The particles in Figure 57 are completely decoupled from the flow. Ironically this leads to a very smooth distribution of particle concentration in Figure 58, with the particles showing little inclination towards either the central or wall regions of the channel. The same is true of the results shown in Figure. 56.
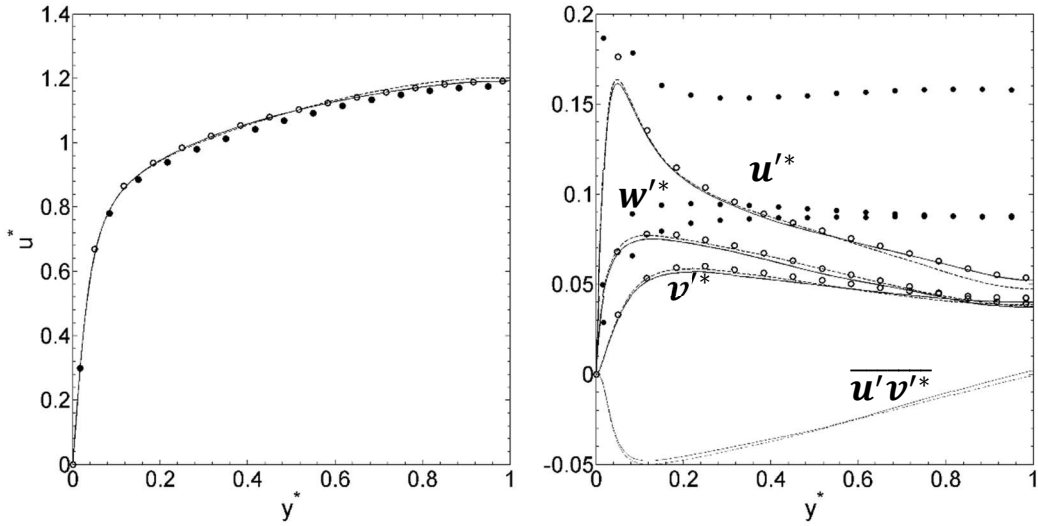
Figure 57: Compared velocities u^*, and normal and shear stresses , $v'^*, w'^*, \overline{u'v'^*}$ for four-way coupled flows with particles collided deterministically and stochastically with fictional particle collision. With 2.2M, 200μm particles. — Deterministic and - - - stochastic fluid, and ○ deterministic and ● stochastic particles.
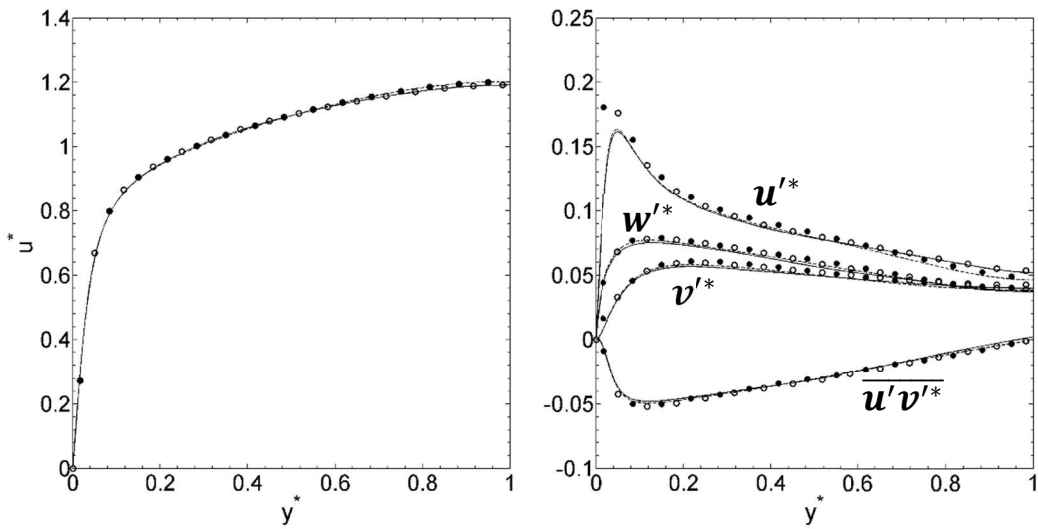
Figure 58: Compared mean streamwise velocities u^*, and normal and shear stresses $u'^*, v'^*, w'^*, \overline{u'v'^*}$ for four-way coupled flows with particles collided deterministically and
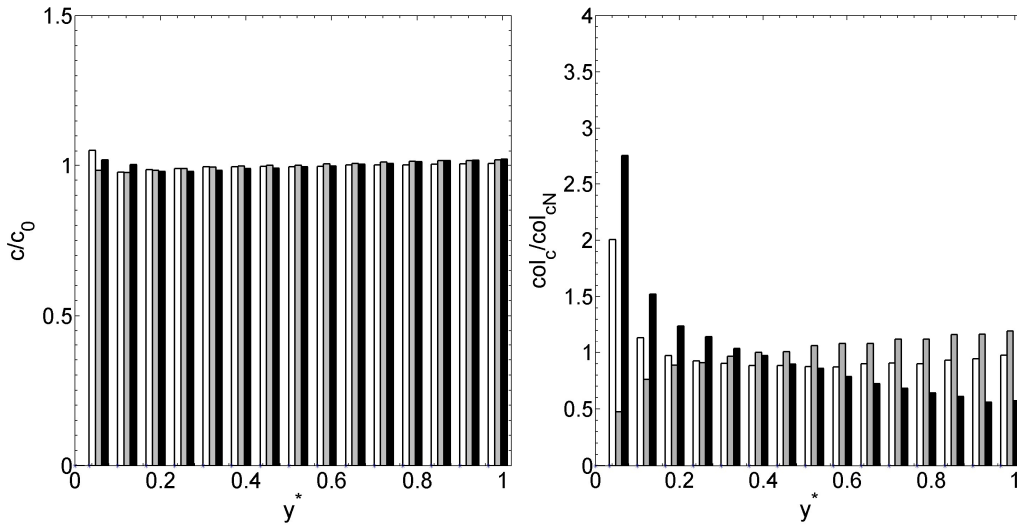
Figure 59: Particle (2.2M, 200μm) concentration (c/c_0, left) and collision distributions (col_c/col_{cN}, right) across the channel for four-way coupled flows using. □ deterministic collisions, ▨ stochastic using fictional particle collisions, and ◼ stochastic using DSMC.

The results of the DSMC technique, Figure 58, are much more reasonable. Though they are not in perfect agreement with the deterministic simulation, the amount of deviation in the particle and fluid stresses has remained fairly consistent, although a reduction in streamwise normal stresses for case 4 would seem to reflect the comparatively reduced collision rate in the bulk flow region. The flow forcing function in the channel is sufficiently dominant that the mean streamwise velocity rarely changes, with the high Stokes number fictional colliders being the only case where the particles have a strong enough influence over the fluid that a change can be seen. Changes to the fluid stresses are also present where the DSMC technique is used, albeit much smaller than for the fictional particle case.

Interestingly, the collision distribution for higher Stokes number particles, Figures 56 and 59, loses the trough near to the wall and the gradual incline towards the channel centre is much reduced for the deterministic case. The resulting distribution resembles that of the DSMC technique, although significant quantitative differences are apparent. This suggests that the DSMC technique will be more accurate when resolving collisions at higher Stokes numbers. Neither stochastic collision distribution changes notably between the cases with different Stokes numbers, an underlying issue with the stochastic technique which suggests room for improvement. Another aspect of stochastic techniques is that it is difficult to directly replicate the reduction in turbophoresis produced with deterministic interparticle collisions. When something like a fictional particle stochastic technique is used, a collision is as likely to propel a particle towards the wall as away from it. Johnson (2020) notes the importance of accurately simulating the anisotropy of near-wall particle motion. Deterministically, the oblique collisions near to the wall go some way towards cancelling out turbophoresis and preventing

all of the particles from simply migrating to that region permanently. The two stochastic techniques investigated here, rather than exactly replicating these effects, simply produce more, or more energetic, collisions in general, flattening the particle distribution in a way that mimics deterministic effects, but with somewhat deleterious effects on particle stresses, particularly in high collision systems, as shown in Figure 57. The next section elaborates on the specific dynamics taking place with the collisions, and discusses how the collision rate is as crucial a factor affecting the particle stresses as the location and energies of the collisions.

5.3 Improvements to the stochastic method

In order for a stochastic particle collision technique to successfully produce accurate results, the interparticle collisions it simulates must bear a resemblance, in location, energy transfer, and number, to the collisions which would occur in reality. It is understandably troublesome to count individual collisions in an experimental channel flow, but there exists no such issue with a deterministic simulation of such a flow. Given that the vast majority of a particle's energy is kinetic and directed in the streamwise direction, the collisions will be assessed through comparing the streamwise velocities of a given particle and its collision partner, fictional or otherwise.
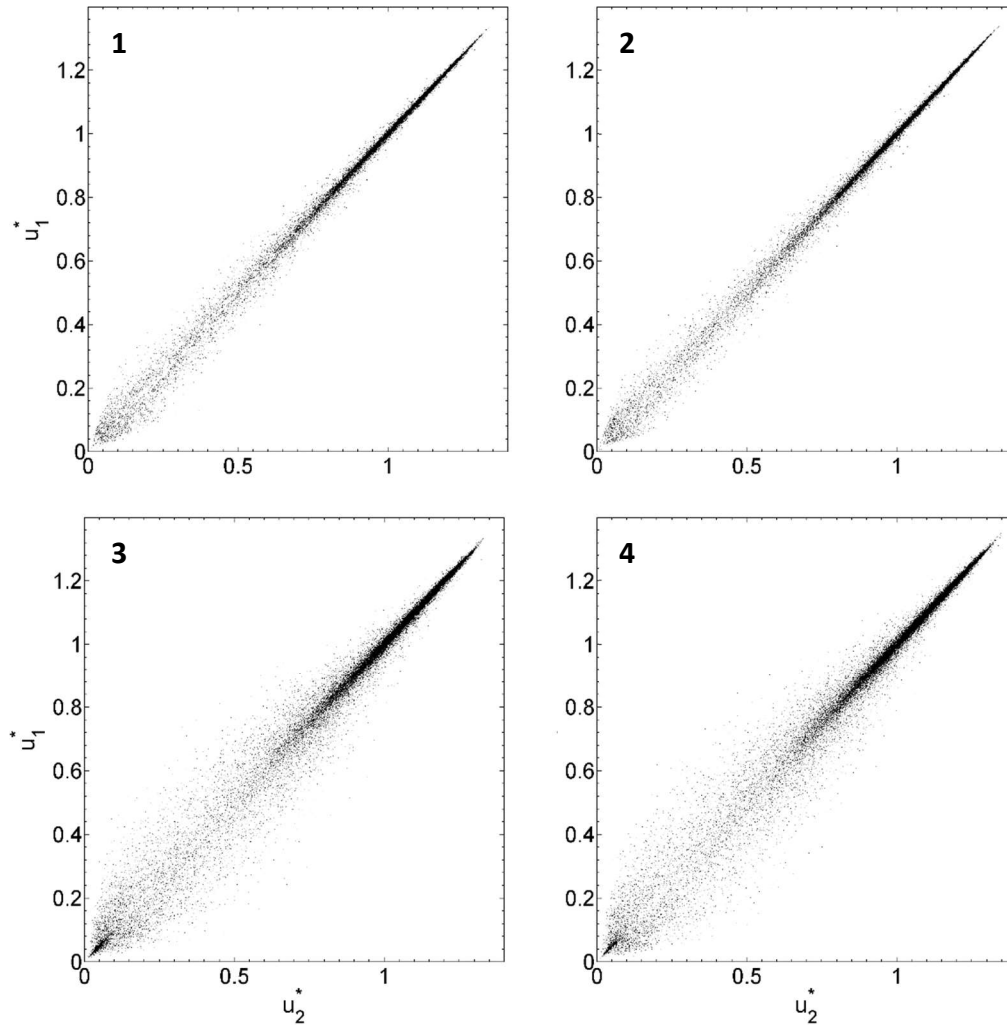
Figure 60: Comparison of streamwise velocities of sampled colliding particle pairs, for deterministic particles from all four test cases (1 and 3 – 300k particles, 2 and 4 – 2 M particles, 1 and 2 – 100μm particles, 3 and 4 – 200μm particles).

For the analysis shown in Figure 60, a collection of 10,000 collisions were randomly sampled from deterministic data on all four test cases. The velocity distribution is noted to be almost identical for the 300,000 and 2.2 million particle cases, but given that overall there are fewer collisions in the former case, the higher concentration simulations were chosen as the superior choice to study from data output alone. Firstly, it can be noted that in all cases, the mean streamwise particle velocity does not drop below 0.8 outside of the wall region, starting at around 0.1 distance units from the edge of the channel. The particles show a very strong tendency to collide with those having similar streamwise velocities, with all cases showing a dense distribution for the particles with higher velocities. This indicates the collisions taking place in the bulk flow region, where the constant acceleration produced by the fluid makes it very unlikely that a particle will ever encounter a neighbour travelling at a much slower speed.

Each case also demonstrates a dense distribution at the slowest velocities. This is produced by particles travelling adjacent to the wall, where the fluid velocity is lowest. This cluster is

especially visible in the cases where the particles are large, appearing in a dense spike shape similar to that seen in the bulk. Between the two is a region where a particle might collide with another having a velocity of 0.2 units difference, or 0.4 units for the higher Stokes number cases. This comparatively wider spread of collision velocities at higher Stokes numbers is produced by the action of turbophoresis and represents cases where a particle has travelled to a low-speed region from a high-speed one but has yet to have its velocity reduced by the action of fluid drag forces and subsequently collides with local slower particles. The spread is very noticeable at higher Stokes numbers, for these are the particles that are less responsive to fluid forces and will therefore retain their speed for longer when moving between regions. Zhao (2015) determined that there is far less velocity correlation between particles and fluid in the wall region when the Stokes number is high. Where particle velocities are less correlated to fluid velocities, it is safe to assume that the velocities of separate particles are also less correlated. This is indeed what is observed in Figure 60.
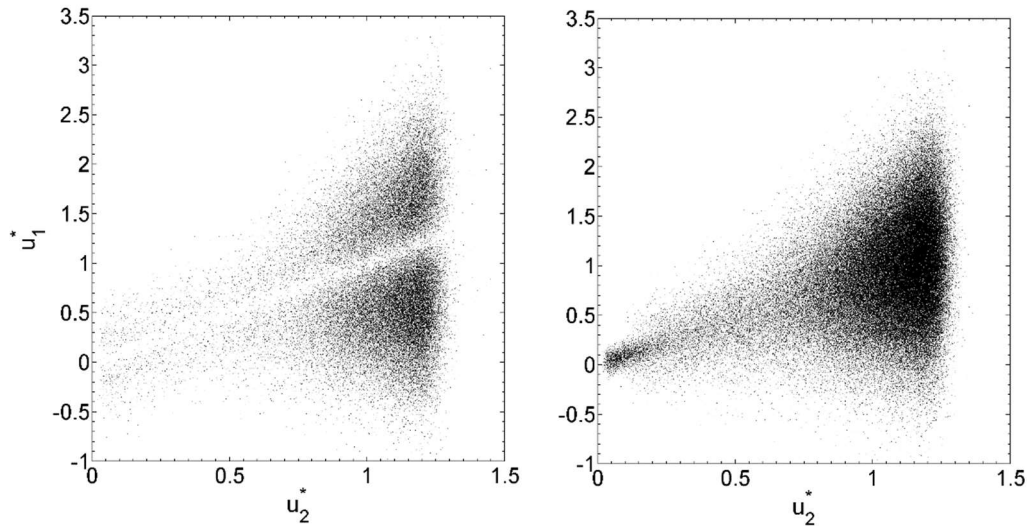
Figure 61: Comparison of streamwise velocities of sampled colliding particle pairs, for fictional particle collision with kinetic theory (left) and with advective theory (right), for the case with 2.2M, 100 micron particles.

Figure 61 shows the collisions determined to take place by the fictional particle stochastic technique, depending on whether kinetic theory or advective theory is used to determine if a collision has occurred. Under the kinetic theory of gases, two given particles are more likely to collide if their velocities are not similar. Specifically, the work of Abrahamson (1975) determined that this will be more the case for particles with uncorrelated velocities, referring to collisions between particles from different fluid flow regions. The advective theory of collision proposed by Saffman and Turner (1956) considers the dissipation rate of the fluid flow when determining the probability of collision, but neglects the effects of particle velocity. It is assumed here that particles are driven to collide solely through the motion of the fluid, making the collision rate an approximately constant value in a particular flow region, based on the dissipation rate and volume fraction alone. This resulted in the increased rate of collisions near to the wall shown in the previous section. The wall region is where the dissipation rate is highest, with many small eddies facilitating the interaction between particles. What both techniques replicate well is the narrowing of the distribution in the low-speed wall region. In this region, the kinetic theory-based technique shows a narrow region of low collision rate in Figure 61, which nevertheless would seem to contradict what is observed in the plot of deterministic collisions, but such a region can be seen in Figure 60 for both high Stokes number cases, suggesting that kinetic theory is a reasonable representation of at least the interparticle behaviour at low velocities.

Though the advective theory-based results match the deterministic results better in the low speed region, a more significant problem shown in both cases is that the fictional particles generated as potential collision partners occupy velocity regions that are not present in the channel flow. The velocity of the fictional particles is based on the velocity of the real ones, but with the magnitude of the velocity translating to the magnitude of the variation that a

fictional particle's velocity will have from its real partner. This is an effect which may not be significant for systems where the particles have small velocities, but for this case particles with very large, and even negative, velocities are generated, which kinetic theory says are more likely to successfully collide. Even for the advective technique, the generation of unrealistically fast particles as collision partners means that energy is being injected into the particle phase of the channel flow unrealistically.
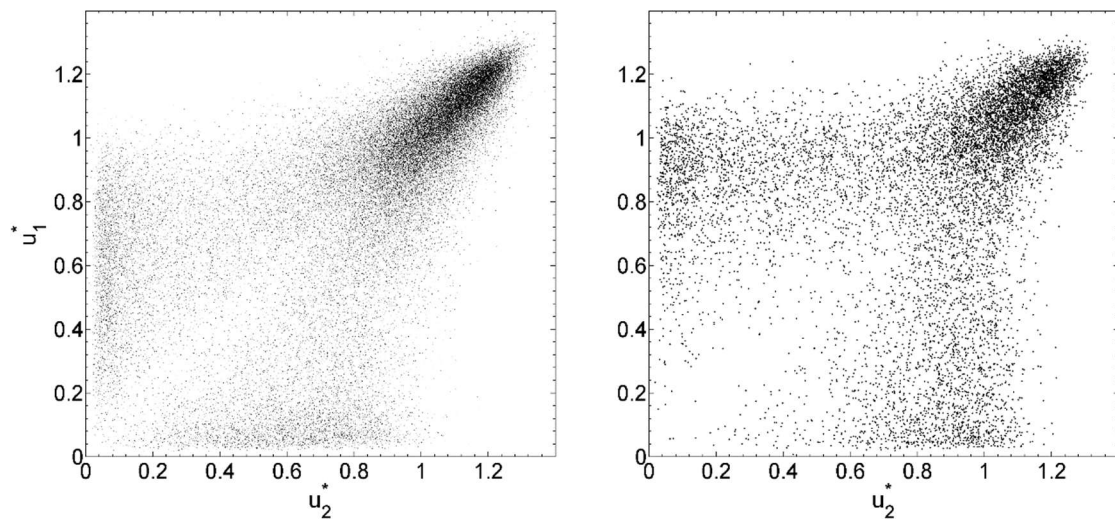
Figure 62: Comparison of streamwise velocity of sampled colliding particle pairs, for DSMC particle collision with kinetic theory (left) and with advective theory (right), for the case with 2.2M, 100 micron particles.

The rate of collision for a stochastic technique using advective theory is not expected to change whether the collision partners are chosen through DSMC or fictional particle creation, except in cases where the fluid is so affected by the collisions that the dissipation rate itself changes. For the samples of collisions from DSMC shown in Figure 62, this shows itself in a dramatic decrease in collision rate for the kinetic theory-based DSMC, compared to the fictional partner generation technique. Collision partners in DSMC are selected from particles within the same region, so it is impossible for collisions to occur at unreasonable velocities here, and a natural maximum is enforced for collision rate. That said, the collision rate itself is still determined to be much higher for the kinetic theory than the advective theory, and both produced more collisions than the deterministic approach, over the same amount of time.

Despite the mismatch in collision rate, the collision velocity distributions for DSMC are a much better match for the distribution of velocities for deterministic collisions. The collisions in the bulk flow region are consistently between particles with similar velocities, in agreement with the deterministic method. The slower particles in the near-wall region, however, seem consistently to be colliding with faster particles from regions nearer to the bulk flow region, hence there is more of a spread of collision velocities in the bottom left corner of the DSMC

plot. This is not what is observed in the plot of deterministic collisions. Such behaviour occurs, certainly, but it is exaggerated by a large margin by the DSMC technique.

For any particle collision simulation code, stochastic or otherwise, there is the concept of a "searching scope", when it comes to deciding whether a particle has collided and what with. For the deterministic technique used here, that searching scope is simply a sphere centred on a particle, two particle diameters across, within which two given particles are 100% likely to collide. A searching scope for a fictional particle technique contains particles that are statistically likely to be collision partners, based on the properties of particles located within the same region. The DSMC searching scope forgoes the step of creating a likely collision candidate by selecting a real particle from within the same region and assuming that to be a statistically likely candidate. The problem is therefore one of a statistical nature.
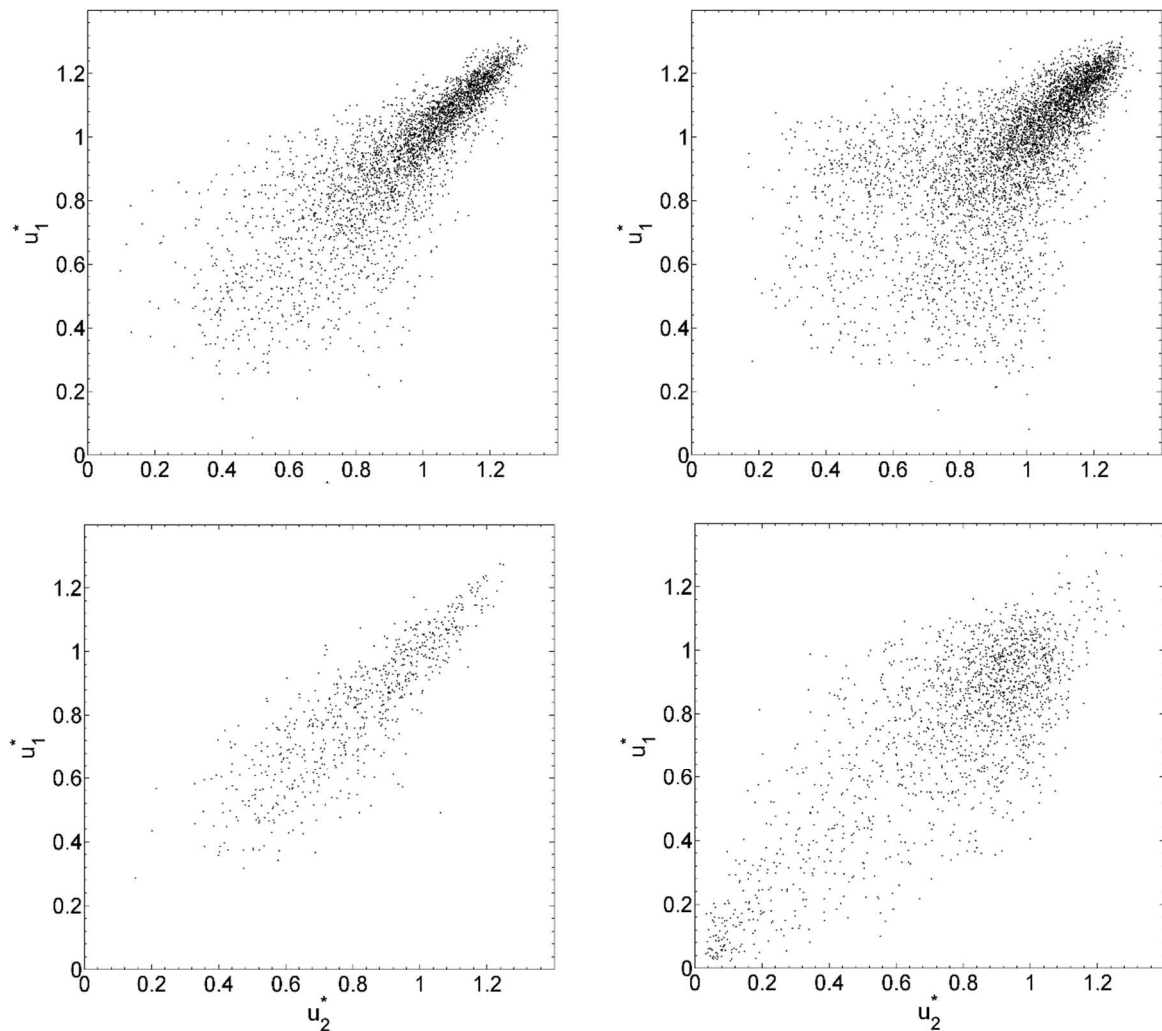
Figure 63: 300k, 100μm particles colliding using stochastic DSMC advective method with various searching scopes: cubes of sides $\delta/15$ (top left), $\delta/7.5$ (top right), $\delta/30$ (bottom left), and slices of width $\delta/15$ (bottom right).

The initial DSMC was performed using a technique which split the channel into equally sized cubes. This was based on a modification of the deterministic technique which limited the number of checks made to verify whether a particle had collided to a small region containing the particle. The nature of this region, relatively unimportant for a deterministic check, becomes extremely relevant when it is being used as the searching scope of a DSMC particle collider.

There are two primary considerations here, bearing in mind the advective theory considers local fluid flow dissipation rate and local particle volume fraction the factors solely responsible for determining the collision likelihood for particles. Firstly, if a searching scope is too small, the particles within it become less of a statistical sample of the local region than a random sample. A single statistically unlikely particle becomes a very likely collision choice if there are few alternatives to select from. In a sense this is the kind of behaviour that is expected in a near-wall region, with the particles removed from the bulk by turbophoresis being faster, and therefore, according to kinetic theory at least, likely to encounter a slower near-wall particle. Though this effect is not considered in advective theory, it is of interest that an incomplete statistical treatment produces the same effects, albeit resembling more the behaviour of a particle with a much larger Stokes number.

Pawar et al. (2014) determined that a minimum of 8 particles are required for the statistical treatment employed in DSMC. An investigation into the searching scope is presented in Figure 63, where the original searching scope is applied to the 300,000 100 micron case, expected to produce the smallest number of collisions. These tests were all performed over the same timescale. The original $\delta/15$ sized cube case produced the same effect resembling an increased Stokes number. When the searching scope was made larger, the magnitude of the effect increased. This, however, relates to the second consideration. A too large searching scope, though evading the statistical issue, nevertheless creates the same problem. In this case, for scopes above a certain size, the cube intersects multiple velocity regimes, meaning that particles with unlikely velocities are considered for collision even though their incidence within the searching scope is statistically correct.

For the case examined here, both of these effects are assumed to be in place for the $\delta/15$ and $\delta/7.5$ scale searching scopes, meaning that the segments are simultaneously too large and too small. Where smaller scopes of $\delta/30$ were tested, the effect of the scope intersecting multiple flow regions was eliminated somewhat, but this reduction in segment size not only retained the statistical problems associated with two few particles per scope, but also produced fewer collisions than the deterministic approach by virtue of segments frequently existing with one particle or fewer. Note that for all three tests with cubic searching scopes, the distribution of velocities only increases as the velocities decreases.

The problem of a scope that is too small was addressed by Pawar et al. (2014) by defining a spherical scope centred on each particle that would change in size depending on the local volume fraction so that the bare minimum of 8 particles was always reached. For the flows

considered herein that solution represents a use of computational resources equivalent to or greater than what is used by the deterministic collision algorithm. The basic principle stands though; a statistically large number of particles must be sampled over a volume that does not intersect differing flow regions. In a channel flow, the flow properties in the streamwise and spanwise dimensions are consistent, so there is no reason that two given points separated by a large spanwise or streamwise distance would have vastly different flow properties at their locations. Indeed, the dissipation rate of the fluid flow from which the collision rate is derived is consistent across a given *x-z* plane of the channel. Given this, the most appropriate searching scope for a channel flow would also be based on a plane.

The bottom-right plot of Figure 63 shows the results of such a searching scope, where slices of height δ/15 are used. The points on that plot produce a more oval shape than any stochastic method used previously. Though generally wider than deterministic results, it is a fair approximation of the shape that the plots of deterministic velocities produce. Slow particles, at last, are by preference colliding with other slow particles.

5.4 Trialling an element based particle selection method
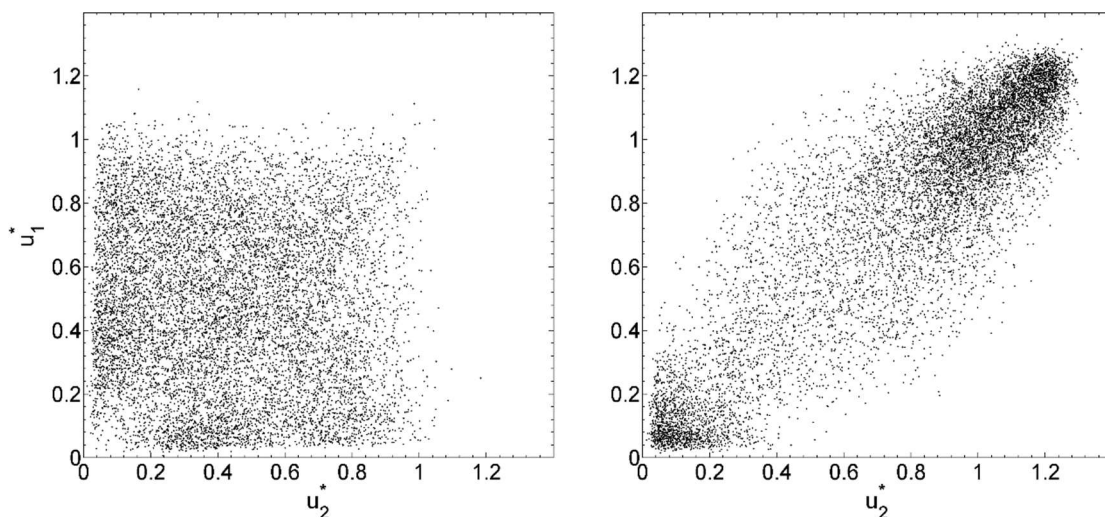
Figure 64: 2.2M, 100μm particles in cubes of sides δ/15 (left), and slices based on fluid detection elements (right).

Considering Figure 7 (Chapter 3), where the computational mesh used to simulate the fluid phase is shown, the fluid elements are more densely distributed the closer they are to the wall. For a channel flow like this one, that is the region in which the most interesting effects are occurring. Where the DSMC searching scope considers a thin cuboid incorporating the entire length and breadth of the channel, too few particles per sample volume is no longer a consideration. There is, however, now a new possibility. If the searching scopes narrow in width normal to the wall as the wall is approached, as the fluid elements do, this may or may not lead to more accurate results. A narrower searching scope or cuboid, regardless of location, would certainly reduce the effects of a scope crossing multiple velocity regimes.

Even very thin slices near to the wall at low concentrations would still have enough particles always present for the DSMC to be statistical rather than random.

This final searching scope technique, with the searching elements corresponding to the fluid element widths across the whole streamwise and spanwise directions in the channel, was tested on the highest concentration of 100μm particles and compared to a searching scope of the cubic variety with a height of δ/15, chosen to eliminate any possibility of there not being enough particles per volume on average. Figure 64 demonstrates that the slice searching scope based on fluid flow elements is significantly better than that based on a small cube, even at high particle concentrations. While it is not straightforward to determine just how superior the element-based large cuboid searching method is to the equally sized volumes tested previously, it has all of the desired properties associated with the deterministic technique, oval in shape, with high speed bulk flow region particles colliding with like particles, and near-wall particles doing the same (with a few exceptions). The distribution is still wider than for the deterministic technique, resembling what might be expected for a particle class with a higher Stokes number. However, as was observed in Section 5.2, the collision distributions of stochastic particle techniques seem to be more resistant to changes in Stokes number than what the deterministic method shows. This is at least true for the turbulent Stokes numbers considered here, which are close to unity.

These results represent a significant improvement on earlier stochastic method implementations, with simulations based on the kind of interparticle collision dynamics present in a channel flow resulting in dramatically overenergetic collisions no longer being present in the bulk or wall flow regions, which is a significant increase in realism when compared to the stochastic techniques previously tested. In the following sub-sections, the new element boundary (EB) based DSMC technique is tested for all four test cases to see how it compares to the deterministic technique.

5.4.1 100μm particles

Though there are small changes present in the RMS streamwise particle and fluid stresses in the wall region (Figure 65), the concentration plot of the first particle case in Figure 65 demonstrates comparatively little change regardless of the level of coupling used or whether the technique employed is stochastic or deterministic. This is consistent with previous results. If nothing else this makes it a good litmus test for simulation techniques, any time the results from this case change noticeably it is worthy of consideration.
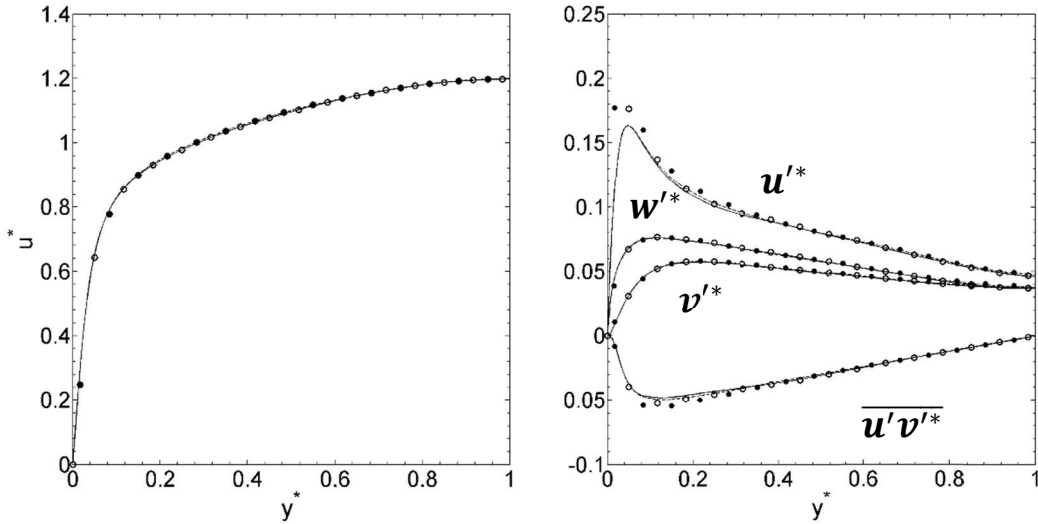
Figure 65: Compared mean streamwise velocities u^*, and normal and shear stresses $u'^*, v'^*, w'^*, \overline{u'v'^*}$ for four-way coupled flows with particles collided deterministically and stochastically with the EB method. With 300k, 100μm particles. —— Deterministic and - - - stochastic fluid, and ○ deterministic and ● stochastic particles.
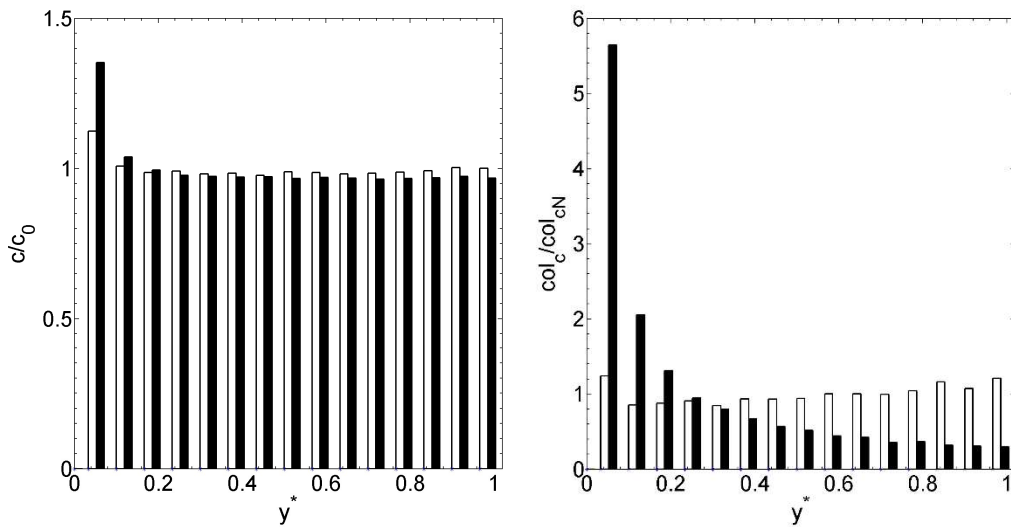
Figure 66: Particle (300k, 100μm) concentration (c/c_0, left) and collision distributions (col_c/col_{cN}, right) across the channel for four-way coupled flows simulated using the: □ deterministic and □ EB stochastic coupling techniques.

As it is, there is also an unexpected drift of particles towards the wall region, showing itself not only on the concentration plot, but also as an increased proportion of collisions taking place in the same region, more biased towards the wall, in fact, than was observed using the original DSMC technique before the element based technique was implemented.
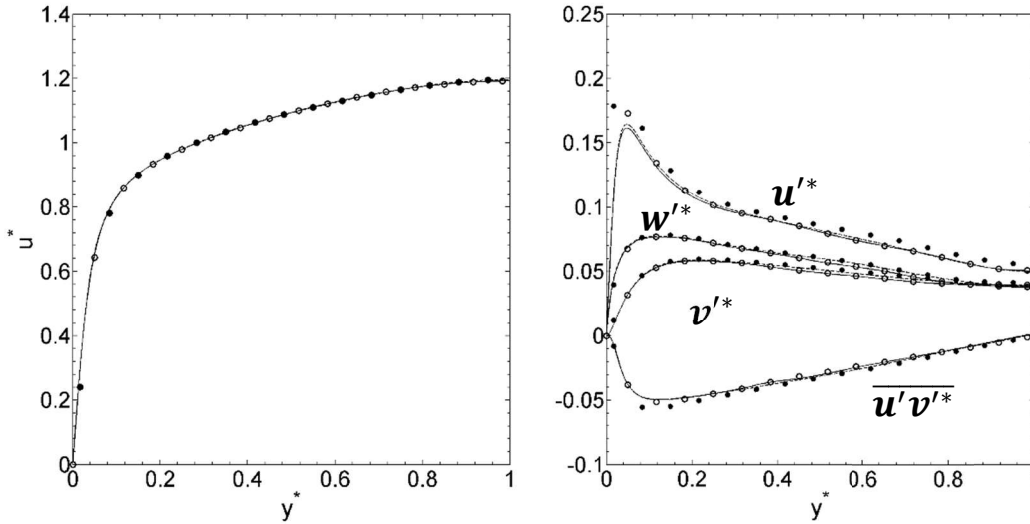
Figure 67: Compared mean streamwise velocities u^*, and normal and shear stresses $u'^*, v'^*, w'^*, \overline{u'v'}^*$ for four-way coupled flows with particles collided deterministically and stochastically with the EB method. With 2.2M, 100μm particles. —— Deterministic and - - - stochastic fluid, and ○ deterministic and ● stochastic particles.
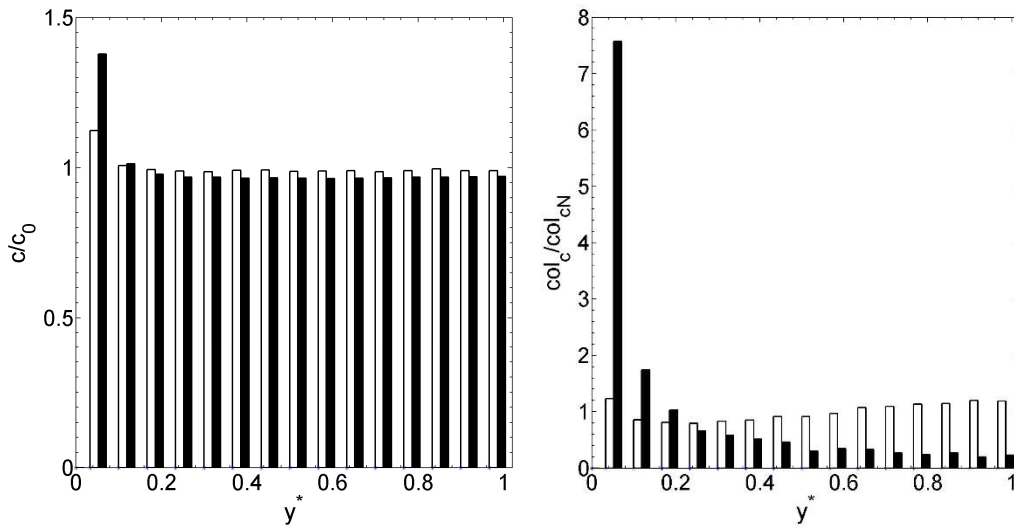
Figure 68: Particle (2.2M, 100μm) concentration (c/c_0, left) and collision distributions ($col_c/colc_N$, right) across the channel for four-way coupled flows simulated using the: □ deterministic and □ EB stochastic coupling techniques.

Shown in Figure 66 is another indication that the particles are more energetic than expected, with slightly enhanced streamwise velocity fluctuations. When the concentration of low Stokes number particles is increased, so too does the collision rate (Figure 68) predicted by the stochastic method, and concentrations in the wall region are also increased. Though the number of collisions is similar between the two methods, the EB DSMC technique is prone to producing collision distributions that resemble that of deterministic collisions at a higher Stokes number. This behaviour could be responsible for the drift of particles toward the wall. Certainly, the wall bias is significantly larger for the higher concentration case. Alternatively, it could be that the lower collision rate near to the centre of the flow is allowing turbophoresis

to go unchecked, however the effect was not nearly this large for the two-way coupled simulations in Chapter 4.

Given the differences between the velocity distributions from the deterministic technique in Figure 60 and the element based stochastic shown in Figure 64, it is possible that collisions are taking place with relatively large wall normal velocities, which are pushing the particles out towards the wall over time. Though the movement of particles toward the wall is problematic, the observations made in the previous section suggest the collisions which take place near to the wall are unenergetic, between particles of low velocities, and therefore would not have a significant impact on the overall statistics.

5.4.2 200µm particles

The two cases where the Stokes number is higher, Figures 69 to 72, show slightly contradictory results from the previous lower Stokes number case. On the one hand case 3 demonstrates an increased motion of particles towards the wall region, suggesting that, similarly to case 2, the particles are being driven towards that region, but the streamwise stresses are markedly normal for that case.
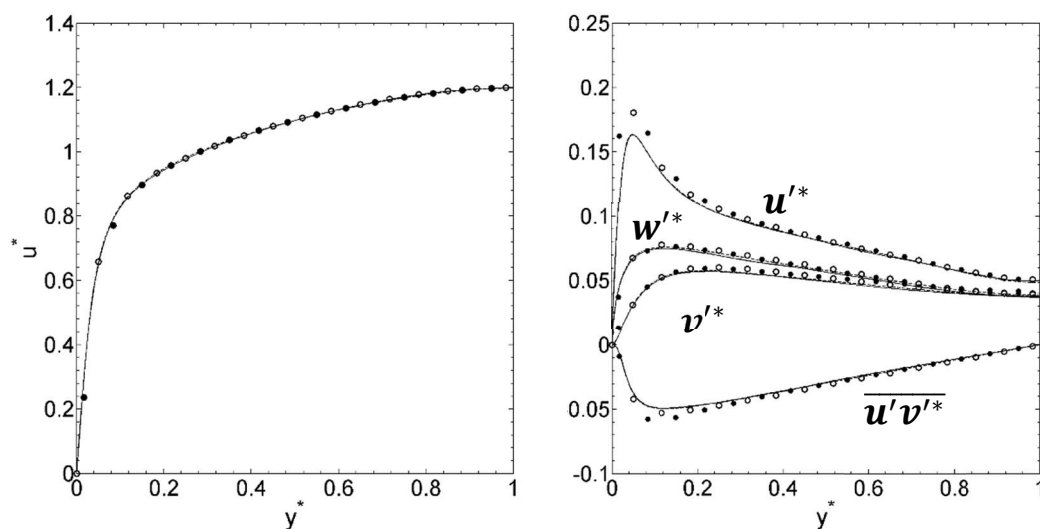
Figure 69: Compared mean streamwise velocities u^*, and normal and shear stresses $u'^*, v'^*, w'^*, \overline{u'v'}^*$ for four-way coupled flows with particles collided deterministically and stochastically with the EB based method. With 300k, 200µm particles. —— Deterministic and - - - stochastic fluid, and ○ deterministic and ● stochastic particles.
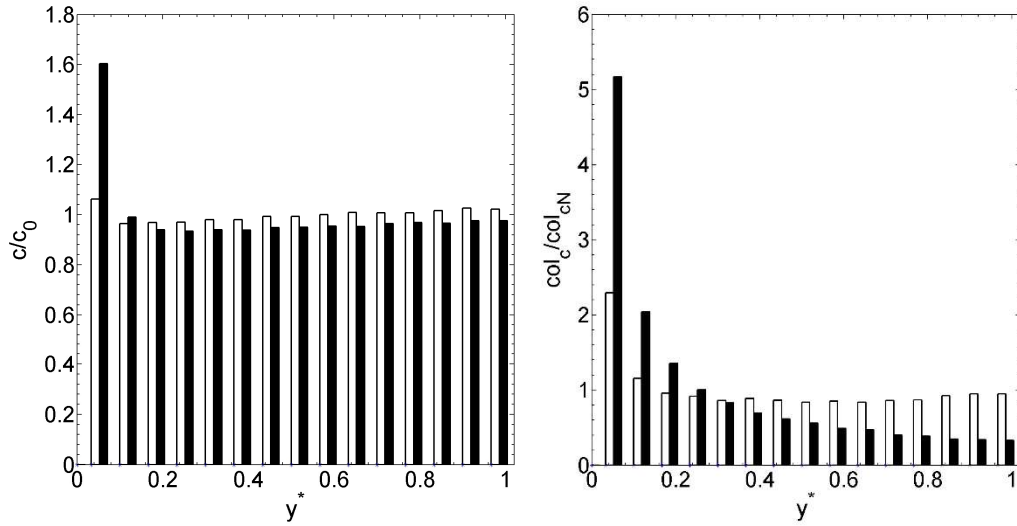
Figure 70: Particle (300k, 200μm) concentration (c/c_0, left) and collision distributions (col_c/col_{cN}, right) across the channel for four-way coupled flows simulated using the: □ deterministic and □ EB stochastic coupling techniques.
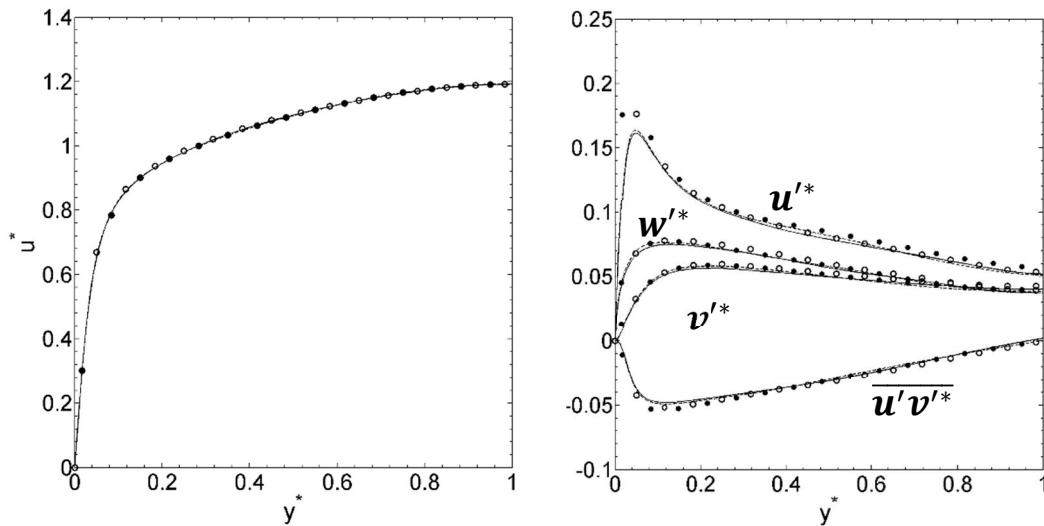
Figure 71: Compared mean streamwise velocities $\boldsymbol{u}^*$, and normal and shear stresses $\boldsymbol{u'}^*, \boldsymbol{v'}^*, \boldsymbol{w'}^*, \overline{\boldsymbol{u'v'}^*}$ for four-way coupled flows with particles collided deterministically and stochastically with the EB method. With 2.2M, 200μm particles. —— Deterministic and - - - stochastic fluid, and ○ deterministic and ● stochastic particles.
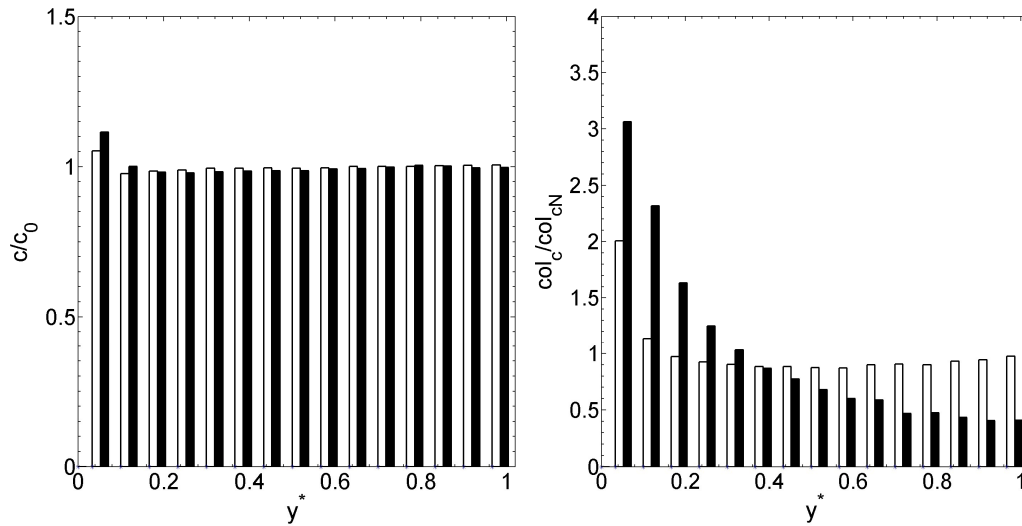
Figure 72: Particle (2.2M, 200μm) concentration (c/c₀, left) and collision distributions (col_c/col_cN, right) across the channel for four-way coupled flows simulated using the: □ deterministic and □ EB stochastic coupling techniques.

Case 4 on the other hand does have enhanced streamwise stresses, but the motion of particles towards the wall has not occurred to the same degree. The interparticle collisions are also less biased towards the wall. Be it the increased isotropy caused by collisions that was observed in Chapter 4, or the increased volume fraction of particles causing the migration of particles towards the wall to be slower, the cause of this difference is of interest. It is expected that a particle would have more difficulty approaching the wall at a high volume fraction, but for this behaviour to be well replicated by stochastic collisions is promising.

Table 6: Comparison of deterministic and stochastic techniques for computational time and collision rate (four-way coupled, no agglomeration)[*].

	Test Case			
	1	2	3	4
Technique	**300k, 100µm particles**	**2.2M, 100µm particles**	**300k, 200µm particles**	**2.2M, 200µm particles**
Deterministic run time	2.26	19.36	2.27	18.61
Deterministic collisions/t[*]	2,217	160,847	10,447	626,401
Stochastic run time	2.26	18.85	2.25	23.88
Stochastic collisions/t[*]	4,688	228,083	37,761	1,812,525

[*]Simulation times are normalised by the time taken for the one-way coupled simulation with 300k, 100µm particles covered in Chapter 4.

Table 6 shows that the new element-based stochastic method has for the most part produced faster simulation times than the deterministic approach, and in general achieved better speedup when the number of collisions was larger. Case 4 is an exception, where although the overprediction of collision rate is qualitatively no worse than in case 3, the quantitative numerical increase accounts for a significant slowdown, which is likely in part a result of the two-way coupling step having to check more particles travelling between fluid cells. These simulations were each given a similar amount of time to run as the four-way coupled particle simulations from table 5, ensuring that the timesteps were consistent between simulations having the same number of particles, with account being made for the increased/decreased simulation speed.

5.5 Conclusions

In this chapter developments were described to duplicate the results from four-way coupled deterministic simulations of multiphase channel flows using stochastic techniques. A stochastic technique is intended to decrease the computational cost of a simulation with, for example, many particles undergoing collisions at each step. Two well explored techniques were implemented to see if they were good candidates for a stochastic technique whilst still obtaining satisfactory accuracy. These were tested on the same four simulation cases studied in the previous chapter.

The two initial stochastic techniques used here were; a method which generated fictional particles as collision partners for a given particle, and a direct simulation Monte Carlo technique which selected a collision partner from among local particles. The results, in terms of particle concentration, mean streamwise velocity, and normal and shear stresses from these simulations were found to be comparable with the deterministically simulated equivalents. At higher concentrations this equivalence breaks down somewhat for the fictional particle generation technique. It was found that the fictional particle technique in the context of a channel flow produced particles with a velocity range much larger than was realistic, a consequence of which is the injection of energy into the particle phase in a system with many high speed collisions. This effect was not nearly so large with particles having small velocities, which implies that the technique is best not applied to a channel flow. Improvements to the technique may involve reducing the range of collision velocities based on the speed of the localised fluid.

The DSMC technique was determined to be the more appropriate method of simulating interparticle collisions for this flow, although this technique still had issues the way it was initially implemented. The rate of collision for the technique was somewhat higher than for the deterministic approach, for instance, and the number of collision events between low speed and high speed particles was exaggerated in a way that did not occur for the fictional particle technique. This effect was analysed in more detail by looking at the particle distributions and was determined to be statistical in nature. The concept of the searching scope from which a local particle is selected to be a collision partner was analysed in detail and one was derived assuming that the properties of particles and fluid were consistent in thin slices across the wall normal axis of the channel, incorporating the entire region in both streamwise and spanwise dimensions. These were selected to be consistent with the computational elements used in the fluid flow calculation, which become narrower closer to the wall region.

The new element boundary DSMC still slightly overestimates the collision rate, but to a lesser degree than the previously tested techniques. The agreement between its results and those from the deterministic technique is good, but not markedly better than the previously used DSMC, having in some cases an over-average drift of particles towards the wall and increased streamwise velocity distributions. However, the fact that the new technique generates collisions between particles which have velocities more consistent with those from the deterministic technique, as well as a more realistic rate of collision and a somewhat improved computational speed, makes this the preferred technique for further study.

Chapter 6 Prediction of Particle Agglomeration

Chapter 4 considered the way in which levels of particle fluid coupling in a multiphase simulation will affect the resulting flow behaviour. For a given multiphase flow, taking into consideration via computations more interfluid/particle effects will increase the accuracy of the simulation. This is a given, and it is also known that for any additional factor considered, there will be a related computational cost. In general this cost will be associated with the number of fluid cells that the associated equations must be calculated over, and/or the number of individual particles which exist in the system. The latter case is especially true for any kind of deterministic simulation, with stochastic simulations as discussed in Chapter 5 potentially allowing for a reduction in the amount of operations required.

The simplistic model of interparticle collision assumed in the previous chapters only represents some of the behaviour demonstrated by a multiphase system. Interparticle forces in a typical fluid-particle system are liable to promote the formation of agglomerates, at a rate dependent on the chemical properties of the particles and the fluid (Afkhami et al., 2015). This chapter will investigate the use of an additional simulation mechanism which allows for the generation of agglomerates. In doing so, it will be determined how Stokes number and volume fraction affect this process, and how this affects the fluid and particle bulk flow statistics. The chemical properties assumed here are those of calcite, which is a simulant for nuclear waste material (Afhkami et al., 2015). This is expected to result in the production of a proportion of particles with larger Stokes numbers, changing the way the particle phase as a whole interacts with the fluid phase, and with itself. The concentration of particles across the channel, as well as the collision rate, are factors also likely to be affected.

With the implementation of an agglomeration technique there are potentially going to be more operations performed per timestep in a simulation. Since computation time is a key consideration in this study, investigations will be made into how this changes under the new conditions accounting for agglomeration. Further to this, an assessment will be made into the effectiveness of the stochastic simulation developed in Chapter 5, in the case where agglomeration takes place. Sommerfeld (2001) describes how a stochastic technique may be used to handle particles of different size classes. This method was used here and was simply a weighting of the collision probabilities based on number density. It is assumed that the slice based searching scopes developed in the previous chapter will continue to be effective, with the slices chosen containing enough particles of differing classes to prevent the previously stated issue of unlikely particles consisting of a too large proportion in a given searching scope.

6.1 Investigating the effects of agglomeration using a deterministic approach

The initial investigations in this chapter consider the rate at which agglomeration occurs for the four fluid-particle cases considered previously using a deterministic approach, and explore any effect this has on the properties of the fluid and particle phases. It can be

expected that in cases with a significant amount of agglomeration taking place, the resulting creation of particles with larger Stokes numbers will have some manner of effect, at least to the particle concentration. Agglomerates consisting of more than 8 of the low Stokes number particles used in cases 1 and 2, using 100 micron diameter particles, as well as any agglomerates for the 200 micron diameter particles with higher Stokes numbers in cases 3 and 4, will have larger Stokes numbers than have been investigated previously in this study, albeit in much smaller quantities than for the initial particles.

The initial cases considered below were simulated for roughly equivalent timescales, within the same orders of magnitude, but the computation times were much larger for the high concentration cases so the final timestep from which the results were gathered differs between the cases. On the other hand, the development of flows containing larger volume fractions of particles exhibit an increased agglomeration rate anyway, as more collisions lead more quickly to the formation of larger structures, meaning that the rates of change over time are similar. The rate of production of agglomerates by number and by mass shall be analysed over the course of this chapter, and the results of the simulations will be compared to the results of simulations which only consider four-way coupling effects without agglomeration.

6.1.1 300k, 100μm particles (Case 1)

Figure 73 demonstrates the effect of the production of agglomerates on the fluid and particle normal and shear stresses to be relatively small, although the mean streamwise velocity does in fact show a slight change in terms of the mean streamwise particle velocities. In the $0.2 < y^* < 0.8$ region, therefore, the particle velocities are larger with agglomeration. Since particles gradually increasing in size would lead to a gradual increase in the effects of turbophoresis on said particles, according to Crowe et al. (1985), the larger agglomerates drifting towards the wall region, and retaining their bulk velocities, would potentially account for this velocity increase in that region, thereby skewing the particle velocity data for the non-bulk flow regions. Given a longer simulation time it is possible that with the formation of larger and larger agglomerates, the particle velocity in the wall region would become affected in the same way. That said, in previous chapters it has been observed that the particle concentration is highest at the wall, giving an influx of high speed agglomerates comparatively little statistical weight.
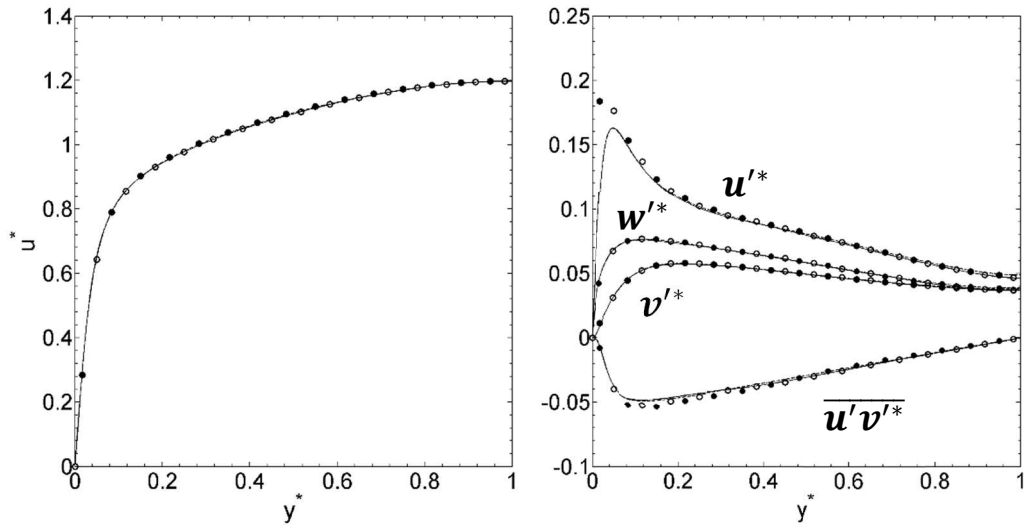
Figure 73: Compared mean streamwise velocities u^*, and normal and shear stresses $u'^*, v'^*, w'^*, \overline{u'v'^*}$ for fluid flows with particles collided with and without agglomeration. With 300k, 100μm particles. Fluid simulated —— with and - - - without agglomeration, and particles ● with and ○ without agglomeration.
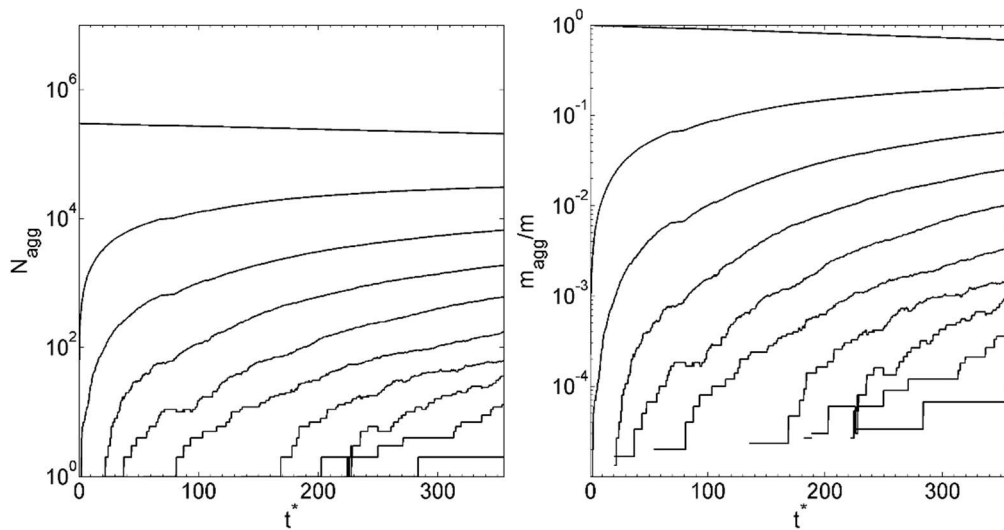
Figure 74: Compared number, N_{agg}, of differently sized agglomerates for 300k, 100μm deterministic particles (left), and m_{agg}/m, the total mass of a single particle size class as a proportion of the total particulate mass (right), over time, for particles with sizes 1, 2, 3 …9 and 10, 15, … 50 (top to bottom).

124
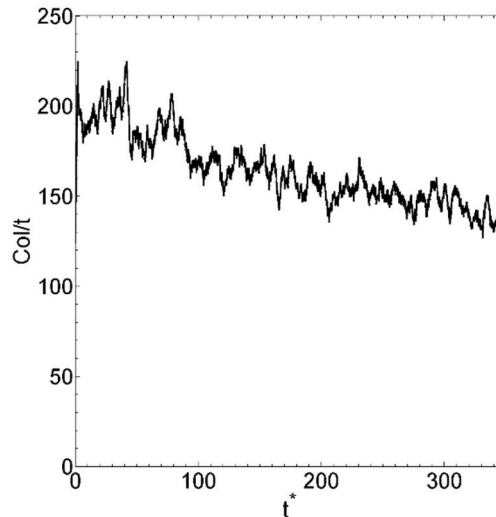
Figure 75: Average number of collisions over time for 300k, 100μm particles colliding with agglomeration.

Over the simulation time, the agglomerates shown in Figure 74 reached a size of no more than 10 of the initial particles, with the agglomerates consisting of ten initial particles forming shortly before t* = 300, and with no further decaplets forming within the given timeframe. All of the other agglomerate classes larger than doublets continue to increase in number after their first instance. These agglomerate size classes all display a short initial burst of rapid growth, which decreases as the simulation progresses. This growth rate is driven partially by the reduction in number for that class of particles, as agglomerates begin colliding to produce larger agglomerates, but the bulk of collisions still involve the original singlets. Case 1 has a small volume fraction, which equates to a comparatively small rate of collision, shown in Figure 75 to be barely more than 200 collisions per bulk time unit, or about 4 per timestep, using a typical step length of 0.02 bulk time units. As the number of singlets drops to around 70%, so too does the collision rate, by nearly the same factor.

6.1.2 2.2M, 100μm particles (Case 2)

As with case 1, Figure 76 shows that the mean streamwise particle velocity has increased slightly for the case with agglomeration, and would likely increase further with more simulation time. The fluid and particle normal stresses for this case have actually attenuated slightly, as Zhao et al. (2015) predicted for systems with high Stokes number particles. This effect, like the particles, is comparatively small, but given the increasing volume of particles with larger radii, it is likely that this effect will increase in magnitude given time.
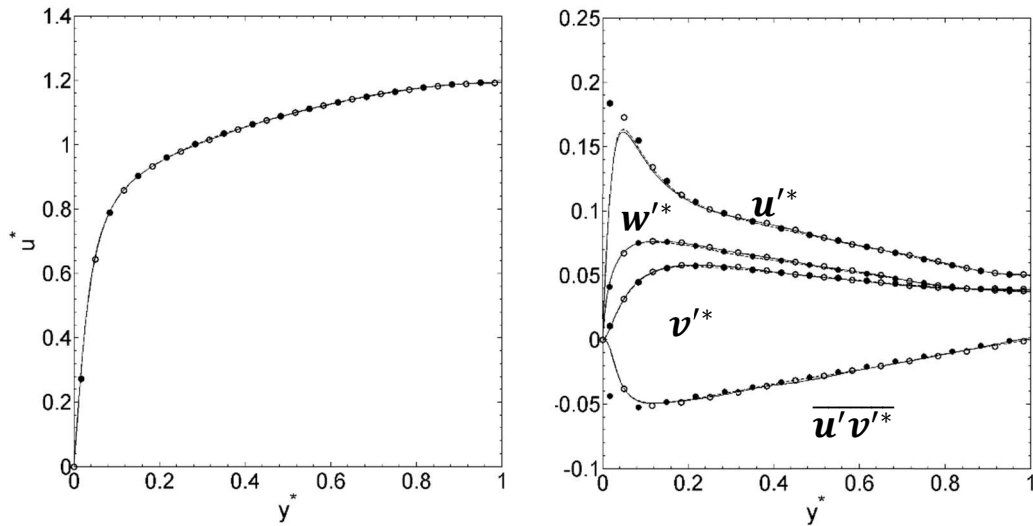
Figure 76: Compared mean streamwise velocities u^*, and normal and shear stresses $u'^*, v'^*, w'^*, \overline{u'v'}^*$ for fluid flows with particles collided with and without agglomeration. With 2.2M, 100μm particles. Fluid simulated, and particles ● with and ○ without agglomeration.
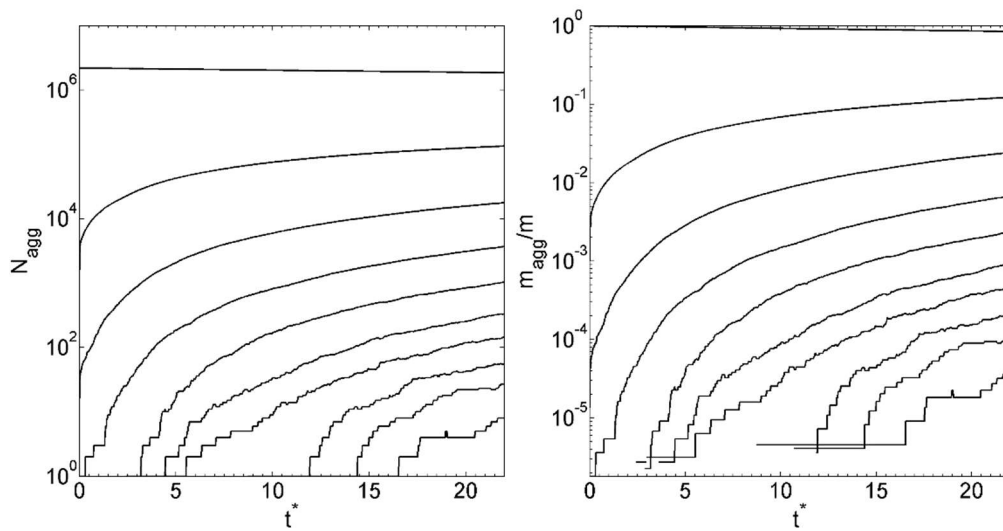
Figure 77: Compared number, N_{agg}, of differently sized agglomerates for 2.2M, 100μm deterministic particles (left), and m_{agg}/m, the total mass of a single particle size class as a proportion of the total particulate mass (right), over time, for particles with sizes 1, 2, 3 … 9 and 10, 15, … 50 (top to bottom).
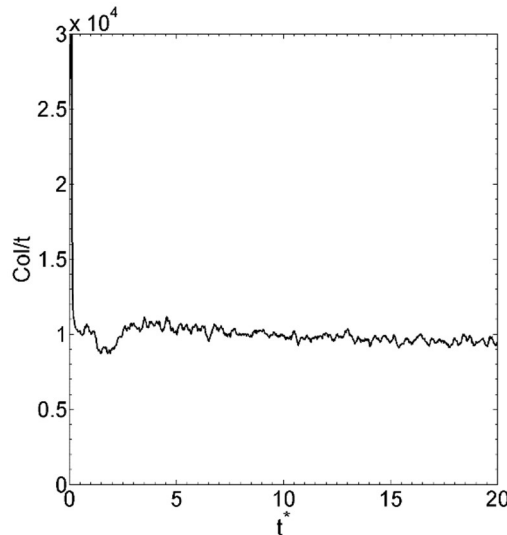
Figure 78: Average number of collisions over time for 2.2M, 100µm particles colliding with agglomeration.

Case 2 has approximately 7 times as many particles in the system as that considered in the previous section, but the collision rate in Figure 78, compared to case 1, with the same Stokes number, is around 50 times higher, seemingly having scaled with the square of the volume fraction. Although this simulation became sufficiently slow that it was difficult to perform it for 1/10th of the bulk time units of case 1, its particles also reached a maximum agglomerate constituent number of at least 10 over the timescale considered. Over the course of 20 bulk time units of this simulation, over 10% of the singlets can be observed to have agglomerated in Figure 77. By comparison it took case 1 until $t^* = 120$ to reach this state. The collision rate decreases over time, as in the first case, but by an accordingly smaller amount, approximately 90%, in accordance with the number of singlets.

The sharp spike in collision rate at the start of the simulation is derivative of the fact that the simulations of agglomeration were initiated from a previously settled flow using deterministic four-way coupling without agglomeration. Surprisingly, that system has a substantially greater collision rate, a fact that will be discussed later in the chapter, but because of this the simulations of agglomeration performed for this chapter would often require a few timesteps for the collision rate to settle down, using a shortened timestep for some of the simulations with higher volume fractions.

6.1.3 300k, 200µm particles (Case 3)

The effects of agglomeration on the flow statistics for this case, in Figure 79, are an increase in mean streamwise particle velocity, again in a region away from the central bulk flow region, where the velocity has actually dropped. The mean streamwise normal stress as well as the shear stress decrease in magnitude throughout the flow. In the 0.2 < y* < 0.4 region, however, the flow with agglomeration seems more energetic, at least in the wall normal direction, where the stresses are enhanced. These effects would seem to correspond with the

127

movement of particles with increased mass towards the wall. Since this system is generating agglomerates consisting of tens of constituent particles, these larger particles would have a proportionately large influence on the particles and fluid near to the wall.
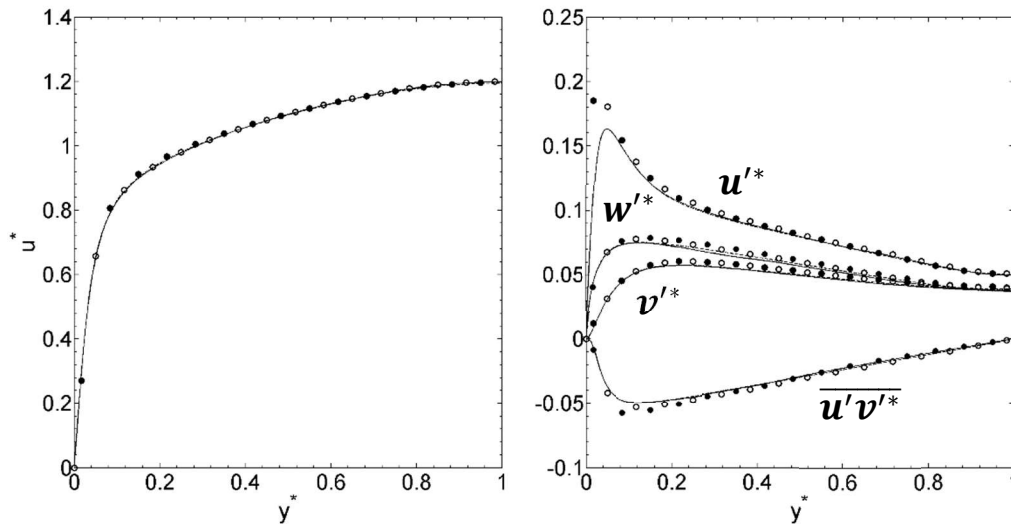
Figure 79: Compared mean streamwise velocities u^*, and normal and shear stresses $u'^*, v'^*, w'^*, \overline{u'v'}^*$ for fluid flows with particles collided with and without agglomeration. With 300k, 200μm particles. Fluid simulated —— with and - - - without agglomeration, and particles ● with and ○ without agglomeration.
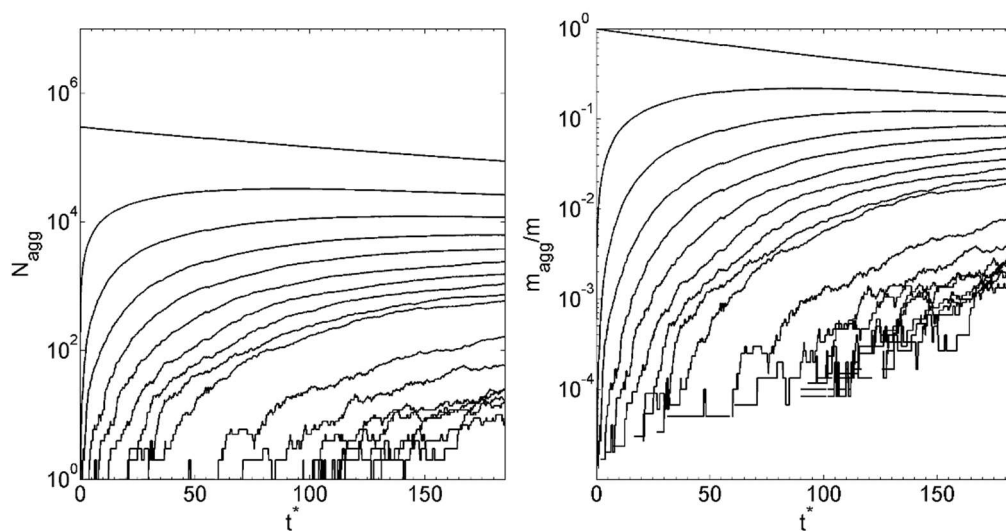
Figure 80: Compared number, N_{agg}, of differently sized agglomerates for 300k, 200μm deterministic particles (left)), and m_{agg}/m, the total mass of a single particle size class as a proportion of the total particulate mass (right), over time, for particles with sizes 1, 2, 3 … 9 and 10, 15, … 50 (top to bottom).

128
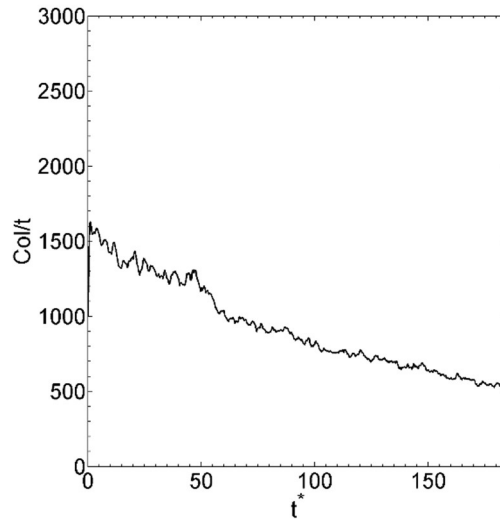
Figure 81: Average number of collisions over time for 300k, 200μm particles colliding with agglomeration.

Having a much higher collision rate than the previous two cases, yet also being simple enough that it could be run at length without too much difficulty, this case allowed for the formation of much larger agglomerates. Over the course of the simulation, Figure 80 shows the proportion of singlets by mass decrease to 20%, and noticeably, the doublets and triplets actually reach a peak and then start decreasing in number as well. At the same time, the collision rate is less coupled with the number of singlets after a certain point, not dropping to 20% of the original rate, but decreasing at a slower rate, likely levelling out at some point at a later time. The agglomeration efficiency depends partially on particle size, so at some point the number of particles, and hence the collision rate, can be expected to level out.

For case 3, the low concentration high Stokes number simulation, the initial collision rate in Figure 81 starts off at exactly 8 times the collision rate of case 1, illustrating the direct relationship between particle radius and collision rate. Considering that cases 2 and 3 intentionally have similar volume fractions, and yet increasing the particle number had an effect on collision rate proportional to the square of the volume fraction, while increasing particle size only increased the collision rate by the same factor, it can be determined that both volume fraction and particle number are factors which directly affect the collision rate.

6.1.4 2.2M, 200μm particles (Case 4)

In Figure 82 it can be seen that the streamwise particle and fluid stresses are impeded in the bulk flow region under these conditions. The mean streamwise velocity is enhanced in this region, however, for both fluid and particles. Since the vast majority of collisions result in the formation of an agglomerate, (over 90%) this behaviour in the bulk region reflects observations made in Chapter 4, i.e. that the particle concentration increases to a shallow peak in the bulk flow region in cases where the Stokes number is high. This would produce a rapid onset of agglomeration events for this case where agglomeration is turned on, leading

129

to the production of large, fast moving particles that with their high inertia have a delayed response to the turbulence in that region. If large particles are being generated in the centre of the channel faster than turbophoresis can sweep them out towards the wall, this will undoubtedly cause the bulk region to become less turbulent.
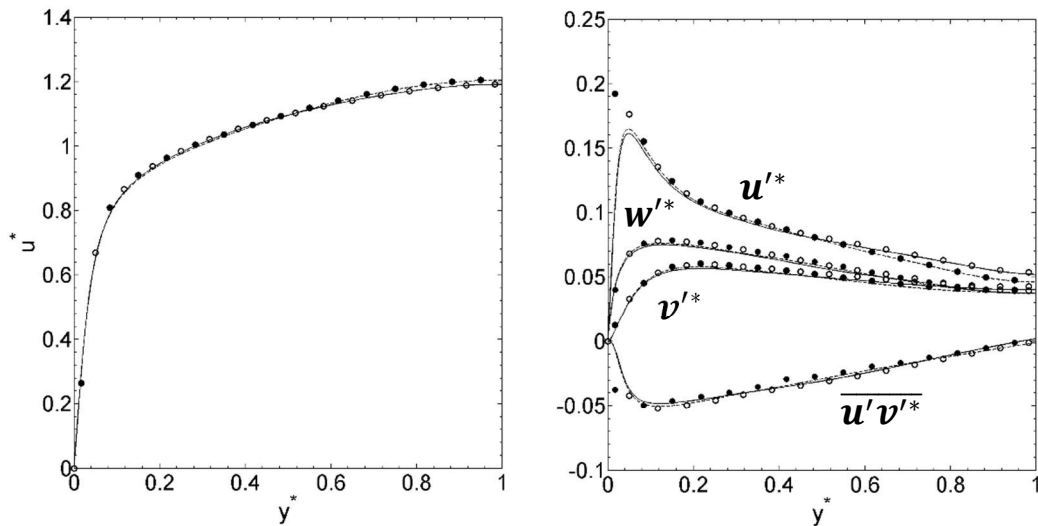
Figure 82: Compared mean streamwise velocities u^*, and normal and shear stresses $u'^*, v'^*, w'^*, \overline{u'v'}^*$ for fluid flows with particles collided with and without agglomeration. With 2.2M, 200μm particles. Fluid simulated —— with and - - - without agglomeration, and particles ● with and ○ without agglomeration.
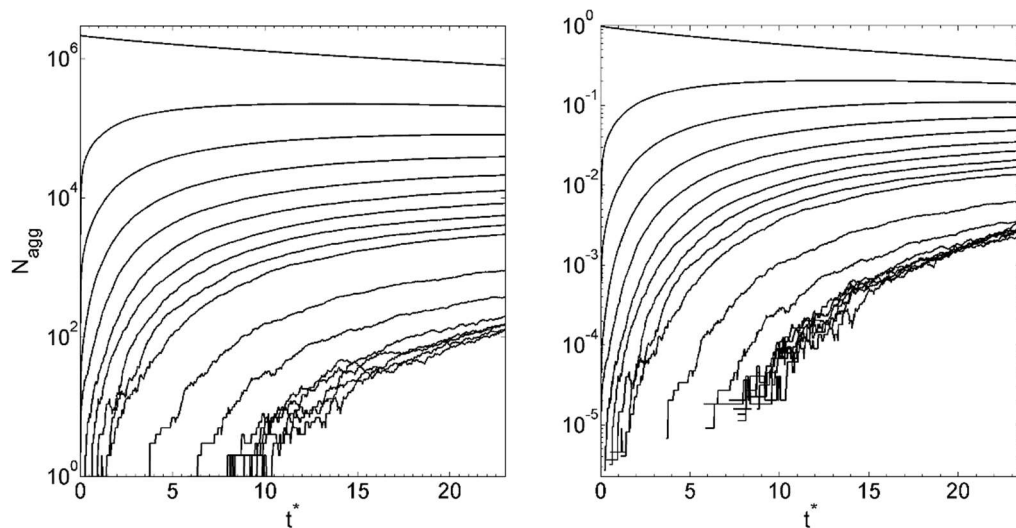
Figure 83: Compared number, N_{agg}, of differently sized agglomerates for 2.2M, 200μm deterministic particles (left), and m_{agg}/m, the total mass of a single particle size class as a proportion of the total particulate mass (right), over time, for particles with sizes 1, 2, 3 … 9 and 10, 15, … 50 (top to bottom).
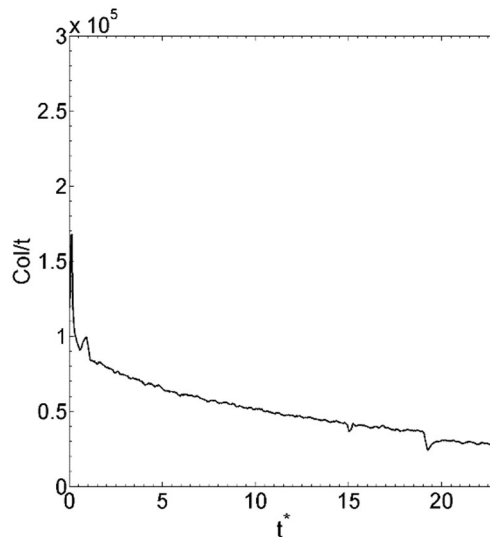
Figure 84: Average number of collisions over time for 2.2M, 100µm particles colliding with agglomeration.

As expected, the simulation of case 4 starts with the largest collision rate of all the cases considered, with Figure 84 showing almost 10^5 collisions per non-dimensional time unit, an order of magnitude larger than the second case, which is to be expected. With this many collisions per time unit, large agglomerates form very quickly. Within 10 bulk time units agglomerates with sizes of 25 singlets and more begin to be formed. An interesting observation is that agglomerates of that size and above form a contiguous group on the mass distribution plots. This can be seen in Figure 83 as well as Figure 80, the two cases where agglomerates of those sizes are formed. The agglomeration happens so quickly in this case that the line depicting the number of remaining singlets is visibly curved, rather than appearing straight, as it did within the timescales of the other three cases. The collisions over time profile is also visibly curved, though it decreases at a slightly slower rate than the number of singlets.

6.2 An alternative stochastic method for simulating agglomeration

During the investigation of the four-way coupled deterministic simulations which included agglomeration, some interesting facts came to light which warrant further investigation for this part of the study. Firstly, the collision rate was notably smaller for a system with agglomeration. This will be addressed later in the chapter. In addition to this, the implementation of an agglomeration model involves additional computational steps which prolong the interparticle collision phase. Although the effects on runtime from this may be small on their own, this study has already investigated the use of stochastic techniques for reducing the computation time of inter-particle behaviour. Testing the technique in this situation where agglomeration has been implemented is a logical extension to previous work.

6.2.1 Observations of the effects on particle collision rate

Table 7: Comparisons of deterministic collision rates per bulk time unit for cases with and without agglomeration.

Case	1	2	3	4
Collisions without agglomeration	2,218	160,847	10,447	626,401
Collisions with agglomeration	214	10,299	1,707	220,020

Table 7 shows the number of collisions per bulk time unit predicted by the four-way coupled deterministic simulations of the four cases, averaged over the time it takes the bulk fluid to travel the length of the channel. Compared to the collision rates at the beginning of each case with agglomeration implemented, the collision rates for the cases without agglomeration are substantially larger, although consistent in that an increase in particle number has a much larger impact than an increase in particle size.

The difference in the collision rate between having agglomeration and not having agglomeration is consistently around an order of magnitude, with the large Stokes number particles having the smallest change when agglomeration is implemented. This information is extremely useful in finding the cause of the change in collision rate. This turns out to be an effect that grows in magnitude as the Stokes number decreases.
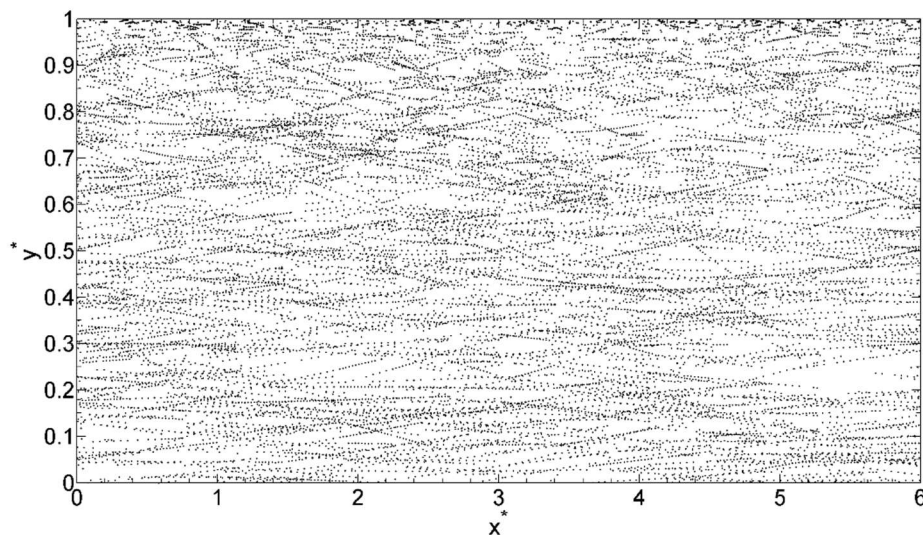
Figure 85: Visualisation of the location of deterministic collisions in the streamwise and wall-normal dimensions for a section of a channel flow in which the 300k, 100μm particle case is being simulated with four-way coupling.
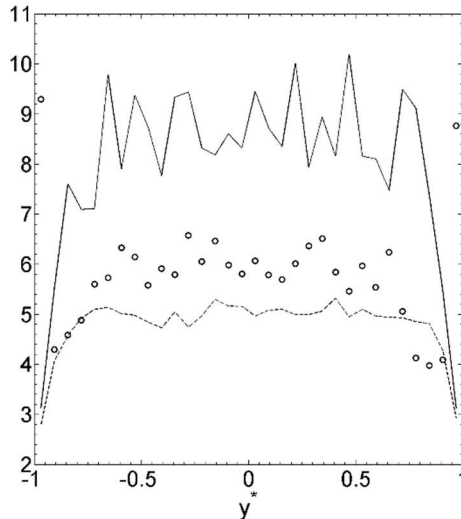
Figure 86: The proportion of deterministic collisions taking place across the channel which are not unique for three of the particle cases simulated in this study. —— case 1, - - - case 2, ○ case 3.

What can be observed in Figure 85 is a selection of collisions over 100 timesteps for a four-way coupled channel flow simulating case 1, where 0 represents the centre line of the flow in both the streamwise and wall normal directions, thus showing a scaled-up quarter of the total channel flow. The vast majority of collisions present in the visualisation form long lines or streaks which can be assumed to be roughly following the fluid streamlines in the x^* direction, given that this is the case with the lowest Stokes number particles. Given that this is also the case with the smallest particle volume fraction, it can be presumed that a given particle would take a comparatively long time to come in contact with another once isolated. What is occurring here, however, are multiple collisions occurring between the same particle pairs, and sometimes groups of particles. The multiple collision events are shorter and more chaotic near to the wall, but account for large numbers of collisions in the bulk flow region of the channel. It is these repeating collisions that cease to occur once agglomeration is implemented, thereby reducing the total number of collisions. It should be noted that the agglomeration efficiency in this case is very close to unity, with the majority of collisions resulting in the formation of a new agglomerate in all four cases studied.

The deterministic collision model correctly predicts the initial meeting and subsequent sequence of collisions between two particles caught in the same turbulent eddy. The implementation of agglomeration means that the same two particles might only collide once or twice before becoming a single isolated agglomerate. Each particle in the simulation has a specific numerical identity. These identities were compared for the duration of a short simulation to identify unique collisions, comparing the total number of collisions to the number of individual pairs of particles. Each collision between a pair of particles which has not collided before is considered a new, unique collision. Figure 86 shows the quantity of unique collisions to be nearly an order of magnitude smaller than the total number of

133

collisions for 3 of the cases studied, indicating that the vast majority of collisions are repeated between a smaller number of particle pairs. The number of repeated collisions actually scales down with the collision rate. This is because new unique collisions are more likely in a system with more or larger particles, an effect likely to interfere with the grouping of particles within turbulent eddies. The number of repeat collisions for each case concurs with the results in Table 5, with the number of additional collisions predicted for the non-agglomerated cases accounted for by the additional repeated collisions.

These conclusions about unique verses repeated collisions suggest an issue with using the DSMC based stochastic model that was developed in Chapter 5. Certainly the collision rate there was on a par with the deterministic rate in terms of quantity, but each collision resolved stochastically was performed between two random particles from within the same region, based on a particle response time calculated from the local dissipation rate. In its current state, a simulation using a stochastic agglomeration technique is likely to collide and accumulate particles at a greatly exaggerated rate, since it is hardly likely for the dissipation rate to change noticeably within the timeframe of particle collisions.

A simple simulation of agglomeration using the DSMC model in the smallest particle case was enough to confirm that this is indeed the case. No change to the collision rate occurred due to agglomeration being accounted for, and so the rate of agglomeration was many times greater than the deterministic model would predict, due to the repeated collision effect. A study by Wang et al. (2000) describes an accumulation effect taking place where small turbulent eddies cause particles to be distributed in a non-uniform manner, increasing the collision rate. This is arguably the same effect that causes the repeated collisions observed in this study. The latter paper describes equations for calculating the magnitude of this effect in different flow regions, and hence its influence on the particle collision rate across a given simulation. For the purposes of this study, modifications to the stochastic model are proposed and implemented such that the collision rate would be reduced by the magnitude of the accumulation effect, as described in the Chapter 3 Methodology. This approach will ideally reduce the collision rate, and hence the rate of agglomeration, to a more reasonable level. The results of this technique are assessed in the following sections.

6.2.2 300k, 100μm Particles (Case 1)

Figure 87 shows that the predicted mean streamwise velocity and the fluid and particle normal and shear stresses by themselves do not fully illustrate the issues under consideration here, with reasonable agreement observed between the deterministic and stochastic techniques. Figures 88 and 90 demonstrate that despite the modifications to the stochastic technique, agglomeration predicted by that technique remains high relative to that of the deterministic case, with significantly more agglomerates forming over the timescale of the simulations. This results, as shown in Figure 91, in both the average Stokes number of particles in the flow, and that of the largest particle present, predicted by the stochastic technique significantly exceeding values obtained from the deterministic approach

134
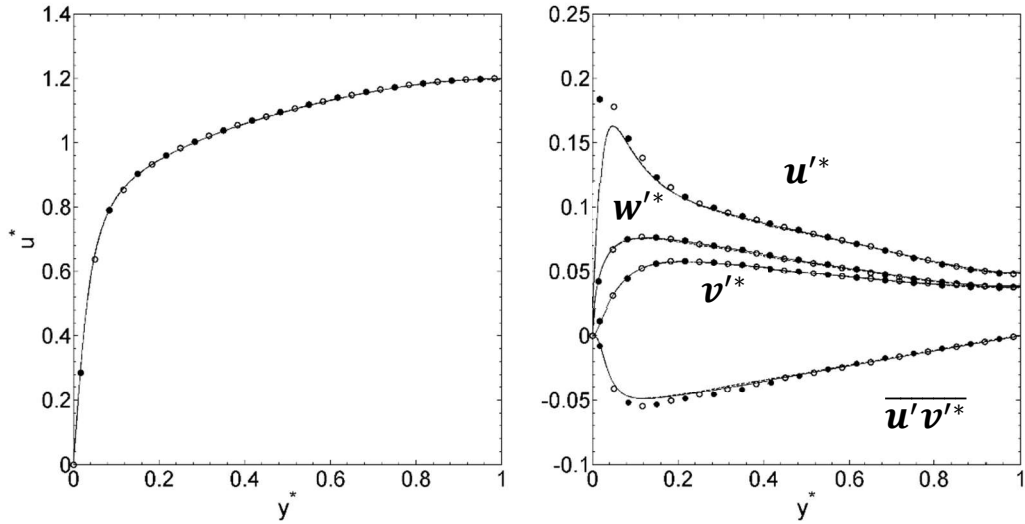
Figure 87: Compared mean streamwise velocities $\boldsymbol{u}^*$, and normal and shear stresses $\boldsymbol{u'}^*, \boldsymbol{v'}^*, \boldsymbol{w'}^*, \overline{\boldsymbol{u'v'}^*}$ for fluid flows with particles collided using deterministic and stochastic inter-particle collision techniques with agglomeration. With 300k, 100μm particles. —— Deterministic and - - - stochastic fluid, and particles with ● deterministic and ○ stochastic collisions with agglomeration.
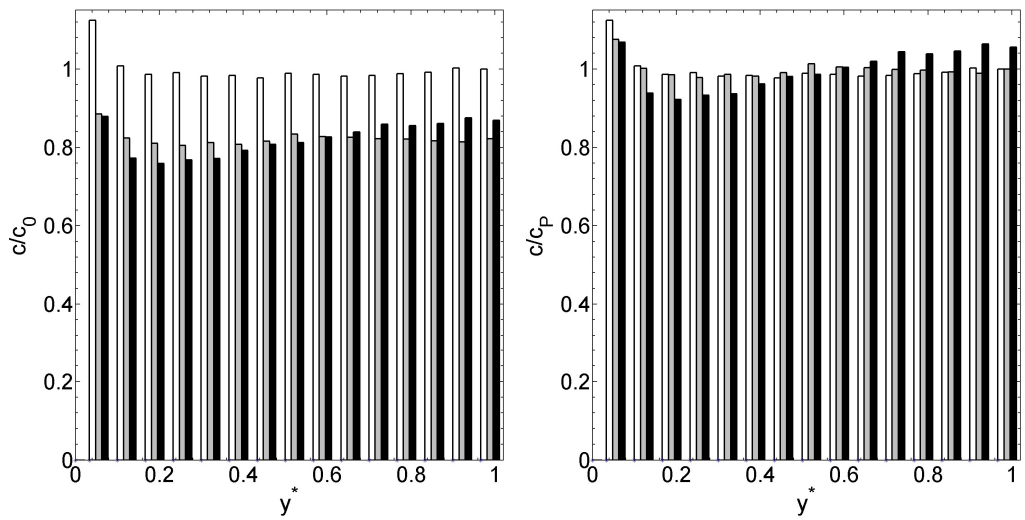
Figure 88: 300k, 100μm particle concentration (c/c₀), and concentration (c/cₚ) relative to total number of particles across the channel for four way coupled flows with □ no agglomeration, ▨ deterministic agglomeration, and ■ stochastic agglomeration.
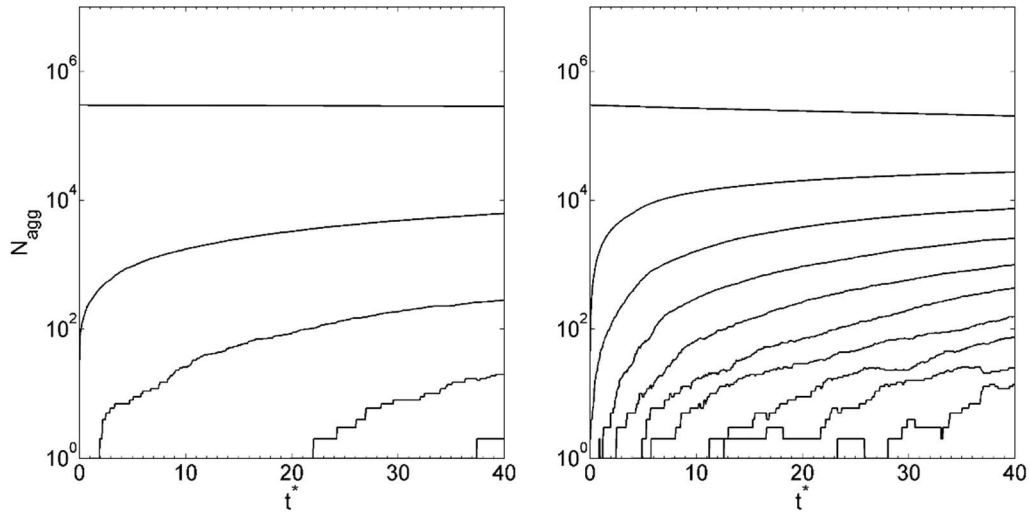
Figure 89: Number of differently sized agglomerates N_{agg} over time for agglomeration using deterministic (left) and stochastic (right) techniques for 300k, 100μm particles, for particles with sizes 1, 2, 3… 9 and 10, 15, … 50 (top to bottom).
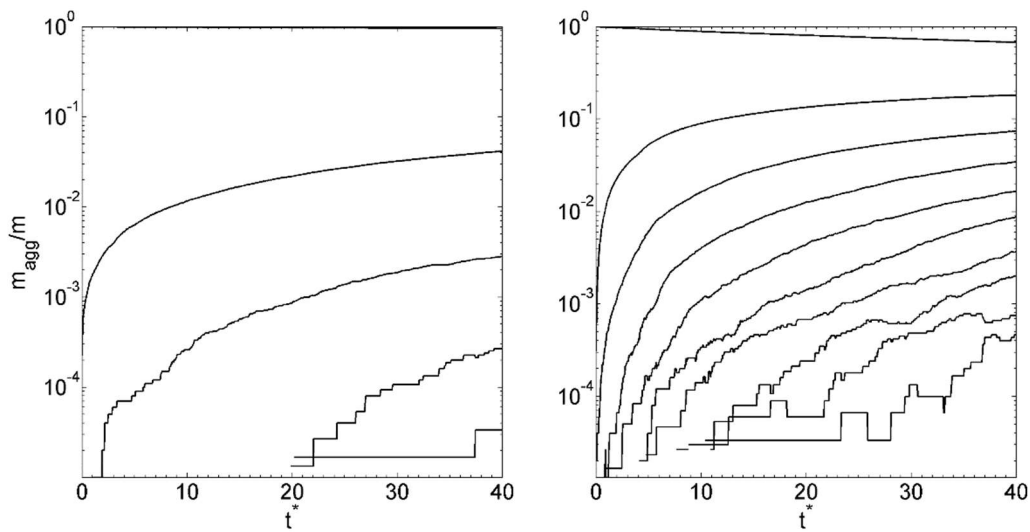
Figure 90: Compared mass of differently sized agglomerates relative to total mass of particles for deterministic (left) and stochastic (right) over time for 300k, 100μm particles, for particles with sizes 1, 2, 3 … 9 and 10, 15, … 50 (top to bottom).
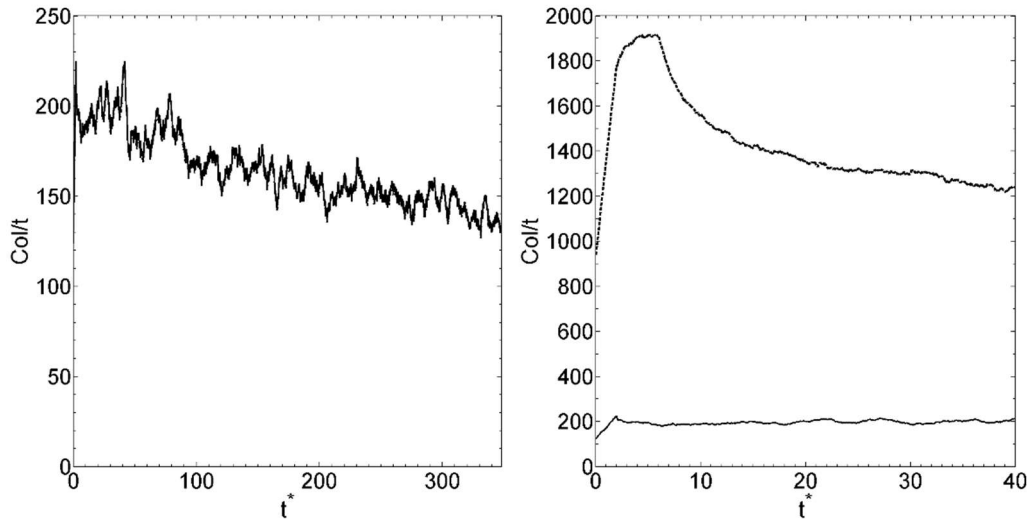
Figure 91: Average number of collisions over time for 300k, 100μm particles, deterministic (left) and deterministic versus stochastic (right). ⎯⎯ Deterministic, - - - stochastic.
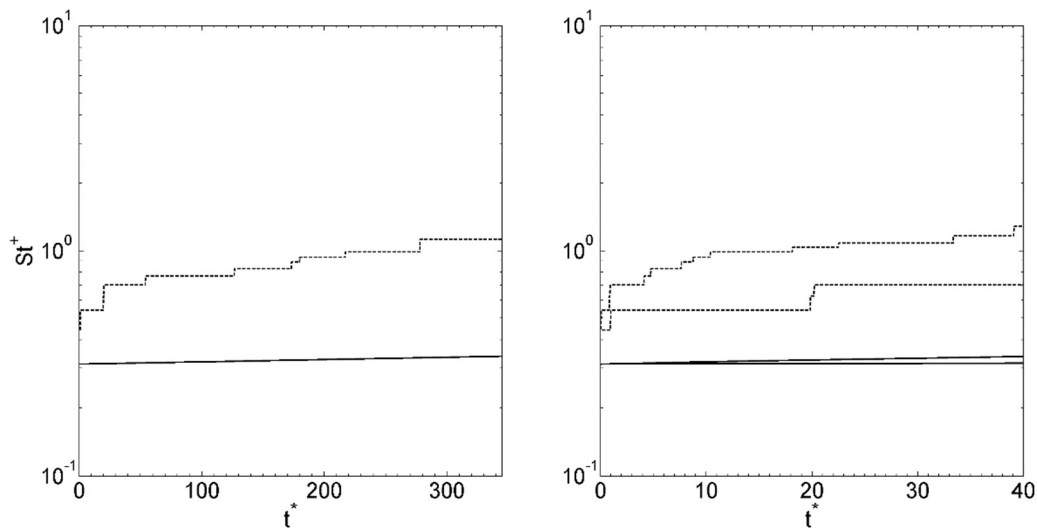
Figure 92: The mean turbulent Stokes number St^+ over time (⎯⎯) compared to the Stokes number of the largest particle present (- - -) for 300k, 100μm particles. Deterministic (left) and deterministic versus stochastic (right) – upper lines represent stochastic results.

Concentrations for the particles across the channel were taken at points in time with similar particle number totals for both the deterministic simulation with agglomeration, and the modified stochastic simulation with agglomeration, and are compared with those of the deterministic approach without agglomeration in Figure 88. The changes in distribution are not large in either of the cases with agglomeration, but the modified stochastic model displays slightly fewer particles near to the wall region. The quantity of particles near to the wall itself remains comparatively large for both methods of agglomeration, though in the stochastic case there is also a bias in particle concentration towards the bulk flow region. This resembles the distribution displayed by the higher Stokes number particles which was observed in Chapter 4, but the shape is slightly different, with the concentration gradually dropping and

137

then rising again near to the wall. The fact that there are more particles in the centre of the channel is counterintuitive, as the larger agglomerates would be expected to migrate towards the wall over time, however this can be explained by the fact that the DSMC technique shows a preference for collision near to the wall, where the dissipation rate is largest. There also may not have been sufficient time for the larger agglomerates to migrate towards the wall, which would counteract this effect.

Even with the modifications to the stochastic technique noted above, the collision rate for the stochastic model remains high, as shown in Figure 91, and, though it is not quite an order of magnitude higher, still significantly larger. For this case, however, the increases in collision rate and in the rate of agglomerate formation do not affect the overall statistics within the timescales considered. Note that the time scale itself is shorter for the stochastic case because agglomeration at the high rate predicted had a tendency to adversely affect the simulation itself. The algorithm which governs the two-way coupling in the simulation must regularly check when a particle moves from one cell to another, so cases like this where that happens frequently often require shorter timesteps to progress the simulation.

Both the DSMC stochastic and the deterministic methods of collision were shown in Chapter 5 to have uneven distributions of collisions, but the particle concentration remains fairly flat across the channel with deterministic agglomeration, showing that the increased collision rate towards the centre of the channel balances out the increased turbophoresis of larger agglomerates. This is evidently not the case for the DSMC where the highest rates of collision are near the wall region.

6.3.2 2.2M, 100μm particles (Case 2)

Though many more collisions have taken place and more agglomerates have formed in this case compared to case 1, with the first 9 particle agglomerate forming by $t^* = 1$, from the results shown in Figs. 94 through 98, the actual distribution of particles has not changed very much between the first two cases. Though flatter towards the bulk flow region (Figure 93), the concentration profile still shows the same decrease towards the wall for the stochastic case. Both the deterministic and stochastic simulations produced a significant number of agglomerates (Figs 95 and 96), albeit within considerably different lengths of time. The mean streamwise velocity and normal and shear stresses shown in Figure 93 seem almost as unaffected as they were in the lower concentration case. The stochastic particles are slightly faster in the streamwise direction, near to the bulk flow region, and both the particles and the fluid display smaller streamwise stresses in the bulk region. From what was observed in Table 5, the number of particles has a greater impact on the number of collisions. Larger but less numerous agglomerates, therefore, would have a similarly low incidence of collisions. This is observed across plots of the collision rate such as Figure 84, and in this case Figure 97, throughout this chapter. The rate does not decrease greatly over time for case 2, however, regardless of the simulation technique used. This may indicate the

need for a lengthier study, for in the low Stokes number cases the number of singlets, which is related to the collision rate, does not drop by a significant amount in the given timescale.
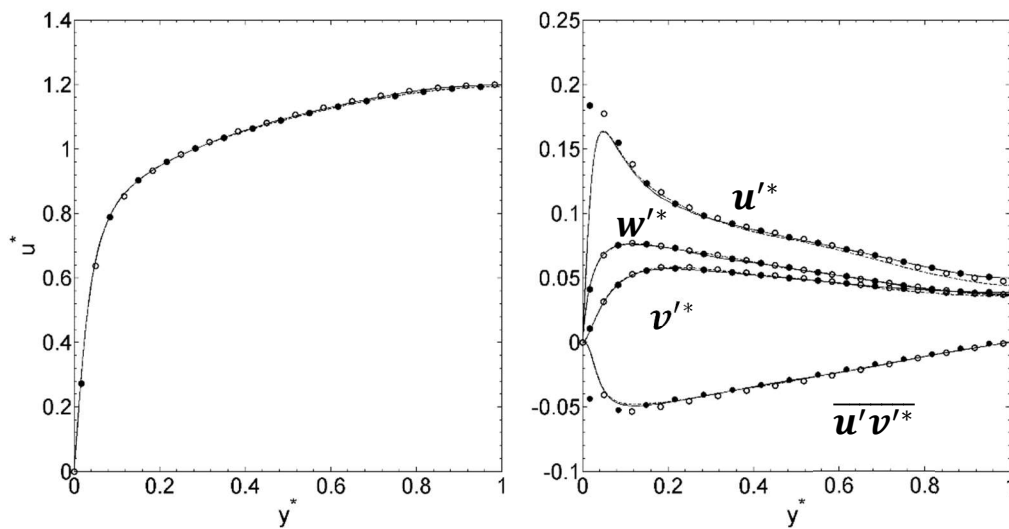
Figure 93: Compared mean streamwise velocities u^*, and normal and shear stresses $u'^*, v'^*, w'^*, \overline{u'v'^*}$ for fluid flows with particles collided using deterministic and stochastic inter-particle collision techniques with agglomeration. With 2.2M, 100μm particles. —— Deterministic and - - - stochastic fluid, and particles with ● deterministic and ○ stochastic collisions with agglomeration.
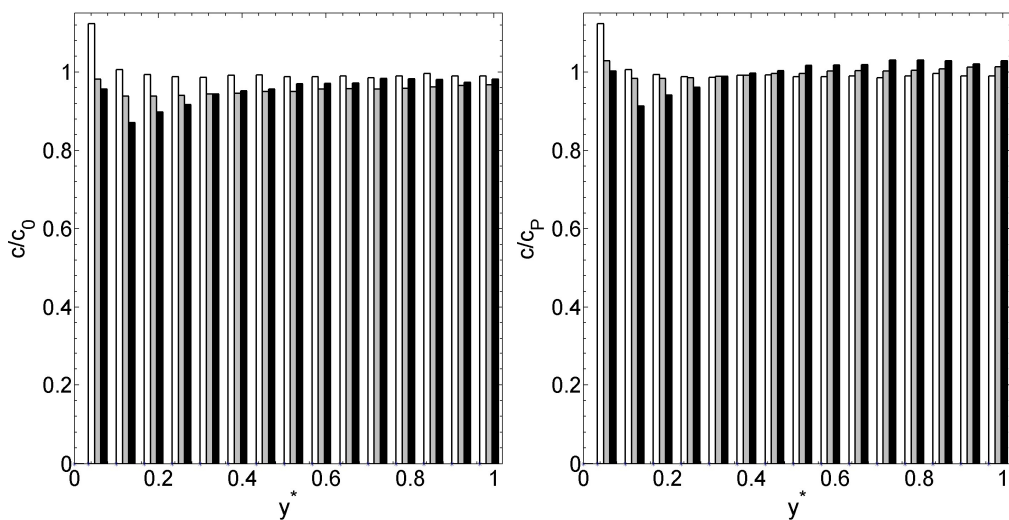
Figure 94: 2.2M, 100μm particle concentration (c/c₀), and concentration (c/cₚ) relative to total number of particles across the channel for four way coupled flows with □ no agglomeration, ▨ deterministic agglomeration, and ■ stochastic agglomeration.
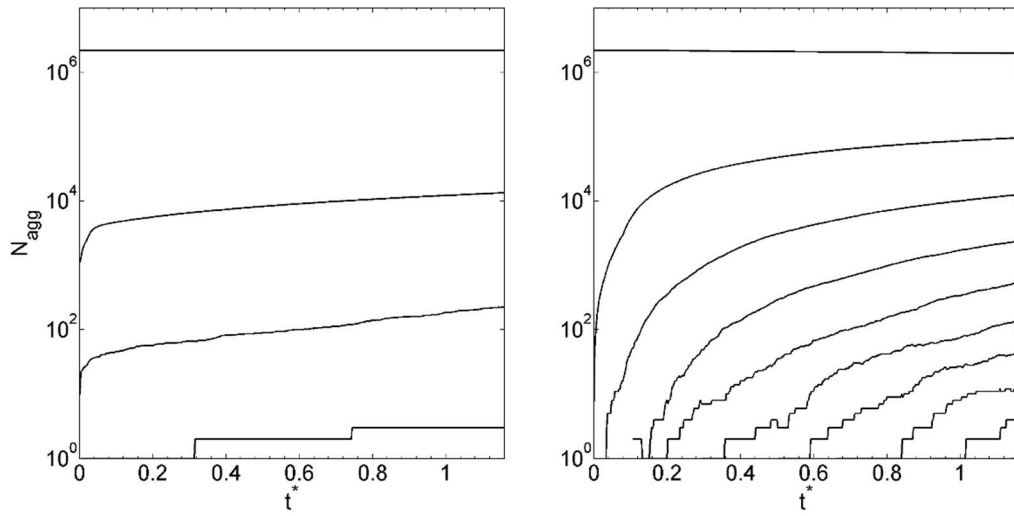
Figure 95: Number of differently sized agglomerates N_{agg} over time for agglomeration using deterministic (left) and stochastic (right) techniques for 2.2M, 100µm particles, for particles with sizes 1, 2, 3 … 9 and 10, 15, … 50 (top to bottom).
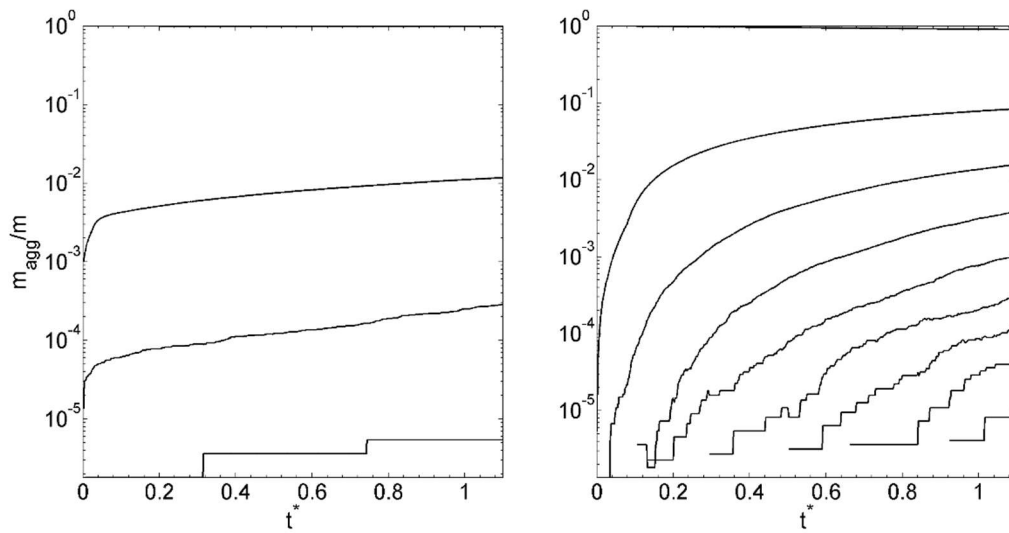
Figure 96: Compared mass of differently sized agglomerates relative to total mass of particles for deterministic (left) and stochastic (right) over time for 2.2M, 100µm particles, for particles with sizes 1, 2, 3 … 9 and 10, 15, … 50 (top to bottom).
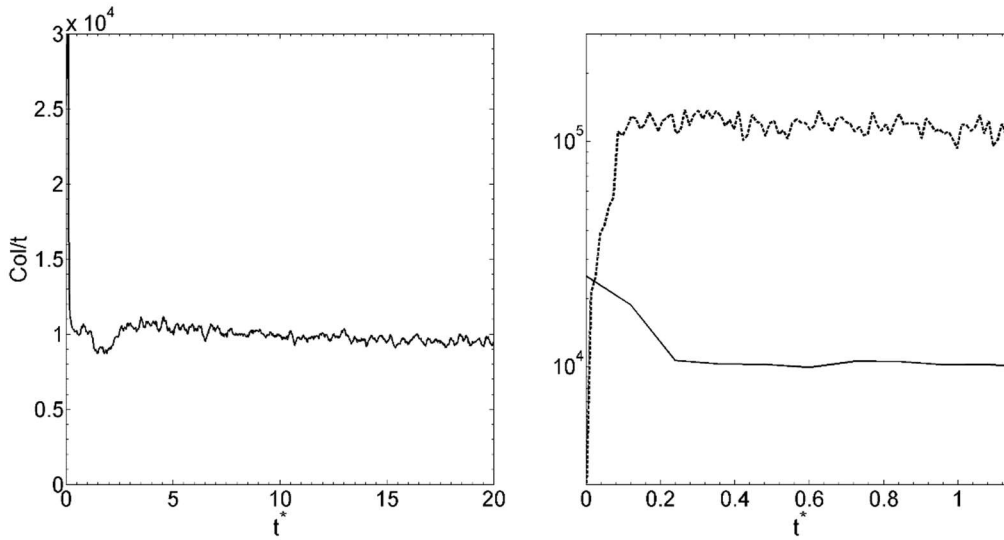
Figure 97: Average number of collisions over time for 2.2M, 100μm particles, deterministic (left) and deterministic versus stochastic (right). ⎯⎯ Deterministic, - - - stochastic.
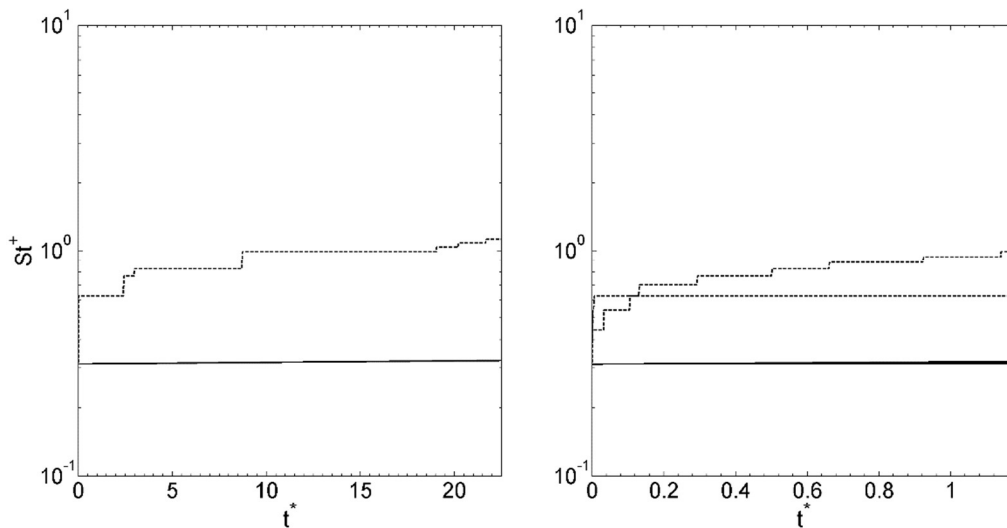
Figure 98: The mean turbulent Stokes number St^+ over time (⎯⎯) compared to the Stokes number of the largest particle present (- - -) for 2.2M, 100μm particles. Deterministic (left) and deterministic versus stochastic (right) – upper lines represent stochastic results.

The concentration profile for the deterministic technique has a peak near the wall, but like the stochastic case curves towards the centre of the channel. This is once again the same behaviour as for the higher Stokes number particles. Though this high concentration case was difficult to simulate indefinitely, given the high rate of agglomeration (Figs. 95 and 96), the similarity in particle distributions between the two low Stokes number cases simulated using both stochastic and deterministic techniques suggests that the shape is due to a combination of effects, i.e. the motion of particles between the bulk and wall regions, and the collision rate itself causing new large agglomerates to arise. It remains to be seen whether the particles

141

would settle into a flatter distribution over time, as is observed for the deterministically simulated agglomerates.

As for case 1, Figs. 95 and 96 again demonstrate that despite modification the stochastic approach again predicts a higher rate of agglomeration, with significantly more agglomerates formed, than for the deterministic case. Figure 98, which shows the change in the mean and maximum turbulent Stokes number in the particle phase over the course of the simulation, also shows that values predicted by the stochastic technique significantly exceed those obtained from the deterministic approach. In this case, however, neither the deterministic nor the stochastic technique shows any great change over time which explains the lack of effect over the timescale considered.

6.3.3 300k, 200μm particles (Case 3)

Case 3 covers an informative middle ground between the low concentration and high concentration cases studied previously in this section. Possessing a high collision rate, but a low particle concentration corresponding to a relatively short simulation time, information can be gathered regarding longer term development of the flow.
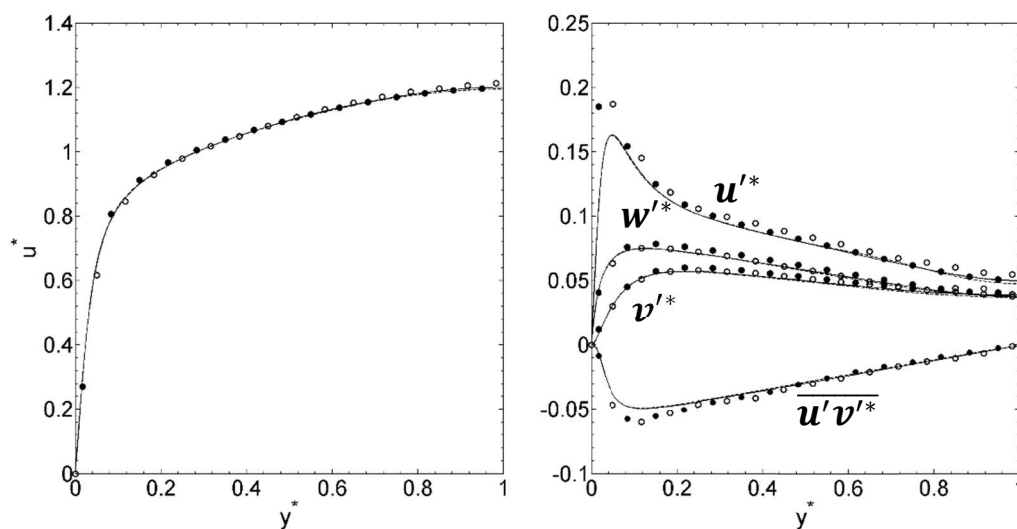
Figure 99: Compared mean streamwise velocities u^*, and normal and shear stresses $u'^*, v'^*, w'^*, \overline{u'v'}^*$ for fluid flows with particles collided using deterministic and stochastic inter-particle collision techniques with agglomeration. With 300k, 200μm particles. ⎯ Deterministic and - - - stochastic fluid, and particles with ● deterministic and ○ stochastic collisions with agglomeration
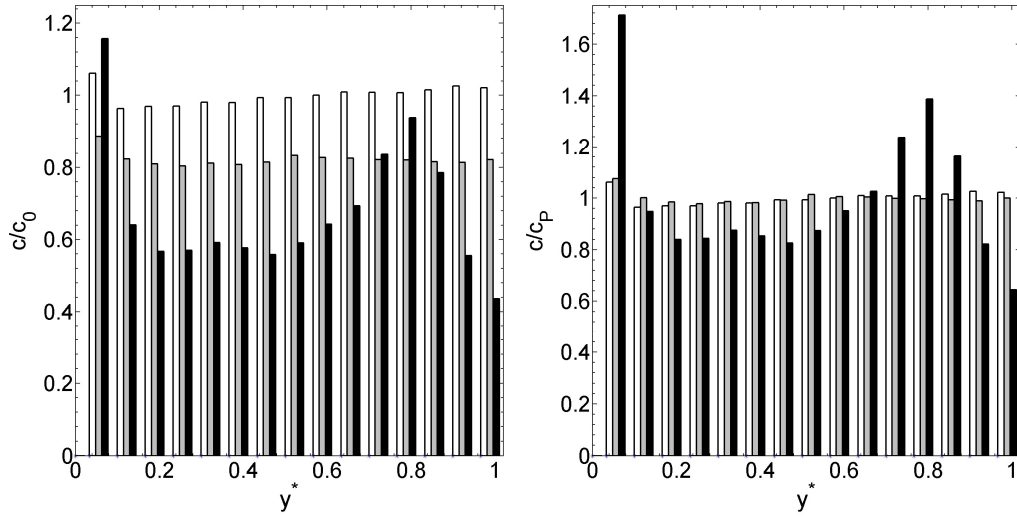
Figure 100: 300k, 200μm particle concentration (c/c_0), and concentration (c/c_P) relative to total number of particles across the channel for four way coupled flows with □ no agglomeration, ▨ deterministic agglomeration, and ▪ stochastic agglomeration.
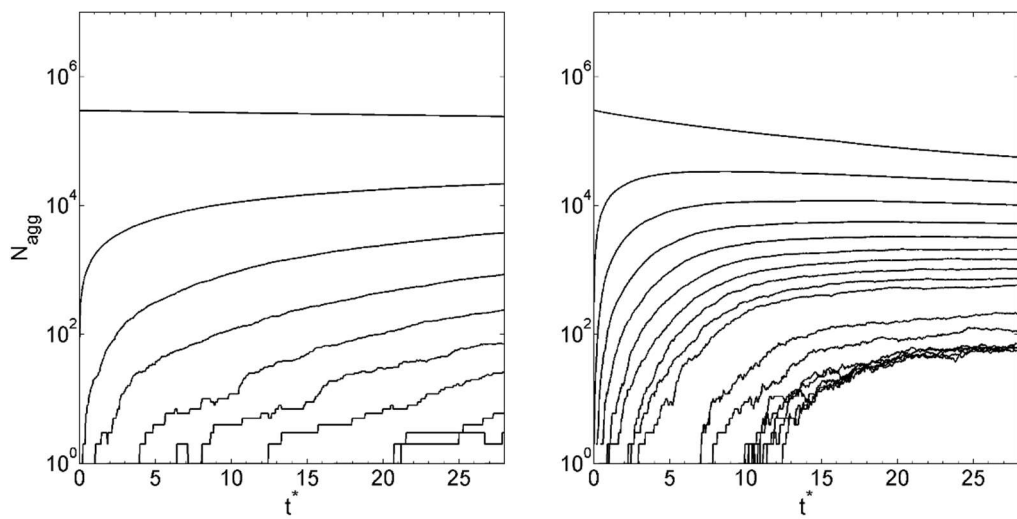
Figure 101: Number of differently sized agglomerates N_{agg} over time for agglomeration using deterministic (left) and stochastic (right) techniques for 300k, 200μm particles, for particles with sizes 1, 2, 3 … 9 and 10, 15, … 50 (top to bottom).
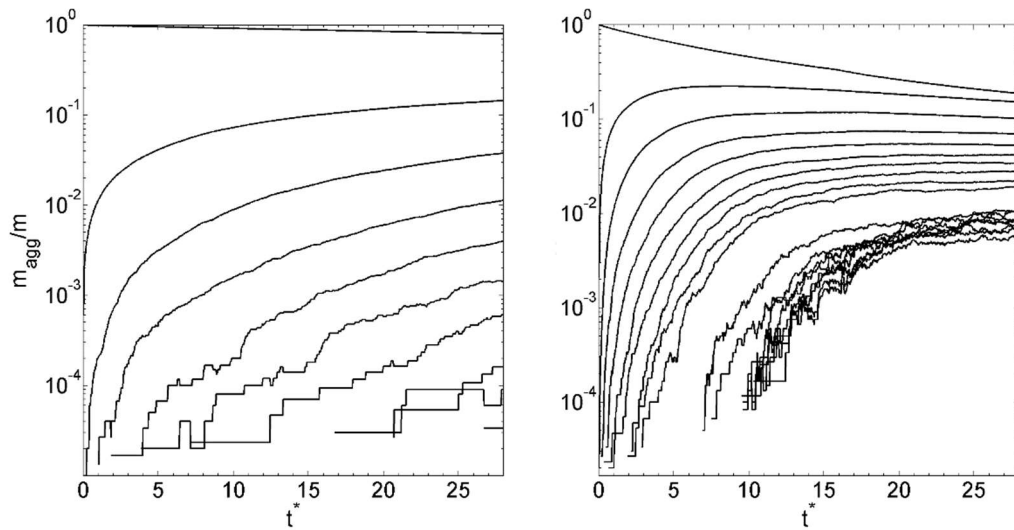
Figure 102: Compared mass of differently sized agglomerates relative to total mass of particles for deterministic (left) and stochastic (right) over time for 300k 200μm particles, for particles with sizes 1, 2, 3… 9 and 10, 15, … 50 (top to bottom).
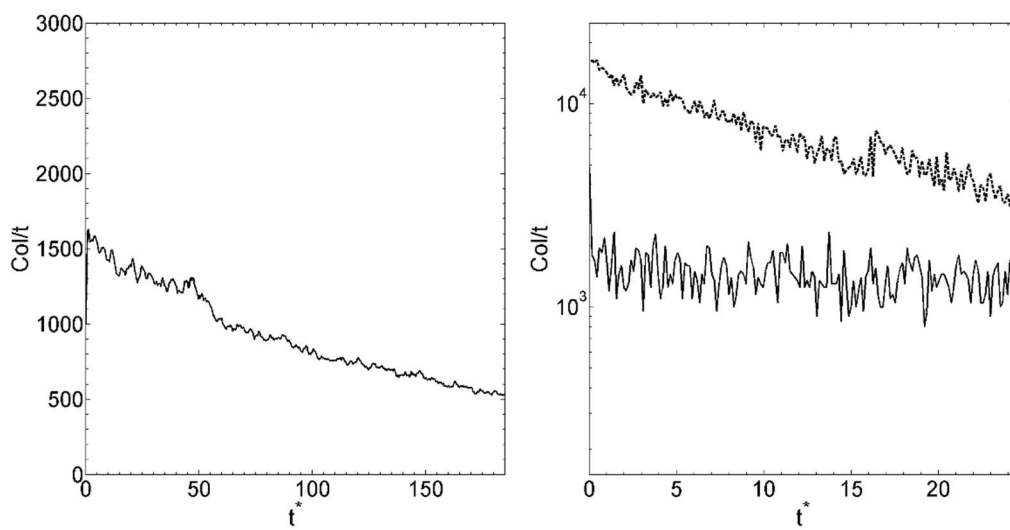
Figure 103: Average number of collisions over time for 300k, 200μm particles. deterministic (left) and deterministic versus stochastic (right). —— Deterministic, - - - stochastic.
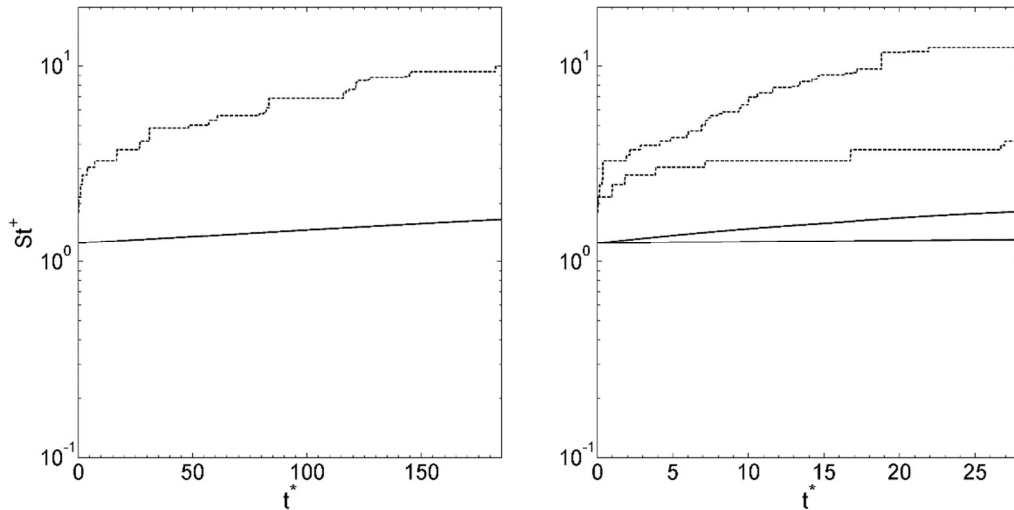
Figure 104: The mean turbulent Stokes number St^+ over time (——) compared to the Stokes number of the largest particle present (- - -) for 300k, 200μm particles. Deterministic (left) and deterministic versus stochastic (right) – upper lines represent stochastic results.

The collision rate in Figure 103, for example, drops rapidly for both techniques, though of course more so for the stochastic approach, which starts an order of magnitude higher but drops to around twice that of the deterministic results. Large agglomerates are quickly formed (Figures 101 and 102) in the stochastic case, forcing the flow to respond, in this case (Figure 99) increasing the bulk mean streamwise velocity, and the streamwise normal stresses together with the shear stress in parts of the flow. The normal stresses in the other two coordinate directions are, however, slightly reduced. Otherwise, the influence of the stochastic technique generally relates to a faster production of agglomerates. The very fast production of very large particles in the centre of the channel produces a dip in concentration (Fig. 94) as these particles are pushed towards the wall by turbophoresis. This effect is visibly larger for this case than it has been in the previous ones, even for the high Stokes particles, though it is notable that there is still a second peak near to the bulk flow region as well as one near the wall. The particle distribution for the deterministic simulation remains flat by comparison. Despite this, the mean turbulent Stokes number does not even double over the timeframe for either simulation technique (Figure 104), which implies that changes to the state of the flow as a whole go hand in hand with this more long term effect.

6.3.4 2.2M, 200μm particles (Case 4)

The largest case in terms of volume fraction clearly has the greatest collision rate, however the actual amount of overestimation produced by the stochastic technique remains similar to previous cases, and barely an order of magnitude more (Figure 109) than the deterministic predictions. This would undoubtedly pose a greater problem were the fluid a less dominant part of the system, such as in the case used for validation in Chapter 4, Marchioli and Soldati (2007), which used flyash in air. In that situation, however, the higher Stokes number would cause more ballistic collisions and would require a stochastic model based more on kinetic

theory than that used in the present work. For these cases which assume calcite particles in water, the increased agglomeration rate does not affect the overall statistics of the flow a great deal. That said, this high volume fraction case understandably makes for an exception. As with the stochastic method considered in Chapter 5 which used fictional particles, the greatly increased collision rate shown here has increased the particle normal stresses across the channel, with emphasis on the bulk region of the flow (Figure 105). Similarly, the mean streamwise velocity has been reduced.
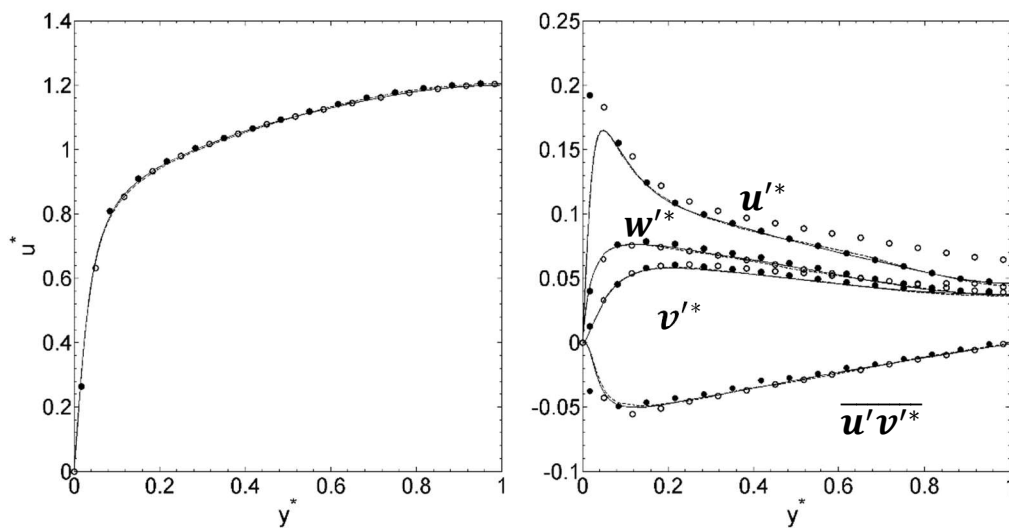
Figure 105: Compared mean streamwise velocities u^*, and normal and shear stresses $u'^*, v'^*, w'^*, \overline{u'v'}^*$ for fluid flows with particles collided using deterministic and stochastic inter-particle collision techniques with agglomeration. With 300k, 200μm particles.
—— Deterministic and - - - stochastic fluid, and particles with ● deterministic and ○ stochastic collisions with agglomeration.
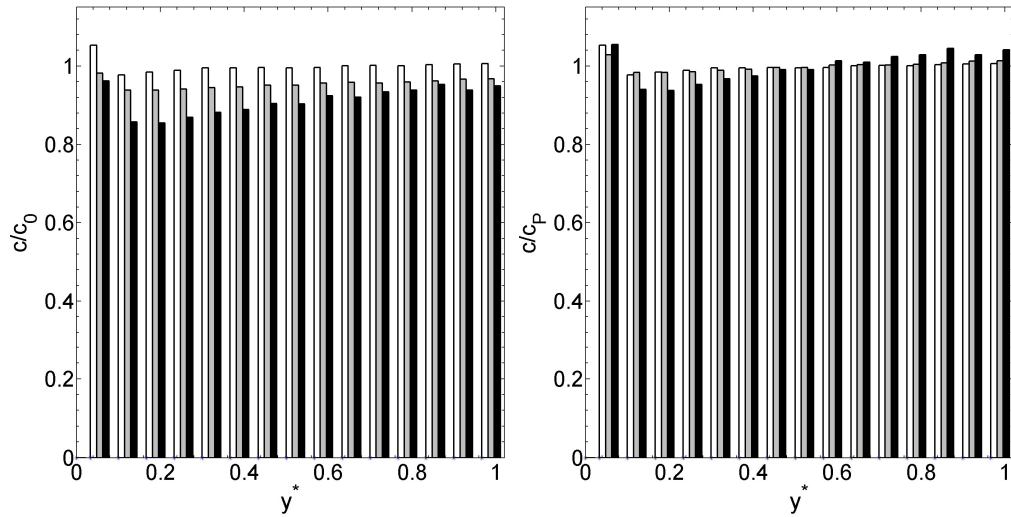
Figure 106: 2.2M, 200μm particle concentration (c/c₀), and concentration (c/cₚ) relative to total number of particles across the channel for four way coupled flows with □ no agglomeration, ▣ deterministic agglomeration, and ◼ stochastic agglomeration.
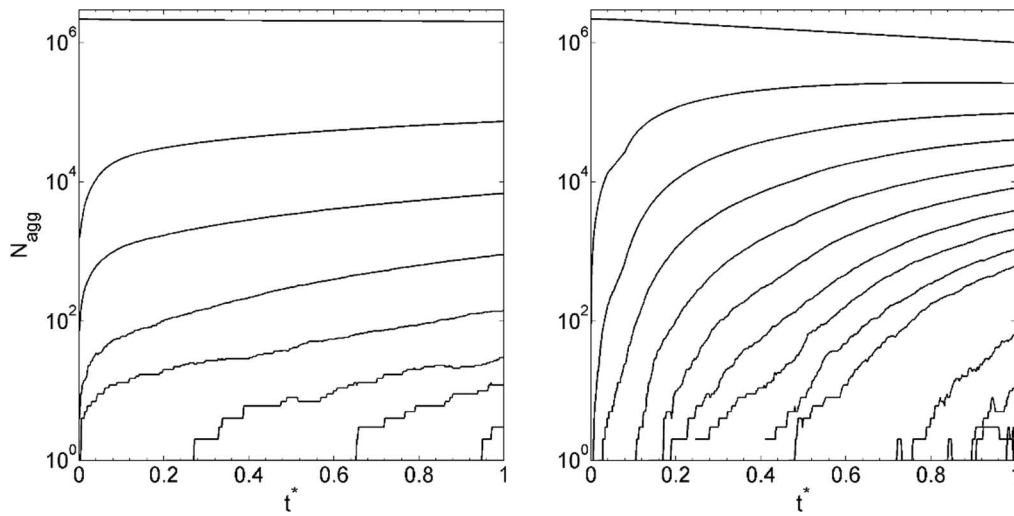
Figure 107: Number of differently sized agglomerates N_{agg} over time for agglomeration using deterministic (left) and stochastic (right) techniques for 2.2M, 200μm particles, for particles with sizes 1, 2, 3… 9 and 10, 15, … 50 (top to bottom).
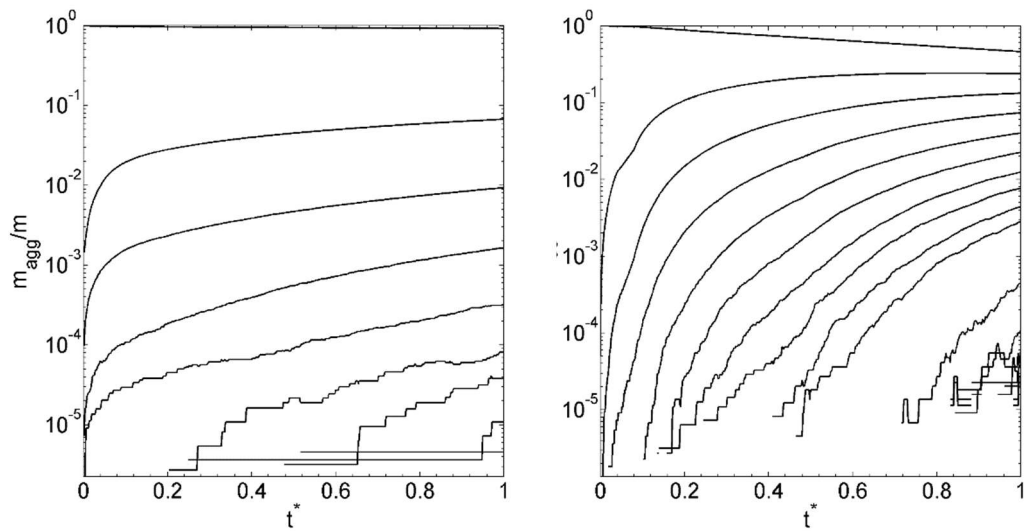
Figure 108: Compared mass of differently sized agglomerates relative to total mass of particles for deterministic (left) and stochastic (right) over time for 2.2M, 200μm particles, for particles with sizes 1, 2, 3… 9 and 10, 15, … 50 (top to bottom).
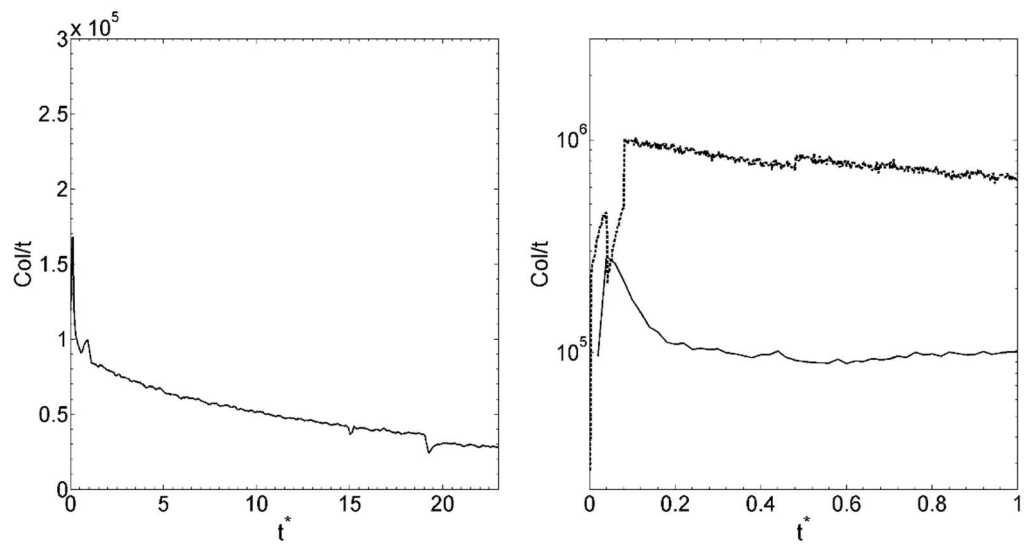
Figure 109: Average number of collisions over time for 2.2M, 200μm particles. deterministic (left) and deterministic versus stochastic (right). —— Deterministic, - - - stochastic.
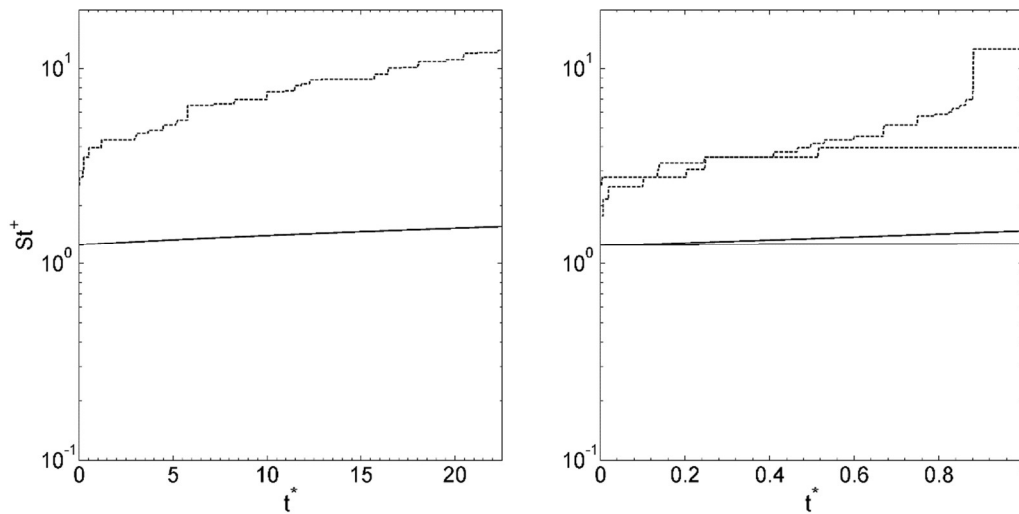
Figure 110: The mean turbulent Stokes number St^+ over time (——) compared to the Stokes number of the largest particle present (- - -) for 300k, 200μm particles. Deterministic (left) and deterministic versus stochastic (right) – upper lines represent stochastic results.

Comparing this set of results to those of case 3 with the lower concentration of particles suggests that the key factor is one of timescale. The distribution of particles across the channel (Figure 106), taken at points where the particle concentrations were similar between the two agglomeration techniques, shows the dip near to the wall, but retains the rise towards the centre of the channel of the channel observed in most of the high Stokes number cases. However, the shape completely changes over a longer timescale, as shown in Figure 100. Large particles are expected to migrate outwards over time, but in high concentration cases this movement may well be arrested by the action of smaller particles. Either the reduction of the number of single particles, or a lower limit on particle size, allows turbophoresis to go unchecked. For case 3, in both the deterministic and stochastic cases, the mass of singlets drops to less than 10% of the original (Figs 107 and 108). The stochastic technique forces an enhanced rate of agglomeration, potentially faster than the process of turbophoresis can move the particles outwards in the flow, which would explain the peculiar shape of the distribution in Figure 100, and this is perhaps due to it being in some kind of transitional state. For case 4, the distribution is still approaching that transitional state, and hence qualitatively is similar to that of cases 1 and 2. At a certain point, the maximum Stokes number in Figure 110 for the stochastic technique spikes on the right hand plot. The observations of Figure 107 suggest that at this point large agglomerates are being produced which are rapidly colliding and growing further. A particle such as that may agglomerate multiple times in a single timestep, which is what is being observed here.

Table 8: Comparison of deterministic and stochastic techniques for computational time and collision rate (four-way coupled, with agglomeration)[*].

	Test Case					
	1	**2**		**3**	**4**	
Technique	**300k, 100µm particles**	**2.2M, 100µm particles**		**300k, 200µm particles**	**2.2M, 200µm particles**	
Deterministic run time, no agglomeration	2.26	19.36		2.27	18.61	
Deterministic run time	2.43	32.68	17.75 [*2]	3.09	39.86	25.09 [*2]
Deterministic collisions/t[*]	214	10,299		1,707	220,020	
Stochastic run time	2.19	13.41[*2]		2.53	14.73[*2]	
Stochastic collisions/t[*]	1,895	72,862		15,291	263,725	

[*]Simulation times are normalised by the time taken for the one-way coupled simulation with 300k, 100µm particles covered in Chapter 4.

[*2]Simulations carried out with 0.1x shorter timestep, normalised in the same way.

The increase in compute time for the simulations when agglomeration is accounted for is quite dramatic, particularly where the particle concentration is high, as shown in Table 8. This is presumably the result of increasingly large agglomerates travelling within the channel, without regard to fluid effects, and undergoing comparatively rapid turbophoresis. The reduction in run time produced by the stochastic technique is also quite considerable, but in this case with agglomeration that may simply be due to the rapid reduction in particle numbers due to the enhanced collision rate, which was earlier noted to facilitate the production of agglomerates at a rate faster than the rate at which turbulent transport effects occur. For the stochastic cases with larger particles, the rate of collision was sufficiently high that the simulations required shorter timesteps, making it impossible to obtain meaningful measurement of the computational time necessary on the same basis as was done for the other cases. The difference between the stochastic and deterministic runtimes is more dramatic with the shorter timeframe, since the slowing effects of turbophoresis are reduced but the inter-particle collision step is consistent between the simulation rates.

6.4: Conclusions

In this chapter research was reported that allows understanding of how the effects of agglomeration affect the statistics of the channel flow. Agglomeration was implemented for each of the four particle-fluid cases, as considered in the previous chapter. The rate of agglomeration as well as the particle collision rate over time were investigated as part of this. The relatively low particle/fluid density ratio for these channel flows meant that the overall effects of agglomeration on the channel flow properties were not especially large, except in the highest volume fraction case. In that case the streamwise velocity fluctuations were impeded near to the centre of the channel, an effect similar to that predicted by Zhao et al. (2015) was caused by high inertial particles near to the wall. In this case the central bulk region of the channel maintains a relatively high concentration of particles, which would enhance the production of agglomerates, since the observations of Chapter 5 show the collision rates of the deterministic model to be high in that region. It is suggested that newly formed large agglomerates are impeded from travelling towards the wall, despite the actions of turbophoresis, because of the number of single particles present in the channel which offer more of an obstacle to the larger particles.

It is also noted that the collision rate for all cases, which drops over time, is strongly correlated with the number of single particles, with only the highest volume fraction case being the exception to that rule, where the collision rate begins to level out as the larger sized agglomerates increase in quantity such that they account for more of the collisions. For the high Stokes number cases, the agglomeration progresses to the point where particles with sizes greater than 1 start to decrease in number. Analysis of how the collision rate is affected by particle volume fraction, particle number, and particle radius, show both particle volume fraction and particle number play a significant role, both being correlated directly with the collision rate. It is discovered that the implementation of agglomeration causes a significant drop in the collision rate. This drop was found to be caused by the effect of repeated collisions, where pairs or groups of particles remain in the same flow region and collide multiple times over consecutive timesteps. This effect was found to be most dominant away from the wall region, but nonetheless accounted for the majority of collisions in the version of the model without agglomeration. In order to develop a stochastic version of the agglomeration technique, this effect needed to be taken into account.

By calculating the accumulation effect using the methodology of Wang et al. (2000), a version of the stochastic technique was developed that predicted fewer collisions per unit time, in an attempt to develop a stochastic agglomeration model that would match the collision reduction displayed by the deterministic technique. Despite the modifications, the model overpredicted the rate of collision by a significant amount, although this amount was still significantly less than what would have been displayed by the unaltered model. The enhanced rate of collision allowed for an analysis on how the agglomeration rate and the turbophoretic motion of particles interacted. The unaltered deterministic technique showed fairly flat distributions of particles, aside from the peaks at the wall, implying that the new

agglomerates were travelling away from the bulk flow region at a rate similar to their rate of formation. Results from the DSMC stochastic version of the agglomeration technique implied that agglomerates which formed in the central region do not respond instantaneously to turbophoresis, and a sufficiently high rate of agglomeration, or a sufficiently high number of particles, form uneven particle distributions which change over time. Potentially, the implementation of a breakup model, or analysis of the system over a longer period of time, would provide more elucidation of these effects. Nevertheless, the stochastic technique demonstrates the potential to accurately simulate flows with a particularly high particle volume fraction. There are indications that such techniques work well, not least the fact that the technique tested here did not lose accuracy even as the volume fraction increased.

7.0 Conclusions

7.1 Conclusions

An in-depth assessment into the efficiency of various particle-laden flow simulation techniques has been performed. The intention of the study was to develop knowledge surrounding the best approaches to use for accurately predicting two-way coupling, particle collisions and agglomeration using direct numerical simulation and Lagrangian particle tracking. These techniques have been tested, and further adapted in novel ways, specifically the implementation of stochastic methods of inter-particle collision and agglomeration which were adjusted for greater effectiveness in wall-bounded flows where two-phase CFD is employed. The ability to produce DNS benchmark results for a variety of cases quickly and efficiently improves the progress of development of more pragmatic CFD techniques used in industry, such as Reynolds-averaged Navier-Stokes modelling and to a lesser extent large eddy simulation, a pre-requisite for understanding the many practical particle-laden flows which arise as part of nuclear waste transport and decommissioning programmes. It is worthy of note that the decontamination and clean-up of legacy nuclear facilities are pressing issues that the UK government recognises as a national priority.

The computational power required to perform CFD of turbulent flows tends to be proportional to the turbulent Reynolds number of the flow being studied, a problem for DNS in particular, since this involves resolution of the fluid dynamics taking place at even the smallest (Kolmogorov) length scales. When computational operations extend to calculations across multiple dimensions, simply doubling the Reynolds number can increase the computational cost elevenfold. To alleviate this, modern codes use parallel computations to reduce the timescales associated with simulation steps. This study employed the fully-parallelised spectral element-based DNS solver, Nek5000, that is both efficient, open-source, and therefore adaptable.

The baseline case this solver was used to simulate was a turbulent channel flow with a shear Reynolds number of 300. This is a relatively uncommon case, based on those studied in the literature, and has complex properties, being on the turbulent edge of the transitional Reynolds numbers. The works of both Morinishi and Tamano (2005) and Marcholi and Soldati (2007) were used to validate the model, and the element mesh was designed with the parameters of the latter study in mind. The resulting simulations showed excellent agreement with these previous works.

The computational particle-laden channel flow study by Marcholi and Soldati (2007) was also used to validate the Lagrangian particle tracker which runs concurrently with Nek5000. This solver employs the fourth order Runge-Kutta algorithm to calculate the trajectories and velocities of the given particles, taking into consideration the forces of drag, lift, virtual mass, and pressure gradient. It is also capable of modelling the effects of particle-fluid interaction (two-way coupling) and deterministic interparticle collisions (four-way coupling), as well as

153

particle agglomeration. The results from the use of LPT for the three particle classes, $St^+ = 1, 5, 25$, which were simulated in the Marchioli and Soldati (2007) paper were, like the fluid phase predictions, also in good agreement.

In the first main results chapter, Chapter 4, initial investigations were made into four cases where the effects of particle numbers and radii were compared. The density ratio between the particles and the fluid was chosen to be equivalent to glass beads in water. Assuming a channel height of 0.02 metres, the particle classes used would have diameters of 100μm and 200μm, which were injected into a previously settled turbulent flow in quantities of either 300k or 2.2M particles. These simulations were performed at one-way, two-way and four-way levels of coupling. It was determined that at a shear Reynolds of 300, there is a discernible effect on the behaviour of the fluid and particles produced by changing the amount of coupling simulated; small decrements in turbulence when higher levels of coupling were used, and changes in the near-wall concentration which depended on the particle size. These effects were not very large in any of the four cases, however, since the two particle sizes used both possessed shear Stokes numbers close to or below unity, a result which is in agreement with previous findings.

The effects of turbophoresis were apparent for all four cases, and enhanced for the cases with higher Stokes numbers and accounting for two-way coupling. In general, particles would migrate towards and preferentially concentrate close to the channel wall, though the distribution of particles across the wall-normal direction of the channel was fairly uniform overall. The results from the simulations that employed two-way and four-way coupling highlighted the importance of particle-particle coupling for channel flows of this nature, in order to capture additional effects not present in the one-way coupled cases. Turbophoresis was enhanced for the two-way coupled cases compared to the one-way coupled cases, but was suppressed somewhat when four-way coupling was implemented, due to the high near-wall collision rate having a tendency to mix particles back into the bulk of the flow, as reported by Kuerten (2016). Two-way coupling may, therefore, be appropriate in cases with a lower rate of collision than has been reported here.

Increasing the number of particles in the channel had a significant effect on the computational cost of the simulation, with both the two-way and four-way coupling algorithms contributing to large increases in the computing timeframe. An unexpected effect was that the suppression of turbophoresis caused by simulating particle-particle interactions impacted on the number of particles leaving their fluid cells which sometimes resulted in a shorter overall runtime. In some cases, the reduction in the number of operations caused by this was more than the total number of operations required to perform the interparticle collision step. To reduce the computational complexity and runtime requirements of the four-way coupling model, stochastic techniques were investigated and implemented, aiming to further reduce the operations required to simulate interparticle effects for this channel flow.

Two stochastic techniques were considered initially, one which generates fictional particles as potential collision partners based on the instantaneous local particle conditions, and the direct simulation Monte Carlo method, which instigates collisions between pre-existing particles in the local region. For low particle concentrations, both techniques produced acceptable results in terms of the particle concentration, mean streamwise velocity, and normal and shear stresses for the simulations when compared to predictions of the deterministic approach. However, the fictional particle technique drastically overestimated the RMS velocity fluctuations for the higher Stokes number particles, whilst the DSMC technique produced results closer in agreement with the deterministic approach.

Analysis of the collisions being predicted by these techniques indicated that a high number of overly energetic collisions were being predicted by the fictional particle technique. The DSMC technique, while superior in many respects such as collision rate and the shear stresses predicted, produced the same issue to a lesser degree and for a different reason. The fictional particle technique was found to be generating collision partners with a high variance of velocity, which increased as the collider velocity increased, to the point that particles with very high and even negative velocities were being generated. The DSMC approach on the other hand was instigating collisions between high speed and low speed particles at a rate that was significantly above what was expected. All this considered, the fictional particle technique performed an adequate job of simulating low speed collisions, and the high speed collisions produced by the DSMC were as expected. Neither model was completely effective at producing interparticle collision distributions similar to those observed in a deterministic four-way coupled simulation. For those, the correlation between the velocities of colliding particles was very high, with a dependency on the Stokes number of the particles. Larger Stokes numbers led to a wider distribution, with particles of differing velocities colliding with each other more frequently. The collision inaccuracies of the DSMC technique bore a resemblance to those of a particle with an arbitrarily high Stokes number.

Since the DSMC technique was still the superior stochastic method, it was used as a foundation for further development. Improvements were made to it in order to make the approach more appropriate for use in generic wall-bounded flows, such as the channel flow case considered in this work. These improvements were based on the notion that particle and fluid properties were generally consistent across the length of the channel. Previous works by such as Pawar et al. (2014) discussed the necessity of a sufficiently large statistical selection of particles when the DSMC technique was being used. Previously, the searching scopes used to select particles were not only insufficiently large, but also crossed between flow regions, which promoted the selection of high speed particles as collision partners for low speed ones. The proposed technique improvements selected the particles from large streamwise orientated channel slices. This not only resolved the statistical sample size problem, but since these new sample regions were narrow enough in the wall-normal dimension, the fluid region crossing problem was also solved. The results for this technique in terms of normal and shear stresses and particle concentration across the channel were not markedly better than those

from the unaltered DSMC, but the distribution and number of collisions was in much better agreement with the deterministic simulations. It was also generally faster, except for in the highest volume fraction case, where the overprediction of collision rate was qualitatively large, which caused the simulation to slow down.

In realistic situations the previous interparticle model of purely hard sphere collisions does not always apply. DVLO theory is a broad approach to the treatment of van der Waals attraction and electric double-layer Coulombic repulsion forces that exist between particles. These forces between the particles are at times adhesive, causing them to form agglomerates, which vary the particle Stokes number, effective radius, and hence the subsequent dynamics. The significance this has on the properties of the fluid and particle flow was assessed in the final results chapter, Chapter 6. Outside of the highest volume fraction case, agglomeration using the deterministic approach had only a small impact on the channel flow fluid phase properties. Furthermore the expected increase to the effect of turbophoresis due to increases in the mean Stokes number did not occur, most likely due to the increased collision rate associated with larger particles causing their movement towards the wall to be disrupted. This is similar to the observation made earlier of four-way coupling dampening turbophoresis. The change in the number of agglomerates over time as well as the collision rate were also analysed, with the collision rate remaining proportional to the number of singlet particles throughout the simulation.

Expecting that the process of agglomeration would add additional compute time to the simulations, an attempt was made to apply the stochastic technique of inter-particle collision developed earlier to particle agglomeration. It was determined that the stochastic DSMC technique would not suffice in its current state. The reduction in the number of collisions did not correspond to volume fraction, particle number, or particle radius, all factors the stochastic technique considered when calculating collision probability. Investigation into the deterministic model showed that the cause was a repeat collision effect which occurred when particles trapped close to the same streamwise orientated streamlines would collide over and over, increasing the recorded collision rate. Given the high aggregation efficiency for the case with agglomeration, these collisions would not exist once agglomeration was implemented. The stochastic technique, once applied to agglomeration, would effectively be still performing these repeat collisions despite the occurrence of agglomeration.

Further adjustments made to the stochastic technique were based on calculations of the accumulation effect proposed by Wang et al. (2000). The probability of a collision was reduced based on these values to produce a technique which ultimately still overpredicted the collision rate by a significant amount, but which was smaller than the one anticipated assuming a rate matching the DSMC technique without modification. The results from this technique were still of interest despite the inaccuracy. For instance, the rate of agglomeration speed-up affected the distribution of the particles because they were now no longer being redistributed across the channel at the same rate as their rate of formation. The nature of the

over-time effects that were produced with the implementation of agglomeration and the stochastic techniques open new avenues for research. This study was intended to examine the simulation techniques themselves and their relation to both the computational time and the accuracy of results, so the final stochastic agglomeration model produced still represents a step forward. Though it was not so effective as desired, the stochastic technique still had the intended effect of reducing the computational cost, which means that any further improvements to the technique in terms of increased accuracy will come with a net benefit.

7.2 Recommendations for Further Work

This study was based around analysis of various simulation techniques, and how different fluid and particle cases affected both their accuracy and their efficiency. However, the present work was limited to consideration of a single fluid-particle system, modifying only particle radius and particle number in accordance with the dispersion of glass beads in water. There are many alternative cases that are worthy of consideration using the techniques developed here, such as the glass particles in air, as studied by Mortimer et al. (2019). Zhao et al. (2015) also described many near-wall and turbulence effects caused by an increase in Stokes number which were not immediately apparent in the current study, but would be expected in cases using such higher Stokes number particles. Further studies for a wider range of Stokes numbers would therefore also be beneficial.

Further, higher Stokes number situations would require the employment of a stochastic technique that employs kinetic theory. Arguably, the higher Stokes number case from this study had sufficient kinetic properties to warrant some aspects of kinetic theory in the equations used for probability. Wilkinson et al. (2006), for instance, employed a technique applying both advective and kinetic considerations to the problem. A more thorough test to find the Stokes number regions where kinetic theory and advective theory are most effective, and most redundant, would be beneficial. Particularly, an assessment of whether different variations of a channel flow affect this boundary, since previous authors have recorded success in using various stochastic collision techniques outside of a channel flow.

In addition, the LPT code used in this study has been developed such that the implementation of non-spherical particles can be considered. Non-spherical particles are known to have significant effects on flow turbulence which deviate from those caused by spherical particles. It is feasible to analyse these effects using the same techniques used in this study. Furthermore, collisions between elliptical particles take more operations than a standard spherical particle model due to the necessity to know both the shape and orientation at point of impact, so the development of a stochastic technique for such cases would be of great value.

The repeated collision effect discussed in the last chapter merits further observation as well. Its existence was only so significant in this study because the agglomeration efficiency was close to unity. Studies with different materials, and lower agglomeration efficiencies, would

potentially reduce the change between the models with or without agglomeration. Collision handling that uses techniques besides the hard sphere model would also be interesting to investigate. Considering breakup as a factor is part of the agglomeration model that was neglected for this study, but again, the techniques developed here have the potential to be employed for a model that considers both particle agglomeration and breakup. Determining how all of these factors affect a deterministic agglomeration model is an important step towards developing a model that can predict the same behaviour through use of a stochastic method.

Lastly, in this project methodologies were developed using DNS, and LPT, such that fluid flow benchmark problems could be subsequently studied to give much needed predictions to compare existing, more pragmatic predictive methods against. This approach was undertaken due to the absence of reliable experimental data in flow geometries of academic and industrial interest. However, with improving measurement capabilities, e.g. phase Doppler anemometry, it is now possible to measure the distribution of particle statistical size and velocity moments in a fluid flow, as well as particle concentration and local size-velocity correlations. There remains a pressing requirement for detailed and reliable experimental data that can be used to validate the types of model studied in this work, and well as being of value in elucidating the dynamics of particle-laden flows.

8.0 References

Abrahamson J. Collision rates of small particles in a vigorously turbulent fluid. Chemical Engineering Science, 30, pp. 1371-1379, (1975).

Afkhami M., Hassanpour A., Fairweather M., Njobuenwu D.O. Fully coupled LES-DEM of particle interaction and agglomeration in a turbulent channel flow. Computers & Chemical Engineering Volume 78, pp. 24-38, (2015).

Adams J. F. W. Particle Deposition, Dispersion and Re-suspension Behaviour in Turbulent Square Duct and Circular Pipes Flows. PhD dissertation University of Leeds, (2011).

Aly A. M. M., Trupp A. C., and Gerrard A. D. Measurements and prediction of fully developed turbulent flow in an equilateral triangular duct. Journal of Fluid Mechanics, 85(1), pp. 57-83, (1978).

Bagchi P. and Balachandar S. Effect of turbulence on the drag and lift of a particle. Physics of Fluids. 15(11), pp. 3496-3513, (2003).

Balachandar S. and Maxey M. Methods for evaluating fluid velocities in spectral simulations of turbulence. Journal of Computational Physics. 83(1), pp. 96-125, (1989).

Berg J. M., Romoser A., Banerjee N., Zebda R., Sayes C. M. The relationship between pH and zeta potential of 30 nm metal oxide nanoparticle suspensions relevant to in vitro toxicological evaluations. Nanotoxicology 3(4), pp. 276-283, (2009).

Bird A. Molecular Gas Dynamics and Direct Simulation of Gas Flow. Clarendon Press: Oxford, (1976)

Boersma B. J. Direct numerical simulation of turbulent pipe flow up to a Reynolds number of 61,000. Journal of Physics: Conference Series, 318(4), (2011).

Boivin M., Simonin, O. and Squires K.D. Direct numerical simulation of turbulence modulation by particles in isotropic turbulence. Journal of Fluid Mechanics. 375, pp. 235-263, (1998).

Brenner H. The Stokes resistance of an arbitrary particle. Chemical Engineering Science, 18(1), pp. 1-25, (1963).

Brenner H. The Stokes resistance of an arbitrary particle-II: An extension. Chemical Engineering Science, 19(9), pp. 599-629, (1964).

Brenner H. The Stokes resistance of an arbitrary particle-III: Shear fields. Chemical Engineering Science, 19(9), pp. 631-651, (1964).

Brenner H. The Stokes resistance of an arbitrary particle-IV: Arbitrary fields of flow. Chemical Engineering Science, 19(10), pp. 703-727, (1964).

Breuer M., Alletto M., and Flow F. Efficient simulation of particle-laden turbulent flows with high mass loadings using LES. International Journal of Heat and Fluid Flow, 35, pp. 2-12, (2012).

Breuer M. and Almohammed N. Modeling and simulation of particle agglomeration in turbulent flows using a hard-sphere model with deterministic collision detection and enhanced structure models. International Journal of Multiphase Flow. 73, pp. 171-206, (2015).

Brundrett, E. and Baines, W.D. The Production and Diffusion of Vorticity in Duct Flow. Journal of Fluid Mechanics. 19(3), pp. 375-394, (1964).

Caraman N., Borée J., Simonin O. Effect of collisions on the dispersed phase fluctuation in a dilute tube flow: experimental and theoretical analysis. Phys. Fluids, 15(12), pp. 3602-3612, (2003).

Chakravarti A., Patankar N. A., and Panchagnula M. V. Aerosol transport in a breathing alveolus. Physics of Fluids 31, (2019).

Cenedese A., Costantini A., and Romano, G. P. LDA spectral measurements in a turbulent boundary layer. Experimental Thermal and Fluid Science, 5(3), pp. 281-289, (1992).

Cenedese A., Romano G. P., and Di Felice F. Experimental testing of Taylor's hypothesis by L.D.A. in highly turbulent flow. Experiments in Fluids, 11, pp. 351-358, (1991).

Clark J. A. A Study of Incompressible Turbulent Boundary Layers in Channel Flow. J. Basic Eng 90(4), pp. 455-467, (1968).

Clift R., Grace J. R., and Weber M. E., Bubbles, Drops and Particles. Courier Corporation (2005).

Coleman G. N., Sandberg R. D. A Primer on Direct Numerical Simulation of Turbulence – Methods, Procedures and Guidelines. Technical Report AFM-09/01a (March 2010), (2010).

Crowe, C., Gore, R. and Troutt, T. Particle dispersion by coherent structures in free shear flows. Particulate Science and Technology. 3(3-4), pp. 149-158, (1985).

Crowe C., Sommerfeld M., and Tsuji Y. Multiphase flows with particles and droplets. CRC Press, New York, (1998).

Crowe, C.T. Multiphase flow handbook. CRC press. (2005).

Dandy D. S., Dwyer H. A. A sphere in shear flow at finite Reynolds number: effect of shear on particle lift, drag, and heat transfer. Journal of Fluid Mechanics 216, pp. 381-410, (1990).

Deardorff J. W. A numerical study of three-dimensional turbulent channel flow at large Reynolds numbers. Journal of Fluid Mechanics, 41(2), pp. 453-480, (1970).

Demuren A. O., and Rodi W. Calculation of turbulence-driven secondary motion in non-circular ducts. Journal of Fluid Mechanics, 140(Mar), pp. 189-222 (1984).

Denslow K. M., Bontha J. R., Adkins H. E., Jenks J. WJ., Burns C. A., Schonewill, Philip P., Hopkins D. F., Thien M. G., and Wooley T. A. Continued Evaluation of the Pulse-Echo Ultrasonic Instrument for Critical Velocity Determination during Hanford Tank Waste Transfer Operations. Waste Management Symposium (WM 2012), Paper No. 12518, (2012).

Derjaguin B. and Landau, L. Theory of the stability of strongly charged lyophobic sols and of the adhesion of strongly charged particles in solutions of electrolytes. Acta Physicochim: USSR, 14(6), pp. 633-662, (1941).

Dritselis C.D. and Vlachos N.S. Numerical study of educed coherent structures in the near-wall region of a particle-laden channel flow. Physics of Fluids. 20(5), 055103 (2008).

Durst F., Melling A., and Whitelaw J.H. Principles and practice of laser-Doppler anemometry. NASA STI/Recon Technical Report A. 76, (1976).

Eckelmann H., The structure of the viscous sublayer and the adjacent wall region in a turbulent channel flow. Journal of Fluid Mechanics 65(3), pp. 439-459, (1974).

Eggels J.G.M., Westerweel J., Nieuwstadt F.T.M., and Adrian R.J. Direct numerical simulation of turbulent pipe flow. Applied Scientific Research, 51(1-2), 319-324, (1993).

Eggels J., Unger F., Weiss M., Westerweel J., Adrian R., Friedrich R., and Nieuwstadt F. Fully developed turbulent pipe flow: a comparison between direct numerical simulation and experiment. Journal of Fluid Mechanics, 268, pp. 175-210, (1994).

Efremenkov V.M. IAEA Bulletin, 4 (1989), pp. 37-42, (1989).

Einstein A. Eine neue Bestimmung der Moleküldimensionen. Annalen der Physik, 19, pp. 289-306, (1896), corrected in 34, pp. 591-592, (1911).

El Khoury G.K., Schlatter P., Noorani A., Fischer P.F., Brethouwer G., and Johansson A.V., Direct Numerical simulation of turbulent pipe flow at moderately high Reynolds numbers. Flow, Turbulence and Combustion 91, pp. 475-495, (2013).

Elghobashi S. Particle-laden turbulent flows: direct simulation and closure models. Applied Scientific Research. 48(3-4), pp. 301-314, (1991).

Elghobashi S. On predicting particle-laden turbulent flows. Applied Scientific Research, 52(4), pp. 309-329, (1994).

Elghobashi S. An Updated Classification Map of Particle-Laden Turbulent Flows. In: IUTAM Symposium on Computational Approaches to Multiphase Flow: Proceedings of an IUTAM

Symposium held at Argonne National Laboratory, October 4-7, 2004: Springer Science & Business Media, p.3, (2007).

Fairweather M., and Hurn J.-P. Validation of an anisotropic model of turbulent flows containing dispersed solid particles applied to gas–solid jets. Computers & Chemical Engineering, 32(3), pp. 590-599, (2008).

Fairweather M. and Yao J. Mechanisms of particle dispersion in a turbulent, square duct flow. AIChE Journal, 55(7), pp. 1667-1679, (2009).

Farmer, R.A. Liquid droplet trajectories in two-phase flow. Thesis, Massachusetts Institute of Technology, (1969).

Fessler J. R., Kulick J. D., and John K Eaton. Preferential concentration of heavy particles in a turbulent channel flow. Physics of Fluids, 6(11). pp. 3742-3749, (1994).

Fischer P.F., Lottes J.W., and Kerkemeier S.G. Nek5000. http://nek5000.mcs.anl.gov, (2008).

Forney L.J. and Spielman L.A. Deposition of coarse aerosols from turbulent flow. Journal of Aerosol Science, 5(3), pp. 257-271, (1974).

Friedlander, S. and Johnstone, H. Deposition of suspended particles from turbulent gas streams. Industrial & Engineering Chemistry, 49(7), pp. 1151-1156, (1957).

Gavrilakis S. Numerical simulation of low-Reynolds-number turbulent flow through a straight square duct. Journal of Fluid Mechanics, 244, pp. 101-129, (1992).

Gessner F. B. and Jones J. B. On some aspects of fully-developed turbulent flow in rectangular channels. Journal of Fluid Mechanics, 23, pp. 689-713, (1965).

Gessner F.B., Po J.K., and Emery A.F. Measurements of developing turbulent flow in a square duct. Turbulent Shear Flows I, pp. 119-136, Springer Berlin Heidelberg, (1979).

Grigoriadis D. G. E. and Geurts B. J. Reduced turbophoresis in two-way coupled particle-laden flows. Direct and Large-Eddy Simulation VIII (Springer, 2011) pp. 207–212, (2011)

Gnanamanickam E. P., Nottebrock B., Große S., Sullivan J. P., and Schröder W. Measurement of turbulent wall shear-stress using micro-pillars. Measurement Science and Technology, Volume 24, Number 12, (2013)

Graham J., Kanov K., Yang X. I. A., Lee M., Malaya N., Lalescu C. C., Burns R., Eyink G., Szalay A., Moser R. D., Meneveau C. A Web services accessible database of turbulent channel flow and its use for testing a new integral wall model for LES. Journal of Turbulence, 17, 12, (2016)

Grant I. Particle image velocimetry: a review. Proceedings of the Institution of Mechanical Engineers, Part C: Journal of Mechanical Engineering Science, 211(1), pp. 55-76. (1997).

Grigoriadis D.G.E., Geurts B.J. Reduced turbophoresis in two-way coupled particle-laden flows. In: Kuerten H., Geurts B., Armenio V., Fröhlich J. (eds) Direct and Large-Eddy Simulation VIII. ERCOFTAC Series, vol 15, Springer, Dordrecht. (2011)

Große, S. and Schröder W. Dynamic wall-shear stress measurements in turbulent pipe flow using the micro-pillar sensor MPS 3. International Journal of Heat and Fluid Flow, 29(3), pp. 830-840. (2008).

Guha D., Ramachandran P.A., and Dudukovic M.P. Flow field of suspended solids in a stirred tank reactor by Lagrangian tracking. Chemical Engineering Science, 62(22), pp. 6143-6154. (2007).

Hill R.J. Models of the scalar spectrum for turbulent advection. Journal of Fluid Mechanics, 88(3), pp. 541-562 (1978).

Hinsch K.D. Holographic particle image velocimetry. Measurement Science and Technology, 13(7), pR61. (2002).

Hoagland L.C. Fully developed turbulent flow in straight rectangular ducts: secondary flow, its cause and effect on the primary flow. Thesis, Massachusetts Institute of Technology. (1962).

Höhne T., Krepper E., Rohde U. Application of CFD Codes in Nuclear Reactor Safety Analysis, Science and Technology of Nuclear Installations. Volume 2010, Article ID 19875, (2010).

Holmén V. Methods for vortex identification. Thesis, Lund University (2012).

Ilori T.A. Turbulent deposition of aerosol particles inside pipes. Thesis, University of Minnesota, (1971).

Jeffery G. B. The motion of ellipsoidal particles immersed in a viscous fluid, Proceedings of the Royal Society of London, Ser. 102, pp. 161-179 (1922).

Johnson P.L. Predicting the impact of particle-particle collisions on turbophoresis with a reduced number of computational particles. International Journal of Multiphase Flow, 124, p. 103182, (2020).

Kajishima T. and Miyake Y. A discussion on eddy viscosity models on the basis of the large eddy simulation of turbulent flow in a square duct. Computers & Fluids, 21(2), pp .151-161, (1992).

Kiger K. and Pan C. Suspension and turbulence modification effects of solid particulates on a horizontal turbulent channel flow. Journal of Turbulence, 3(19), pp. 1-17. (2002).

Kim J., Moin P., and Moser R. Turbulence statistics in fully developed channel flow at low Reynolds number. Journal of Fluid Mechanics, 177, 133-166, (1987).

Kolmogorov A. AN Kolmogorov, Dokl. Akad. Nauk SSSR 30, 301 (1941). In: Dokl. Akad. Nauk SSSR, p.301, (1941).

Kreplin HP. and Eckelmann H. Behavior of the three fluctuating velocity components in the wall region of a turbulent channel flow. Physics of Fluids, 22(7), (1979).

Kruis F.E., Kusters K.A. The collision rate of particles in turbulent flow. Chemical Engineering Communications, 158(1), pp. 201-230, (1997).

Kuerten J.G.M. Point-particle DNS and LES of particle-Laden turbulent flow - a state-of-the-art review. Flow, Turbulence and Combustion, 97(3), pp. 689-713 (2016).

Kuerten J.G.M. and Vreman A.W. Can turbophoresis be predicted by large-eddy simulation? Phys. Fluids, 17(1), 011701, (2005).

Kuerten J.G. and Vreman A. Effect of droplet interaction on droplet-laden turbulent channel flow. Physics of Fluids, 27(5), p053304, (2015).

Kulick J., Fessler J., Eaton J. Particle response and turbulence modification in fully developed channel flow. Journal of Fluid Mechanics, 277, pp. 109-134, (1994).

Kussin J., Sommerfeld M. Experimental studies on particle behaviour and turbulence modification in horizontal channel flow with different wall roughness, Experiments in Fluids, 33(1), pp. 143-159 (2002).

Laufer J. Investigation of turbulent flow in a two-dimensional channel – Thesis, California Institute of Technology. (1950).

Laufer J. The structure of turbulence in fully developed pipe flow. National Advisor Committee for Aeronautics. p1174. (1954).

Launder B. E. and Ying W. M. Secondary flows in ducts of square cross-section. Journal of Fluid Mechanics, 54, pp. 289-295, (1972).

Lee S.L. and Durst F. On the motion of particles in turbulent duct flows. International Journal of Multiphase Flow, 8(2), pp. 125-146, (1982).

Lee I.B., Pascual J., Hong S.W., Seo I.H., Kwon K.S., Bartzanas T. et al. The past, present and future of CFD for agro-environmental applications. Computers and Electronics in Agriculture, 93, pp. 168-183, (2013).

Lee J. and Lee C. Modification of particle-laden near-wall turbulence: Effect of Stokes number. Physics of Fluids. 27(2), p023303. (2015).

Li A. and Ahmadi G. Dispersion and deposition of spherical particles from point sources in a turbulent channel flow. Aerosol Science and Technology, 16(4), pp. 209-226, (1992).

Li A., Ahmadi G., Bayer R. G., and Gaynes M. A. Aerosol particle deposition in an obstructed turbulent duct flow. Journal of Aerosol Science, 25(1), pp. 91-112, (1994).

Li J., Wang H., Liu Z., Chen S., and Zheng C. An experimental study on turbulence modification in the near-wall boundary layer of a dilute gas-particle channel flow. Experiments in Fluids. 53(5), pp. 1385-1403, (2012).

Li Q., Song J., Li C., Wei Y., and Chen J. Numerical and experimental study of particle deposition on inner wall of 180° bend. Powder Technology. 237, pp.241-254, (2013).

Li Y., McLaughlin J.B., Kontomaris K., Portela L. Numerical simulation of particle-laden turbulent channel flow, Physics of Fluids, 13(10), pp. 2957-2967, (2001).

Lin J.T. Velocity spectrum of locally isotropic turbulence in the inertial and dissipation ranges. The Physics of Fluids, 15(1), pp. 205-207, (1972).

Liu B. Y. H. and Agarwal, J. K. Experimental Observation of Aerosol Deposition in Turbulent Flow. Journal of Aerosol Science, 5, pp. 145-155, (1974).

Longmire E.K., Khalitov D.A. and Pothos S. Experiments on Turbulent Particle-Laden Flows. Energy and Environment. Springer, pp. 221-238, (2001).

Loth E. Numerical approaches for motion of dispersed particles, droplets and bubbles. Progress in Energy and Combustion Science 26, pp. 161-223, (2000).

Lund E. Mean flow and turbulence characteristics in the near corner region of a square duct. University of Washington., (1977).

Madabhushi R.K. and Vanka, S. Large eddy simulation of turbulence-driven secondary flow in a square duct. Physics of Fluids A: Fluid Dynamics, 3(11), pp. 2734-2745 (1991).

Maday Y., Patera A. Spectral element methods for the Navier–Stokes equations, Noor, A.K. (ed.) State of the Art Surveys in Computational Mechanics ASME, pp. 71-143, (1989)

Marchioli C., Giusti A., Salvetti M.V., and Soldati, A. Direct numerical simulation of particle wall transfer and deposition in upward turbulent pipe flow. International Journal of Multiphase flow, 29(6), pp. 1017-1038. (2003).

Marchioli C. and Soldati A. Mechanisms for particle transfer and segregation in a turbulent boundary layer. Journal of Fluid Mechanics, 468, 283-315, (2002).

Marchioli C. and Soldati A. Reynolds number scaling of particle preferential concentration in turbulent channel flow, Advances in Turbulence XI, Springer 162 Proceedings in Physics, 117, 298-300. (2007).

Marchioli C., Soldati A., Kuerten J., Arcen B., Taniere A., Goldensoph G., Squires K., Cargnelutti M., and Portela L. Statistics of particle dispersion in direct numerical simulations of wall-bounded turbulence: Results of an international collaborative benchmark test. International Journal of Multiphase Flow, 34(9), pp. 879-893. (2008).

Marchioli C., Fantoni M., and Soldati A. Orientation, distribution, and deposition of elongated, inertial fibers in turbulent channel flow. Physics of Fluids, 22, 033301 (2010).

Maxey M.R. and Riley J.J. Equation of motion for a small rigid sphere in a nonuniform flow. The Physics of Fluids, 26(4), pp. 883-889. (1983).

McCoy D. and Hanratty T. (1977). Rate of deposition of droplets in annular two-phase flow. International Journal of Multiphase Flow, 3(4), pp. 319-331.

McLaughlin J.B. Aerosol particle deposition in numerically simulated channel flow. Physics of Fluids A: Fluid Dynamics, 1(7), pp. 1211-1224. (1989).

Mei, R. An approximate expression for the shear lift force on a spherical particle at finite Reynolds number. International Journal of Multiphase Flow, 18(1), pp. 145-147. (1992).

Melling A. and Whitelaw J. H. Turbulent flow in a rectangular duct. Journal of Fluid Mechanics, 78(2) pp. 289-315, (1976).

Moin P. and Kim J. The structure of the vorticity field in turbulent channel flow. Part 1. Analysis of instantaneous fields and statistical correlations. Journal of Fluid Mechanics, 155, pp. 441-464. (1985).

Morinishi Y. and Tamano S. Study on Differences in Turbulence Statistics between Compressible and Incompressible Low-Reynolds Number Turbulent Channel Flows Using Semi-Local Scaling. JSME International Journal Series B, 48(4), pp. 743-749 (2005).

Mortensen P. H., Andersson H. I., Gillissen J. J. J., and Boersma B. J. Dynamics of prolate ellipsoidal particles in a turbulent channel flow, Physics of Fluids, 20(9), (2008).

Mortimer L. F., Njobuenwu D. O., and Fairweather M. Effect of Four-Way Coupling on the Turbulence Field in Multi-Phase Channel Flows. In: Proceedings of the 11th International ERCOFTAC Symposium on Engineering Turbulence Modelling and Measurements. ETMM11, 21-23 Sep 2016, Palermo, Italy, (2016).

Mortimer L. F., Njobuenwu D. O., and Fairweather M. Near-wall dynamics of inertial particles in dilute turbulent channel flows. Physics of Fluids, 31, 063302. (2019).

Moser R. D., Kim J., and Mansour N. N. Direct numerical simulation of turbulent channel flow up to Reτ=590. Physics of Fluids, 11(4), (1999).

Moser R.D., and Moin P. Direct numerical simulation of curved turbulent channel flow. (1984).

Moser R.D. and Moin P. The effects of curvature in wall-bounded turbulent flows. Journal of Fluid Mechanics, 175, pp. 479-510, (1987).

NAO. Progress on the Sellafield site: and update. Comptroller and Auditor General. (2015).

NDA. Research and Development - Needs, Risks and Opportunities in Authority ND, ed. (2006).

NDA. NDA Annual Report and Accounts 2016 to 2017. Nuclear Decomissioning Authority, (2017).

NDA. Nuclear Provision: the cost of cleaning up Britain's historic nuclear sites. Nuclear Decomissioning Authority, (2019).

Nikuradse J. Untersuchung uber die geschwindigkeitsverteilung in turbulenten stromungen. Thesis, III, (1926).

Njobuenwu D.O., and Fairweather M. Dynamics of single, non-spherical ellipsoidal particles in a turbulent channel flow. Chemical Engineering Science, 123, pp. 265-282. (2015a).

Njobuenwu D.O., and Fairweather M. Deterministic modelling of particle agglomeration in turbulent flow. In: ICHMT DIGITAL LIBRARY ONLINE: Begel House Inc. (2015b).

Oesterle B., Petitjean A., Simulation of particle-to-particle interactions in gas–solid flows. International Journal of Multiphase Flow, 19, pp. 199-211 (1993)

O'Rourke P.J. Collective drop effect on vaporizing liquid sprays. Ph. D. thesis, Mechanical and Aerospace Engineering, Princeton University USA. (1981)

Owolabi B. E., Poole R. J., and Dennis D. J. C., Experiments on low-Reynolds-number turbulent flow through a square duct. Journal of Fluid Mechanics 798, pp. 398-410, (2016).

Pan, Y. and Banerjee, S. Numerical simulation of particle interactions with wall turbulence. Physics of Fluids. 8(10), pp. 2733-2755. (1996).

Pao, Y.H. Structure of Turbulent Velocity and Scalar Fields at Large Wavenumbers. The Physics of Fluids, 8(6), pp. 1063-1075. (1965).

Parsheh M., Brown M., and Aidun C. K., "On the orientation of stiff fibres suspended in turbulent flow in a planar contraction," Journal of Fluid Mechanics 545, 245, (2005).

Paschkewitz J. S., Dmitropoulos C. D., Hou Y. X., Somandepalli V. S. R., Mungal M. G., Shaqfeh E. S. G., and Moin P., An experimental and numerical investigation of drag reduction in a turbulent boundary layer using a rigid rodlike polymer. Physics of Fluids, 17(8), 085101, (2005).

Patera A. T. A Spectral Element Method for Fluid Dynamics: Laminar Flow in a Channel Expansion. Journal of Computational Physics, 54, pp. 468-488 (1984).

Pawar S.K., Padding J.T., Deen N.G., Jongsma A., Innings F., Kuipers J.A.M. Lagrangian modelling of dilute granular flow – modified stochastic DSMC versus deterministic DPM. Chemical Engineering Science, 105, pp. 132-142 (2014).

Po J.K. Developing Turbulent Flow in the Entrance Region of a Square Duct. University of Washington, (1975).

Pope S.B. Turbulent flows. IOP Publishing. (2001).

Prandtl D. Uber den reibungswiderstand stromenderluft. Ergebnisse der Aerodynamischen Versuch zu Göttingen, (1927).

Prat A., Sautory T., Navarro-Martinez S. A Priori Sub-grid Modelling Using Artificial Neural Networks International Journal of Computational Fluid Dynamics, Volume 34, 397-417, (2020)

Puragliesi R., Dehbi A., Leriche E., Soldati A. Deville M.O. DNS of buoyancy-driven flows and Lagrangian particle tracking in a square cavity at high Rayleigh numbers. International Journal of Heat and Fluid Flow, 32(5), pp. 915-931, (2011).

Rai M. M., Moin P. Direct Simulations of Turbulent Flow Using Finite-Difference Schemes, Journal of Computational Physics 96(1), pp. 15-53, (1991).

Raynal L., Augier F., Bazer-Bachi F., Haroun Y., Pereira da Fonte C. CFD Applied to Process Development in the Oil and Gas Industry – A Review. Oil & Gas Science and Technology. 71(3), 42, (2016).

Reynolds O. On the dynamical theory of incompressible viscous fluids and the determination of the criterion. Philosophical Transactions of the Royal Society of London, A. 186, pp. 123-164. (1895).

Richardson, L.F. Weather prediction by numerical process. Cambridge: University Press. (1922).

Riley J.J. and Patterson Jr G. Diffusion experiments with numerically integrated isotropic turbulence. The Physics of Fluids, 17(2), pp.292-297 (1974).

Rouson, D.W. and Eaton, J.K. On the preferential concentration of solid particles in turbulent channel flow. Journal of Fluid Mechanics, 428, pp. 149-169. (2001).

Rupp D. A., Njobuenwu D. O., and Fairweather M. Particle volume fraction effects in simulations of turbulent channel flows. In: Proceedings of the 12th International ERCOFTAC Symposium on Engineering Turbulence Modelling and Measurements. ETMM12, 26-28 Sep 2018, Montpellier, France. (2018).

Saffman P. G., Turner S. J. On the collision of drops in turbulent clouds. Journal of Fluid Mechanics, 1, pp. 16-30, (1956).

Saffman P. G. The lift on a small sphere in a slow shear flow. Journal of Fluid Mechanics, 22, 385, (1965).

Saffman P. G. Corrigendum to "The lift on a small sphere in a slow shear flow". Journal of Fluid Mechanics, 31, 624, (1968).

Sardina G., Picano F., Schlatter P., Brandt, L. and Casciola, C.M. Statistics of particle accumulation in spatially developing turbulent boundary layers. Flow, Turbulence and Combustion, 92(1-2), pp. 27-40. (2014).

Sardina G., Schlatter P., Brandt L., Picano F. and Casciola C.M. Wall accumulation and spatial localization in particle-laden wall flows. Journal of Fluid Mechanics, 699, pp. 50-78. (2012).

Schiller L. Neue quantitative Versuche zur Turbulenzentstehung. ZAMM-Journal of Applied Mathematics and Mechanics/Zeitschrift für Angewandte Mathematik und Mechanik, 14(1), pp. 36-42. (1934)

Schmidt, S., McIver, D., Blackburn, H.M., Rudman, M. and Nathan, G. Spectral element based simulation of turbulent pipe flow. In: 14th Australasian Fluid Mechanics Conference, Adelaide, Australia, Dec, pp. 10-14. (2001).

Secker, J., Young, M., Bradfute, J. Evaluation and mitigation of crud induced power shift. In: 19th KAIF/KNS Annual Conference, (2004).

Sehmel, G.A. Particle and gas dry deposition: a review. Atmospheric Environment (1967), 14(9), pp.983-1011, (1980).

Sharma G. and Phares D J. Turbulent transport of particles in a straight square duct. International Journal of Multiphase Flow, 32(7), 823, (2006).

Short M.P., Hussey D., Kendrick B.K., Besmann T.M., Stanek C.R., Yip S. Multiphysics modeling of porous CRUD deposits in nuclear reactors. Journal of Nuclear Materials, 443(1-3), pp. 579-587, (2013).

Smagorinsky J., Manabe S., and Holloway J. L. Jr. Numerical Results from a Nine-Level General Circulation Model of the Atmosphere. Monthly weather review, 93(12), pp. 727-768, (1965).

Snyder W.H., Lumley J.L. Some measurements of particle velocity autocorrelation functions in a turbulent flow, Journal of Fluid Mechanics, 48, 41, (1971).

Soldati A. and Marchioli C. Physics and modelling of turbulent particle deposition and entrainment: Review of a systematic study. International Journal of Multiphase Flow, 35(9), pp. 827-839. (2009).

Sommerfeld M. Interparticle Collisions in Turbulent Flows: A Stochastic Lagrangian Model. Tenth International Symposium on Turbulence and Shear Flow Phenomena, 44, (1999)

Sommerfeld M. Validation of a stochastic Lagrangian modelling approach for inter-particle collisions in homogeneous isotropic turbulence. International Journal of Multiphase Flow, 27(10), pp. 1829–1858, (2001).

Sommerfeld M., Zivkovic G., Recent advances in the numerical simulation of pneumatic conveying through pipe systems. In: Hirsch, et al. (Eds.), Computational Methods in Applied Science First European Computational Fluid Dynamics, Brussels, pp. 201–212 (1992).

Stokes, G.G. On the effect of the internal friction of fluids on the motion of pendulums. Pitt Press Cambridge, (1851).

Su, M. and Friedrich, R. Investigation of fully developed turbulent flow in a straight duct with large eddy simulation. Journal of Fluids Engineering, 116(4), pp. 677-684. (1994).

Süli E., Mayers D. An Introduction to Numerical Analysis, Cambridge University Press, ISBN 0-521-00794-1. (2003).

Tao, B., Katz, J. and Meneveau, C. Application of HPIV data of turbulent duct flow for turbulence modeling. In: 3rd ASME/JSME Joint Fluids Engineering Conference, pp. 18-22. (1999).

Tanaka T., Tsuji Y. Numerical simulation of gas–solid two-phase flow in a vertical pipe: On the effect of inter-particle collision. Gas–Solid Flows ASME FED-121, pp. 123-128 (1991).

Tracy H. J. Turbulent flow in a three-dimensional channel. PhD thesis, Georgia Institute of Technology, (1965).

Tsuji, Y. and Morikawa, Y. LDV measurements of an air-solid two-phase flow in a horizontal pipe. Journal of Fluid Mechanics, 120, pp. 385-409, (1982).

Tsuji, Y., Morikawa, Y. and Shiomi, H. LDV measurements of an air-solid twophase flow in a vertical pipe. Journal of Fluid Mechanics, 139, pp. 417-434, (1984).

Tsuji Y., Tanaka T., Yonemura S. Cluster patterns in circulating fluidized beds predicted by numerical simulation (discrete particle model versus two-fluid model). Powder Technology, 95, pp. 254-264 (1998)

Tsuo Y.P., Gidaspow D. Computation of flow patterns in circulating fluidized beds. AIChE Journal, 36(6), pp. 885-896 (1990).

Ueda H., and Hinze J. O. Fine-structure turbulence in the wall region of a turbulent boundary layer. Journal of Fluid Mechanics, 67(1), pp. 125-143, (1975).

Uijttewaal W. and Oliemans R. Particle dispersion and deposition in direct numerical and large eddy simulations of vertical pipe flows. Physics of Fluids, 8(10), pp. 2590-2604, (1996).

Van Wachem B., Zastawny M., Zhao F., Mallouppas G. Modelling of gas–solid turbulent channel flow with non-spherical particles with large Stokes numbers, International Journal of Multiphase Flow, Volume 68, 80–92, (2015).

Verwey E.J.W. and Overbeek J.T.G. Theory of the stability of lyophobic colloids. Journal of Colloid Science, 10(2), pp. 224-225. (1955).

Vreman A. Turbulence attenuation in particle-laden flow in smooth and rough channels. Journal of Fluid Mechanics, 773, pp.103-136. (2015).

Vreman A. Particle-resolved direct numerical simulation of homogeneous isotropic turbulence modified by small fixed spheres. Journal of Fluid Mechanics, 796, pp.40-85. (2016).

Vreman B., Geurts B.J., Deen N., Kuipers, J.A. and Kuerten, J.G. Two-and four-way coupled Euler-Lagrangian large-eddy simulation of turbulent particle-laden channel flow. Flow, Turbulence and Combustion, 82:47-71. (2009).

Vreman A. W., Kuerten J. G. M. Comparison of direct numerical simulation databases of turbulent channel flow at Reτ = 180, Physics of Fluids, 26(1), (2014).

Wang L. P., Wexler A. S, and Zhou Y. Statistical mechanical description and modelling of turbulent collision of inertial particles. Journal of Fluid Mechanics, vol.415, pp.117-153, (2000).

Wang Q. and Squires K. Large eddy simulation of particle deposition in a vertical turbulent channel flow. International Journal of Multiphase Flow, 22(4), pp. 667-683. (1996a).

Wang Q. and Squires K.D. Large eddy simulation of particle-laden turbulent channel flow. Physics of Fluids, 8(5), pp. 1207-1223. (1996b).

Wattendorf F.L. A study of the effect of curvature on fully developed turbulent flow. In: Proceedings of the Royal Society of London A: Mathematical, Physical and Engineering Sciences: The Royal Society, pp. 565-598. (1935).

Wilcken, H. Effect of curved surfaces on turbulent boundary layers. (1967).

Wilkinson M., Mehlig B., Bezugly V., Caustic activation of rain showers. Physical Review Letters, 97 (4), 048501. (2006).

Williams J.J.E., Crane R.I. Particle collision rate in turbulent flow, International Journal of Multiphase Flow, 9(4), pp. 421-435, (1983).

Winkler C.M., Rani S. L., and Vanka S. P. Preferential concentration of particles in a fully developed turbulent square duct flow. International Journal of Multiphase Flow, 30(1), pp. 27-50, (2004).

Winkler C. M., Rani S. L., and Vanka S. P. A numerical study of particle wall-deposition in a turbulent square duct flow. Powder Technology, 170(1), 12, (2006).

WMSYM. Sellafield Additional Sludge Retrievals, A Significant Step in Decommissioning Part of the U.K.'s Nuclear Legacy. WMSYM, (2016).

Yao J. and Fairweather M. Inertial particle resuspension in a turbulent, square duct flow. Physics of Fluids, 22(3), (2010).

Yeh, Y. and Cummins, H. Localized fluid flow measurements with an He–Ne laser spectrometer. Applied Physics Letters, 4(10), pp. 176-178, (1964).

Yeung, P. and Pope, S. Lagrangian statistics from direct numerical simulations of isotropic turbulence. Journal of Fluid Mechanics, 207, pp. 531-586. (1989).

Zamansky R., Vinkovic I., and Gorokhovski, M. DNS and LES with stochastic modelling of subgrid acceleration applied to solid particles in a high reynolds number channel flow. In: TSFP DIGITAL LIBRARY ONLINE: Begel House Inc. (2011).

Zhang H., Ahmadi G., Fan F. G., and McLaughlin J. B. Ellipsoidal particles transport and deposition in turbulent channel flows. International Journal of Multiphase Flow, 27(6), pp. 971-1009, (2001).

Zhang J., Tao B., and Katz J. Turbulent flow measurement in a square duct with hybrid holographic piv. Experiments in Fluids, 23(5), pp. 373-381 (1997).

Zhao F., Van Wachem B. G. M. A novel Quaternion integration approach for describing the behaviour of non-spherical particles, Acta Mechanica, 224(12), 3091-3109, (2013).

Zhao F., George W. K., and Van Wachem B. G. M. Four-way coupled simulations of small particles in turbulent channel flow: The effects of particle shape and Stokes number, Physics of Fluids, 27, 083301 (2015)

Zhao L., Andersson H.I. and Gillissen J. Turbulence modulation and drag reduction by spherical particles. Physics of Fluids, 22(8), p081702. (2010).

Zhu Z., Direct Numerical Simulation of Turbulent Flow in a Straight Square Duct at Reynolds Number 600, Journal of Hydrodynamics, Ser. B 21(5), pp. 600-607, (2009).